CLEARANCE MANAGEMENT IN TWIN SCREW COMPRESSORS

DAVID MALCOLM BUCKNEY

Thesis submitted for the degree of Doctor of Philosophy

in Mechanical Engineering

City, University of London

School of Mathematics, Computer Science and Engineering

August 2017

Table of Contents

List of Figures

List of Tables

Acknowledgements

This work was made possible through collaboration between my employer - Howden Compressors in Glasgow, and the Centre for Positive Displacement Compressor Technology at City, University of London; where I enrolled as an external student in 2010. Thanks must go to the management team in Howden for the continuing support of this work in light of ongoing business pressures. Thank you to Prof. Ahmed Kovacevic, Jim Fairbairn and Graeme Cook, among others, for having the vision to initiate this work. I am indebted to many other colleagues who have been supportive of this work over the years. Dr. Manoj Heiyantuduwa and Dr. Maria Wilson have provided valuable advice about their own postgraduate study experience and are great examples to me of how PhD graduates can play a valuable leading role in a commercial research environment.

Regularly visiting and working with the staff and students of the Compressor Centre has been a fantastic opportunity - thank you to City, University of London and all those involved in making my role as an external student possible. It's been a privilege to share in the vast knowledge and experience of the Compressor Centre. My first supervisor – Prof. Ahmed Kovacevic - has been instrumental in this work and has always generously dedicated time and energy to helping me. I'm grateful to have received both the patient encouragement I needed and the less patient encouragement when required. My meetings with my second supervisor – Prof. Nikola Stosic – were less frequent but always inspiring and have had a significant influence on the direction of this work. Thanks must also go to Professor Ian Smith for kindly proof reading and suggesting improvements.

Finally, thank you to my family who have helped get me to this point, particularly my wife Kirsteen who has supported me throughout my studies while we also embarked on other adventures together including finding a home, planning a wedding, and most recently, bringing up our daughter, Erin.

David Buckney

Glasgow, August 2017

Declaration

I confirm that this work is my own except where indicated by reference in the text.

I agree for this work to be submitted to the Institutional Repository of City, University of London for use in accordance with the Thesis Deposit Agreement.

David Buckney

Glasgow, August 2017

Abstract

Although the performance of twin screw compressors is heavily dependent on the rotor clearances within them, chamber models, used as design aids, allow for the specification of their magnitude and distribution but do not account for how these may vary during operation, as a result of internal temperature changes caused by the compression process.

A validated procedure has therefore been developed to enable a chamber model to predict compressor performance, while including the effects of rotor and casing distortion resulting from dependant thermal effects. This has been achieved by the use of surface boundary mapping to calculate the rotor and casing temperature exposure within the compression chamber resulting from initial performance estimates. These detailed temperature distributions are processed analytically using appropriate assumptions that allow calculation of component temperatures and thermal growth.

A program for calculation of leakage area curves has been adapted to support locally calculated variations in clearances. These updated area curves can then be fed back into the chamber model in an iterative procedure to simulate performance with thermally distorted clearances.

The inclusion of thermal clearance corrections generally improved the accuracy of the chamber model when predictions from it were compared with test results over a wide range of operating pressures and temperatures.

Furthermore, this work was found to be applicable in the evaluation of the interlobe clearance distribution between the rotors. Predicting clearance distortions and likely areas of rotor to rotor contact at a particular operating duty allows clearances to be optimised for the correct balance between performance and reliability; the results thus obtained were supported by findings from available test and tear down results.

Notation

Symbol	Units	Description
A	[m]	distance between rotor axes
A_I	[m^2]	interlobe leakage area
A_R	[m^2]	radial leakage area
C	[-]	rotor chamber identifier
D	[m]	rotor diameter
G_A	[m]	axial gap
G_I	[m]	local interlobe gap
G_I	[-]	interlobe boundary point
G_R	[m]	local radial gap
G_R	[-]	radial boundary point
H	[m]	rotor addendum
h	[kJ kg^{-1}]	specific enthalpy
h	[m]	lead length
L	[m]	rotor length
l	[m]	distance from suction plane
l_I	[m]	interlobe sealing line length
$\dot{m}$	[kg s^{-1}]	mass flow rate
N	[rpm]	main rotor speed
n	[-]	integer / point number
p	[Bara]	pressure
P	[-]	point on rotor or casing surface
Q	[kW]	heat
r	[m]	radius / polar co-ordinate
r_c	[m]	radius to casing bore
r_o	[m]	max radius (at outer diameter)
r_w	[m]	pitch radius

S	[-]	co-ordinate system
s	[-]	surface parameter along transverse rotor curve
T_a	[°C]	ambient temperature
T_B	[°C]	time averaged local temperature on rotor bore
T_{CP}	[°C]	averaged temperature over full casing plane
T_G	[°C]	gas temperature
T^*_R	[°C]	instantaneous local rotor boundary temperature
T_R	[°C]	time averaged local rotor boundary temperature
T_{RP}	[°C]	planar averaged rotor boundary temperature
U	[kJ]	internal energy
V_1	[m^3]	chamber volume at closing of inlet port
V_2	[m^3]	chamber volume at opening of outlet port
V_i	[-]	volume index – ratio V_2 / V_1
X, x	[m]	Cartesian co-ordinate
Y, y	[m]	Cartesian co-ordinate
Z, z	[m]	Cartesian co-ordinate
z	[-]	number of lobes (gear teeth) on rotor
α_F	[°]	polar flank angle measured from radial line
β	[°]	local angle parameter
β_{sl}	[°]	β at the *start* of cycle at the *leading* tip
β_{st}	[°]	β at the *start* of cycle at the *trailing* tip
γ	[°]	main rotor wrap angle from suction plane
ε	[-]	normalized surface parameter along curve s
θ	[°]	cycle angle measured at main rotor
θ_l	[°]	minimum cycle angle for a given point on casing
θ_t	[°]	maximum cycle angle for a given point on casing
θ_M	[°]	meshing angle
θ_{local}	[°]	local cycle angle on rotor surface
λ	[°]	local transverse profile rotation

μ_C	[°C^{-1}]	coefficient of thermal expansion for casing
μ_R	[°C^{-1}]	coefficient of thermal expansion for rotors
φ	[°]	polar co-ordinate
φ_c	[°]	angle to casing cusp (intersection of casing bores)
φ_{off}	[°]	main rotor lobe offset angle
φ_s	[°]	offset angle to start of cycle
φ_w	[°]	rotor wrap angle at length, L
φ_{gate}	[°]	gate tip angle at home position
ψ	[°]	transverse rotor surface normal measured on rotor co-ordinate system
ψ_H	[°]	local helix angle
ψ_{PA}	[°]	pressure angle - transverse rotor surface normal measured on global co-ordinate system
ω	[rad s^{-1}]	rotational speed

Additional Subscripts

1	main rotor / co-ordinate system fixed to casing at main rotor / inlet
2	gate rotor / co-ordinate system fixed to casing at gate rotor / outlet
01, 02	co-ordinate systems fixed to rotors
T, x, y	transverse, x, y components
in, out	inflow, outflow
l, t	leading, trailing
a, b, c	misc. labels

Acronyms

1D	1-dimensional

2D	2-dimensional
3D	3-dimensional
BH	blow hole
CAD	computer aided design
CFD	computational fluid dynamics
CMM	co-ordinate measurement machine
FEA	finite element analysis
HP	high pressure
LP	low pressure
OD	outer diameter
SCORPATH	screw compressor optimal rotor profiling and thermodynamics
SL	sealing line
SRM	Svenska Rotor Maskiner
SYM	symmetric profile

Chapter 1
Introduction

1.1 MOTIVATION

Twin screw compressors are widely used in the refrigeration and gas processing industries. They have increased in popularity over the decades and have replaced reciprocating compressors in many applications (Ohama, Kurioka et al. 2006). As a consequence of their widespread use, achieving modest gains in performance can result in a significant reduction in global energy consumption. One possible way to increase performance is to match the screw compressor to the application, i.e. the properties of the working fluid and the operating duty, by using uniquely optimised rotors as suggested by Singh et al. (Singh, Onuschak 1984) and demonstrated by Stosic et al. (Stosic, Smith et al. 2003). This has not traditionally been attempted by screw compressor manufacturers due to the specialised nature of designing the rotor profile geometry and the expense and lead time associated with modifying or procuring tooling to manufacture bespoke rotors. With the current availability of modern flexible profile generation tools (Stosic, Hanjalic 1997) and advanced manufacturing techniques (Holmes 2008), tailoring rotor designs for specific applications is more feasible. However there are still considerable challenges that need to be addressed in order to achieve this.

This work contributes to practical rotor optimisation for industrial applications within the constraints of a commercial manufacturing environment where there is a need to rationalise and limit the number of design variants engineered and manufactured. To make optimisation of rotor profile viable, the procedure must be reliable, fast and easy enough to implement for small batches of rotors. It was found from a review of relevant literature and experience gained, while working in industry, that existing rotor design and modelling tools are still

reliant on empirical observations, particularly in the prediction of absolute performance results and the specification and analysis of reliable clearances.

Improving clearance analysis and design will allow an optimum balance between performance and reliability to be achieved with minimum adaptation of rotor tooling and manufacturing programs. While much work has been published on the general design and optimisation of rotor profiles and twin screw compressor configuration, more fundamental research in the area of clearance analysis would be a useful contribution that would make the practical application of rotor optimisation more achievable.

1.2 THE TWIN SCREW COMPRESSOR

1.2.1 BASIC PRINCIPLES

The twin screw compressor, though complex in design, essentially comprises of only two principle moving parts. These are the two helical screw rotors which are usually designed with integrated shafts for drive, bearings and seals. All moving parts are in balanced rotating motion allowing high operational speeds and power density.

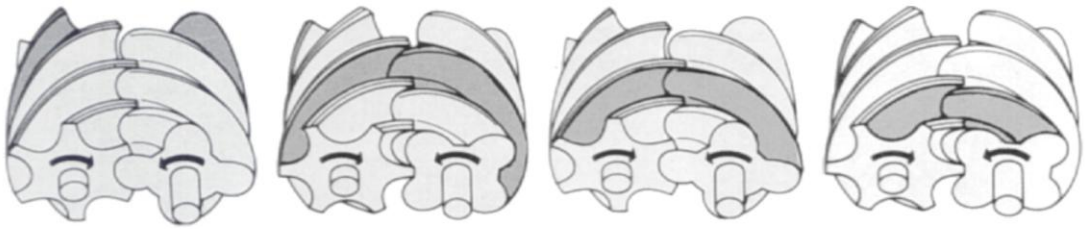

Figure 1-1: Compressor operation

Figure 1-1 shows a representation of the rotors in mesh at various stages of the compression cycle. These rotors are enclosed within a closely fitting casing, resulting in the cavities that become the working chambers of the compressor. As the rotors turn these cavities translate axially and change in volume due to the helical form of the rotors. At the suction end new cavities are formed which increase in volume. At the discharge end these cavities decrease in volume and

eventually disappear. The rotor on the right, with 4 lobes in this example, will be referred to as the 'main' rotor and the rotor on the left, with 6 lobes, as the 'gate' rotor.

It is vital that clearances are maintained where close interaction between the rotors and casing exists. As these clearances define part of the boundary for a given chamber they are also referred to as the *sealing lines*. The clearances along these sealing lines introduce leakage paths which need to be controlled for efficient operation. The area of the leakage path depends on the length of the sealing line and on the size of the clearance gap. Minimising the effect of leakage paths is one of the main aims when designing twin screw compressors (Fleming, Tang 1995).

1.2.2 PORTS AND INTERNAL COMPRESSION

A twin screw compressor does not require valve actuation for its operation because the working chambers move past stationary ports, periodically exposing each chamber to suction and discharge. In Figure 1-2 the *axial* and *radial* parts of the discharge port are shown in blue and green respectively. The chamber highlighted red has reached its smallest volume before it will be exposed to the discharge ports. This represents the volume, V_2, at the end of compression. The suction port, situated on the opposite side from that shown, will have closed when the maximum chamber volume is achieved to give the volume, V_1.

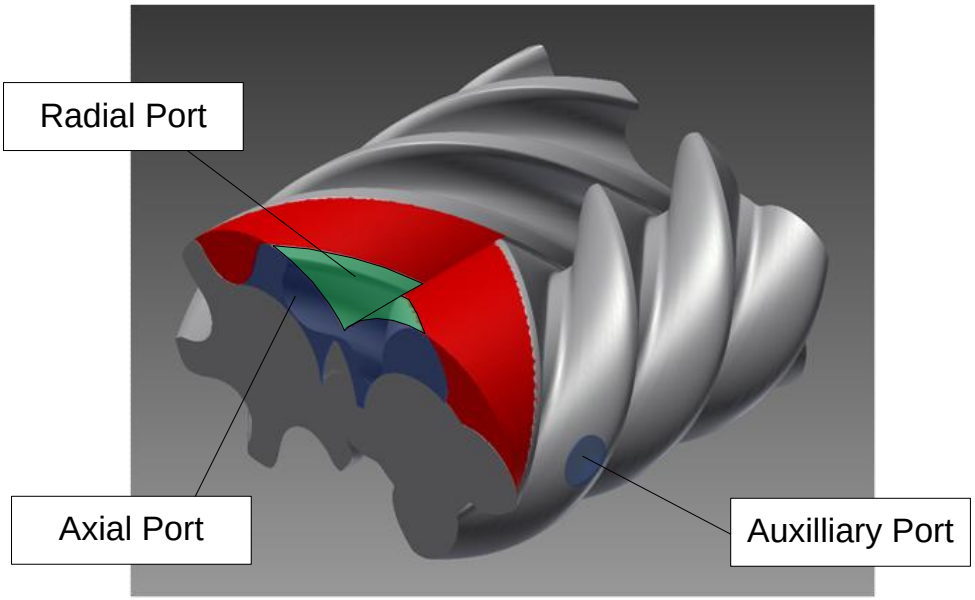

Figure 1-2: Meshing rotors highlighting single compression chamber

The volume index, or 'Vi', is the ratio of the inlet and outlet chamber volumes: V_1/V_2. The compressor should be designed to match the internal and external pressure increase so the target volume index is dependent on the compression ratio and gas properties. Systems have been introduced that allow the size of the ports to be altered, allowing a variable volume index. Ideally the port shapes should be as large as possible to minimise flow velocity and consequent losses. Depending on the casing design, the suction and discharge ports may only consist of an axial or a radial opening.

1.2.3 Capacity Control

In principle the capacity control of a rotary positive displacement compressor can be very straightforward as the speed of the drive is proportional to the volume delivered. However, due to the prevalence of fixed speed motors, compressors commonly use slide valves (O'Neill 1977, SRM 1966) or poppet valves which allow recirculation from the chamber back to suction, prior to compression. As a consequence of the internal leakage being virtually unchanged, higher temperatures will occur within the compressor at reduced capacity, making this an important operating condition for the analysis of clearances and reliability.

1.2.4 Oil Injection and Compressor Arrangement

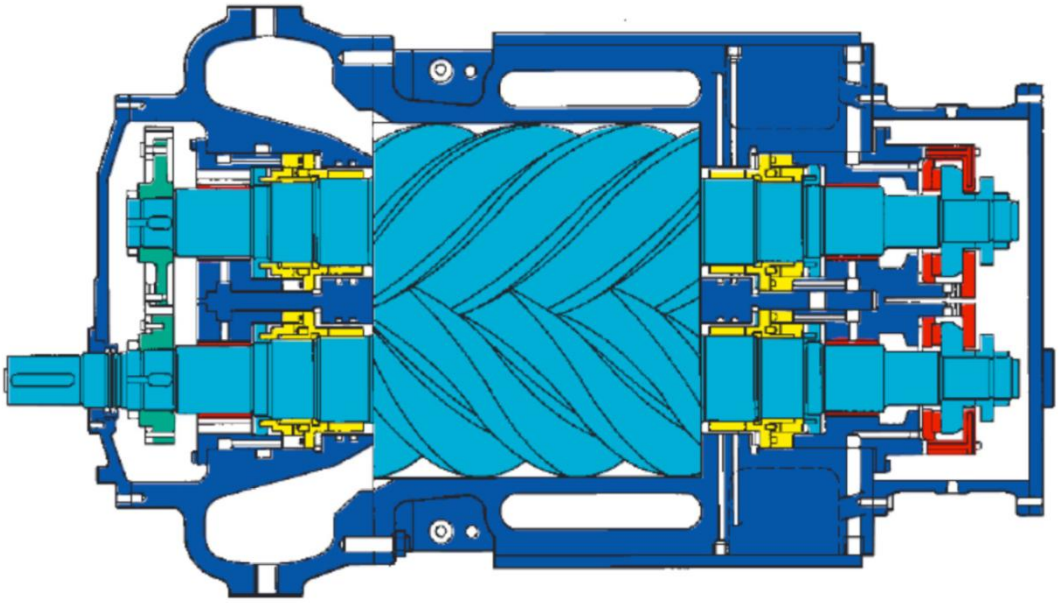

Figure 1-3: Oil free compressor

Twin screw compressors can be 'oil injected' or 'oil free' (O'Neill 1966). Figure 1-3 shows a sectional view of an oil free compressor highlighting some of the main components in different colours. The radial and axial bearings are highlighted in red; the seals are highlighted in yellow; and the timing gears are highlighted in green. With oil injected compressors the gate rotor is typically driven directly from the main rotor along a contact band on the rotors, eliminating the need for expensive timing gears. Another advantage of oil injected machines is that oil can drain directly into the compression chamber from the bearings eliminating the need for internal mechanical seals. Oil injected twin-screw compressors are capable of achieving higher compression ratios due to the presence of liquid in the clearance gaps and cooling of the compression gas by the liquid. However the viscous losses associated with oil injection limit the operational speed and therefore the capacity compared to an oil free compressor. Oil injected machines are dominant in refrigeration and air compression whereas oil free machines are common in gas processing applications in which contamination of the gas stream is not acceptable.

Oil injected compressors will typically operate at discharge temperatures less than 100°C while oil free compressors may operate with discharge

temperatures in excess of 200°C. So the clearance requirements are quite different for these machines. In addition to oil free compressors having larger overall clearances, extra measures are sometimes used such as tapering the rotors to introduce larger clearances at the hot outlet end, or introducing liquid cooling passages in the casings and/or rotor bodies. As oil injected compressors feature direct drive via rotor to rotor contact the rotor to rotor clearances must be designed in such a way that contact only occurs at a specific area where the relative sliding motion between the rotor surfaces is small (Stosic, Smith et al. 2005).

1.3 DESIGN AND OPTIMISATION

1.3.1 INDUSTRIAL APPLICATIONS

Screw compressors have been adopted for a wide range of industrial applications including:

- Refrigeration / Air-conditioning industries (cold stores, freezing)
- Extractive industries (mining, oil and gas)
- Process industries (chemical, petroleum refining, refrigeration, cement)
- Power generation (steam recovery and compression system, gas booster for gas turbine)
- Manufacturing industries (pneumatic applications)

These applications cover a wide range of operating duties in terms of: capacity; suction pressure and temperature; and pressure ratio. Typical process gases handled (Howden Compressors Ltd. 2008) include: Carbon dioxide; Helium; Hydrogen; Ammonia; Butane; Chlorine; Coke oven gas; Sour hydrocarbons; Ethane; Propane; Town gas; Natural gas; Steam; and Refrigerants. Different operating fluids can result in significantly different discharge temperatures and internal leakages depending on their specific heat ratio and molecular weight.

Figure 1-4: Howden WRV range (courtesy of Howden Compressors Ltd.)

In order to meet the demand of different markets, a number of compressor ranges have been developed over the years (O'Neill 1977). Figure 1-4 shows the Howden WRV range of oil injected compressors which are popular in the petrochemical and refrigeration industries. Generally, standard parts are used as far as possible for each size; which includes standard rotor designs. Some rotor options are available, for example in the Howden 'HS' oil-free range, the standard temperature limitations can be extended by introducing rotor cooling and rotor tapering. In this range, rotor cut-back is an option used to adjust the displacement capacity of the rotors for a given speed. Similarly on the 'WRV' range, some rotors with the same diameter but different lengths use the same rotor tooling, effectively resulting in a cut-back or extension of the same rotor design. These measures help to limit the need for more tooling and parts.

Using a standard rotor profile for a range of compressors is a far cry from early predictions (Singh, Onuschak 1984) and more recent examples in the literature of rotor profile optimisation (Stosic, Smith et al. 2003). This work initially set out to apply well documented rotor profile optimisation methods to small batches of industrial compressors in a commercially viable way. Research based on this remit identified some practical and design challenges without clear solutions, namely, precisely how to design optimum clearances that safely accommodate duty dependent distortions during operation and how to capture the impact of clearance distortions during modelling. Tackling these challenges

led to a research niche that focuses specifically on clearance design and evaluation rather than overall optimisation; this is explained in more detail in the following sections.

1.3.2 OPTIMISATION

A thorough overview of screw compressor optimisation was presented by Stosic (Stosic, Smith et al. 2003). This describes target functions; identification of suitable optimisation parameters and constraints; and application of a method to find local minima. Using a number of case studies, Stosic shows that different rotor designs are optimal for different applications, this depends on whether they are oil-injected or oil-free and on the working fluid and operating conditions. Other optimisation methods have also been demonstrated to be successful (Stosic 2005, Wu, Fong 2009, Hauser, Brummer et al. 2008). The advent of accurate thread grinding (Holmes 2008) brings flexibility, as changes can more readily be made to the form of the tool, making the possibility of optimising smaller batches of rotors more realistic and economical.

The design and optimisation of twin screw compressors can be broken down into three areas, namely: 'General Design', 'Profile Design' and 'Clearance Design'. The group of design variables that fall within each of these areas are often constrained together such that different levels of optimisation can be broadly described as shown in Table 1-1. These different areas will be elaborated on in the following sections.

Table 1-1: Commonly grouped constraints

<table>
<tr><th>Variable Group</th><th colspan="3">Optimisation Level</th></tr>
<tr><td>General Design</td><td>Constrained</td><td>Constrained</td><td rowspan="3">3</td></tr>
<tr><td>Profile Design</td><td>Constrained</td><td rowspan="2">2</td></tr>
<tr><td>Clearance Design</td><td>1</td></tr>
</table>

1.3.3 GENERAL DESIGN

'General Design' relates to the basic geometric proportions of a twin screw compressor; whether it is oil injected or oil free; and other features such as the type of bearings. Basic geometric parameters include the rotor diameter (D) for a given rotor centre distance; the rotor lobe gear ratio (z1/z2); the *wrap angle* describing the helix of the main rotor (φ_w); and the ratio of rotor length over diameter (L/D).

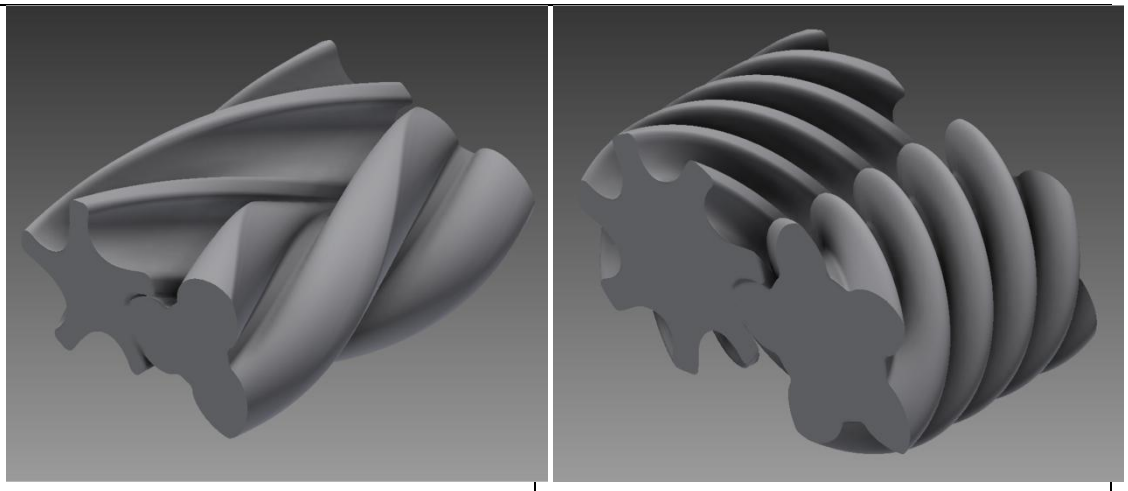

a) 3/5 lobe combination, L/D = 1.65, wrap angle = 200°	*b) 5/7 lobe combination, L/D = 1.10, wrap angle = 300°*

Figure 1-5: Comparison of rotors with different basic geometry parameters

A small lobe number combination, such as on the 3/5 lobe rotors shown in Figure 1-5a, results in a compressor well suited to high flow applications. This type of rotor geometry is often seen in applications such as engine superchargers where the inlet air is 'boosted' to increase mass flow with only a modest pressure increase.

The 5/7 lobe rotors shown in Figure 1-5b result in more working chambers but the compressor will have a smaller net capacity for a given rotor diameter. This larger number of lobes is well suited to higher pressure applications as the differential pressure between working chambers will be smaller. The rotors in Figure 1-5b also feature a smaller L/D ratio which when combined with the larger root diameter for the 5/7 lobe combination, results in very rigid rotors that can accommodate large bearings for high pressure operation.

Increasing the wrap angle of the rotors increases the ports areas and decreases the rate of filling and discharge due to a slightly longer cycle time. These factors both help reduce dynamic losses. However, the slower cycle time that reduces the flow rate in the ports also has the negative consequence of increasing the time over which leakage can occur.

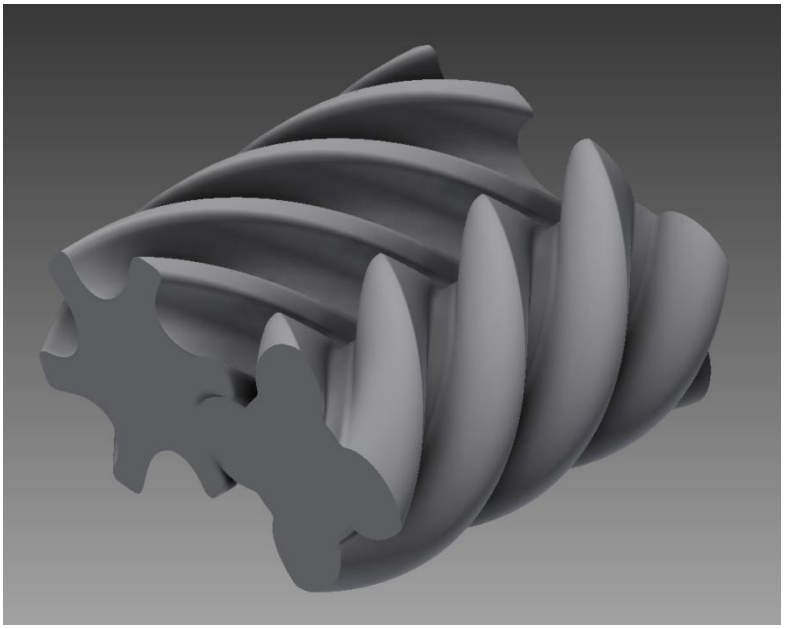

Figure 1-6: SRM standard rotor geometry. Equal diameters; 4/6 lobes; L/D = 1.65; wrap angle = 300°.

The need to optimise the general rotor arrangement is most applicable when designing a new range of compressors. When retrofitting rotors or designing rotors for a range of standard machines with finite casing geometry variations, it is common for the general rotor arrangement to be mostly constrained. Figure 1-6 shows the commonly used general rotor parameters used in the most popular compressor ranges in Howden Compressors. This design was based on experimental work and reports produced by SRM (SRM 1952) and provides good performance over a wide range of duties.

1.3.4 ROTOR PROFILE DESIGN

'Rotor Profile Design' relates to the geometry of the actual rotor lobes; referred to as the 'rotor profile'. This profile is usually defined on the transverse cross section for a single rotor lobe. An example profile is given in Figure 1-7.

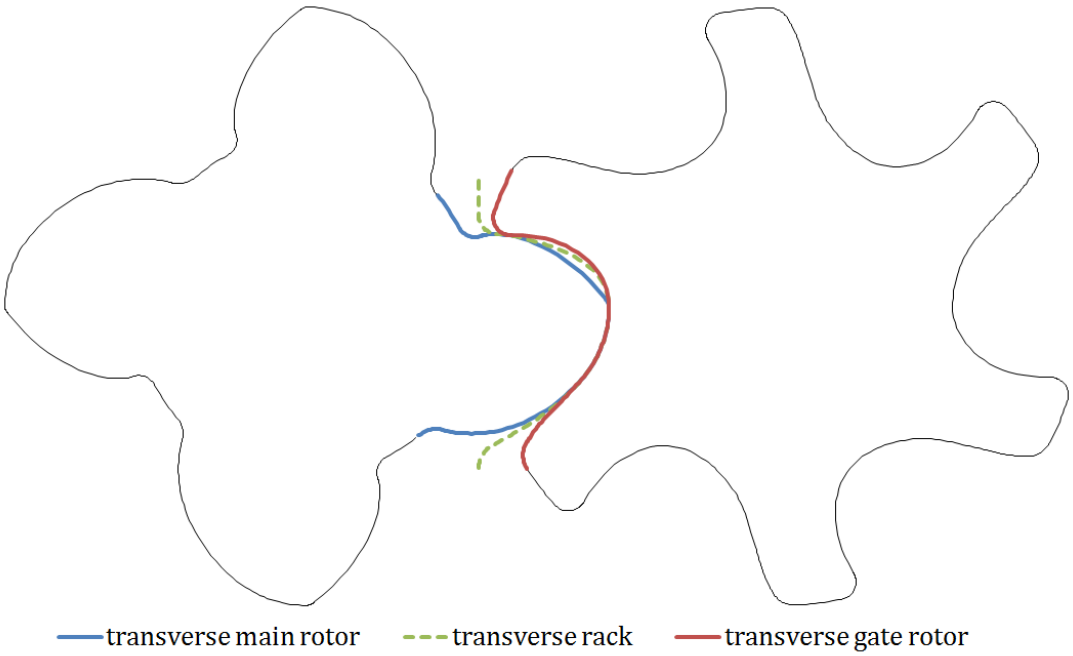

Figure 1-7: Rotor profile on transverse view

In order to maintain sealing, the rotor pair must be *conjugate*, resulting in continuous 'line contact' between the rotor surfaces (Litvin, Fuentes 2004). To meet this condition, the relative velocity between two rotor surfaces at the moment of 'contact' must be tangential to the rotor surfaces. Applying the conjugate condition it is possible to calculate any of the transverse segments from one of the others. The transverse rack segment is calculated as a rotor with an infinite number of lobes, or infinite rolling 'pitch' radius. This is useful as it is common for the main and gate rotor pair.

The rotor profile is defined using a *rotor generation* procedure that is usually patented; if publically disclosed. Rotor generation procedures commonly describe the profile on either the rotor or rack using various explicit curves with known derivatives that allow analytical calculation of the profile conjugates. Each rotor generation procedure has its own unique set of parameters that define the component curves of the profile. Modern generation procedures such as 'N' profile generation (Stosic, Hanjalic 1997, Stosic 2001), used in this research, provide a high degree of flexibility to the profile design while generating robust, reliable profiles. Rotor generation procedures will be discussed in more detail in the next chapter.

1.3.5 Clearance Design

'Clearance Design' does not, typically, come under the umbrella of rotor optimisation in the literature but if altering rotor designs for significantly different operating duties then this is a critical part of the design process that cannot be overlooked. The location and type of each clearance gap is highlighted in Figure 1-8. These are the rotor to rotor 'interlobe' gap, the rotor to casing 'radial' gap, and the rotor to casing 'axial' gap. The optimisation of clearance gaps involves finding an acceptable balance between performance and reliability for a given operating duty.

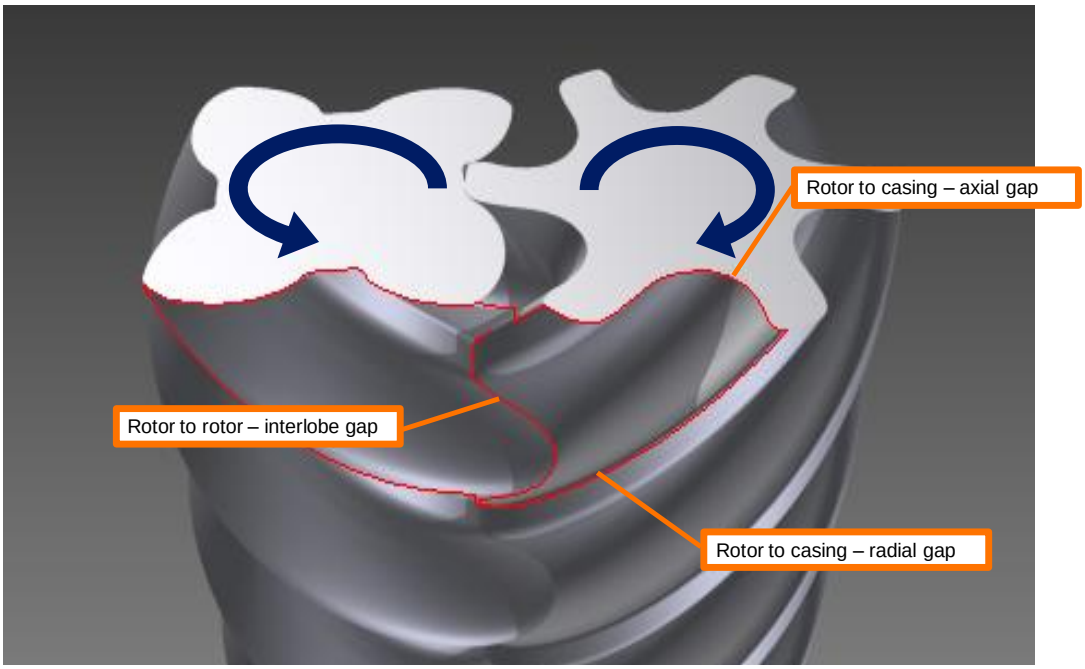

Figure 1-8: Rotor clearance gaps

A considerable challenge in this process is that it is difficult to determine what the actual clearances are. Clearances specified on paper will not reflect the clearances achieved once all component parts of the compressor are machined and assembled. Furthermore, clearances measured after assembly will not reflect the operational clearances which are subject to complex pressure and temperature distributions. These issues and others related to clearance design will be discussed in the following chapter. Later in this chapter the section 'Preliminary Studies' will introduce in more detail how clearances impact on the performance.

1.3.6 DESIGN SOFTWARE

Specialised software called SCORPATH, developed at City University, was used during this research. This software allows the user to generate new rotor profiles with full control over all of the rotor design parameters previously discussed. Critically, the software includes a simulation model allowing the performance of the newly designed rotor to be evaluated. This simulation model is detailed in the book: 'Screw Compressors, Mathematical Modelling and Performance Calculation' (Stosic, Smith et al. 2005) and will be discussed in more detail in the next chapter.

1.4 PRELIMINARY STUDIES

1.4.1 PERFORMANCE SENSITIVITY TO CLEARANCE

Reviewing clearance designs of previously tested compressors is a valuable input to designing new clearances. Mechanical testing is a requirement for all new compressors to ensure reliability therefore there is a growing bank of empirical data. Testing is unfortunately an expensive and time consuming process and, in an industrial manufacturing environment, reliability is prioritised; – often the intended operating duty might be well below the maximum design limit and may lead to non-optimal clearances.

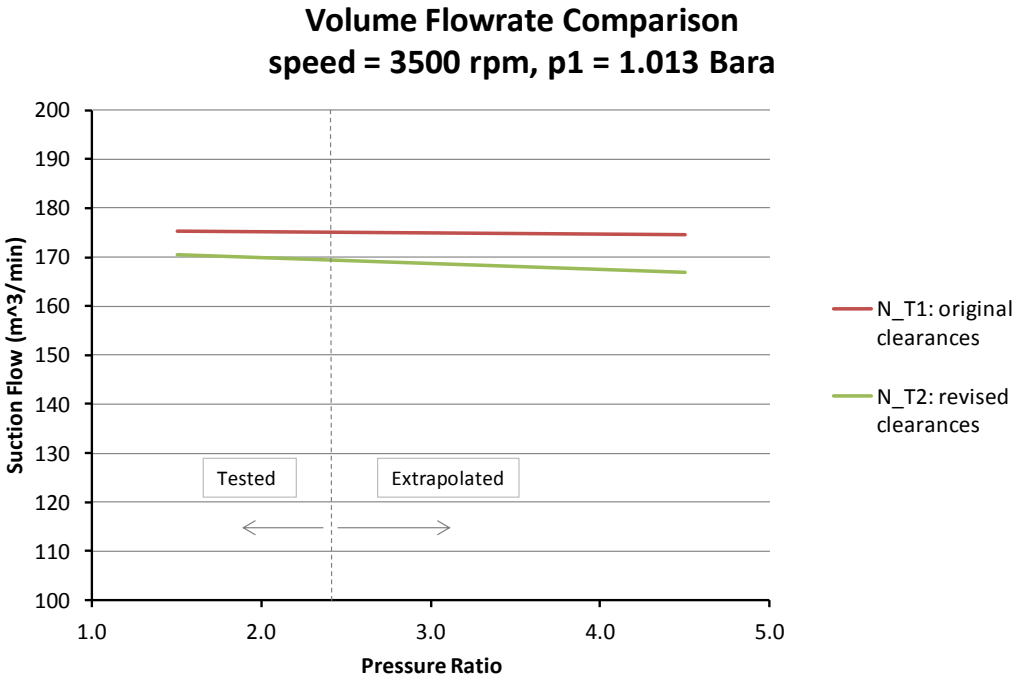

Figure 1-9: Rotor retrofit test results with different clearances

Figure 1-9 shows results from a Howden HS408165, oil free compressor. The compressor was retrofitted with newly designed N profile rotors (N_T1); these results are shown in red. Unfortunately, this rotor pair encountered serious rotor contact issues and testing was stopped. After conservatively relaxing the clearances, a second rotor pair was manufactured and tested (N_T2) with results shown in green. This performed well in terms of reliability however the flow was impaired as shown.

1.4.2 Clearance Influences and Behaviour

Due to the clearance sensitivities that relate to manufacturing and assembly tolerance there is always likely to be some degree of error between a simulation model based on ideal design clearances and actual test results. Stosic et al. (STOSIC, SMITH et al. 2003) highlighted the relative importance of the compressor housing and bearings on the interlobe clearances and presents a mathematical analysis to quantify potential clearance reductions. Assembled clearance deviations can be assessed with thorough examination of all compressor components as shown in other work by Sauls et al. (Sauls 1996).

However, not all clearance sensitivities are unique to a particular compressor build - it is possible to broadly distinguish clearance sensitivities as follows:

Duty INDEPENDENT clearance sensitivities:

- Manufacturing tolerance
- Assembly tolerance
- Bearing clearances

Duty DEPENDENT clearance sensitivities

- Pressure distortions
- Thermal distortions

Some operational clearance distortions can be considered to be dependent on the operating duty and should in theory behave in a systematic and repeatable manner for a given compressor design.

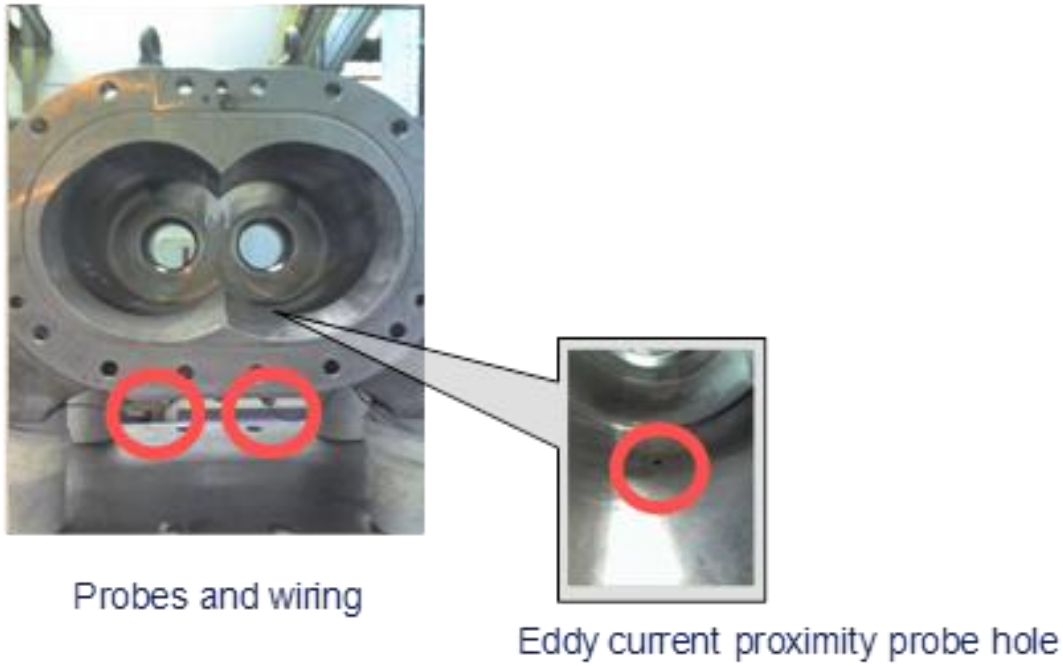

Figure 1-10: Location of proximity probe

This is supported by test results where the radial gap between the rotor and the casing was directly measured using a proximity probe at the location shown in Figure 1-10. These test results are later utilised in the last case study in chapter

6 where more detail will be provided. Figure 1-11 shows the measured radial gap plotted against the 'temperature increase' across the compressor; i.e. the difference between the discharge temperature and the suction temperature where in this case the suction temperature is the same as ambient. Different temperatures were achieved by testing the compressor over a range of compression ratios. The nominal gap size in this case is 0.150mm. The radial clearance can be seen to reduce at higher temperatures. This is only a limited sample of data but it does show a fairly linear relationship between gap distortion and operating temperature.

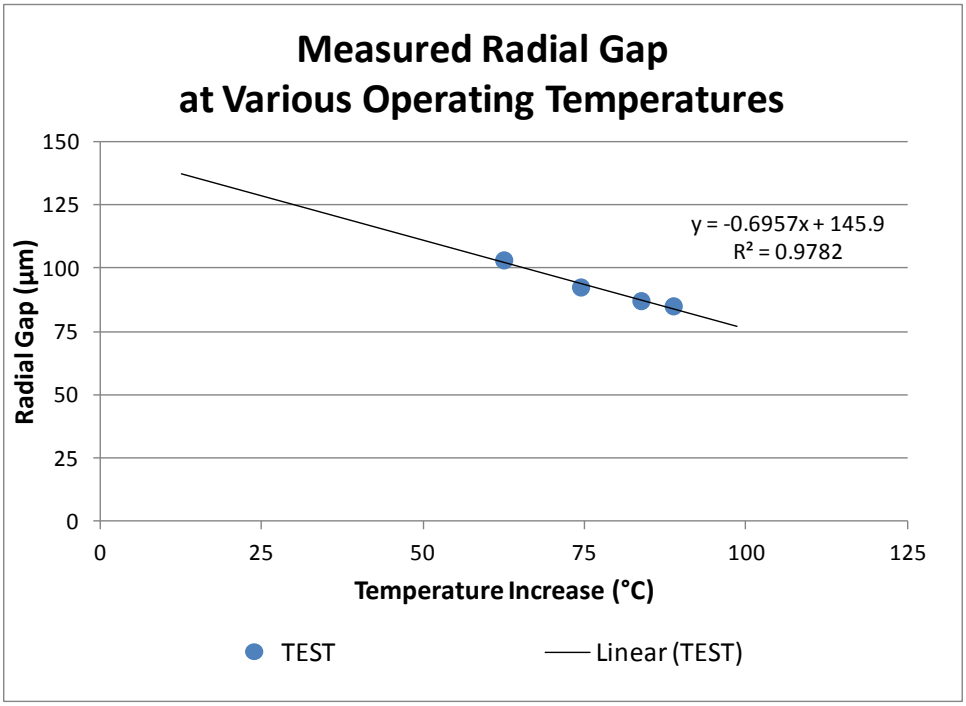

Figure 1-11: Measured relationship between operating temperature and clearance reduction

Thermal distortions have been analysed in detail in the literature by Sauls et al. (Sauls, Powell et al. 2007) and by Kovacevic et al. (Kovacevic, Stosic et al. 2002a) who showed that this is the dominant cause of operational deflections for oil free compressors. Assuming a simplified 2D cross-section with uniform rotor and casing temperatures, it is easy to visualise how clearances are affected. The left hand side of Figure 1-12 represents the effect of rotor thermal growth assuming no change in the casing geometry, including the rotor centre distance, A. With uniform heating of the rotors, the measured gap 'GapR' will

decrease in a very predictable manner. The change in the rotor overlap from H to H' represents the reduction in the horizontal, transverse component of the interlobe clearance.

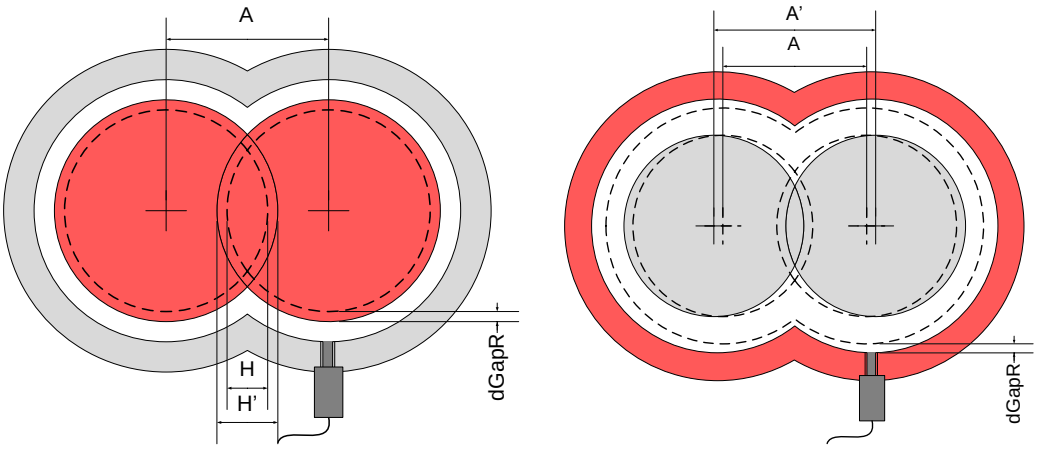

Figure 1-12: How rotor thermal growth and casing thermal growth affect clearances

The right hand side of Figure 1-12 shows the scenario of the casing thermal expansion without any deformations of the rotors. In this case the bearing centres will move apart, due to thermal expansion of the casing that houses the bearings. Due to this increase in centre distance from A to A' the interlobe clearance gap will increase. Additionally, the casing thermal growth will increase the measured radial gap 'GapR'.

In short, heating of the rotors acts to decrease clearances and heating of the casing acts to increase clearances. With a uniform temperature increase over the entire compressor where the rotors and casing are at the same temperature, the change in clearance gaps would be negligible since all dimensions would scale uniformly.

With this simplified model of clearance behaviour it is easy to imagine how operational clearance adjustments could potentially be integrated into a performance simulation model. The considerable difficulty lies in obtaining realistic rotor and casing temperature distributions and distortions.

1.5 CONCLUDING REMARKS

Full optimisation of twin screw compressors for specific applications would ideally involve a multivariable optimisation of every parameter that affects performance, however, there needs to be some rationalisation of the number of design variables. Modification of clearances requires minimum alteration to manufacturing setup and tools so in a commercial manufacturing environment this aspect of profile design and optimisation has the most potential to provide significant benefits for the smallest cost.

In most commonly used compressor simulation models (Hanjalic, Stosic 1997, Fleming, Tang et al. 1998b, Fujiwara, Kasuya et al. 1984, Sangfors 1984), operating clearances are treated as an input parameter that must be assigned by the design engineer. The effect of clearance distortions at elevated temperature is shown in Figure 1-11. Changing clearances has a considerable effect on compressor performance as observed in the results of Figure 1-9 and as reported in the work of Fleming et al. (Fleming, Tang 1995). It follows that if operational clearance deviations can realistically be represented in a compressor simulation model, then the model will predict performance more realistically over a wider range of operating conditions, without the need to revise the clearance input parameters manually. Such a model would also be invaluable in addressing the necessity to calculate optimal duty specific clearances accurately.

Further research that contributes towards the goal of designing rotor clearances for optimum balance between performance and reliability is required and would be a valuable contribution to the field of twin screw compressors. The sensitivity of the clearances to the operating duty and the consequent effect on performance and reliability is a critical factor in any rotor optimisation and is something that is not well addressed in available chamber models. An important question that this research aims to address is how far commonly used chamber models can reasonably be extended to predict and correct for duty dependant thermal effects.

1.6 THESIS OVERVIEW

Chapter 1: Introduction

This chapter covers the motivation behind this research, introduces the reader to some twin screw compressor basics and to the concept of optimising the compressor rotors for specific applications. In summary this chapter discusses the importance of clearance analysis and design to the rotor optimisation process and highlights this as an area that would benefit from additional research.

Chapter 2: Background Theory and Literature Review

This chapter draws on literature to set out details of twin screw compressor rotor geometry generation and analysis that are important foundations of this research. Some of the established geometry calculations used will be described here or referred to in appendices. This chapter continues to discuss established compressor models that will be used. Limitations in applying these current tools to clearance analysis are discussed.

Chapter 3: Research Objectives, Methods and Expected Contribution

Within this chapter the research goals are set out along with specific details of the expected contribution.

Chapter 4: Boundary Map for Rotor and Casing Surfaces

This chapter describes work to map the fluid properties from a chamber model to the rotor and casing geometry.

Chapter 5: Operational Clearance Distortions

Building on Chapter 4, it is described how approximated rotor and casing temperature distributions can be used to calculate possible operational clearance distortions. Variations in the local clearances are fed into the geometry calculation procedure in order to recalculate leakage areas used by the chamber model. In this way it is possible to calculate the effect of operational clearances on performance iteratively.

Chapter 6: Case Studies

This chapter presents case studies in which the methods outlined in Chapters 4 and 5 can be applied to the design and analysis of clearances for oil free and oil injected compressors.

Chapter 7: Conclusions and Future Work

Finally, this chapter will conclude this thesis and identify any future work.

Chapter 2
Background Theory and Literature Review

2.1 INTRODUCTION

This chapter draws on available literature to: describe the work that the current research is based on, introducing relevant theory as necessary; and clarify exactly where new contributions are required. The generation of rotor profiles is a necessary starting point for this research so this will be discussed first. This is followed by a review of how the clearances are designed. Once the rotor geometry has been generated the task of fully evaluating the geometry characteristics of the assembled rotor and casing is considerable. So this is also covered. Modelling of twin screw compressors is then reviewed; considering both performance prediction and thermal analysis methods.

2.2 ROTOR DESIGN

2.2.1 PROFILE GENERATION

Figure 2-1 introduces some basic terminology used to describe rotor profiles. The direction of rotation shown by the arrows is for compressor operation. Assuming compressor operation the leading and trailing flanks of each protruding lobe can be identified. The *leading main* flank meshes with the *trailing gate* flank and vice versa so this terminology is not always ideal. The flanks can also be referred to as the *round* flank or the *straight* flank as labelled. The tangent circles projected on the main and gate rotors represent the pitch circles; where rolling contact would occur.

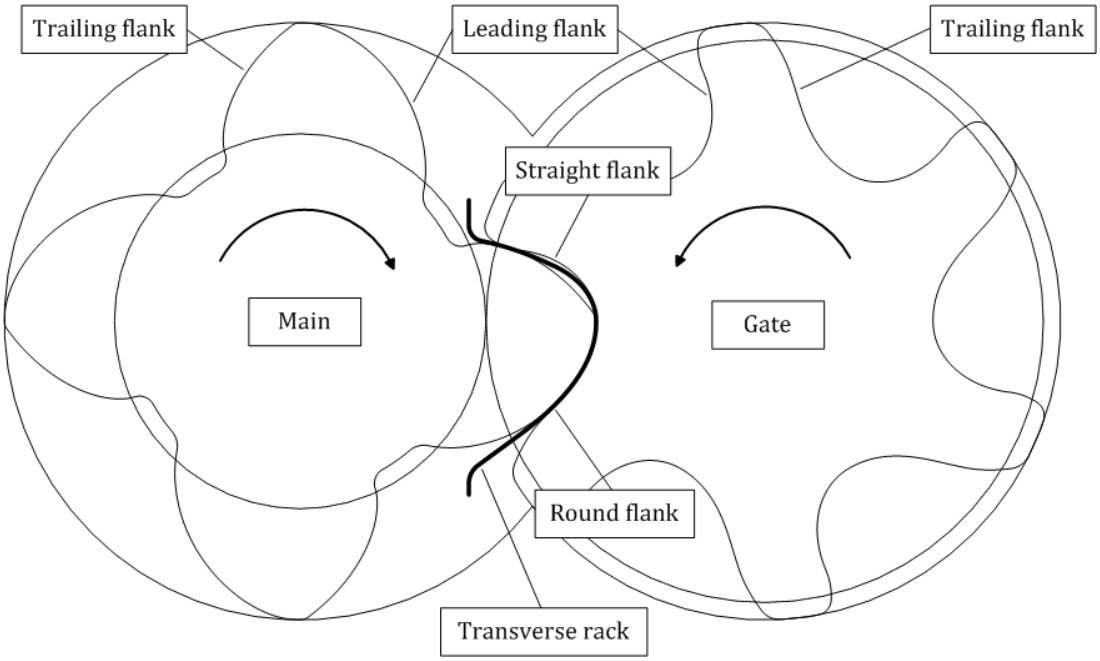

Figure 2-1: Transverse profiles showing terminology

The development of rotor profile generation procedures for screw compressors has been well documented (Stosic, Smith et al. 2005, Stosic, Smith et al. 2010). The following is a summary of some of the key developments. Figure 2-2 shows the end on view of two types of rotors which are significantly different in terms of lobe width and shape. The rotors in the top part of Figure 2-2 are a symmetric 'circular' profile which was used in the first manufactured screw compressors; note that the profile lobes are symmetrical and both the leading and trailing flanks of the main rotor are circular in shape. The rotors in the lower part of Figure 2-2 have a modern asymmetric rotor profile and have distinguishable round and straight flanks.

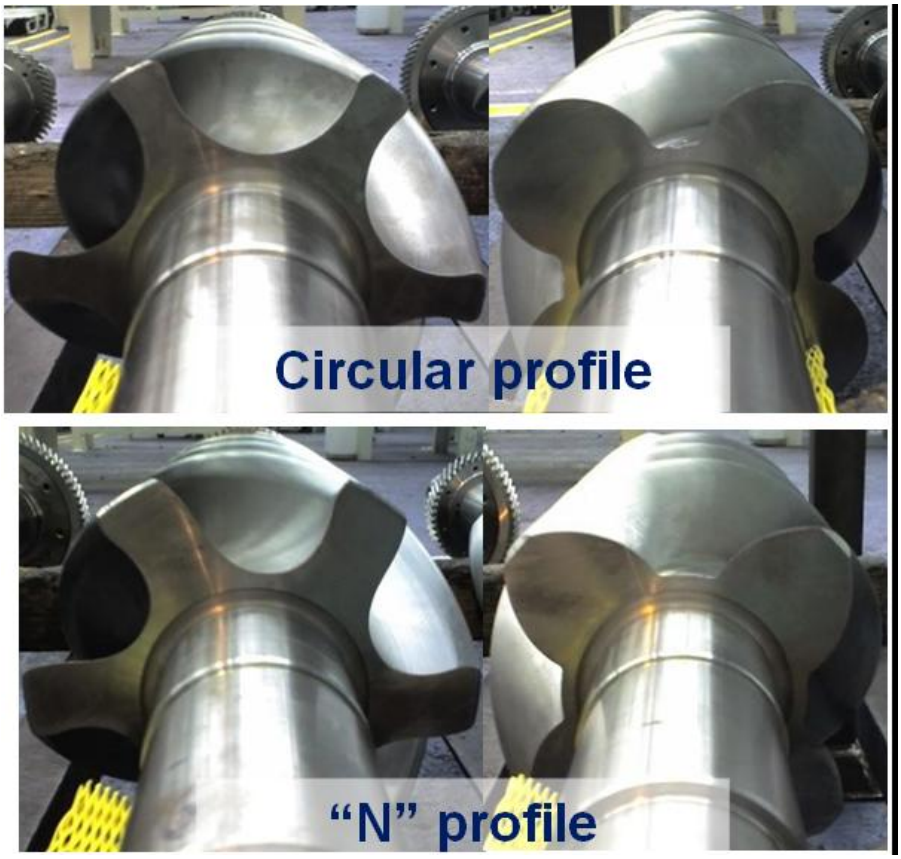

Figure 2-2- Photo comparing symmetric and N-rotor profile rotors

This asymmetry is one of the most important developments in screw compressors and was first introduced by SRM in the 'A' Profile (Schibbye 1979). In order to create the straight flanks, curves were generated by an undercutting action so that single points on the main and gate rotors trace the curves on the opposite rotors. It is this undercutting that allows the degree of asymmetry required for the straight flank on the gate lobe to curve forward in the direction of rotation and meet the tip of the main rotor closer to the cusp of the casing, considerably reducing the blowhole area whilst ensuring continuous 'contact' between the rotors. The blowhole will be explained in more detail in the following sections. Since the symmetric 'circular' and asymmetric 'A' profile, many new designs have been patented by SRM and others; they all now use asymmetric profiles.

The enveloping theory used to calculate conjugate rotors is explained by Stosic et al. (Stosic 1998). Calculating the conjugate section of the generated profile directly from the generating profile is most common. However, different

approaches have been proposed including the 'transverse rack generation method', the 'normal rack generation method' (Wu 1995), and 'meshing line generation' (Zaytsev, Infante Ferreira 2005). An early version of the transverse rack generation method described by Rinder (Rinder 1987) highlighted the advantages of rack generation. The use of straight lines on the transverse rack in the pitch line area results in involute curves on the rotors with constant pressure angle and excellent force transmission. The limitation of Rinder's rack was that the range of lines and circles used to define the rack resulted in a large blow hole area.

Stosic's N-profile improved the rack definition of the straight flank, and thus reduced the blowhole area. This was achieved by generating the straight portion of the rack from two small radii defined on the main and gate rotors (Stosic 2001), similar to the SRM 'D' profile (Astberg 1984). The use of small fillet radii rather than singular points is beneficial when designing a practical profile that requires carefully controlled clearances. The N-profile rotors in Figure 2-3 show a meshing rotor pair on the right and on the left the transverse rack from which they were generated. The letters identify the extents of the individual curve segments used to define the profile.

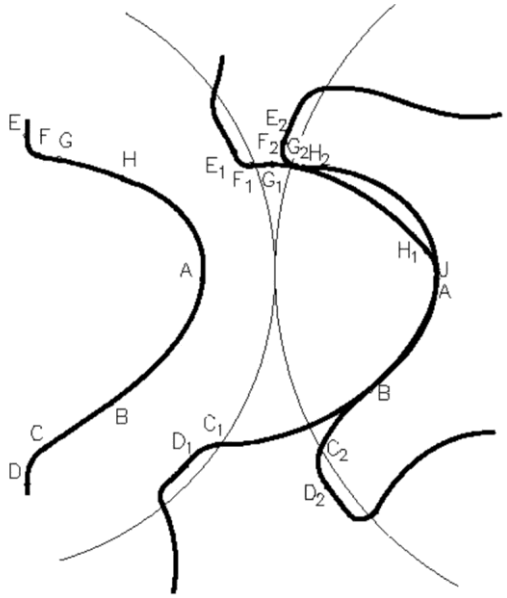

Figure 2-3: 'N' rotor rack generation

There are other interesting rack generation methods that have been proposed such as using a number of discrete points connected using a spline (Sundt 1997) rather than the traditionally used set of explicit curves. Furthermore, it is possible to derive meshing profiles using the Boolean operations built into modern CAD packages (Stosic, Mujic et al. 2008) without the need to calculate the meshing conditions. These types of approach are likely to gain more favour among profile designers, due to the freedom they bring, providing numerical errors are within acceptable limits.

It is important to understand that using the same profile generation method will not always result in the same profile shape; this is because modern methods allow several profile design parameters to be altered. For example, the rotor segment BC defined in Figure 2-3 is defined by the N profile generation procedure to be a straight line that results in involute curves on both rotors however the angle of this line is a parameter that can be readily adjusted for a specific N profile.

The patented 'N' profile procedure (Stosic 2001, Stosic, Hanjalic 1997) draws together the strengths of previous profiles: such as the asymmetry of the A and D profiles; and the involute curves at the pitch circle used in the Rinder rack; while bringing new benefits, due to the novel rack generation method which provides far more flexibility in the form of the remaining curves. This generation method is accessible to rotor design engineers as part of a commercially available design suite (Mujic, Kovacevic et al. 2010) and was used for all new rotors designed during this research.

2.2.2 CLEARANCE DESIGN

Modern manufacturing methods allow rotor profiles to be machined to a tolerance of 5 microns (Kovacevic, Stosic et al. 2002a) but consideration must be given to manufacturing and assembly errors of all other compressor elements (Stosic, Smith et al. 2003) and particularly to the operating deformations which are generally larger than the manufacturing tolerances (Sauls, Powell et al. 2007). As well as defining the size of the clearance gap it must be specified how the clearances are to be applied between the

components. The radial and axial clearances that occur between the rotors and the casing are fairly straightforward to implement; for example by designing the rotors to a slightly smaller diameter than the casing bore diameter. The interlobe clearance is introduced by removing material from one or both of the generated profiles. Fleming (Tang, Fleming 1994) investigated suitable practises to introduce interlobe clearances with tooling offsets however modern rotor design tools such as for the 'N' profile generation allow a high degree of control over the clearance distribution when designing the profiles.

Clearance distributions usually vary around the profile and can be significantly different in local areas. Figure 2-4 shows a transverse rack view with clearances mapped onto it. Clearances are represented by magnified vectors perpendicular to the rotor rack curve. The point numbers, e.g. '#01', on this figure represent inspection points where the designed clearances may have different values. The number that follows is the normal clearance gap (measured perpendicular to the surface) in microns, e.g. '+90'. In this figure the clearances are smaller on the round flank, on the left hand side, because this is the side where contact normally occurs. The larger clearances on the straight flank, on the right hand side, allow for rotor 'backlash' which is a necessary design feature of any practical gear system.

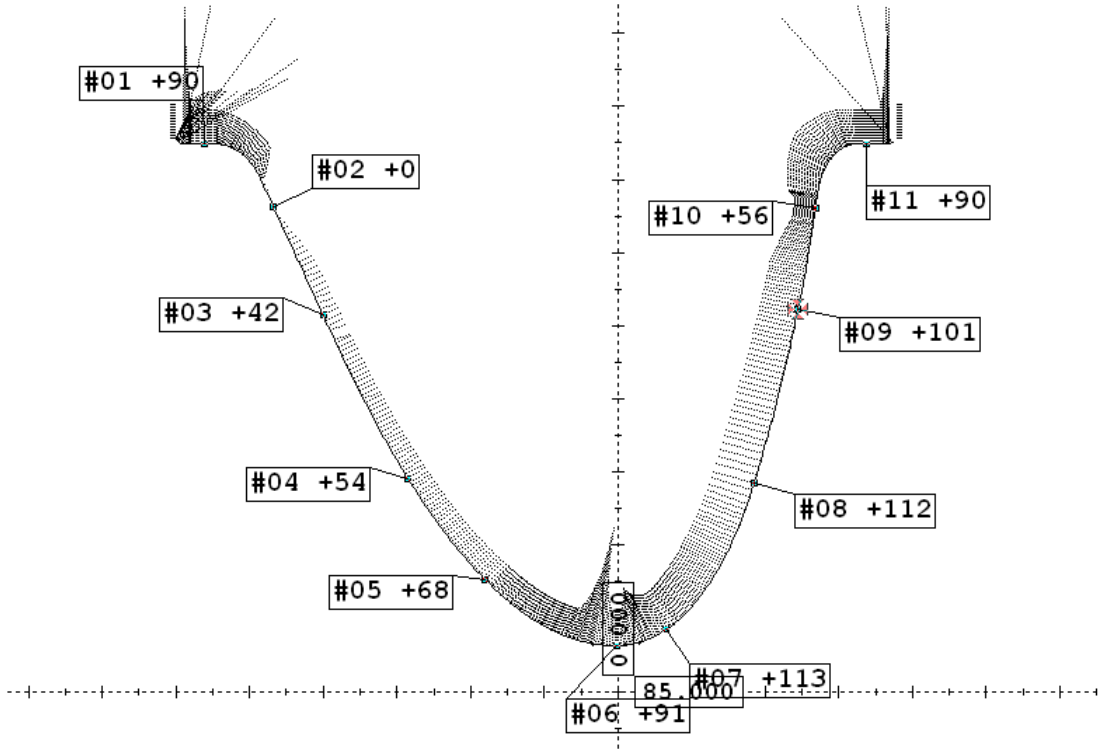

Figure 2-4- Clearance distribution on a rack projection

In one sense the clearances in oil injected machines are easier to manage than in oil free machines, because the temperatures are usually kept within much lower limits. However the lack of timing gears and the direct rotor to rotor drive adds more complexity to clearance analysis. Rotor contact is necessary for one rotor to drive the other; the objective is to control precisely where contact is to occur. Best practice for direct drive clearance design ensures only rolling contact at the pitch radius of each rotor as presented by Stosic et al (Stosic, Smith et al. 2005). Deviations from nominal design clearances, whether due to manufacturing and assembly variations or due to operational distortions, can result in a shift in the relative rotation between the main and gate rotors (Sauls, Powell et al. 2007): this further distorts the interlobe clearance distribution and must be considered in clearance evaluation for direct drive, oil injected compressors.

The discontinuities at each side, on the top and at the bottom of the clearance distribution in Figure 2-4, are introduced by 'tip seals', or 'wear strips' located at the outer diameter of each rotor. These narrow bands of protruding metal are a compromise that slightly increases the total interlobe leakage area but they

allow the radial clearance gap to be kept to a minimum without compromising reliability. It was claimed in Fleming et al (Fleming, You et al. 1994) that, if correctly designed, sealing strips can even reduce the viscous drag between the rotors and casing in oil injected compressors.

On the topic of clearance management, Stosic (Stosic, Smith et al. 2005) describes a sensible approach wherein the designed clearance distribution during *operation* should be such that rotor contact is not possible in any location that would lead to damage. Therefore the *design* clearance distribution is the target *operating* clearance distribution with additional allowance built in for thermal expansion. The optimal clearance design is therefore dependent on the operating temperature. More specifically it is dependent on the thermal distribution and distortion of the compressor components which are considerably more difficult to predict. Designing clearance allowance for operational distortions requires the temperature distribution within the compressor to be calculated. Examples of using numerical methods to calculate temperature distribution on the rotors and casing and thus the change in clearances have been given by Kovacevic et al (Kovacevic, Stosic et al. 2002a) and by Sauls et al (Sauls, Powell et al. 2006b). The former uses Computational Continuum Mechanics to allow the solution of both the solid and fluid domains on a 3D numerical mesh of the actual compressor geometry while the latter uses temperature results from a chamber model that are mapped to a 3D finite element grid. Both approaches showed good correlation when compared with experimental data.

2.3 GEOMETRIC CHARACTERISTICS

2.3.1 IDENTIFICATION OF GEOMETRIC CHARACTERISTICS

Compressor models used for the calculation of screw compressor thermodynamic and fluid flow processes, from non-dimensional thermodynamic chamber models (Singh, Onuschak 1984, Hanjalic, Stosic 1997, Seshaiah, Ghosh et al. 2007, Stosic, Hanjalic et al. 1986, Fujiwara, Kasuya et al. 1984, Sauls 1996) to three-dimensional computational fluid dynamics (CFD)

procedures (Kovacevic, Stosic et al. 2006, Kovacevic, Stosic et al. 2002b), require accurate representation of the rotor geometry. With 3D modelling methods, that represent the full fluid domain, the effect of the geometry on the thermodynamic result is inherent however when working with non-dimensional models, identification and quantification of geometric parameters such as the chamber volume, port areas and leakage areas is needed. Such parameters vary throughout the cycle and it is necessary to know the instantaneous value and gradient of each one.

As the helical rotors rotate within the compressor casing the actual volume of trapped gas within any one of the compressor chambers is continuously changing in shape, size and position. Each compression chamber is comprised of one main rotor and one gate rotor flute. These are the individual channels threading their way around the rotors. As the compression volume moves through the compressor it interacts with fixed ports (refer back to Figure 1-2) in the casing, resulting in port areas that continually vary and exist for only a certain portion of the cycle. Due to the necessity for clearances, leakage paths also exist at the sealing boundaries. Again these are continuously changing in shape, size and position throughout the compression cycle. Calculating these geometric characteristics of the twin screw machine, that are relevant to its performance, can become very complex depending on the level of realism and accuracy required.

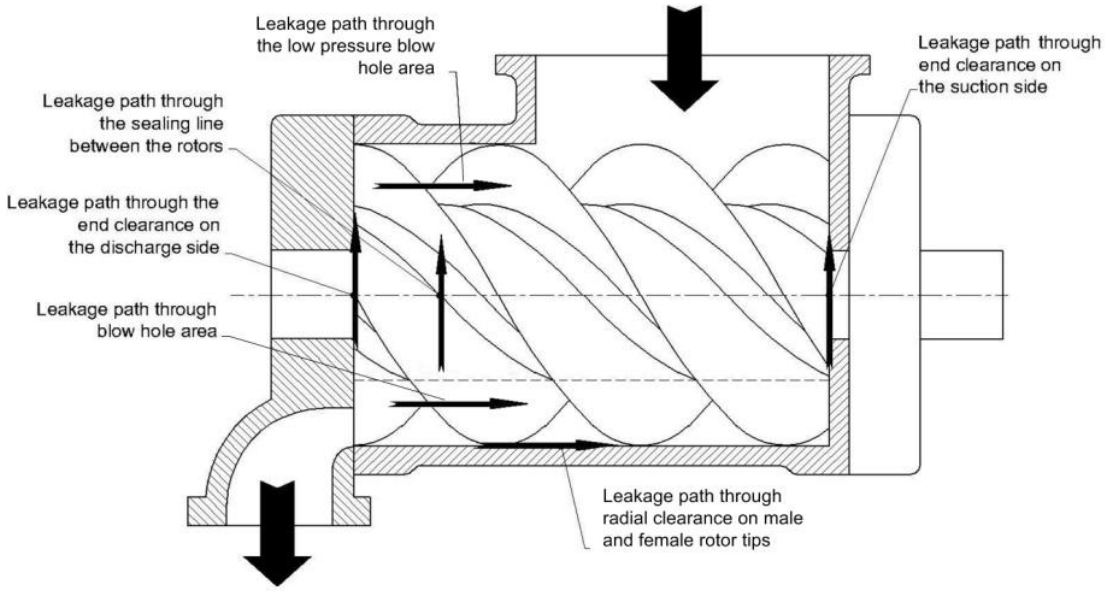

Figure 2-5: Defining discrete leakage paths

Accurate presentation of screw compressor geometry was given in the comprehensive screw compressor textbook by Sakun (Sakun 1960) and the screw compressor handbook by Amosov (Amosov 1977), both published in Russian. Rinder (Rinder 1979) presented a similar work in German. SRM, who were the first to license twin screw compressor technology have published numerous reports detailing how to analyse twin screw compressor geometry (SRM 1954, SRM 1953) however this material is still only available to licensees. Singh and Onuschak (Singh, Onuschak 1984) provide an overview of the main screw compressor geometric characteristics. Further work was published by Singh et al describing in more detail the methods used to calculate the geometric parameters (Singh 1990, Singh, Bowman 1990). Fleming and Tang (Fleming, Tang 1995) presented a model which described 6 distinct leakage paths – the interlobe gap; the radial gap; the discharge face axial gap; the suction face axial gap; the high pressure (HP) blowhole; and the low pressure (LP) blowhole; these discrete leakage paths are illustrated in Figure 2-5. Other geometric factors that can be considered include injection ports and part load re-circulation passages. Detailed breakdown of the flow areas can vary but the principle of describing volumes and areas as a function of the cycle is the same. Hauser et al (Hauser, Brummer 2010) demonstrated a procedure whereby

abstracted geometric parameters could be directly used for efficient optimisation of profile thermodynamic performance.

Of the leakage paths shown in Figure 2-5, the radial gap and interlobe gap are directly related to the design clearances. The discharge end face gap - also called the axial gap, is an assembly feature while the blow-hole area is an inherent feature of the rotor profile geometry. Not all leakages paths are present for the entire duration of a compression cycle and the size and shape of the leakage path will vary. Defining each of the leakage areas as a function of the cycle angle sufficiently captures the most important leakage characteristics in a very efficient manner. This efficiency comes at the cost of losing details such as how the area evolves along the path of the leakage flow. When describing leakage areas with non-dimensional area curves the simple objective is to calculate the minimum instantaneous area along each flow path as accurately as possible.

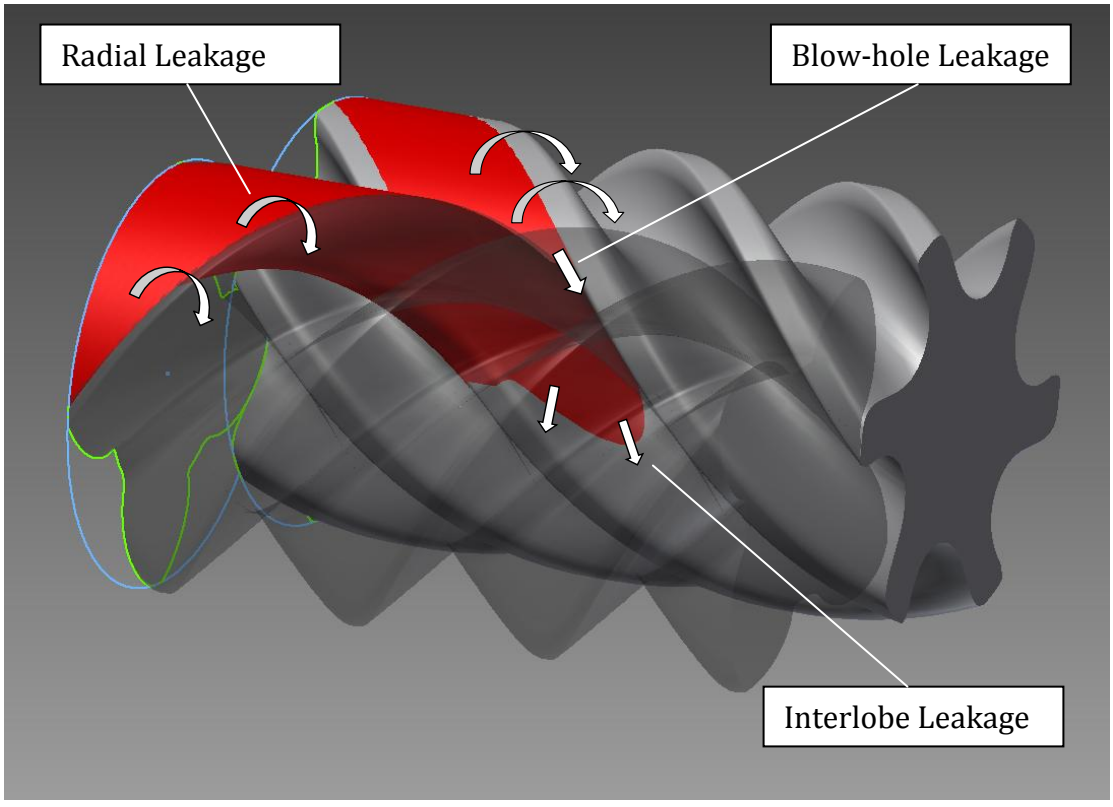

Figure 2-6: Leakage flow from chamber volume

The radial leakage path for outflow can be visualised as the flow along the curved arrows shown in Figure 2-6. For a given rotor position the length of this sealing line is easily calculated as it follows two helical paths that terminate at

the casing cusp where the main and the gate rotors meet, or at one of the axial end faces. If the radial clearance gap is constant, then the leakage area is the product of the sealing line length and the clearance gap. This simple representation of the clearance gap is common and has shown to be sufficiently accurate for many models in predicting the general performance metrics of compressors.

Adding a little more sophistication by allowing the local clearance gap to be varied along the length of the sealing line opens up the potential for investigation such as by Wu (Hsiao, Wu et al. 2012) who assessed how different clearance distributions along the interlobe sealing line affected performance. This approach also allows for investigation of how local clearances are affected by relative movements of the rotors and casing, for example, due to the relative rotation of the rotors. This was discussed by Stosic (Stosic, Smith et al. 2005) who highlighted that when contact occurs on the trailing flank of the main rotor (straight side) the net leakage area is reduced due to a longer sealing line on this side of the rotor profile. In these examples of non-uniform clearance analysis, the interlobe gap varies around the rotor profile but was considered constant along the length of the rotor and throughout the cycle. Additional sophistication is needed if the effect of tapered rotors or thermal distortions in local rotor hotspots is to be investigated.

2.3.2 CALCULATION OF GEOMETRIC CHARACTERISTICS

A screw compressor geometry calculation program name 'GEOM', developed at City University, was made available during this research. This featured accurate calculation of the actual port area, as described by Mujic (Mujic 2009). This program allows the detailed calculation of geometric characteristics and provided a basis for the novel work described in Chapters 4 and 5; therefore it is worth providing a brief overview.

The objective of 'GEOM' is to produce all necessary geometric characteristics required for the assessment and thermodynamic simulation of any given pair of twin-screw rotors for a positive displacement compressor or expander. The requirements are defined:

- to accurately calculate the required geometric characteristics of a screw compressor independently, prior to thermodynamic calculations
- to represent them as a function of the main rotor angle, θ
- to give the output of all the rotor geometric parameters in a single matrix
- to accept rotor co-ordinates, of any type and from any source, for calculation, allowing flexibility and independent rotor comparisons
- to support the use of arbitrary ports
- to support non-uniform clearance distributions along sealing lines and to allow local clearance modifications to be applied

The last point that is underlined was introduced during the course of this research to allow specific analyses of the clearances. An example of some of the typical results obtained is shown in Figure 2-7.

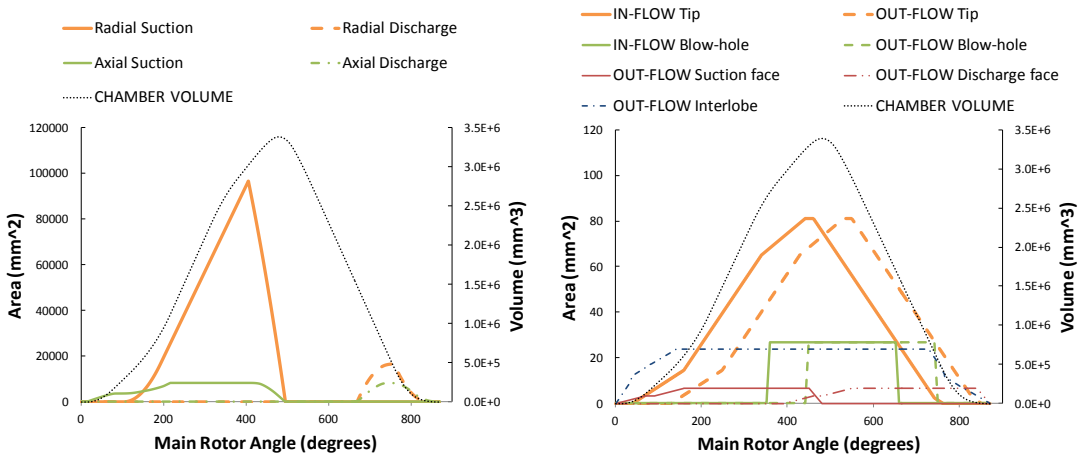

a. port areas

b. leakage areas

Figure 2-7: Volume and area curves

The port areas are shown in Figure 2-7a while the smaller leakage path areas are shown in Figure 2-7b, from which it can be seen that different leakage paths exist during different phases of the compressor cycle and for a particular working chamber there can potentially be two of each type of leakage path: one for in-flow from the previous chamber or from discharge; and one for out-flow to the next chamber or to suction. Details on the calculation of the volume curve and selected areas are included in Appendix A.

2.4 Review of Twin Screw Compressor Models

2.4.1 Chamber Models

Screw compressors are positive displacement machines which when modelled at a basic level can be represented by the compression cycle of a single control volume which is analogous to a piston cylinder arrangement. Calculated geometric characteristics and discrete leakage paths described as functions of the cycle can be utilised in a thermodynamic simulation to predict the expected performance of the new rotors without the need to fully represent the complex 3D geometry. By the 1980's there were a number of examples in literature of relatively mature computer programs to calculate screw compressor performance using such non-dimensional models (Singh, Onuschak 1984,

Hanjalic, Stosic 1997, Seshaiah, Ghosh et al. 2007, Stosic, Hanjalic et al. 1986, Fujiwara, Kasuya et al. 1984, Sauls 1996).

Sangfors (Sangfors 1984) published the principles of differential modelling of the screw compressor thermodynamic process. Stosic *et al.* (Stosic, Hanjalic et al. 1986) published a comprehensive application of such a differential model, previously widely used in the modelling of internal combustion engines and reciprocating compressors, to calculate screw compressor performance. Fujiwara et al (Fujiwara, Kasuya et al. 1984) presented a model where the volume curve was obtained using the principle of virtual work. Singh *et al.* (Singh, Bowman 1990, Singh, Onuschak 1984, Singh 1990) presented papers dealing with screw compressor geometry which was then utilised in a performance prediction model. Fleming and Tang introduced a model particularly suited to refrigeration applications (Fleming, Tang et al. 1998b, Tang 1995, Tang, Fleming 1992). The ability to estimate the performance of screw compressors quickly and accurately, as confirmed by many other authors, for example in Fujiwara and Osada (Fujiwara, Osada 1995) has revolutionised the field of the screw compressor design and optimisation and has been identified as a 'success story of the twentieth century', as stated by Fleming *et al.*(Fleming, Tang et al. 1998a, Fleming, Tang et al. 1998b).

By applying initial conditions at the compressor inlet, including pressure, temperature, and the resulting thermodynamic properties for a given working fluid, differential equations of conservation of energy and continuity are solved to describe the compression process. The changing volume of the compression chamber is factored into the energy conservation and the mass balance allows for mass inflow and outflow to simulate flow through the port and leakage paths. The thermodynamic properties throughout the compressor cycle can then be calculated, as a function of time, or shaft angle.

The model used in this research is that described by Hanjalic and Stosic (Hanjalic, Stosic 1997). Here the compression process is described as a classic open thermodynamic system using the non-steady flow energy equation with internal energy as the derived function from which all other properties such as

instantaneous pressure are found. The main thermodynamic assumptions of this model are:

- The fluid flow in the model is assumed to be quasi 1D i.e. only 1D flow through ports and leakage paths is considered while the chamber in non-dimensional
- This assumes that kinetic energy changes of the working fluid within the working chamber are negligible compared to internal energy changes
- Gas or gas-liquid inflow to and outflow from the compressor ports is assumed to be isentropic
- Leakage flow of the fluid through the clearances is assumed to be adiabatic.

Thus the non-steady flow energy equation can be written as:

$$\omega\left(\frac{dU}{d\theta}\right) = \dot{m}_{in}h_{in} - \dot{m}_{out}h_{out} + Q - \omega p\frac{dV}{d\theta} \qquad (1)$$

Each term in equation (1) describes the rate of energy change within the working chamber. On the right hand side the enthalpy of suction, discharge, leakage to and leakage from the chamber are all described with a mass flow balance (other fluids such as oil are included in this total enthalpy). The final terms are the rate of heat transfer and the compression work. Once the compressor has reached a steady operating temperature, the heat transfer, Q, describing the heat flux between the working fluid and the compressor and surroundings, is relatively small compared to the overall compression power and can therefore be neglected in terms of its effect of the thermodynamic process (Stosic, 2015). Therefore, in this work, Q has been set to zero so that the compressor surfaces are adiabatic. Note that this does not mean the compression cycle is adiabatic as heat is transported via leakage paths and to cooling liquid, if present, which have a far more significant impact on the thermodynamic process.

Each mass flow is calculated using orifice or nozzle flow theory and continuity. The areas used are those calculated from the rotor geometry which varies as a function of the compressor angle, θ. Similarly, the last term ωp dV/dθ which

describes the rate of compression work done on the system is dependent on how the volume varies as a function of the compressor angle. From this, all other properties are calculated (Stosic, Smith et al. 2005).

In the current model, the flow through the ports is assumed to be isentropic, corrected using an orifice flow coefficient. In other models the flow through the leakage paths is also often calculated as isentropic (Fujiwara, Mori et al. 1974, Sauls 1996, Seshaiah, Ghosh et al. 2007), if applicable, by using the critical pressure ratio for choked flow. Sachs (Sachs 2002) has confirmed experimentally that supersonic leakage flow can occur. These models neglect the effect of friction resulting in the need for correction factors. Bell (Bell, Groll et al. 2012) presents a numerical leakage model that uses a Fanning friction factor. Results from this model are compared against an isentropic nozzle flow, highlighting the large difference. In the currently used leakage model (Stosic, Smith et al. 2005) the leaking gas velocity is derived from the momentum equation, which accounts for the fluid-wall friction. The mass flow is found by integrating along a gap from the high pressure to the low pressure side so that the flow can be defined as adiabatic Fanno flow. This flow has been described in detail elsewhere (Stosic, Smith et al. 2005); a brief description has been included in B.1.2 Adiabatic Fanno Flow.

It has been demonstrated in a number of models that, for the purposes of performance calculation, simplified approximations of the leakage gap are adequate. In the adopted model the leakage areas between the sealing lines, i.e. through the interlobe, radial and axial gaps (G_I, G_R, and G_A), are assumed to be directly proportional to the length of the sealing line. This takes the clearance gap to be a constant, uniform value, denoted G^*. This is shown in equation (2) which calculates the leakage area A_I through the interlobe gap:

$$A_I = G_I^* l_I \tag{2}$$

What value this average gap size should take is unclear. Assuming nominal values for all manufacturing and assembly tolerances it is possible to calculate what is sometimes described as the 'cold clearance', which is what the gap would be when the compressor is at ambient temperature and stationary. It is

known that the operational clearances can vary significantly when the compressor is running (Sauls, Powell et al. 2007). Fleming dealt with this by using empirically derived flow coefficients to correct the flows predicted using the cold clearances (Fleming, Tang et al. 1998b); this approach is less suitable for a model which must be accurate over a wide range of operation duties and working fluids. If the temperature distribution of the rotors and casing is known, operational clearances can be predicted by considering thermal expansion. In a series of papers (Sauls, Powell et al. 2006a, Weathers, Sauls et al. 2006, Powell, Weathers et al. 2006) Sauls et al accurately predicted the rotor and casing temperature distribution of an oil injected compressor by applying boundary conditions from a chamber model to a finite element model. This analysis deals with duty *dependent* clearance sensitivities and provided excellent insight into the rotor and casing temperature distributions which can be fed back into a chamber model. However, it would be difficult to run such a detailed simulation for numerous rotors, requiring geometry updates; and for different applications, requiring re-calculation of boundary conditions.

Sauls et al have reported on a model which can make thermodynamic predictions based on 3D sealing geometry (Sauls, Powell); in this they tested the assumption that using an average clearance gap will provide accurate results. When comparing results using an average interlobe clearance against the actual interlobe clearance distribution for a number of scenarios, the results showed little difference in the net performance characteristics such as flow and power. However, if the primary interest is in clearance design and reliability it will be useful to fully represent this clearance distribution. The first step towards a full 3D clearance analysis is to calculate the leakage area by integrating the *local* gap value as shown in equation (3); in the case when the local gap can vary along the length of the sealing line. Hence it has been described as a function $G_I(l_I)$:

$$A_I = \int G_I(l_I)\, dl_I \qquad (3)$$

This describes the approach taken by Hsiao et al (Hsiao, Wu et al. 2012) to show how certain non-uniform clearance distributions can indeed have an effect on

compressor performance. However, this approach only really describes the change in the sealing line along the sealing line path with the assumption that the clearance distribution around the rotor profile is the same along the length of the rotor profile. To allow variation in the clearance distribution along the length of the rotors, either for rotor taper or for thermal distortion, that increase towards the hot end of the rotor, the local gap also depends on the cycle angle, θ, which describes where the sealing line is situated along the length of the rotors. It is not detailed by Sauls et al precisely how the local clearance gap is handled but this can generally be described in equation (4). There is a need for detailed procedures to be developed in this work in order to define unique local clearance gap values at any location in the compressor, at any rotor position.

$$A_I = \int G_I(l_I, \theta)\, dl_I \tag{4}$$

Other developments in chamber models in the literature include analysing assembly data acquired for each component using a co-ordinate measurement machine (CMM) and feeding this into the model (Sauls 1996); this deals with duty *independent* clearance sensitivities. Another novel model determines flow coefficients as variable functions by using findings of CFD analysis (Sauls 2011). The philosophy here is different from that of using empirical flow coefficients from test results in that the emphasis is on developing a deeper understanding of the compressor behaviour so that there is less reliance on empirical coefficients. This approach is important so that a design tool can be used reliably over a wide range of conditions with minimum 'calibration'. Such a powerful yet flexible model is a necessity for optimising a rotor profile for specific applications and significant contributions can still be made, particularly in the analyses of duty *dependent* clearance sensitivities.

2.4.2 Alternative Models

Singh and Schwartz (Singh 1990) proposed that for highly 3D problems such as the calculation of the blowhole area, full 3D surface representation would be more appropriate for calculation of leakage areas. Standard 3D CAD modelling packages can be used, but developing a robust procedure for extracting the

minimum cross sectional area on a plane perpendicular to the *actual* flow direction is a challenge. Computational fluid dynamics has been used to describe the full 3D flow field of a twin screw compressor by Kovacevic et al (Kovacevic, Stosic et al. 2003) giving insight into the internal behaviour of the compression volume. It can be argued that the actual flow through a highly 3D blow-hole can only be accurately modelled by using a 3D representation of the flow domain. However, the high level of expertise, computing power, and run time can make the use of CFD prohibitive in some instances.

To find a compromise between the accuracy of the expensive multidimensional calculations and fast, but less detailed chamber models, which is adequate for evaluation and general performance prediction and optimisation, a hybrid model was proposed by Mujic et al. (Mujic 2009) which used chamber models for analysis of flow within the rotor domains and a 3D approach at the compressor ports.

2.4.3 THERMAL ANALYSIS

The prediction of thermal distribution and distortion is beyond the scope of typical chamber models used for performance prediction and requires additional calculation procedures. With the application of reasonable assumptions the temperature distribution of the rotors can be approximated analytically based on the temperature of the operating fluid at the compressor inlet and outlet (SRM 1950). This procedure essentially performs a lumped analysis for each 2D cross section of the rotor based on an empirically observed axial temperature distribution.

If the assumptions are to be minimised, the complexity of the analysis can quickly increase. Generally some assumptions are required to prevent the analysis becoming prohibitively complex, this complexity is clear when considering the physical processes involved: Heat is generated due to compression; and kinetic losses in bearings, seals and oil. The convective heat transfer coefficient can vary locally on surfaces due to the complex flow and changing fluid properties within the compressor. The problem is compounded

by the interdependence between the compression process and component temperature and geometry.

Kovacevic et al (Kovacevic, Stosic et al. 2002a) developed a 3D numerical method to calculate flow and deformation by using a numerical grid for both the solid and fluid domains. This work showed how the 'operational clearances' for a given compressor and compression application are influenced by movement due to pressure and, more significantly in oil free machines, by thermal distortions. This work suggested a more or less uniform temperature across the transverse section of each rotor however because this work focused on analysis of the rotor bodies it is not apparent what impact heat conduction along the shafts, to or from the bearings, would have on the thermal distribution.

A commonly used approach to facilitate analysis is to de-couple the calculation of the thermodynamic boundary conditions from thermal analysis of the solids. The thermodynamics are calculated independently then used as an input for the thermal analysis. Hsieh et al (Hsieh, Shih et al. 2011) use the thermodynamic boundary conditions from a lumped parameter, chamber model. These boundary conditions were used with a finite element model of the rotors to calculate the temperature distribution in oil injected screws. This work discusses the numerous boundary conditions that the full rotor shafts are exposed to; including the bearing surfaces. The main challenge in this work was in establishing empirical constants to calibrate the unknown heat transfer coefficients. This is achieved by adjusting multiple coefficients to try and match temperatures at 3 points on each rotor, which were measured on test. The reported results state that there is a heat flux from the discharge end bearings, along the rotor bodies and outwards toward the compression fluid. For this to be the case the implication is that the main rotor outlet bearing temperature is greater than the bulk temperature of the working fluid. It is not clear from this work how the boundary conditions from the chamber model are applied to rotor surfaces though it is implied that the discharge end of the rotor is exposed to higher gas temperatures. Interestingly, the temperature variation from the

hot to the cold end of the rotors is actually said to be due to the larger heat flux from the discharge bearing, rather than the gas temperature distribution.

The last two examples resulted in quite different rotor temperature distributions over the transverse cross section of the rotors, demonstrating how sensitive these kinds of analysis are to any difference in the way boundary conditions are defined. In the thermal analysis done by Sauls et al, referred to previously (Sauls, Powell et al. 2006b, Sauls, Powell et al. 2006c), using a chamber model and FEA, the first of these papers goes into detail about how surface boundary conditions are extracted from the chamber model results and mapped onto the surface of the compressor casing and rotors. The significance of the interlobe sealing line boundary is discussed although the way in which the full chamber boundary is analysed, is not disclosed. These results show the round, or high pressure, side of the main rotor to be hotter than the opposite flank with the explanation that it is exposed to a high pressure chamber for longer. This result conflicts with Hsieh whose results, discussed previously, show the rotor to be slightly cooler on the round side.

Analyses from closely related fields are interesting to compare. Nilolov et al (Nikolov, Brummer 2012) uses an iterative coupling of a thermodynamic chamber model and FEA thermal simulations. This highlights the interdependence between the thermal distortion, leakage gap size and the thermodynamic performance for a twin screw expander. Gao et al (Gao, Yang et al. 2011) performs a temperature and thermodynamic analysis for a twin screw multi-phase pump in which temperature and pressure transducers are embedded into the rotor bodies. The results from this experiment supports the assumption that the temperature at a point on the rotor surface can be considered to be steady state at it rotates due to the high rotation speed and good thermal conductivity of the rotors. The presented temperature distribution on the rotors shows the surface temperature to increase from inlet to outlet due to the gas temperature increase as would be expected. In the core of the rotor the temperature gradient along the length of the rotors is smaller due to conduction. As a result the transverse cross-section of the rotors at the discharge end of the rotors is hotter outside and cooler inside; at the inlet end

the opposite is true. This paper also considers deformation due to the pressure distribution but notes that this is negligible compared to the temperature deformation. Kovacevic et al apply a solid-fluid interaction analysis to a novel screw compressor-expander (Kovacevic, Stosic et al. 2006a). This analysis is built on in (Kovacevic, Stosic et al. 2006b) which estimates clearance gap distortions using the gas discharge temperature by mapping numerical and experimental results. Both Kovacevic and Gao discuss the need to consider the rotor and casing material properties and how this influences gap distortion during operation.

2.5 CONCLUDING REMARKS

Some relevant background has been given on profile generation and the way in which clearances are applied to the rotors. The concept of abstracting the compressors geometric characteristics for the purposes of modelling and clearance analysis is a balance between efficient modelling and accurately capturing enough detail for the type of investigation required. To investigate the behaviour of clearances in detail, the conventional clearance approximation that assumes uniform gaps is not suitable. Additional sophistication is needed if the effect of thermal distortions in local rotor hotspots is to be investigated.

The need to understand the thermal distribution in the compressor is vital to understanding operational clearance distortions. However, the thermal analysis procedures that should provide the most detail and realism are not necessarily the most appropriate for a robust clearance design and optimisation procedure. This review has identified some variations in rotor temperature distribution results from different analyses; this doesn't necessarily mean that one analysis is wrong but it highlights how these sophisticated tools are still highly subject to the boundary conditions assumed, whether correctly or incorrectly.

Chamber models are well established tools that have been shown to be accurate for general performance prediction, with this in mind it can sometimes be counter-productive to introduce additional complexity since the model efficiency may be reduced without an overall improvement in accuracy due to

other inherent assumptions such as the way in which leakage flow is calculated. However in certain specific analyses, adapting existing chamber models can provide valuable new insights with minimum decrease in model efficiency. For example, when Mujic (Mujic 2009) replaced approximated sine curves with port area curves derived from actual rotor and casing geometry, he enabled the investigation of pressure pulsations due to subtly different port area curves.

An objective of this research was to introduce new modifications that allow compressor analyses, focusing on the estimation of operational deformations in clearance gaps and quantifying how performance and reliability is affected. It has already been shown that the thermodynamic results from a chamber model can provide valuable and detailed boundary conditions for FEA thermal analysis (Sauls, Powell et al. 2006b), thus giving very detailed results, albeit with accuracy still heavily dependent on the assumptions used. On the other hand it has been shown that simple empirical adjustments to clearances, as a function of the discharge temperature, can improve the correlation between a chamber model and test results (Buckney, Kovacevic et al. 2011, Kovacevic, Stosic et al. 2006). There is significant scope to process and utilise the detailed thermodynamic results from a chamber model in a simplified analytical analysis using appropriate assumptions. With minimum additional complexity an adapted chamber model and geometry calculation tool could efficiently provide useful results for the design and optimisation of rotor clearances for specific applications. This effect of duty dependent thermal clearance sensitivities is not directly fed back into any of the existing chamber models reviewed.

Chapter 3
Research Objectives, Methods and Expected Contribution

3.1 STATEMENT OF RESEARCH

Efficient estimation of the size of operational clearances is a critical requirement for reliable calculation of a twin screw compressor performance and reliability; these are necessary inputs for design and optimisation of screw compressors for specific applications.

The aim of this research is to develop and validate procedures which will enable analysis, design and optimisation of the operational clearances in industrial twin screw compressors in order to improve their performance and reliability.

Thermodynamic results obtained from chamber models are readily available but underutilised. Such results could be efficiently processed and, with the application of suitable assumptions, used for the analysis of distortions of compressor elements due to thermal loading. The distortions of the compressor elements, i.e. rotors and casing, cause clearances to change from 'cold' to 'operational' clearances. The operational clearances can be effectively estimated using proposed mapping of two dimensional computational surfaces of rotors and casing and then these can be utilised in a chamber model to predict the performance of screw machines with operational clearances more accurately. This approach sacrifices some of the accuracy and realism of the 3D simulations of the solid and fluid domains in order to maintain the efficiency and speed of calculation with chamber models.

A key output of this research will be validated tools and procedures that can be readily applied to the design and optimisation of twin screw compressors for specific applications.

3.2 OBJECTIVES

Develop a boundary mapping procedure to fully describe exposure of compression chambers to rotor and casing surfaces, thus allowing temperatures and pressures calculated by thermodynamic model to be mapped.

Develop a procedure to estimate change in radial and interlobe clearances due to thermal loading on the rotors and casing.

Integrate boundary mapping and clearance calculation procedures with a thermodynamic model to calculate operational clearances and allow calculation of performance with updated clearances.

Validate the developed procedure for different oil free and oil injected compressors by the use of experimental results.

Study the geometric characteristics of oil free and oil injected rotor profiles.

3.3 METHODOLOGY

Generation of Rotor Profiles:

- For the purposes of this research rotor profiles will be generated using existing methods such as those used for the N-Profile

Calculation of Geometric Characteristics:

- A geometry calculation program (GEOM) will be further developed based on previous work at City University. The input to this program will be the x and y co-ordinates of the rotor profiles, thus allowing profile input data from other sources
- All rotor geometry including swept areas and volumes will be calculated as a function of the compressor cycle angle
- Particular detail will be given to accurately representing leakage paths individually and incorporating functions to vary the leakage areas as a result of operational effects
- Support calculation of areas affected by complex clearance distributions

Calculate Performance:

- The geometry calculation program will provide the input to the chamber model that will calculate the performance of the compressor. The basic integration of the new program is shown in Figure 3-1
- Verify performance predictions with available test data
- Investigate how operational clearances vary at operational temperatures and pressures and quantify the impact this has on predicted performance
- The clearance areas and thermodynamics will be solved iteratively to include operational effects where possible. This should improve the accuracy of performance prediction and form a basis for optimum clearance design for specific applications
- *Study geometry characteristics* of rotor profile using a new program suite
- Validate predicted results and compressor reliability with test results
- Utilise test results to refine models / procedures

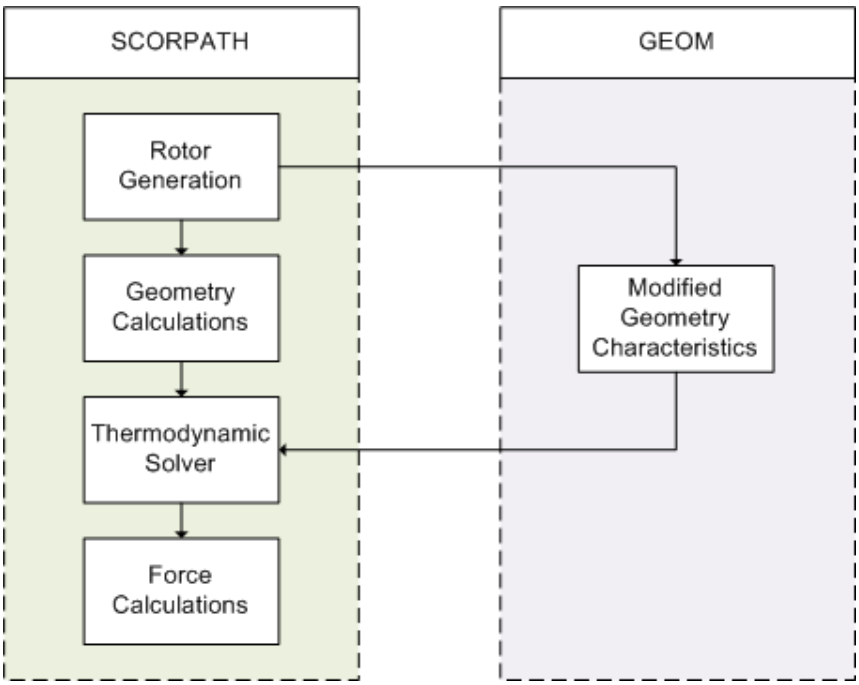

Figure 3-1: GEOM program integration with SCORPATH

3.4 EXPECTED CONTRIBUTION

3.4.1 BOUNDARY MAP

The procedure of mapping properties to the surface of the rotors will utilise a novel 'Rotor Boundary Map'. The rotor boundary map will facilitate input of the distribution of temperatures and pressures on the rotor and casing boundaries i.e. it will define instantaneous boundary conditions for screw compressor rotors and casing. There will be a unique boundary map for the main and the gate rotors; the form of which will depend only on the transverse rotor profiles. This presentation of the rotor boundaries will provide a unique way of visualising and comparing the key geometrical properties of different profiles such as the length of the sealing lines and how the sealing lines are related to the formation of the blow hole leakage area. This will be a direct contribution to compressor technology, since it will define a procedure which has not been used before.

3.4.2 MODEL INTEGRATING OPERATIONAL CLEARANCE MODIFICATION

Results from chamber models are currently underutilised and it is possible to use the temperature and pressure of the fluid within the chamber, calculated throughout the compression cycle, to assess local exposure to rotor and casing surfaces. Knowing local fluid boundary temperatures allows approximate estimates to be made of metal temperature and distortion during operation by using analytical procedures and appropriate assumptions. This allows the clearance reliability to be evaluated at an early design stage with minimum additional complexity. In addition, iterating the thermodynamic performance calculation with modified operational leakage areas is expected to improve the model realism. In particular, this newly developed model supports temperature management of operational clearances.

Chapter 4
Boundary Map for Rotor and Casing Surfaces

4.1 INTRODUCTION

Chamber models simulate compressor performance efficiently by assuming a non-dimensional control volume. This control volume varies in size throughout the compression cycle as a function of the main rotor angle, or cycle angle. At discrete cycle angles the fluid properties within the control volume are calculated thus the fluid properties are described throughout the compression process. From this data, critical performance characteristics such as indicated power are easily derived without the need to represent actual 3D flow domains. However, in order to calculate some performance characteristics such as rotor torque it is necessary to perform additional analysis of the compressor geometry (Stosic, Smith et al. 2005). Taking this analysis further it is possible to establish the instantaneous fluid properties at any local point on the rotor or casing compression surfaces. This allows for more detailed investigation of the inner workings of the compressor.

The objective of this chapter is to define a method by which instantaneous or averaged fluid properties from a non-dimensional chamber model can be mapped onto surfaces that represent the rotor and casing geometry. Fluid properties from the chamber model are known at a given cycle angle therefore the challenge is to establish what portion of the cycle any given point, fixed to the surface of the casing or rotor, is exposed to. This will make it possible to establish the boundary temperature or pressure at any location on the compression surfaces of the rotors and casing.

4.2 DEFINITION OF BOUNDARY SURFACES

4.2.1 COORDINATE SYSTEM CONVENTIONS

The following work refers to the 'compressor' for simplicity, however all calculations are equally applicable to expanders with the only differences being in the direction of rotation and the inlet and outlet directions. In order to generalise the compressor inlet plane, which is the expander outlet, it can also be been referred to as the low pressure (LP) plane.

As twin screw compressors can be installed in various orientations a 'global' co-ordinate system will be fixed to the casing. Before placement of the global co-ordinate system, the compressor orientation needs to be defined. For twin-screw compressors the only significant variable that affects the relative position of the compressor features is whether the main rotor has a right-hand or a left-hand helix, the latter type resulting in a compressor that is the mirror image of the former. To prevent confusion all geometric analysis will be performed assuming a main rotor with a left-hand helix regardless of the actual rotor geometry. To clarify the helix convention – the main rotor shown further on in Figure 4-5 has a left-hand helix. If necessary the rotor helix can easily be corrected at a post-processing stage. Constraining the compressor to have a main rotor with left-hand helix and orientating this compressor to be viewed from the inlet end with the high pressure (HP) cusp at the top, the following convention will always apply:

Table 4-1: Compressor orientation

Main rotor helix:	LEFT-HAND
Compressor orientation:	HP cusp at top (top out discharge port)
Main rotor position (viewed from inlet):	LEFT
Main rotor rotation (viewed from inlet):	CLOCKWISE

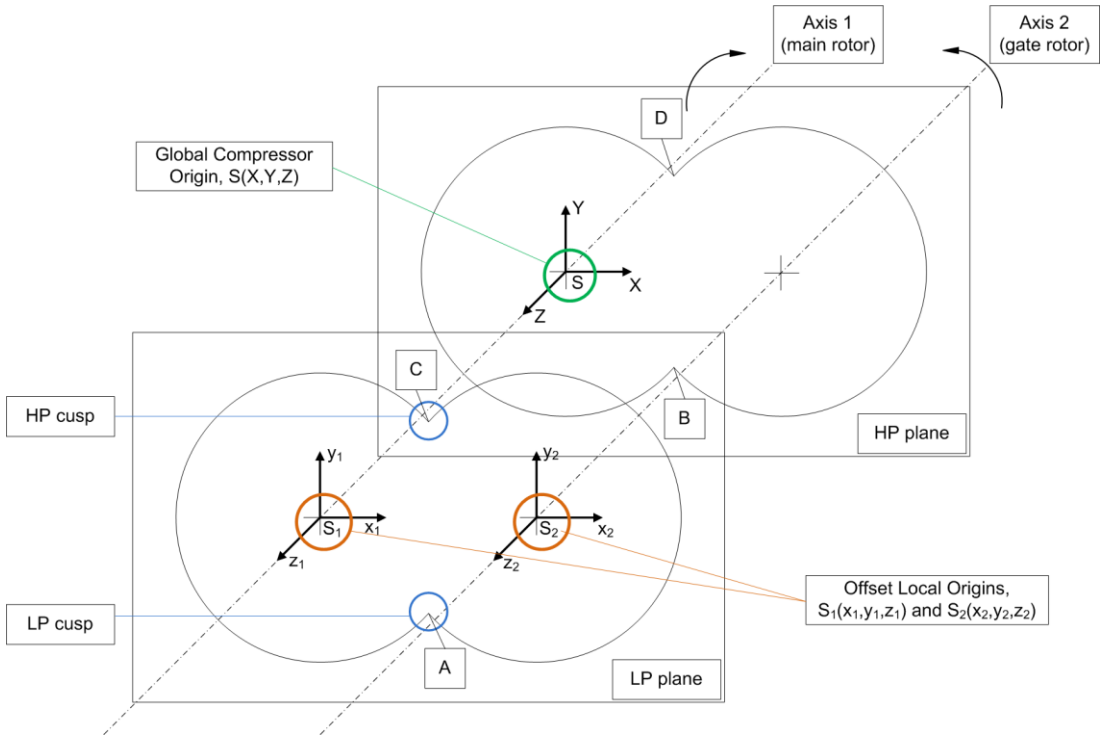

Figure 4-1: Compressor and rotor co-ordinate systems

Any location on the compressor rotors or casing can be described using the global Cartesian co-ordinate system S(X,Y,Z) defined in Figure 4-1. This is located on the high pressure (HP) plane with the z-axis aligned with the main rotor axis. The x-axis is co-incident with the centre line formed between each rotor axis on the HP plane. Additional co-ordinate systems have been defined on the low pressure (LP) plane: $S_1(x_1,y_1,z_1)$ and $S_2(x_2,y_2,z_2)$. These co-ordinate systems are also fixed to the compressor casing and are simply offset from the global origin, S. Any point on these local co-ordinate systems can be related back to the global system, S(X,Y,Z), using the equations (5) to (7). 'L' is the nominal rotor length between the LP and HP plane, and 'A' is the nominal rotor centre distance between the rotor axes:

$$X = x_1 = (x_2 + A) \tag{5}$$

$$Y = y_1 = y_2 \tag{6}$$

$$Z = (z_1 + L) = (z_2 + L) \qquad (7)$$

With the cylindrical form of the rotor bores and the rotational movement of the rotors it will be more convenient to define points using a cylindrical co-ordinate systems located at the origins S_1 and S_2. In the standard convention for a polar co-ordinate system, (r,θ,z), the angle θ is measured counter-clockwise from the x-axis and z is in the direction already defined. To simplify later equations it is preferable to define less conventional angle parameters that are aligned with the direction of rotation of each respective rotor. In addition, it is easier to use an axial length parameter that is aligned from the compressor inlet to outlet.

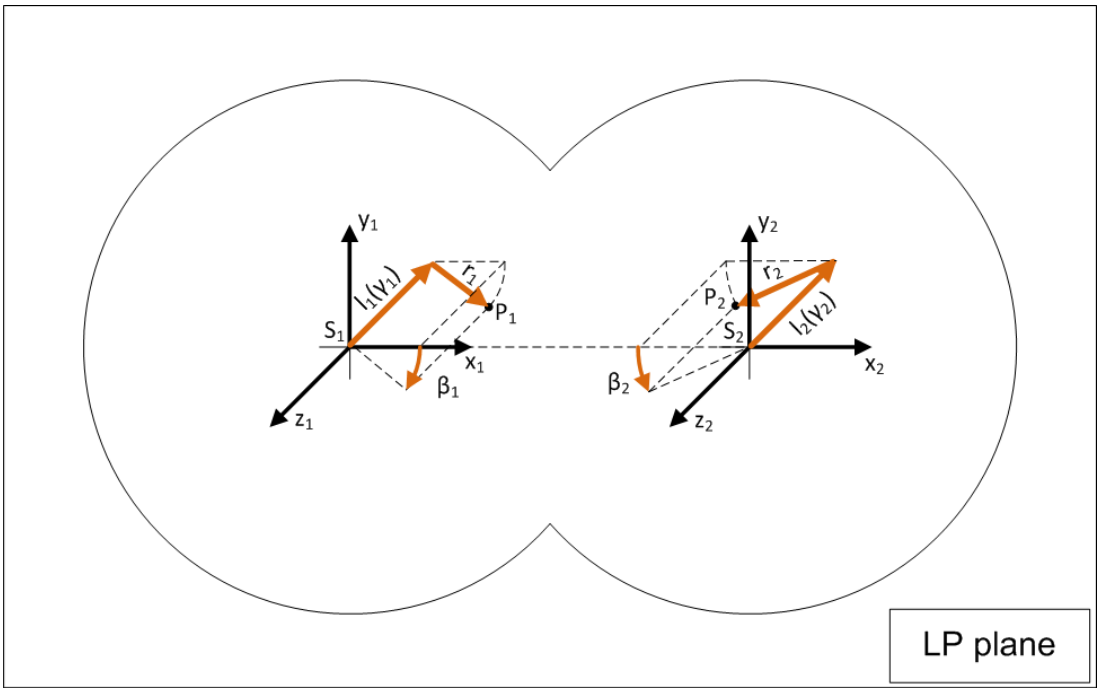

Figure 4-2: Parameters for surface definition

Parameters 'r', 'β' and 'l' have been defined on each co-ordinate system S_1 and S_2 as shown in Figure 4-2. These parameters effectively describe a non standard cylindrical co-ordinate systems where r is the local radius, β is the angle (measured in the same direction as the rotor rotates) and l is a measure of the axial position from inlet.

The rotors on twin screw compressors feature a helical twist along the axis therefore the position along the axis that has been defined by parameter, l, can alternatively be defined by using a new angular parameter, γ; this describes the

local wrap angle measured from the inlet (LP) plane. For the case of rotors with constant pitch helix the relationship is as shown in equation (8) where φ_{w1} is the main rotor wrap angle over the rotor length, L. The parameter γ will always be defined using the *main* rotor wrap angle, whether measured on the main rotor side or on the gate rotor side. It is convenient to describe the axial position in terms of the wrap angle on the main rotor for later calculations.

$$\frac{l}{L} = \frac{\gamma}{\varphi_{w1}} \tag{8}$$

Equations (9) to (14) describe transformations from the parameters r, β and γ, back to the global Cartesian compressor system located at S. The subscripts '1' and '2' for the rotor parameters distinguish whether they refer to the main or gate rotor sides which are measured relative to the origins S_1 or S_2 respectively:

Main rotor side:

$$X = r_1 cos\,(\beta_1) \tag{9}$$

$$Y = -r_1 sin\,(\beta_1) \tag{10}$$

$$Z = L\left(1 - \frac{\gamma}{\varphi_{w1}}\right) \tag{11}$$

Gate rotor side:

$$X = -r_2\, cos(\beta_2) + A \tag{12}$$

$$Y = -r_2 sin\,(\beta_2) \tag{13}$$

$$Z = L\left(1 - \frac{\gamma}{\varphi_{w1}}\right) \tag{14}$$

The internal geometry of the compressor will be broken down into a number of discrete surfaces which are exposed to various compression chambers. These surfaces are: casing inlet plane, casing outlet plane, casing bore and rotor section (ridge or flute). Each of these surfaces is repeated for the main rotor and gate rotor sides of the compressor resulting in a total of eight surfaces. A 2D

computational array can then be defined for each surface in order to efficiently describe any point on each respective surface. The transformation between the 3D spatial domain and the 2D computational domain will be done by utilising the co-ordinate systems and parameters that have been defined. These surfaces will now be defined in more detail.

4.2.2 Casing Surfaces

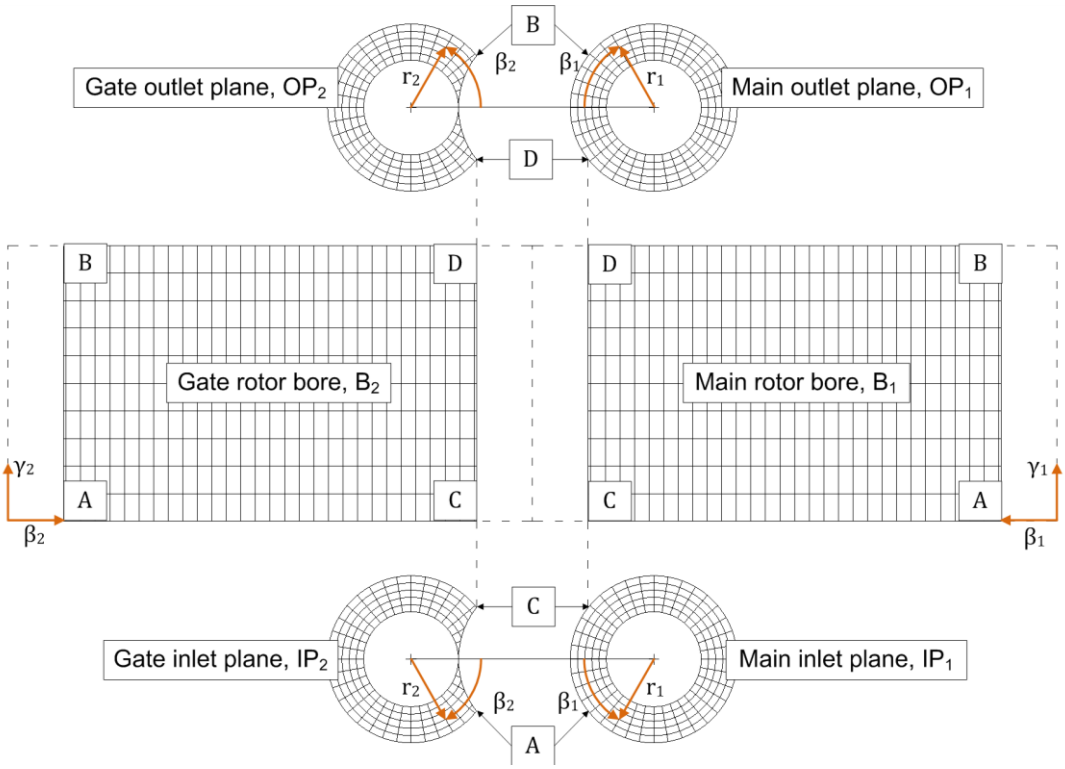

Figure 4-3: Exploded view of casing surfaces

The static casing will be considered first. The six casing surfaces are labelled in Figure 4-3 which shows an exploded view of the inner surfaces of the compressor casing. The vertices A, B, C and D are also shown on Figure 4-1 for reference. This view is formed by cutting along the line AB on the low pressure cusp. To explain Figure 4-3 in reference to Figure 4-1 – imagine lying inside the compressor looking upwards with your head towards the HP plane – this is why the main rotor bore now shown on the right hand side.

This figure shows how the parameters r, β and γ align to these 'unwrapped' 2D surfaces. Table 4-2 summarises how the location on each of the surfaces can be defined using only two of the three parameters.

Table 4-2: Casing surface parameters

Surface Description	Surface Label	Co-ordinates for surface array	Constant
Main rotor side, inlet plane	IP_1	(r_1,β_1)	$\gamma = 0$
Main rotor side, bore	B_1	(β_1,γ_1)	$r_1 = r_{o1}$
Main rotor side, outlet plane	OP_1	(r_1,β_1)	$\gamma = \varphi_{w1}$
Gate rotor side, inlet plane	IP_2	(r_2,β_2)	$\gamma = 0$
Gate rotor side, bore	B_2	(β_2,γ_2)	$r_2 = r_{o2}$
Gate rotor side, outlet plane	OP_2	(α_2,β_2)	$\gamma = \varphi_{w1}$

It is worth clarifying that these casing surfaces, described using parameters 'r', 'β' and 'γ', are representations of idealised casing surfaces that would exist with perfect rotor alignment and zero clearances. This would be inappropriate for other full 3D analysis using FEA or CFD where the clearances would be derived from actual component surface dimensions. The planned analysis will of course use local clearance data however the local clearances will be handled as scalar values only; this vastly simplifies the problem while still providing insight into the 3D clearance distributions.

4.2.3 ROTOR SURFACES

Transverse 2D rotor co-ordinates are defined on $S_{01}(x_{01},y_{01})$ and $S_{02}(x_{02},y_{02})$ for the main and gate rotors respectively; as shown in Figure 4-4. These rotor co-ordinate systems are only partially constrained so that S_{01} freely rotates about the z_1-axis of S_1 and S_{02} freely rotates about the z_2-axis of S_2.

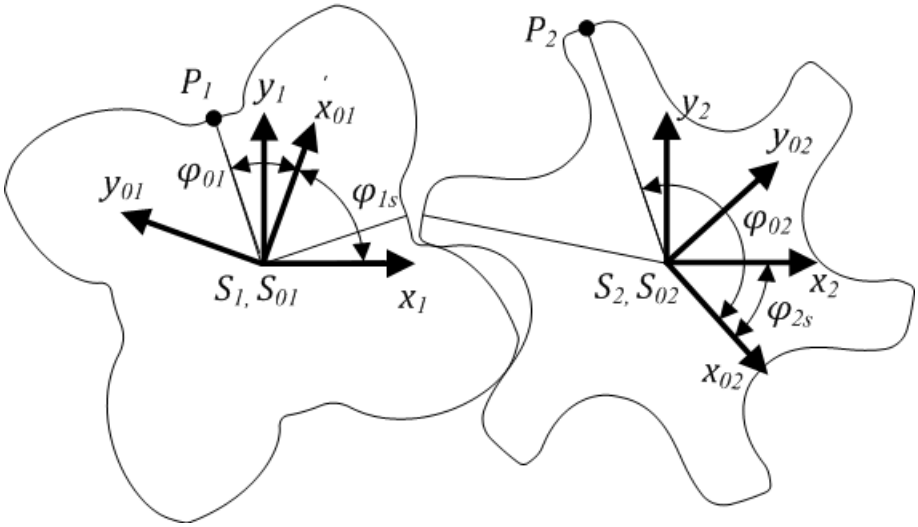

Figure 4-4: Transverse profiles defined at LP plane

The full 3D surface of the rotors (see Figure 4-5) can be derived using the transverse rotor co-ordinates that are extruded along a helical path.

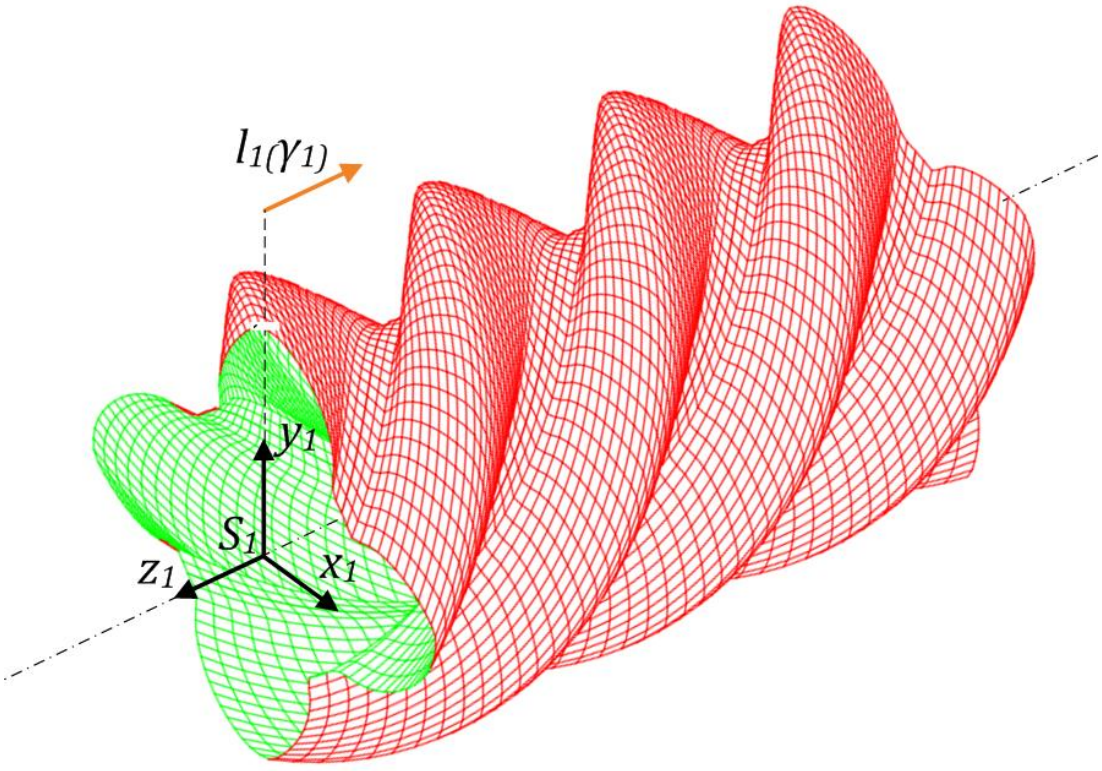

Figure 4-5: Full main rotor surface

An instantaneous point on this rotor surface could be represented globally using (X,Y,Z); locally on origin S_1 using (x_1,y_1,z_1); or with parameters (r_1,β_1,l_1).

The length parameter, $l_1(\gamma)$, a function of γ, is conveniently aligned along the rotor axis from the inlet to outlet and is unaffected by rotor rotation so this is a suitable parameter to describe the axial position on the rotor surface. The local radius, r_1, is also a constant for a given point on the surface however the angle, β_1, is affected by the rotational position of the rotor defined by the cycle angle, θ.

Each rotor lobe is geometrically equivalent and therefore the surface of each lobe can be generated from another by indexing the cycle angle, θ, through $2\pi/z1$, where z1 is always the number of lobes on the main rotor - rotating the rotor pair by cycle angle $\theta = 2\pi/z1$ will index the gate rotor by an angle corrected for the gear ratio: $(z1/z2)2\pi/z1$, in other words by: $2\pi/z2$

A 2D computational array has been defined to simply identify a surface location on a single main rotor ridge; or in the case of the gate rotor, the corresponding flute. This array can be thought of as the surface produced by straightening out the rotor helix and flattening the resulting surface to form a rectangle.

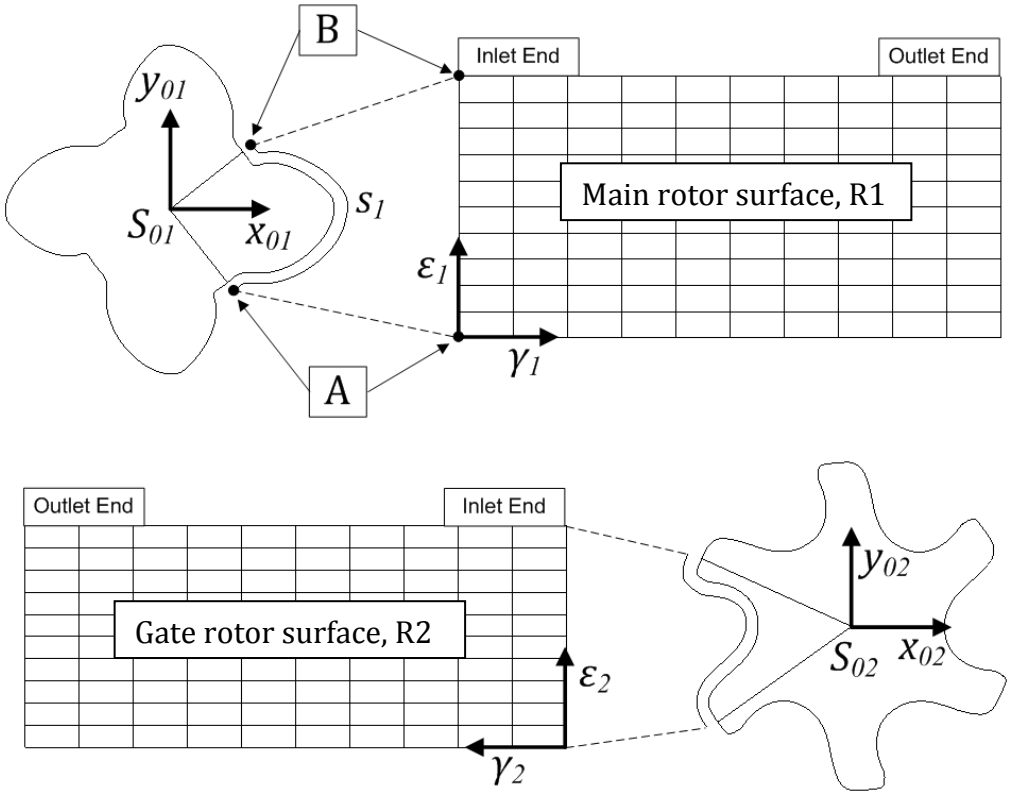

Figure 4-6: Rotor surface arrays

In Figure 4-6 the length of a curve, s_1, between points A and B is:

$$s_1 = \int_A^B \sqrt{dx_{01}^2 + dy_{01}^2} \qquad (15)$$

The parameter, ε, is defined as the relative position along the line, s, of the transverse rotor profile curve such that $0 \leq \varepsilon \leq 1$. This is defined separately for the main and gate rotor segments as shown in Figure 4-6. This allows the rotor surface to be presented two dimensionally and independently of the rotor rotation.

The rotor segments are in this case a main rotor ridge (or lobe) and a gate rotor flute (or interlobe) section. It is later assumed that the limits of ε_2 on the gate rotor form the boundary between adjacent rotor chambers on that rotor so it is important that this point is located approximately central on the gate rotor OD or at the tip seal protrusion, if applicable.

In practise, the parameter ε is numerically approximated by linearly interpolating between discrete profile points. As this parameter is primarily used for lookup purposes in order to relate the computational array to the actual geometry, any approximation errors are not important. In fact, this dimension of the rotor surface array could easily be replaced by identifying the discrete profile point number, n, as was done when developing a program to deploy these procedures. The value of presenting the rotor surface arrays using the ε parameter is that the scale along line s is preserved in the surface array plots and the generalised procedure can be presented in an efficient manner.

4.3 Definition of Cycle Conventions

In order to relate the actual rotor positions to the compression cycle it is necessary to define a datum from which rotations can be measured. Figure 4-7 shows a transverse rotor profile pair in what will be referred to as the 'home position'. The main rotor on the left is rotated so that the tip of one lobe is coincident with the centre line formed between the centre points of the main and gate rotors. The gate rotor is positioned to be in mesh with the main rotor. This datum for rotor rotation is measured on the LP plane; the inlet plane for a

compressor. This convention has been adopted from the N-Profile generated rotors, example coordinates of which are shown in Figure 4-8.

Any rotor position can now be defined by the offset angle of the main rotor tip from this home position. To relate this 2D rotor position at the LP plane to an instant during the compressor cycle it must be explicitly stated whether the referenced tip is on the leading or trailing lobe of the control volume.

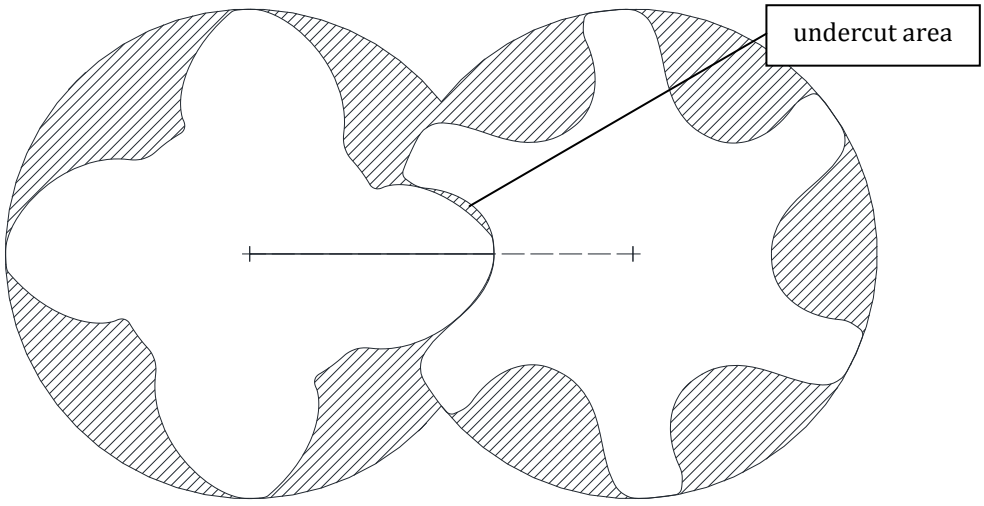

Figure 4-7: Rotor home position

The transverse profile co-ordinates for a single main rotor ridge and its corresponding gate rotor flute are plotted with respect to their local co-ordinate systems in Figure 4-8.

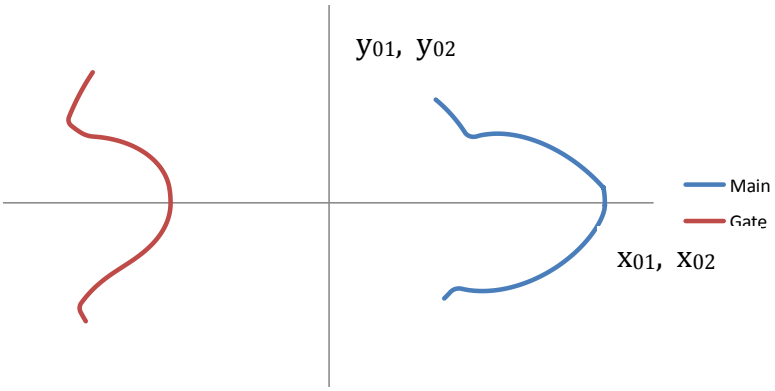

Figure 4-8: Rotor segments

Before defining the rotor position at the start of the compression cycle (when $\theta = 0°$) it is necessary to explain a little about the cycle duration and the various steps that must be considered in its calculation:

1. Full rotation of main rotor – this is the obvious minimum travel before the cycle would repeat
2. Transfer from *leading* main lobe to *trailing* main lobe – the *interlobe* area which defines the volume is initially created by the leading main lobe but will not disappear until the trailing main rotor lobe has advanced to the position of the leading lobe, thus adding $360/z1°$ to the cycle duration.
3. Wrap angle lag – the wrap angle of the main rotor introduces a lag during which the chamber advances axially along the rotors, thus adding the main rotor wrap angle, γ_1, to the cycle duration.
4. Undercut area – all asymmetric rotors will have non-zero area on the trailing flank of the main rotor when in the home position as shown in Figure 4-7. Depending on the rotor profile this requires the rotors to be reversed by approximately 30° before this area, and consequently the chamber volume, is zero. This adds to the cycle duration.
5. Idling gate rotor lobe offset – if z2 – z1 is greater than or equal to 2 then the area formed within a particular main rotor interlobe area and gate rotor interlobe area will not finish with the same gate rotor interlobe. The area formed in the gate rotor interlobe will idle for one additional lobe pass when z2 – z1 = 2, adding $360/z1°$ to the total cycle duration.

The last item listed is often omitted in chamber models. Since the offset of the idling gate interlobe volume would generally by added at the filling stage it is not important for the chamber model accuracy. However in order to represent the net volume accurately for all chambers, at a given instant, this item is important. Likewise, it is necessary for mapping results from a chamber model onto the actual rotor geometry where the full duration of all gate rotor lobes must be described.

Figure 4-9 breaks down how the rotor start position (when θ = 0°) is defined in order to preserve the correct cycle duration. Steps A) to D) of Figure 4-9 show the transverse rotors at the LP plane:

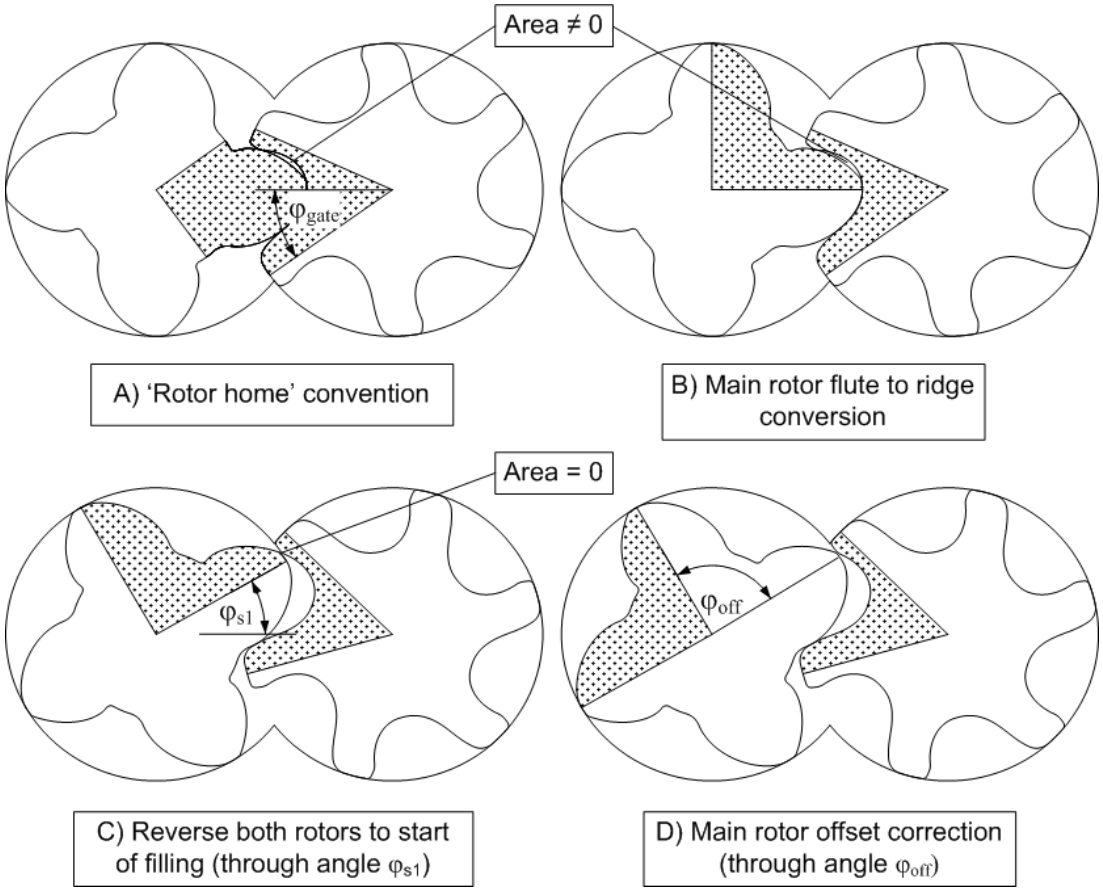

Figure 4-9: Moving rotors to the start of the compression cycle

A) The 'rotor home' position before any adjustments

B) This simply clarifies the interlobe area of interest – the tip of the main rotor in the home position will be the leading tip

C) φ_{s1} is defined as the 'start angle' through which the rotors must be reversed to close the 'Undercut area'

D) φ_{off} is the 'offset angle' to correct for 'Idling gate rotor lobe offset'. Note that this rotation is only applied to the main rotor. This angle is calculated as:

$$\varphi_{off} = \frac{360}{z1}.(z2 - z1 - 1) \qquad when\ (z2 - z1 - 1) \geq 0 \qquad (16)$$

This rotor offset is not an obvious concept to understand and might be slightly better illustrated later in Figure 4-12: Position of rotor chambers in the transverse plane.

The start angle, φ_{s1}, has been defined graphically in Figure 4-9. This angle can be derived from the sealing line because the rotor position in Figure 4-9C is also the maximum rotor reversal before the contact point at the tip of the main rotor is broken off. φ_{s1} equals the meshing angle, θ_M, at the upper limit of the sealing line y_{SL_MAX}. The calculation of the meshing angle and sealing line co-ordinates is explained in Appendix A.

Once both rotors are adjusted for φ_{s1} and the main rotor is adjusted by φ_{off}, if applicable, the rotors will be in the start position as shown in Figure 4-9D. With reference to this start condition the rotor positions for any cycle angle, θ, can now be described.

With the assumption that the compressor is operating at steady state conditions the problem is cyclic in nature and therefore only one chamber has to be considered. For a point on the casing the cycle repeats for every passing lobe of the compressor rotors – therefore only seeing a limited range of the full cycle duration. For a point on the rotors, the cycle repeats for every full rotation of the particular rotor on which the point is located – again only being exposed to a limited range of the overall cycle. The overall compression cycle is distinct from these local exposure cycles because it follows a single control volume as it passes through the compressor.

4.4 MAPPING OF THE CASING SURFACES

The casing surfaces previously presented in Figure 4-3 have been presented again in Figure 4-10 to show the projection of the nearby rotors. At the instant shown, any points on any of the surfaces that are within the hatched areas are in the same chamber.

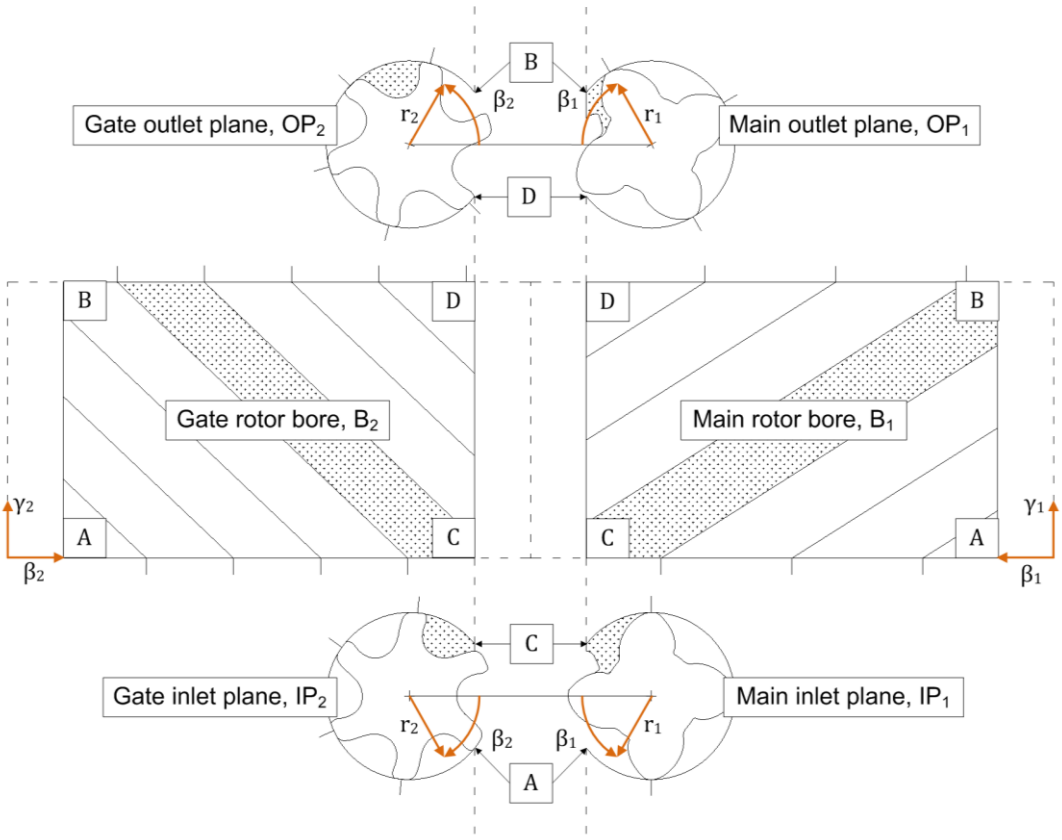

Figure 4-10: Single chamber projected onto casing surfaces

The following paragraphs detail how to calculate the cycle limits that are 'seen' by a fixed point on the static rotor casing. A similar procedure was presented by Sauls et al. (Sauls, Powell et al. 2006b) and describes the cycle limits for a static point on the casing bore by considering the cycle angle at the moment the leading and trailing tip of the rotor pass by.

Consider the rotors in the start position defined in Figure 4-9D. At this position the rotor cycle angle θ = 0. The position of the leading tip on the main rotor can be described using the parameter, β, as described in section 4.2.1 to be positive in the forward direction of rotation for a compressor. Moving the rotors through the angles φ_{s1} and φ_{off}, as defined in Figure 4-9, would result in a backward rotation. At the *start* of the cycle at the *leading* tip on the *main* rotor (subscript *sl1*) the parameter β can be calculated as:

$$\beta_{sl1} = -\varphi_{s1} - \varphi_{off} \qquad (17)$$

At the *trailing* tip (subscript st1); where z1 is the number lobes, or gear teeth, on the main rotor:

$$\beta_{st1} = \beta_{sl1} - \frac{2\pi}{z1} \qquad (18)$$

Referring to the rotor 'home position' defined in Figure 4-9-A: at the *start* of the cycle at the *leading* tip on the *gate* rotor (subscript *sl2*) the rotor is already offset from the rotor centreline by the angle φ_{gate}. The only further adjustment to the gate rotor rotation corresponds to the reverse rotation of the main rotor by the angle φ_{s1} which is adjusted by the gear ratio z1/z2:

$$\beta_{sl2} = \varphi_{gate} - \varphi_{s1}\left(\frac{z1}{z2}\right) \qquad (19)$$

On the gate rotor at the *trailing* tip (subscript st2):

$$\beta_{st2} = \beta_{sl2} - \frac{2\pi}{z2} \qquad (20)$$

Consider a fixed point on the main rotor bore, B_1, described by the parameters β_1 and γ. When the *leading* tip of the main rotor intercepts this point corresponds to one rotor position and cycle angle. When the *trailing* tip of the main rotor intercepts the same point this corresponds to a different rotor position and thus a different cycle angle. For clarity the corresponding cycle angles will be labelled θ_l and θ_t respectively.

The distance that the main rotor must travel through, i.e. the cycle angle, θ, until the leading tip of the active chamber meets the point on the casing is the difference between β_1 and β_{sl1}. When moving away from the inlet plane the effect of the wrap angle along the length introduces a lag which is accounted for by the parameter γ:

$$\theta_l(\beta_1, \gamma) = \beta_1 - \beta_{sl1} + \gamma \qquad (21)$$

The cycle angle at which the trailing tip of the main rotor passes the same point is:

$$\theta_t(\beta_1,\gamma) = \theta_l + \left(\frac{2\pi}{z1}\right) \quad (22)$$

θ_l and θ_t represent the limits of the compression cycle that the point on the casing (β_1,γ) is exposed to.

The calculation of the cycle limits for a point on the gate bore surface is similar; differences are due to the fact that the cycle angle is always referenced from the main rotor position.

$$\theta_l(\beta_2,\gamma) = (\beta_2 - \beta_{sl2})\left(\frac{z2}{z1}\right) + \gamma \quad (23)$$

$$\theta_t(\beta_2,\gamma) = \theta_l + \left(\frac{2\pi}{z1}\right) \quad (24)$$

At every location on any of the static casing surfaces the limits of cycle exposure defined by θ_l and θ_t can be calculated. From these values a single 'average' cycle angle can be calculated at each location:

$$\bar{\theta}(\beta_1,\gamma) = \frac{(\theta_l + \theta_t)}{2} \quad (25)$$

$$\bar{\theta}(\beta_2,\gamma) = \frac{(\theta_l + \theta_t)}{2} \quad (26)$$

Figure 4-11 was generated to show the average cycle angle using a surface colour contour plot. The colour represents the local average cycle angle calculated using the appropriate values of either β_1 and γ or β_2 and γ. These same surface parameters are then fed into equation (8) to (14) in order to

calculate the position in the global co-ordinates (X,Y,Z) at each location (these co-ordinates are as defined in Figure 4-1).

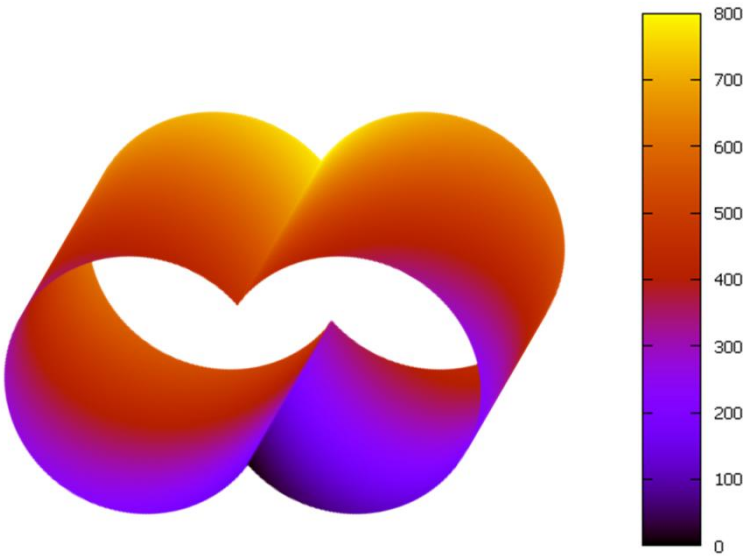

Figure 4-11: Cycle angle mapped onto casing bore surfaces

This surface plot has been smoothed and only serves to show visually how different parts of the casing are exposed to different parts of the cycle. In practice, surfaces B1 and B2 of each rotor bore are discretized using a finite number of points defined by β and γ. The explicit calculations are repeated at each point or node and the number of points has no bearing on the accuracy at a given node.

4.5 Mapping of the Rotor Surfaces

In the same way that the cycle angle has been mapped onto the rotor bore surfaces B1 and B2 in the previous section, this will be done for the rotor surfaces R1 and R2 (surfaces as defined in Figure 4-6). In the previous case of the rotor bore surfaces, the instantaneous boundaries that divided the surfaces into different chambers were simply defined by the rotor to casing sealing lines. In the case of the rotor surfaces, the chamber boundaries are defined by the rotor to casing, radial sealing lines and the rotor to rotor, interlobe sealing line. With this added complexity it was found that the previous method (identifying the cycle limits) was not suitable, furthermore it is useful to be able to calculate

the instantaneous boundary conditions on the rotor surface at any given rotor angle.

Figure 4-12 shows a transverse cross section of the compressor at the inlet plane. This shows the rotor to casing and rotor to rotor interactions that result in separate compression chambers as highlighted with different colours. The key on the right hand side gives the cycle angle that defines each compression chamber. For most chamber cross-sections the entire rotor flute (or interlobe area) is exposed to the same chamber which is separated from its adjacent chambers by the radial rotor to casing sealing points. During rotor to rotor 'contact', typically up to three sealing points will be formed between the rotors. When this transverse section is extended to form the full 3D rotors these sealing points will all fall on the same 3D sealing line.

Considering one meshing rotor segment on the main rotor, identified by the white lines forming a 'slice' of the rotor, it can be seen that the surface of this particular rotor segment is simultaneously exposed to four different compression chambers labelled: blue, green, red and yellow. A procedure is needed to identify the location of the boundaries and the chamber exposure for any given rotor angle.

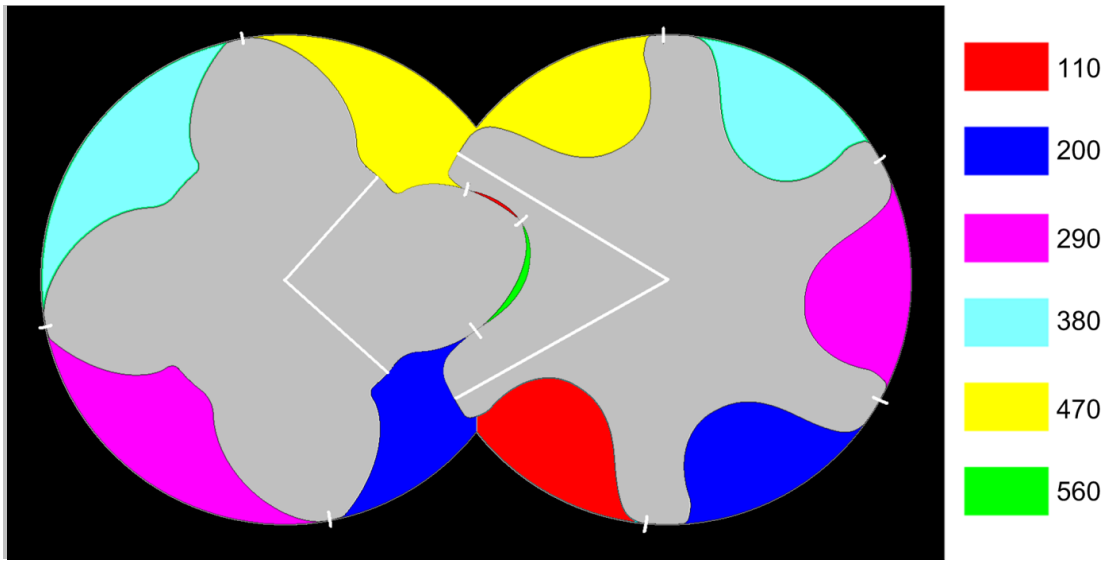

Figure 4-12: Position of rotor chambers in the transverse plane

It can be observed from Figure 4-12 that the adjacent blue and red chambers at the low pressure cusp are not separated – this is not due to any conventionally defined leakage path such as the low pressure blow-hole area and this flow path between chambers is in fact just a consequence of the 4/6 lobe combination. If the gate rotor instead had 5 lobes then the matching chamber sections highlighted in blue would be formed together at suction. This is the rationale behind the rotor offset term previously described in equation *(16)*. This necessary offset is applied at the low pressure side where both chambers will be exposed to the low pressure port anyway. Hence, the interaction between these chambers is not significant. However, neglecting this offset term will result in incorrect cycle duration on the gate rotor side and it must be included in order to relate the compression cycle to the rotor and casing geometry accurately.

Due to the complexity of the chamber boundaries on the rotor surface, work to investigate the cycle exposure led to the development of a rotor surface boundary map which will now be discussed in more depth.

4.6 Definition of Rotor Surface Boundary Map

The following procedure analyses the rotor boundary and chamber interaction along the line of a single transverse rotor profile section from ε = 0 to 1. This abstracted procedure can later be used to map boundaries and fluid properties along the full rotor surface, R1, then the full rotor body for all lobes.

For a given rotor profile the radius, r, varies only as a function of the rotor surface parameter, ε. In practise the value of the corresponding radius can be saved in an array that can be looked up.

$$r_1 = r_{01} = f(\varepsilon_1) \qquad (27)$$

$$r_2 = r_{02} = f(\varepsilon_2) \qquad (28)$$

The original profile co-ordinates were defined on the systems $S_{01}(x_{01},y_{01})$ and $S_{02}(x_{02},y_{02})$ as shown in Figure 4-6 and Figure 4-8. Each of these points can be described using the corresponding polar co-ordinates (r_{01},φ_{01}) and (r_{02},φ_{02}) for

the main and the gate rotor respectively. As was the case for the local radius, the local profile angle is a profile constant that can be described as a function of the rotor surface parameter ε. Again, in practice, the value of the corresponding local angle can be saved in a look up array.

$$\varphi_{01} = f(\varepsilon_1) \tag{29}$$

$$\varphi_{02} = f(\varepsilon_2) \tag{30}$$

Recall that the actual instantaneous geometry of the rotors at any point during the cycle can be represented by the parameters r,β,γ, set out in Figure 4-2. The angle parameters, β_1 and β_2, for a point on the main or gate rotors are calculated:

$$\beta_1 = (-\varphi_{01}) + (\theta - \varphi_{s1} - \varphi_{off} - \gamma) \tag{31}$$

$$\beta_2 = (\varphi_{02} - 180) + (\theta - \varphi_{s1} - \gamma)\frac{z1}{z2} \tag{32}$$

The term λ has been defined below by subtracting the terms for the local profile angle from β; this new parameter more generally describes the movement of the rotor pair rather than individual points on either rotor:

$$\lambda_1 = \beta_1 - (-\varphi_{01}) = (\theta - \varphi_{s1} - \varphi_{off} - \gamma) \tag{33}$$

$$\lambda_2 = (\beta_2 - (\varphi_{02} - 180))\frac{z2}{z1} = (\theta - \varphi_{s1} - \gamma) \tag{34}$$

These equations will be used to relate the *local transverse profile rotation*, λ, to the cycle angle, θ, for the main and gate rotors respectively; as the cycle angle is referenced against the main rotor rotation, λ is also referenced against the main rotor. The subscripts define whether λ refers to the main or gate rotor boundary map. The only difference between these λ values is due to the main rotor offset term, φ_{off}; for rotors with a 5/6 lobe combination it would be the case that λ1 = λ2. In the special case of the point located at the tip of the main rotor, $\varphi_{01} = 0$ and therefore $\lambda_1 = \beta_1$. At the corresponding point at the root of the gate rotor, $\varphi_{02} = 180°$ and therefore $\lambda_2 = \beta_2(z2/z1)$. Going forward it will be

clarified whether the boundary map is for the main rotor or the gate rotor so these subscripts can be dropped.

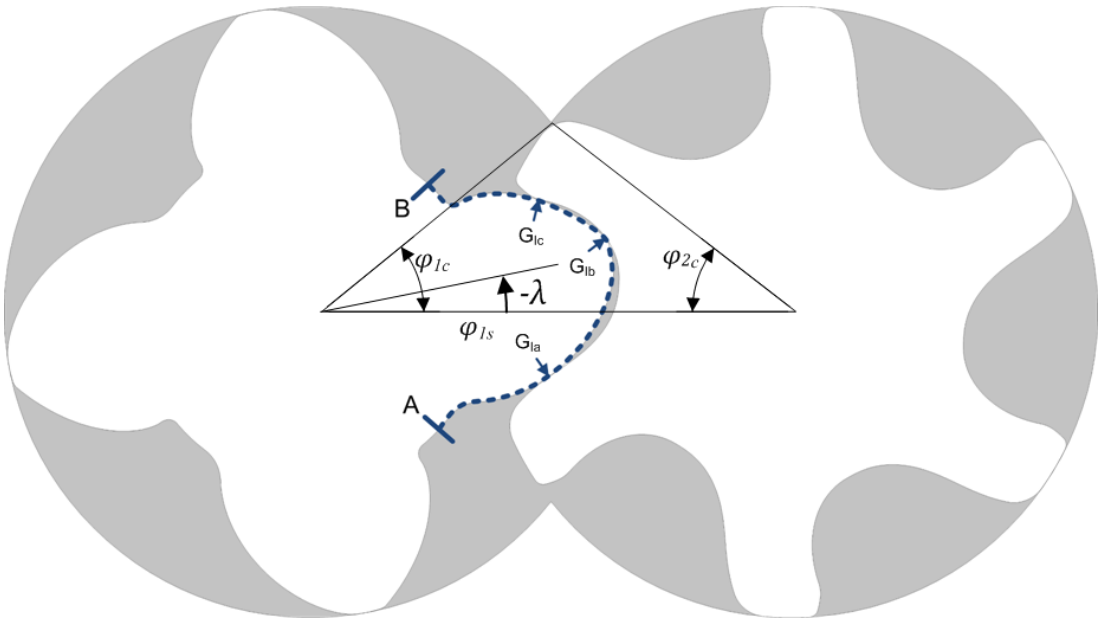

Figure 4-13: Notation used on boundary map

The parameter λ has been shown in Figure 4-13 – note that it is only referenced to the rotation of the main rotor but describes the motion of both rotors. Also note the convention where a negative rotation of the rotors from the 'home position' results in a negative value for λ. The angles to the casing cusp, φ_{c1} and φ_{c1}, are also defined in this figure, which will be used to define the limit of interaction between the rotor and the casing.

The bottom part of Figure 4-14 shows the rotor surface, R1, on which a single transverse section (γ = constant) has been highlighted. The top part of the figure shows the 'Boundary Map' with the rotor surface parameter, ε_1, represented on the horizontal axis. The vertical axis represents the local transverse rotor offset angle, λ_1.

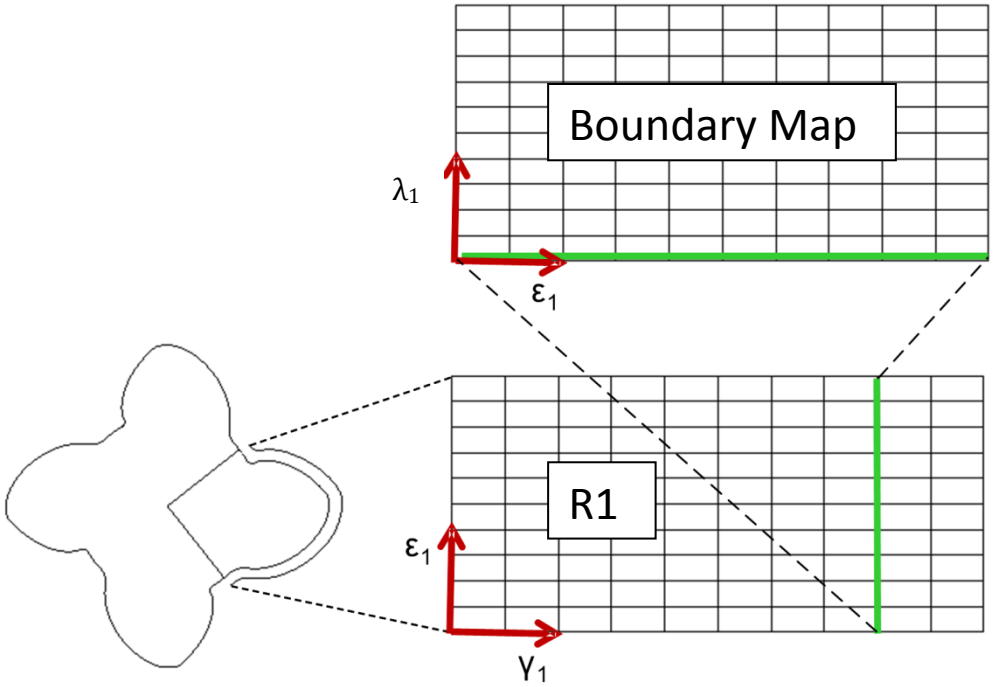

Figure 4-14: Local transverse rotor offset angle, λ, at given axial position, γ.

Because λ is adjusted for the parameter, γ, the Boundary Map is common all along the length of rotor, whatever the value of γ.

This 'Boundary Map' will be used to plot the transverse rotor boundary interactions. A key advantage of this generalised boundary map is that both interlobe and radial boundaries can be plotted. This will allow the analysis of different boundary interactions with the aim to fully define distinct compression chambers on the rotor surface.

The boundaries on this map are created by plotting the radial and interlobe sealing lines with respect to ε and λ. ε represents the local position on the transverse rotor profile while λ defines the relative rotation of the profile. This shows at precisely what rotor position the different boundaries come into play. There will be a unique boundary map for the main and the gate rotors.

The interlobe sealing line boundary is plotted onto the boundary map by setting λ to equal the local meshing angle, θ_M:

$$\lambda_1 = \theta_M(\varepsilon_1) = \theta_M\left(x_{01}, y_{01}, -\frac{dx_{01}}{dy_{01}}\right) \quad (35)$$

The meshing angle is calculated at each location along the rotor profile curve from ε = 0 to 1. The parameter λ is equal to the interlobe meshing angle, θ_M, with the specific condition that $\lambda = \theta_M = 0$ at the tip of the main rotor (as is the case when the meshing angle is calculated when the rotors originate in the 'home position'). The theory for calculation of the meshing angle is provided in Appendix 'A.2 Meshing Conditions for Conjugate Profile'.

The rotor to casing boundary will always occur at the same position on the profile, i.e. at the tip of the rotor. The limits of this boundary depend on the casing geometry. This will be explained in more detail in the following examples. These examples will look at the boundary maps produced for different profiles and how these boundary maps relate to sealing points identified on transverse rotors for various rotor positions. The examples illustrate how the full boundary interactions, which would otherwise need to be presented in 3D or on numerous transverse rotor plots, can be captured in a single 2D boundary map efficiently. The section that follows on from these examples will then pick up on the theory of how to apply the boundary map to analysis of a full 3D rotor.

4.6.1 EXAMPLE: ZERO BLOW-HOLE PROFILE

The concept of the boundary map will be discussed by using idealised, theoretical profile examples. Figure 4-15 shows a simple profile concept in which the root of the main rotor is at the pitch circle – in other words there is a zero dedendum on the main rotor and a zero addendum on the gate rotor. The flanks of the main rotor lobes are solely generated by a point on the tip of the gate rotor to form part of an epicycloid curve; a special type of epitrochoid where the generating point lies on the rolling radius (Weisstein). The gate rotor flute is similarly generated by the tip of the main rotor to form another epitrochoid curve, this time with the generating point offset from the rolling radius. In this profile the sealing line extends to the casing cusp resulting in zero blow-hole.

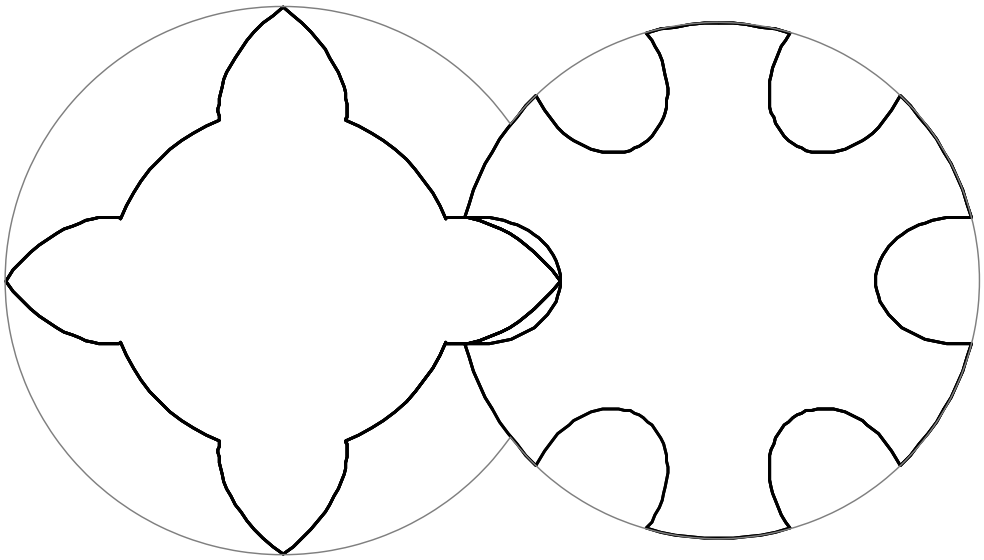

Figure 4-15: Zero blow-hole rotor profile

Because of its limited number of component curves and the fact the interlobe sealing line connects to the radial sealing line it is well suited to analyse the interaction of these various sealing lines and how they form distinct compression chambers. In Figure 4-16, the interlobe SL (sealing line) and radial SL have been plotted onto the main rotor boundary map.

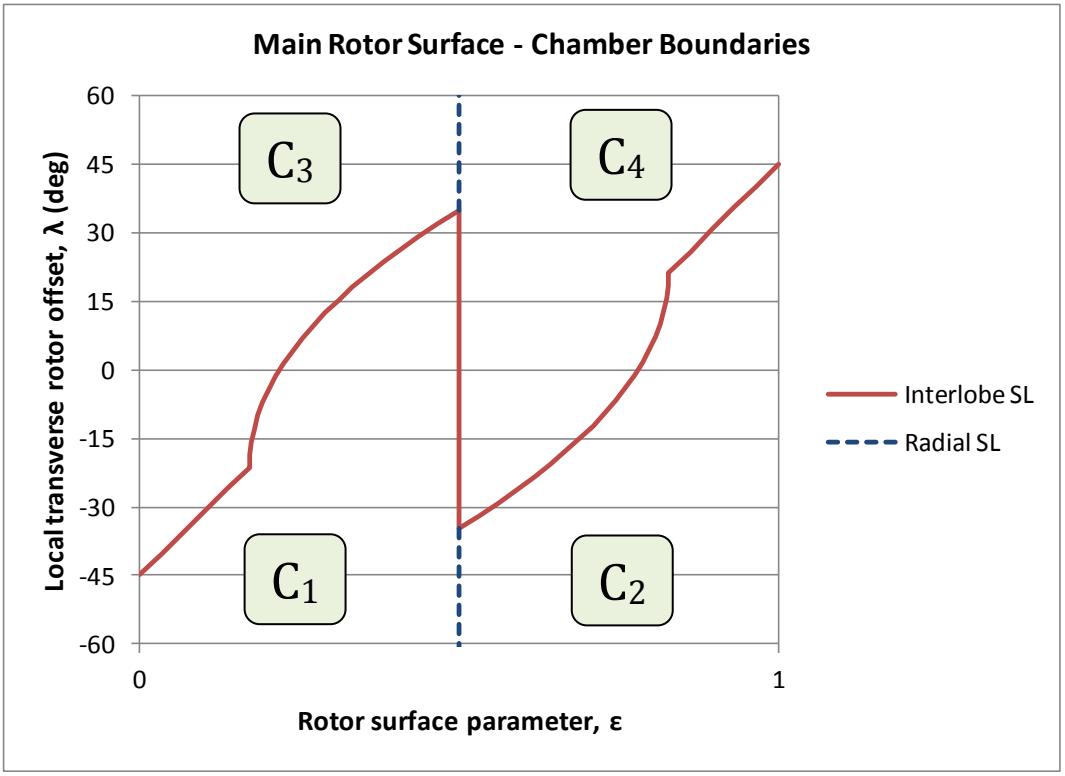

Figure 4-16: Zero BH rotor boundary map for main rotor

The Radial SL occurs at a fixed region on the rotor profile. In the case of this profile the main rotor radial SL is a single point at the tip of the main profile that occurs when parameter ε = 0.5; hence the radial SL will fall along a vertical line. The radial SL on the main rotor does not come into play until the rotor has rotated through the main rotor cusp angle, φ_{c1}. Calculation of the cusp angles is explained in Appendix A.

The Interlobe sealing line is calculated at each location along the rotor profile curve from ε = 0 to 1. The values of the parameter λ for the interlobe SL cover a range equal to 360°/z1. All examples presented in this chapter have 4 lobes on the main rotor so the range is 360°/4 or 90°, in this case from -45° to +45° since the profile is symmetrical. The scale on the y-axis from -60° to +60° degrees allows the important details to be captured for asymmetric rotors. The pattern of the SL boundaries will repeat when λ is offset by 360° therefore it is not necessary to extend the scale any further as simple corrections can be applied for larger values of λ. In this region of interest 4 distinct chambers have been created by the interaction of the interlobe SL and radial SL boundaries. These

chambers have been identified as chambers C1, C2, C3 and C4 in Figure 4-16. At this stage the objective is to clearly identify the boundaries that distinguish these chambers and not what each 'local' chamber cycle angle is.

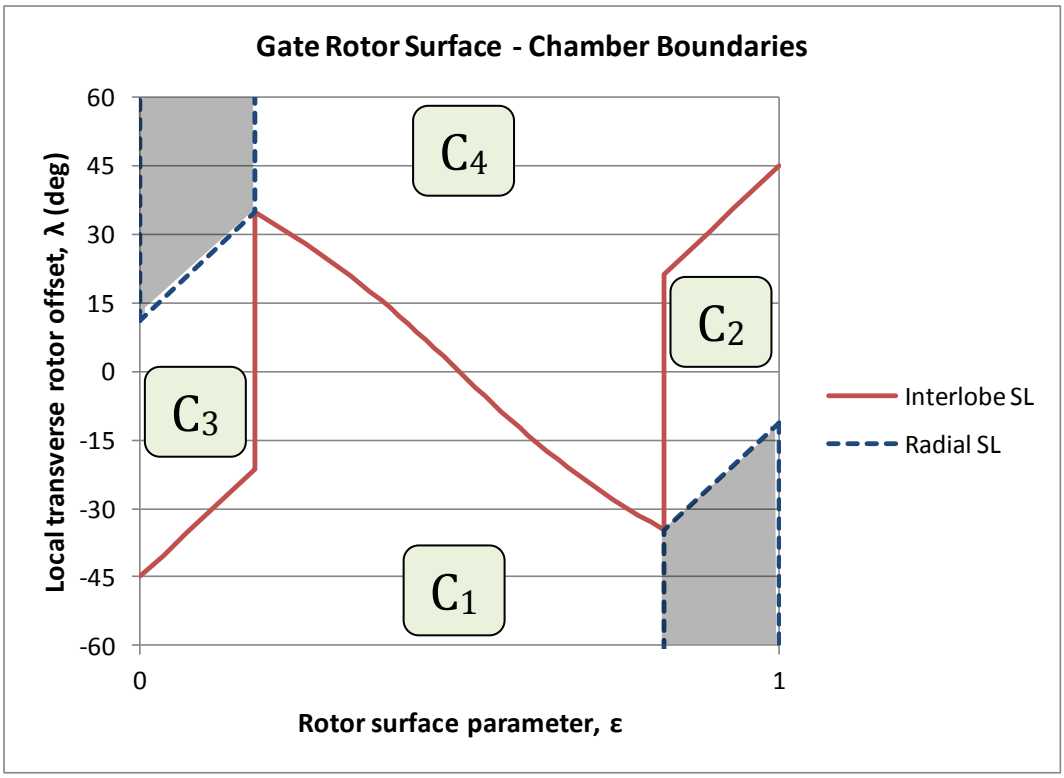

Figure 4-17: Zero BH rotor boundary map for gate rotor

In Figure 4-17 a similar map has been produced for the gate rotor. Recall from Figure 4-6, in which the rotor surface arrays are defined, that the limits of parameter ε_2 correspond to the tip of the gate rotor. Since the gate rotor tip is formed by a cylindrical line of constant outer diameter (OD) for this rotor the parameter ε has been set to zero at the mid-point of this OD line.

On the gate rotor the radial SL can occur for any location on the profile that comes into 'contact' with the casing. The radial SL will come into effect for a given value, ε, at a value of λ which can be derived using the interlobe SL: The lower and upper parallel lines that bound chamber C3 are the interlobe and radial SLs respectively. These lines are offset by a constant related to the gate rotor cusp angle, φ_{c2}. The interlobe contact occurs along the centre line between rotors for a cylindrical curve so that point must then rotate by φ_{c2} to reach the cusp.

It is important to remember that the parameter, λ, used on the gate rotor boundary map references the offset of the *main* rotor. As a consequence, this offset between the interlobe SL and the radial SL for the gate rotor boundary map is actually $\varphi_{c2}(z2/z1)$.

In Figure 4-18 a section of the profile has been highlighted from points A to B on both the main and gate rotors. 'A' corresponds to ε = 0 and 'B' corresponds to ε=1. For this given rotation (λ=0), the boundary points, G, have been highlighted. The first subscript identifies the type of boundary which is either interlobe - I, or radial – R. The lower case letter in the subscript is a unique identifier to distinguish between each point.

The points identified in Figure 4-18 are then plotted on Figure 4-19 and Figure 4-20 in order to highlight the line AB which occurs when λ = 0. This illustrates how for any given rotation angle, λ, the rotor surface boundary map can be used to identify what chamber a given point on the surface is exposed to. For example: a point within the region, $G_{Ia} < \varepsilon < G_{Ib}$, will be exposed to the chamber, C_1, when λ = 0.

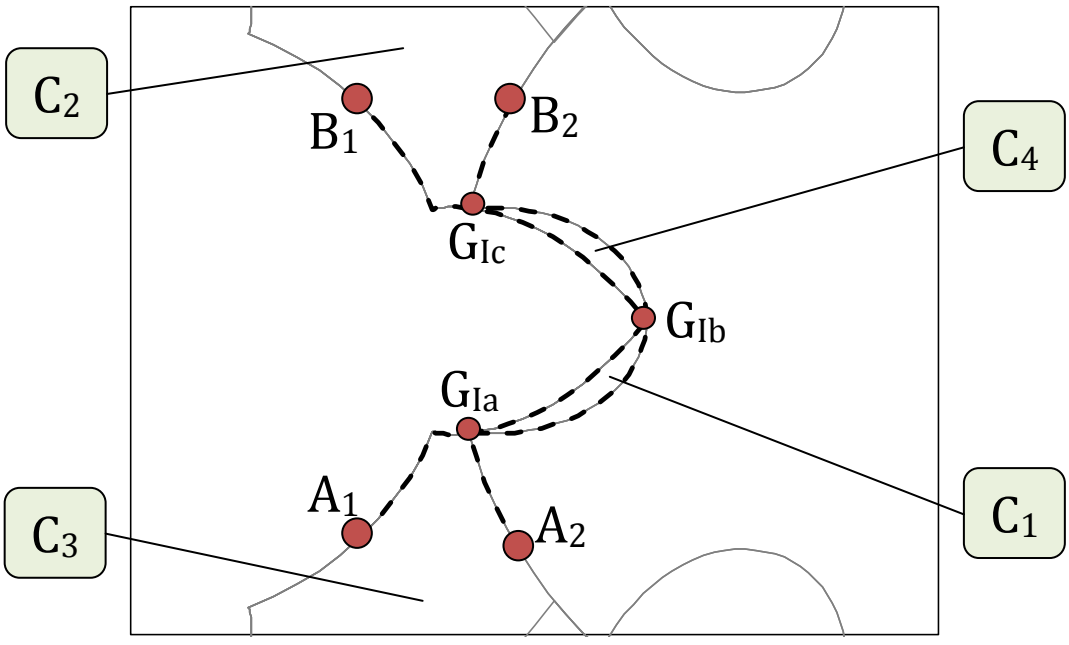

Figure 4-18: Zero BH rotor boundary points (λ = 0)

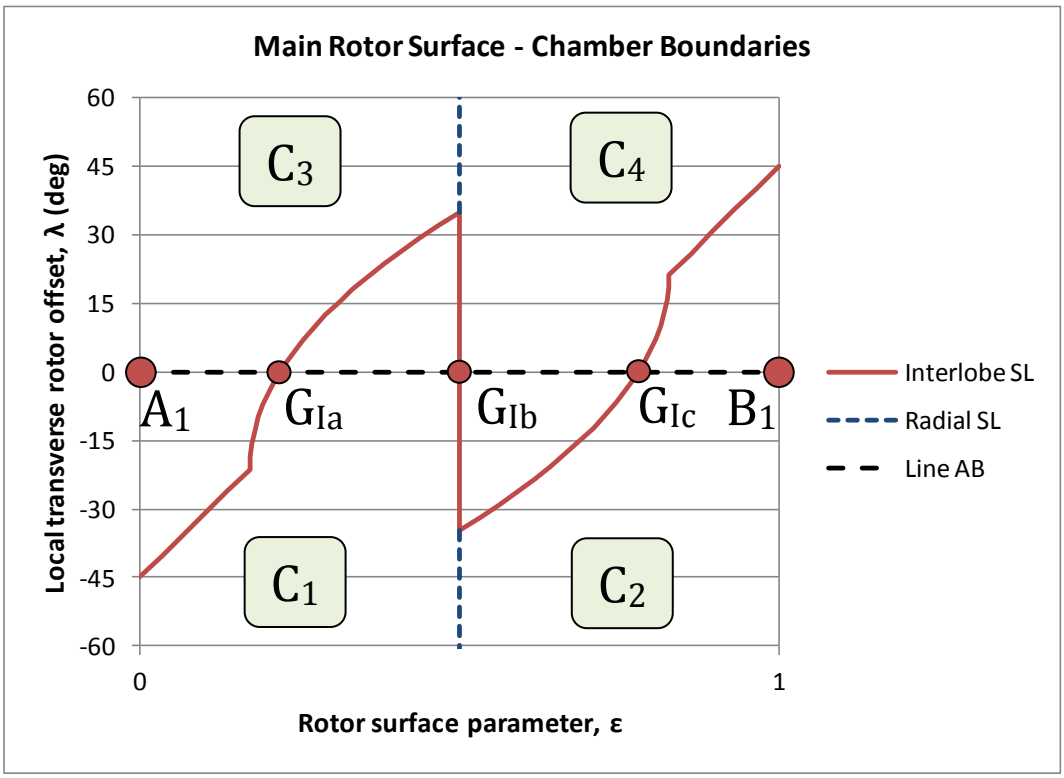

Figure 4-19: Zero BH rotor boundary points on main rotor surface (λ = 0)

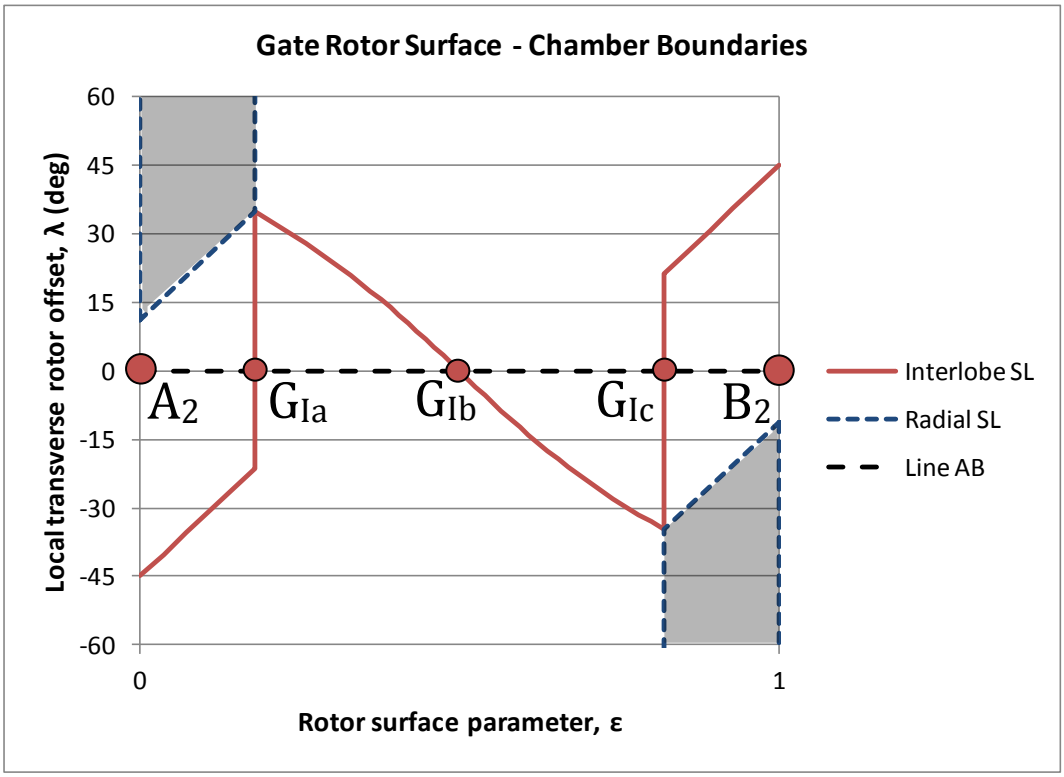

Figure 4-20: Zero BH rotor boundary points on gate rotor surface (λ = 0)

A second rotor position is presented in Figure 4-21, Figure 4-22 and Figure 4-23. The profiles have been rotated backwards until the tip of the main rotor meets the HP cusp. In these figures line AB has now moved down to the appropriate value of $\lambda = -\varphi_{C1}$.

At the tip of the main rotor the interlobe boundary, G_{Ib}, has been identified. At this point the main rotor and gate rotor also both meet the cusp of the casing therefore this point could equally have been identified by the radial boundaries since: $G_{Ib} = G_{R1} = G_{R2}$. This is confirmed on the rotor surface maps that show G_{Ib} is located at the intersection of the interlobe SL and radial SL for both main and gate rotor surfaces.

Between point G_{Ib} and B_2 on the gate rotor it can be observed that the rotor surface is not exposed to any rotor chambers for this rotor angle.

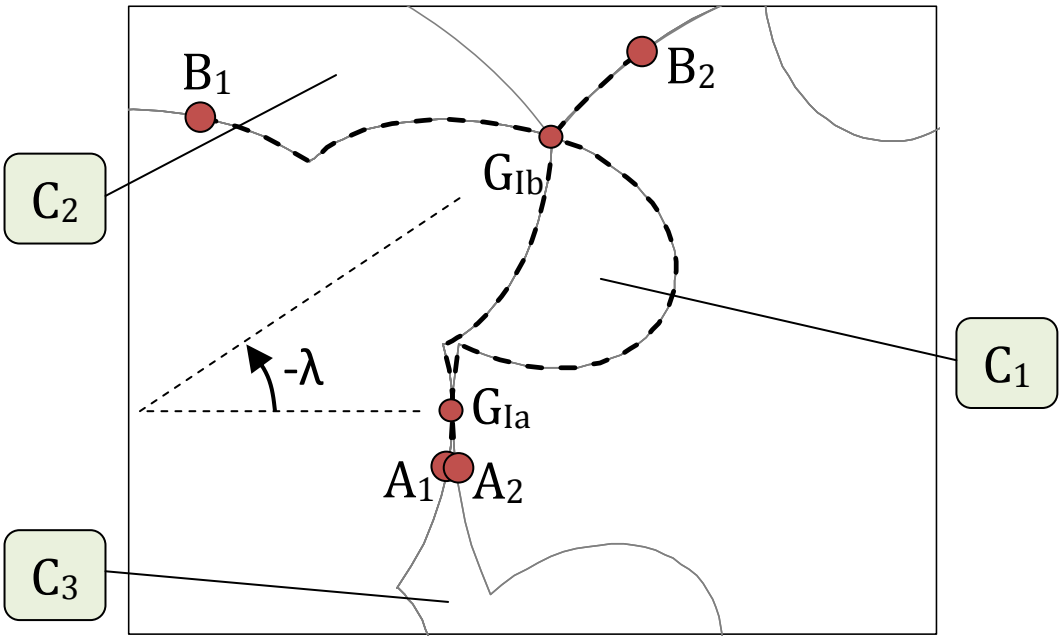

Figure 4-21: Zero BH rotor boundary points ($\lambda = -\varphi_{c1}$)

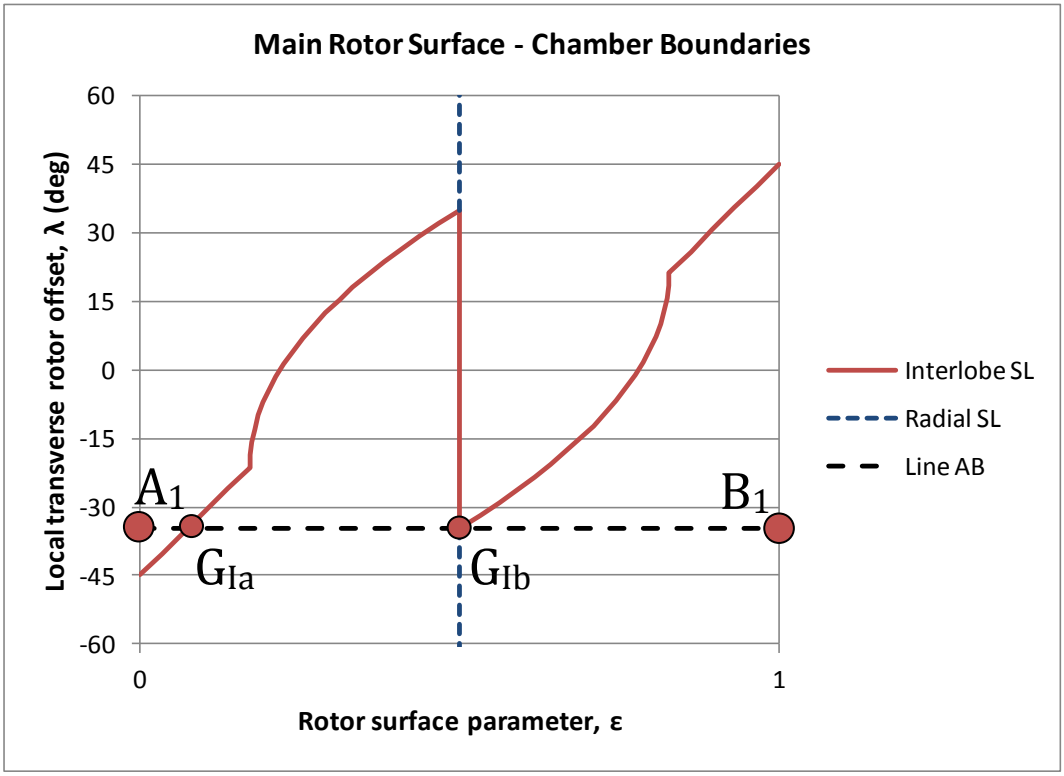

Figure 4-22: Zero BH rotor boundary points on main rotor surface ($\lambda = -\varphi_{c1}$)

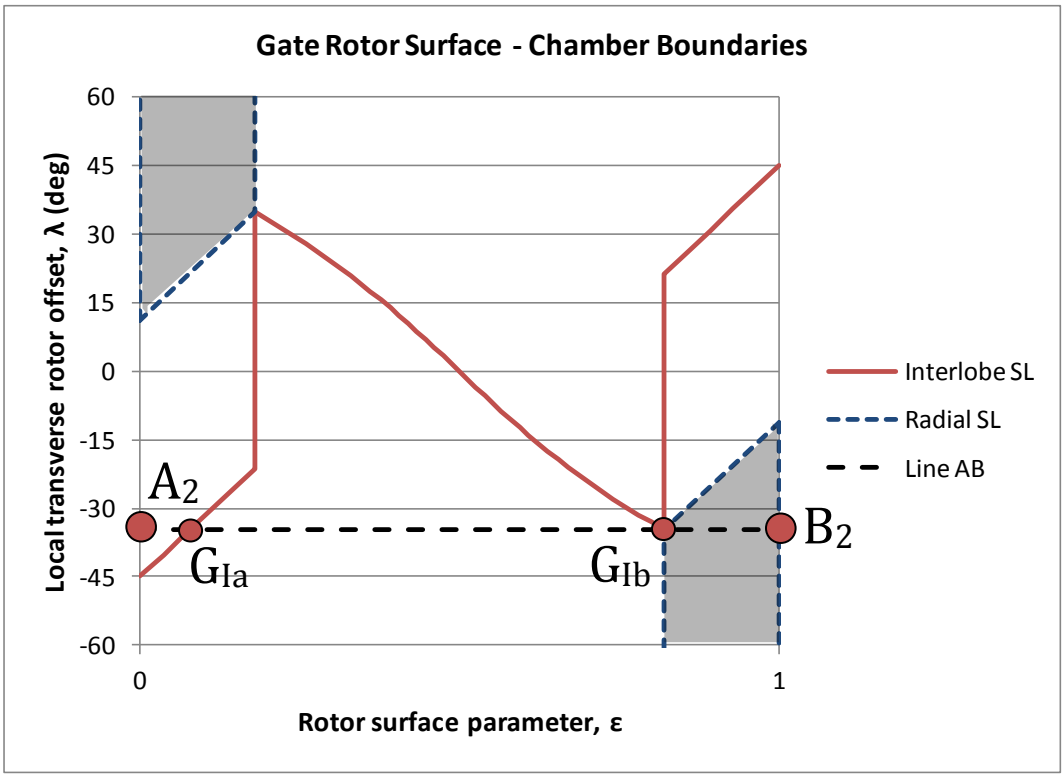

Figure 4-23 Zero BH rotor boundary points on gate rotor surface ($\lambda = -\varphi_{c1}$)

4.6.2 EXAMPLE: SYMMETRIC PROFILE

For various reasons the zero BH profile is not practical for use in twin screw compressors. Figure 4-24 shows a representation of the first manufactured profile - the SRM symmetric profile. The root of the main rotor is now situated on a circle below the pitch circle resulting in a dedendum on the main rotor and an addendum on the gate rotor which is a feature that is present to some degree on all modern profiles. All curves on the gate rotor are circles with centres located on either the axis of the rotor or on the pitch circle. This results in similar circular curves on the main rotor. Only the lower portion of the main flank is non-circular – this is generated by the point on the gate rotor where the small tip radius intersects with the large radius of the flute.

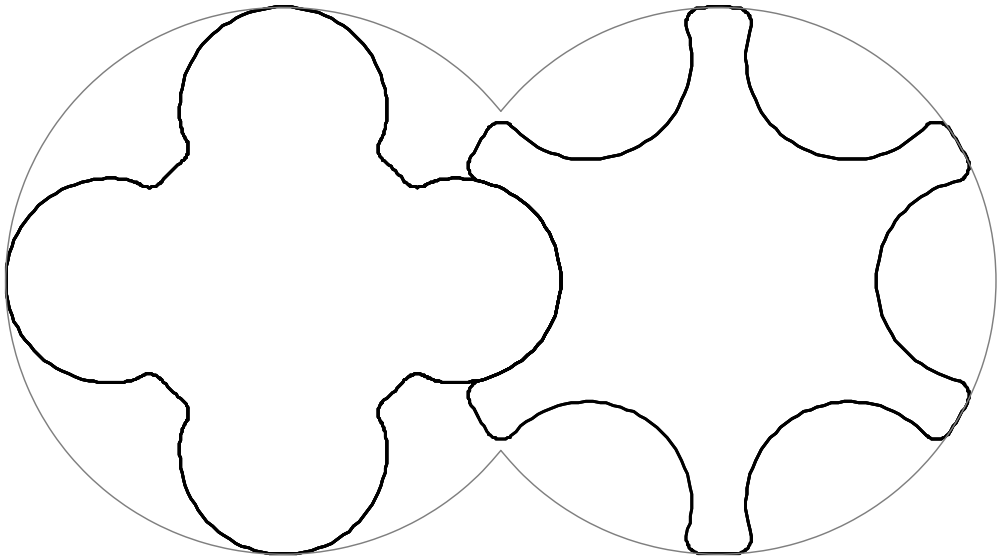

Figure 4-24: Symmetric (circular) rotor profile

This profile presents a complete contrast to the previous example as the interlobe sealing line is very short and does not extend anywhere close to the cusps on the casing. This poses some difficulty when distinguishing clear chamber boundaries and is therefore a useful case study. The chambers and boundaries have been identified on the rotors in Figure 4-25, Figure 4-26 and Figure 4-27 which each show a different rotor position.

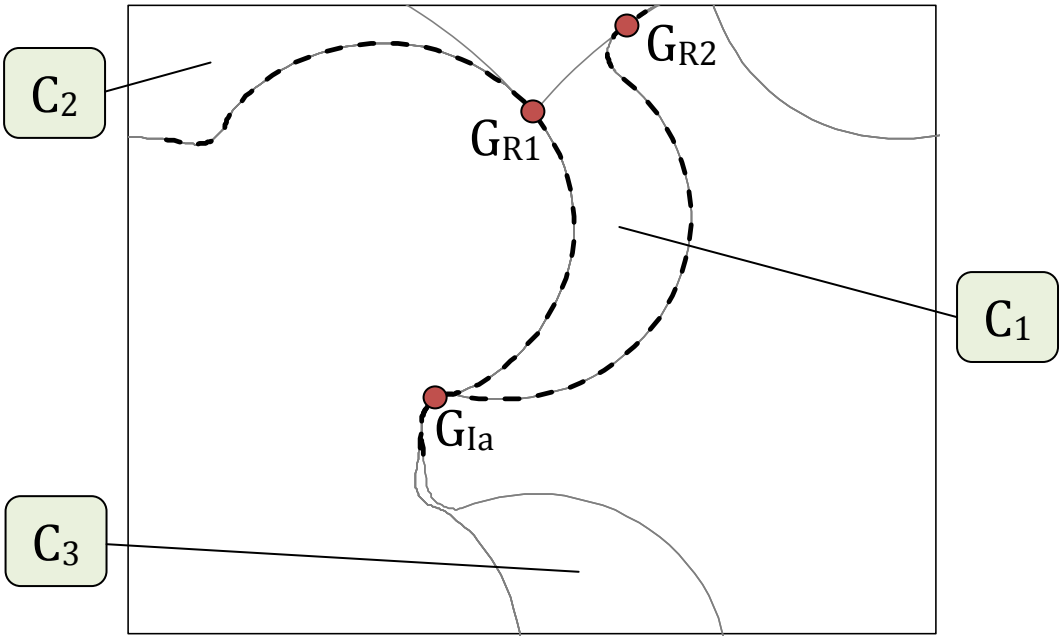

Figure 4-25: Symmetric rotor boundary points ($\lambda = -\varphi_{C1}$)

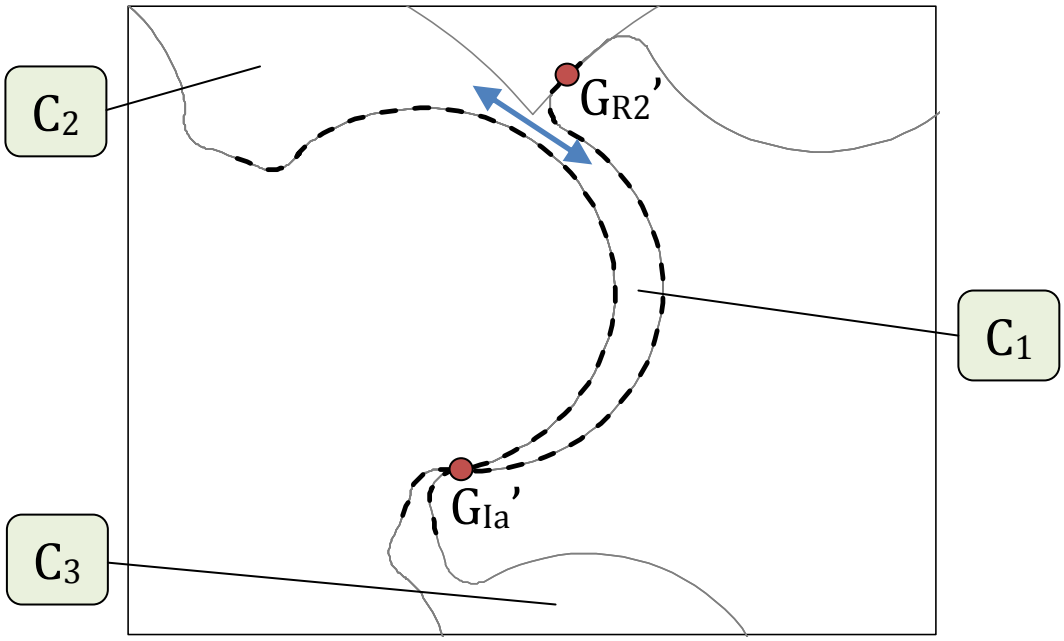

Figure 4-26: Symmetric rotor boundary points ($-\varphi_{C1} < \lambda < 0$)

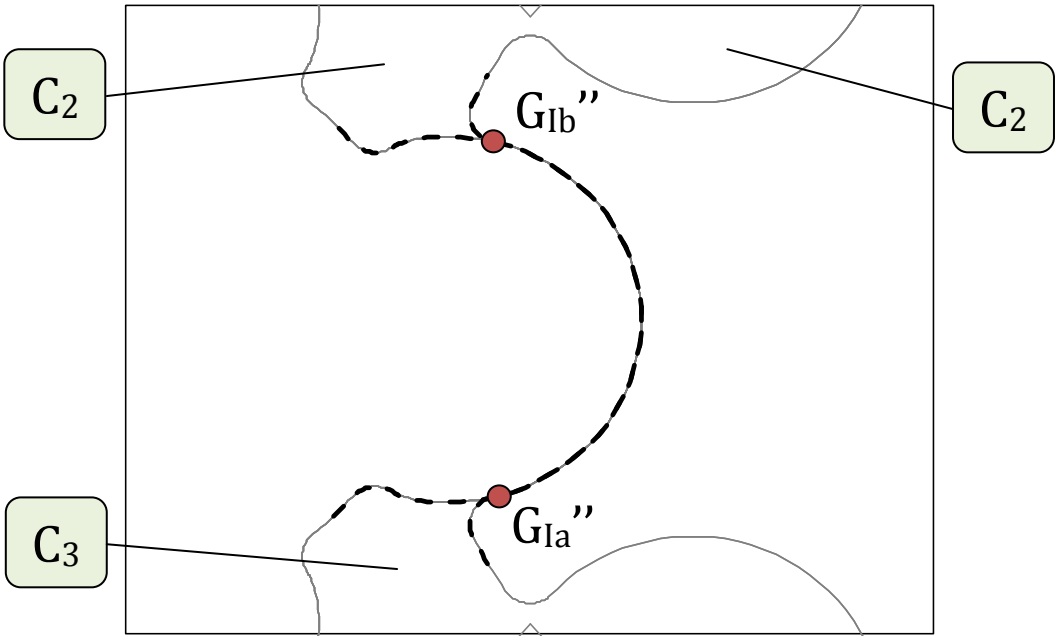

Figure 4-27: Symmetric rotor boundary points (λ = 0)

At rotor position $\lambda = -\varphi_{c1}$ (as in Figure 4-25), chambers C_1 and C_2 are separated by the boundary point G_{R1}. As the rotor angle λ increases this point disappears and a connection is formed between the chambers, known as the BH leakage path. This connection does not actually disappear until the boundary point G_{Ib}'' is formed when $\lambda = 0$ (as in Figure 4-27). At this point the chamber C_1 has reduced to zero cross-sectional area.

The points identified in the previous rotor figures have been plotted on the newly generated symmetric rotor boundary map for the main rotor in Figure 4-28. In this map the four chambers are not fully separated. Figure 4-25 shows that when $\lambda = -\varphi_{c1}$, (the line through $G_{Ia}G_{R1}$ on Figure 4-28) the range of the rotor surface when $\varepsilon > G_{R1}$ is certainly only exposed to chamber C_2. By assessing Figure 4-27, when $\lambda = 0$, it is reasonable to state that just before this, when $\lambda < 0$, the range of the rotor surface $G_{Ia}'' < \varepsilon < G_{Ib}''$ will be exposed to chamber C_1.

Between these two values of λ no boundary exists on the surface between chambers C_1 and C_2. In order to map chamber properties to the surface, the chamber exposure must be explicitly defined. Therefore in Figure 4-29 new boundaries have been defined by linearly interpolating between the known points.

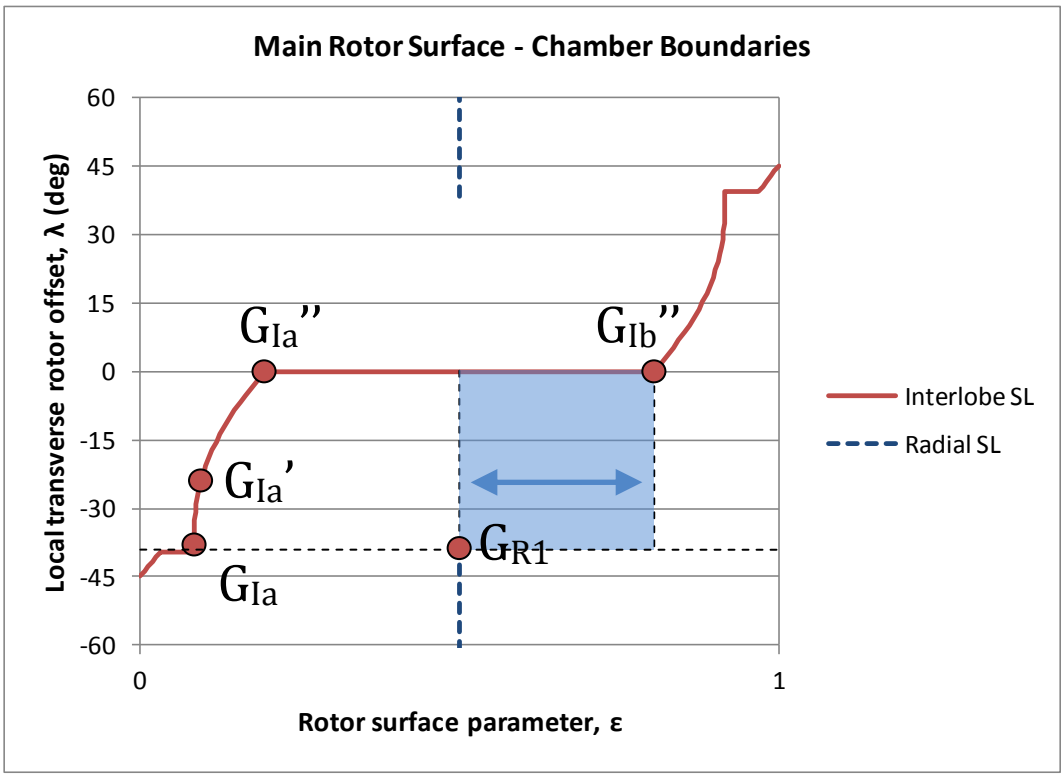

Figure 4-28: Symmetric rotor boundary points on main rotor

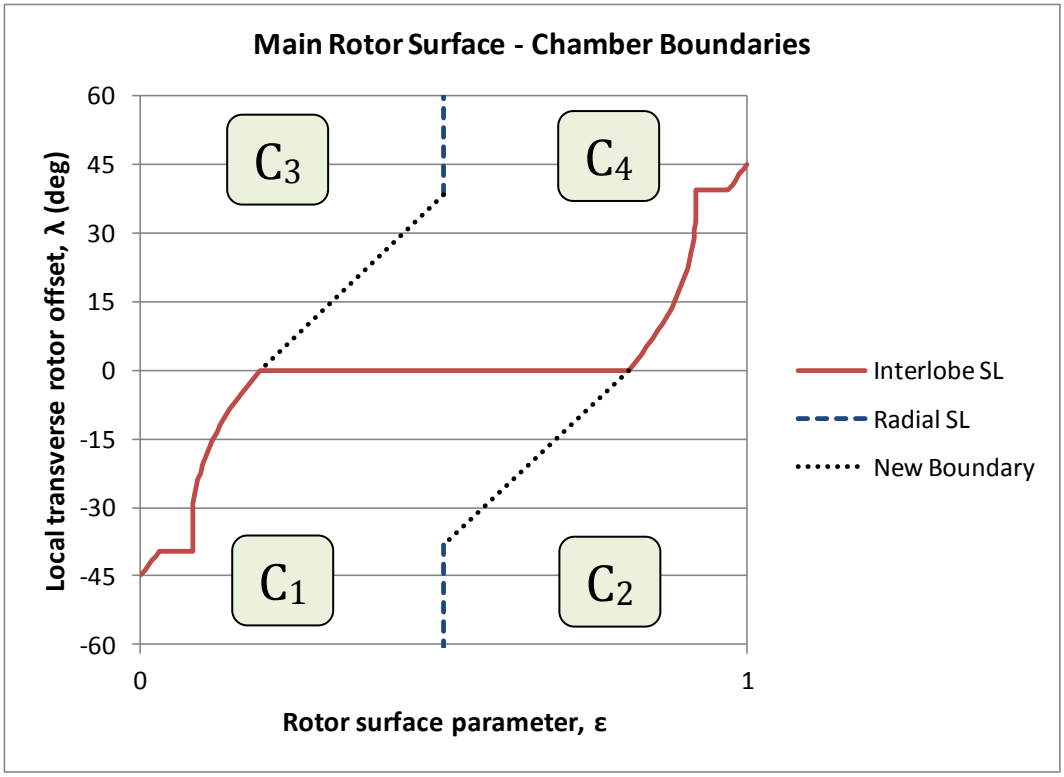

Figure 4-29: Symmetric rotor boundary map for main rotor with new boundaries

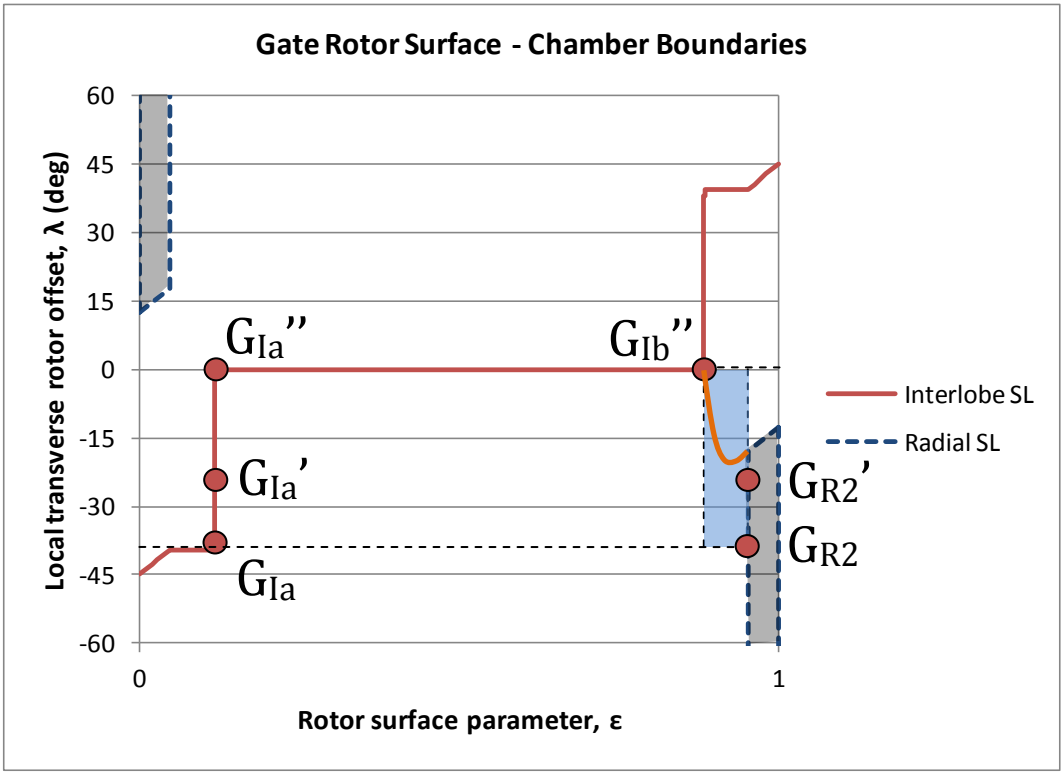

Figure 4-30: Symmetric rotor boundary points on gate rotor

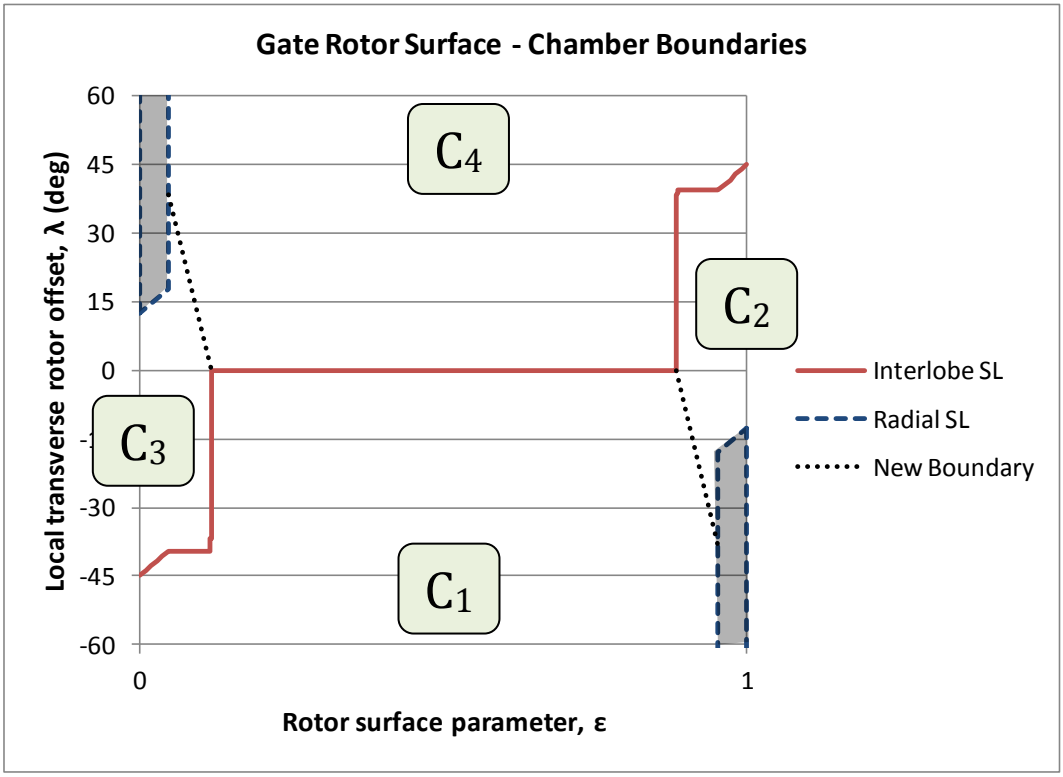

Figure 4-31: Symmetric boundary map for gate rotor with new boundaries

The boundary points have also been plotted on the symmetric rotor boundary map for the *gate* rotor in Figure 4-30. Following a similar procedure as for the main rotor, new boundaries have been generated and plotted in Figure 4-31.

From Figure 4-25 it can be stated that between the points G_{Ia} and G_{R2} the gate rotor surface is exposed to C_1 so it follows that this is true along this horizontal line between these points on Figure 4-30. Similarly from Figure 4-27 it can be stated that when $\varepsilon > G''_{Ib}$ this part of the surface is exposed to C_2. These facts can be stated with some degree of certainty based on this reasoning.

Between these two states no boundary exists and the surfaces between the rotors and casing combine to form a complex 3D flow channel. This area on the boundary map has been highlighted by the blue box. A considerable amount of time was spent trying to define the most appropriate curve to define this boundary on the gate rotor boundary map – the orange curve on Figure 4-30 actually approximates a transformation of the curve formed by the blow hole definition in Appendix 'A.3.3 Blow Hole Area'. Ultimately, any curve relies on an assumed boundary surface in the region of what is a non homogeneous flow in terms of pressure and temperature distributions. It was finally decided to avoid unnecessary, unjustifiable complexity and to stick to linearly interpolating between the two explicit states resulting in the boundaries added to Figure 4-31.

These new boundaries can be referred to as the blowhole boundaries. The new boundary on the left hand side of the boundary map, where the values of ε are smaller, is on the leading flank of the main rotor and forms the LP blowhole. Conversely, on the right hand side which is the trailing flank of the main rotor, the new boundary forms the more important HP blowhole.

4.6.3 EXAMPLE: ASYMMETRIC PROFILE

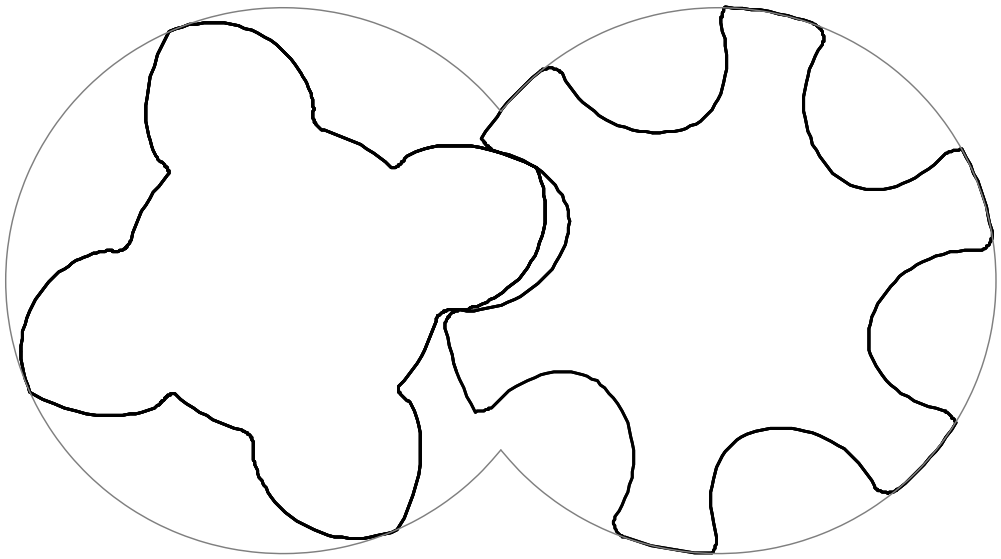

Figure 4-32: Asymmetric rotor profile (hybrid of zero BH and symmetric)

By combining the simple features of the zero BH profile and the symmetric (circular) profile it is possible to approximate a more typical asymmetric profile as shown in Figure 4-32. This example shows how the boundary map generation procedure and the rules defined for creating new boundaries can be applied to any typical profile. Due to the asymmetry of the profile, the tip of the main rotor is now located at a position $\varepsilon > 0.5$, rather than at the mid-point.

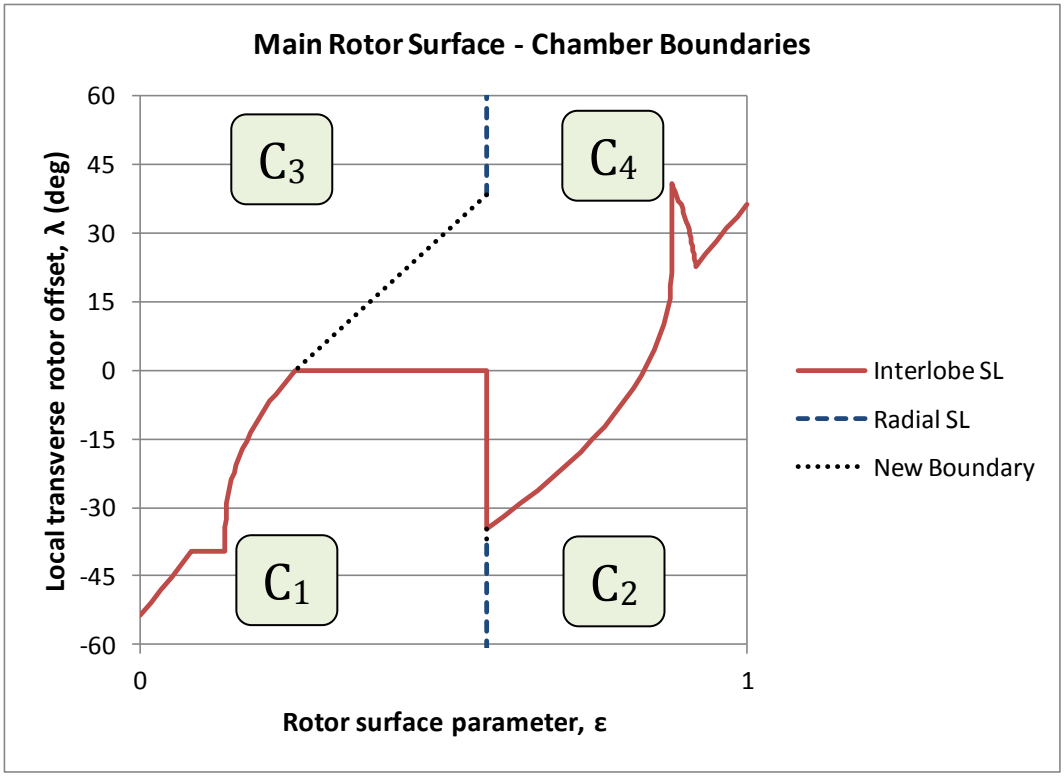

Figure 4-33: Asymmetric rotor boundary map for main rotor

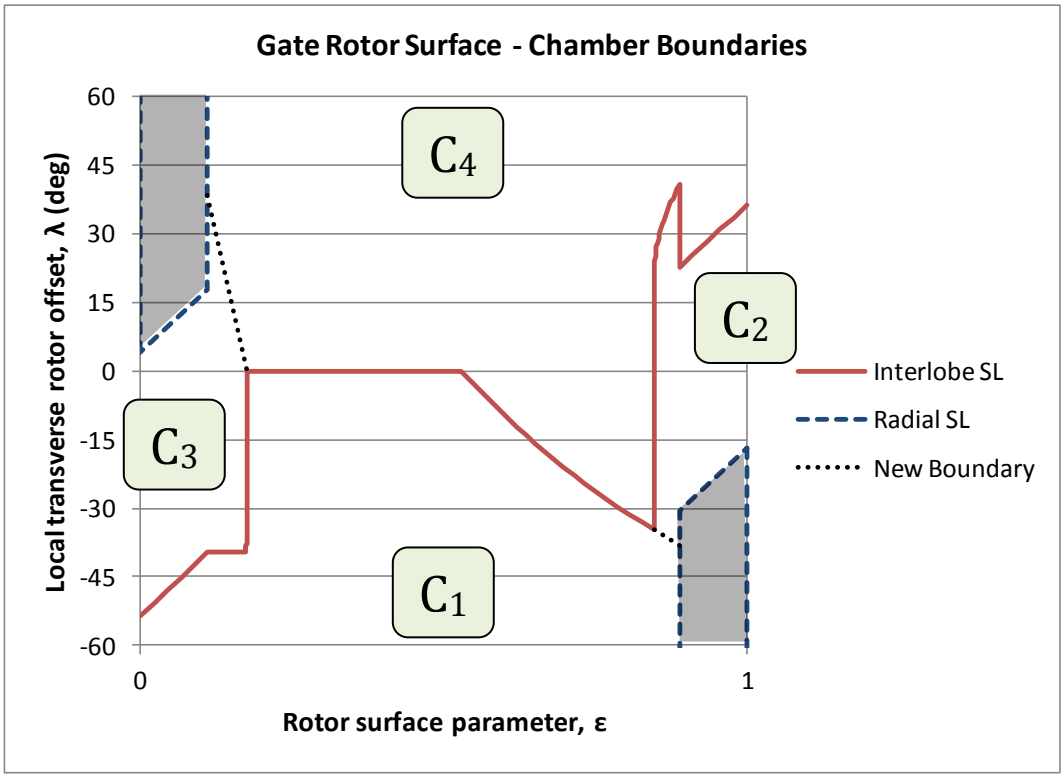

Figure 4-34: Asymmetric rotor boundary map for gate rotor

It can now be observed that with this asymmetric profile the length of the new boundary line required to bridge the gap that forms the blow hole leakage path is considerably smaller on the HP blowhole on the right hand side, particularly on the main rotor boundary map.

When considering the boundary map generated by the gate rotor in all of these examples the most notable difference from the main rotor maps is the greyed out area bounded by the radial SL, within which the rotor surface is not exposed to any chambers. This is certainly true for a theoretical compressor with zero clearances however in practise fluid will exist between the rotor and the casing due to the radial clearance gap. Assessing the fluid properties along the length of this leakage path is somewhat beyond the capabilities of the thermodynamic chamber model currently used. A reasonable compromise for this procedure is to define an arbitrary boundary at the mid-point of the arc that lies on the gate rotor OD. This approach is certainly appropriate if a tip sealing strip is located at this point. This modified boundary map for the gate rotor presented in Figure 4-35 allows boundary conditions to be mapped onto the full surface of the gate rotor.

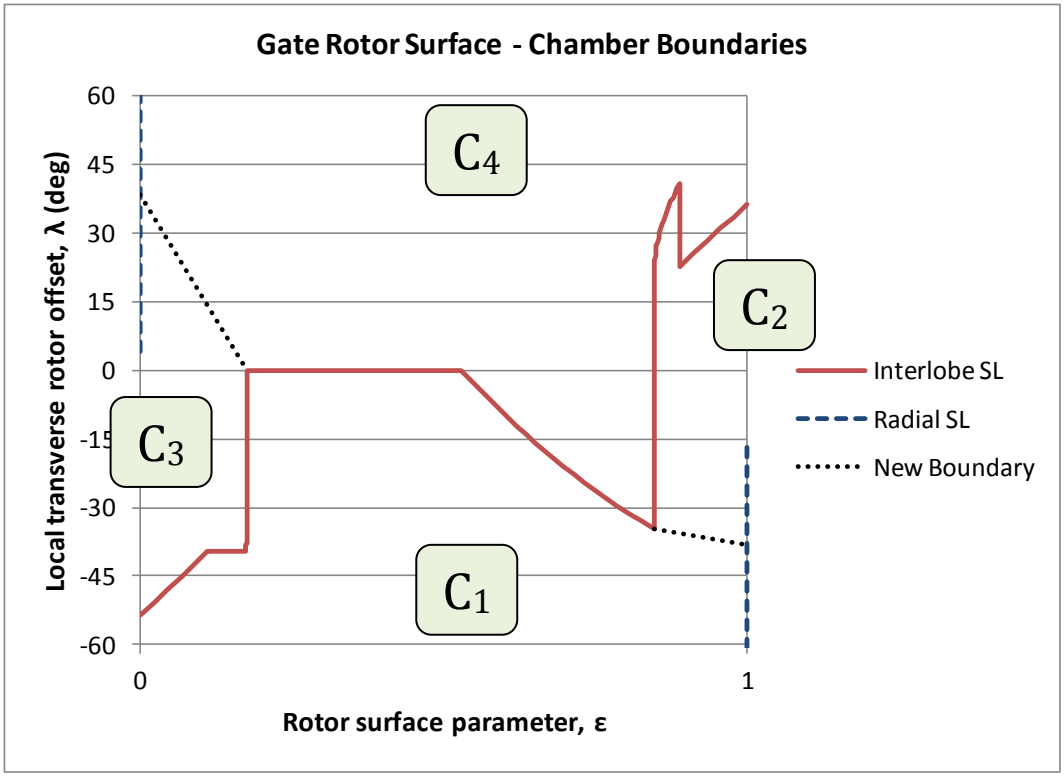

Figure 4-35: Asymmetric rotor boundary map for gate rotor with adjusted radial SL

4.6.4 EXAMPLE: N – PROFILE

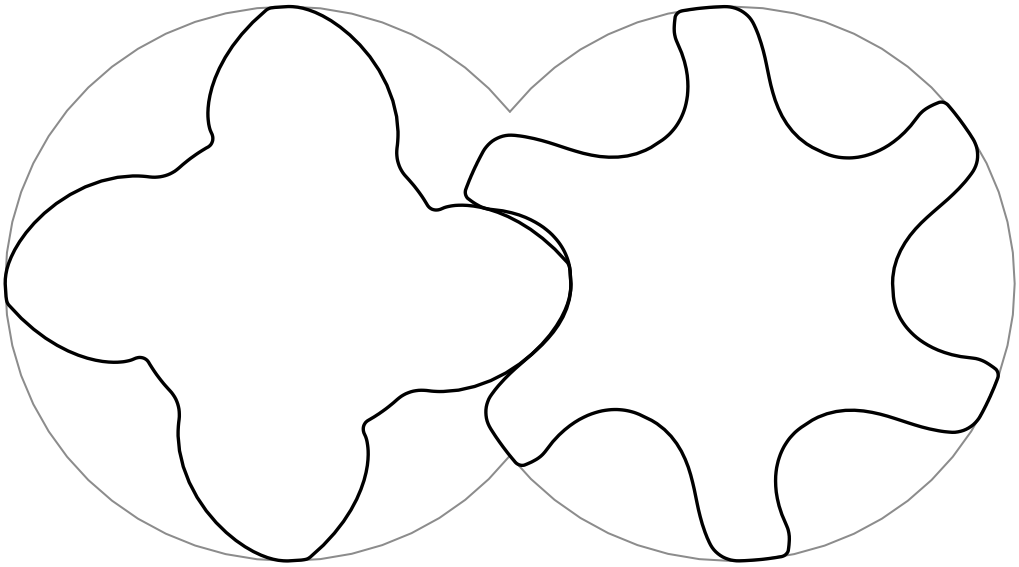

Figure 4-36: N-profile rotors

Figure 4-36 shows a pair of N-profile rotors that are representative of the type of profile used in modern screw compressors. This shares many of the basic features of the asymmetric profile shown in Figure 4-32 but there is much more control over a range of additional design parameters. For example: the flank angles can be adjusted in the vicinity of the pitch circle where involute curves ensure good torque transmission when required; the radius of all curves can be adjusted; and undercutting generation from one rotor to another uses a small radius on the generating profile instead of a single point.

The corresponding rotor boundary maps for this profile are shown in Figure 4-37 and Figure 4-38. These profiles will be used in exemplary figures in the next section which addresses how the four chambers, C_1 to C_4, relate to the more numerous chambers that actually exist within a twin screw compressor at any instant.

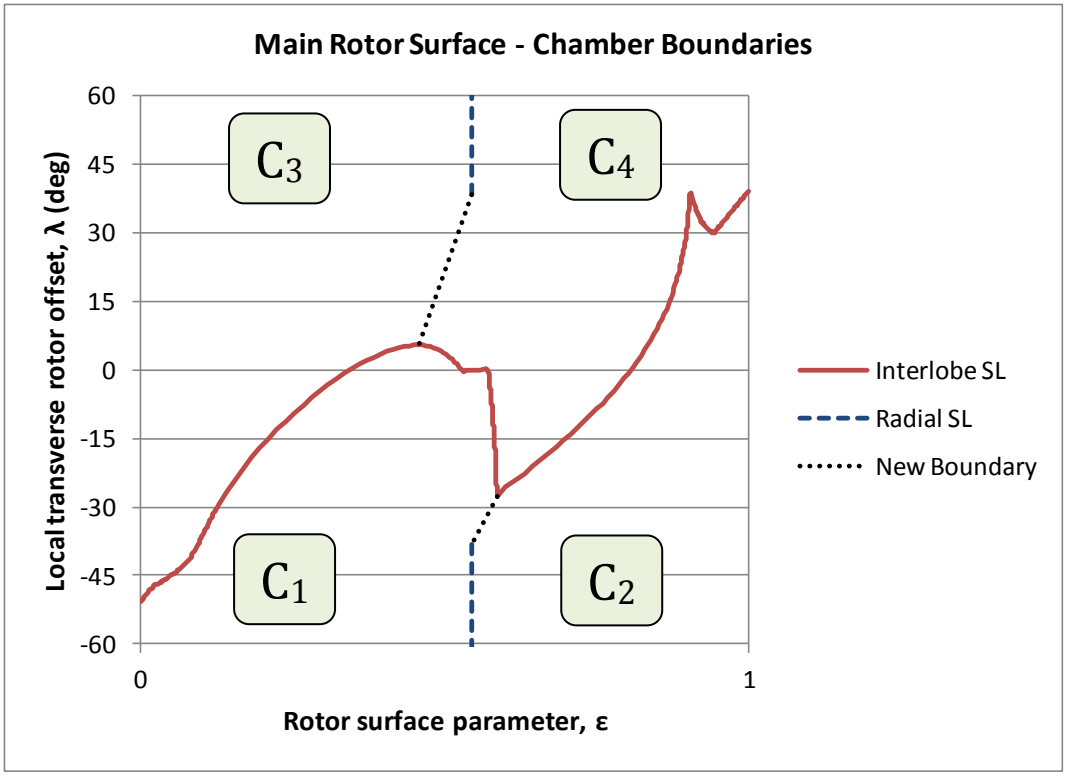

Figure 4-37: N-profile boundary map for main rotor

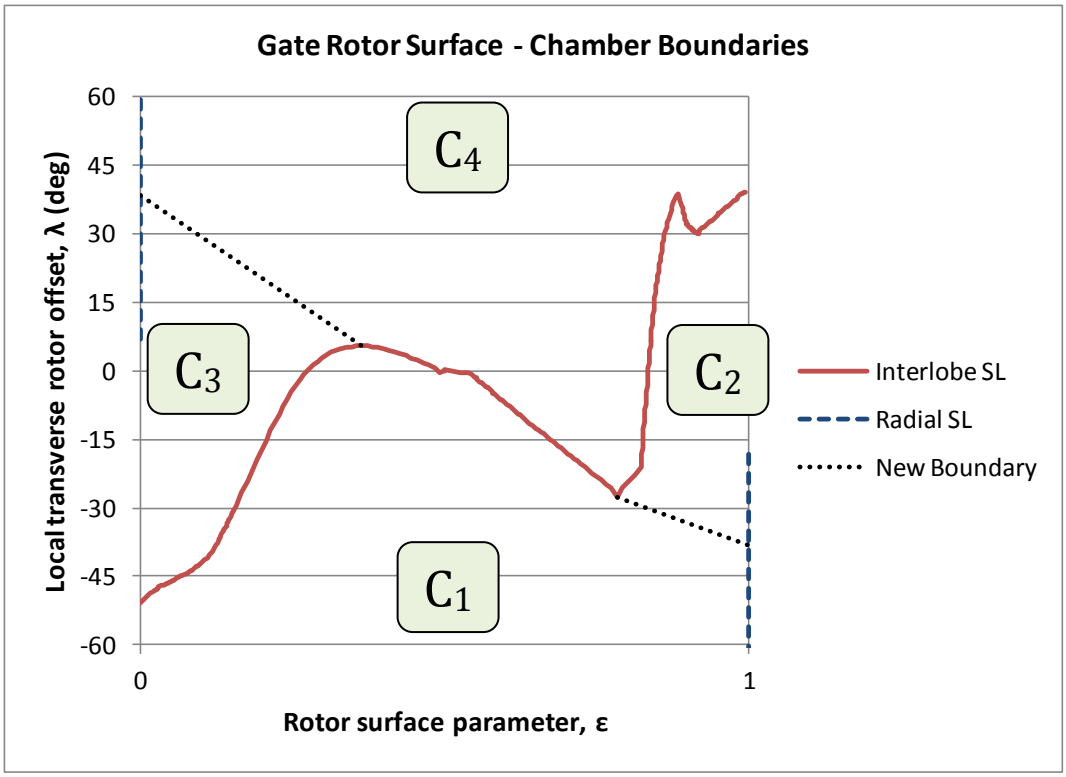

Figure 4-38: N-profile boundary map for gate rotor

4.7 LOCAL CYCLE EXPOSURE OVER FULL ROTORS

The full 3-dimensional rotor surfaces are plotted in Figure 4-39 at a reference compression cycle angle, θ. All rotor sections have been generated from the surface arrays R1(ε_1,γ_1) and R2(ε_2,γ_2) as shown in Figure 4-6. The parameters r and β can be found for a point on the rotor surface at any cycle angle using the equations set out previously. The parameters r, β and γ were then transformed to the global X,Y,Z co-ordinates and plotted using 'Gnuplot' (Williams, Kelley et al. 2013).

In order to build up the full 3D surface, the surface at cycle angle θ is written to memory then the cycle angle is advanced by $2\pi/z1$ and the next surface is written to memory until all lobes have been generated.

Due to the way the respective rotor parameters, r, β and γ, have been defined for R1 and R2 with respect to a reference cycle angle , θ, the rotors would be displayed in mesh once related back to the global Cartesian compressor co-ordinate system, S0. However, in order to show the detail along the meshing line the rotors have been plotted separately and are viewed as if from the other rotor.

The current objective is to set out the procedure by which the instantaneous cycle angle for the local compression chamber at any point on the surfaces displayed in Figure 4-39 can be retrieved. The required parameter is the 'local cycle angle', θ_{local}; this is based on θ which is effectively a 'reference cycle angle' because it only defines the cycle angle for a single 'reference compression chamber' that is used to define the rotor position.

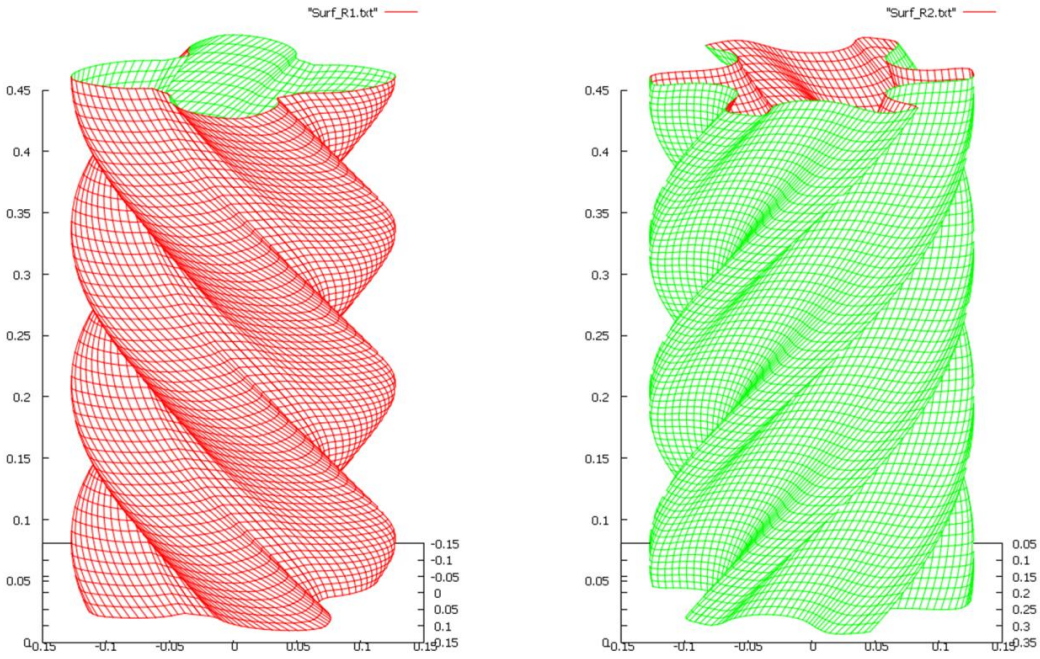

Figure 4-39: Full rotor surfaces (3D domain)

The first step to finding the local cycle angle, θ_{local}, is to identify where the surface point lies on the *rotor boundary map* in order to establish what chamber offset is required. This requires the rotor surface parameter ε; and the local transverse rotor offset λ. The latter is a function of the axial position parameter, γ; and the reference cycle angle, θ, as set out previously and summarised below:

$$\lambda_1 = \theta - \varphi_{s1} - \gamma - \varphi_{off} \qquad (36)$$

$$\lambda_2 = \theta - \varphi_{s1} - \gamma \qquad (37)$$

In order to use the rotor chamber boundary map the offset should lie in the range: $-180 < \lambda_1 < 180$. In the case of the gate rotor: $-180(z2/z1) < \lambda_1 < 180(z2/z1)$. To ensure the parameter λ is within this range a correction must be applied:

$$\lambda_1' = \lambda_1 + 360n \quad (38)$$

$$\lambda_2' = \lambda_2 + 360n\left(\frac{z2}{z1}\right) \quad (39)$$

Where n is an appropriate positive or negative integer. The maximum value of this integer is limited by the fact that the reference cycle angle used to define the cycle angle in the reference chamber cannot exceed the maximum cycle angle for the rotor pair.

Once known, λ is used along with the rotor surface parameter, ε_1 or ε_2, for the main and gate, to identify the relevant rotor chamber as C_1, C_2, C_3 or C_4 by using the rotor boundary maps of Figure 4-37 and Figure 4-38 for the main and gate rotors respectively.

Figure 4-40 has been created based on the same boundary map of Figure 4-37 in order to illustrate how the local cycle angle needs to be adjusted for each of the four chambers. Chamber C_4 has been set as the reference chamber. By assuming that $-180 < \lambda < 180$, no adjustment of λ is required and the local cycle angle in chamber C_4 will equal the reference angle θ. Crossing the radial SL from C_4 to C_3 advances the local cycle angle by 360/z1. Crossing the interlobe SL from C_4 to C_2 advances the local cycle angle by 360. Crossing the radial SL again from C_2 to C_1 results in a total offset of 360 + 360/z1.

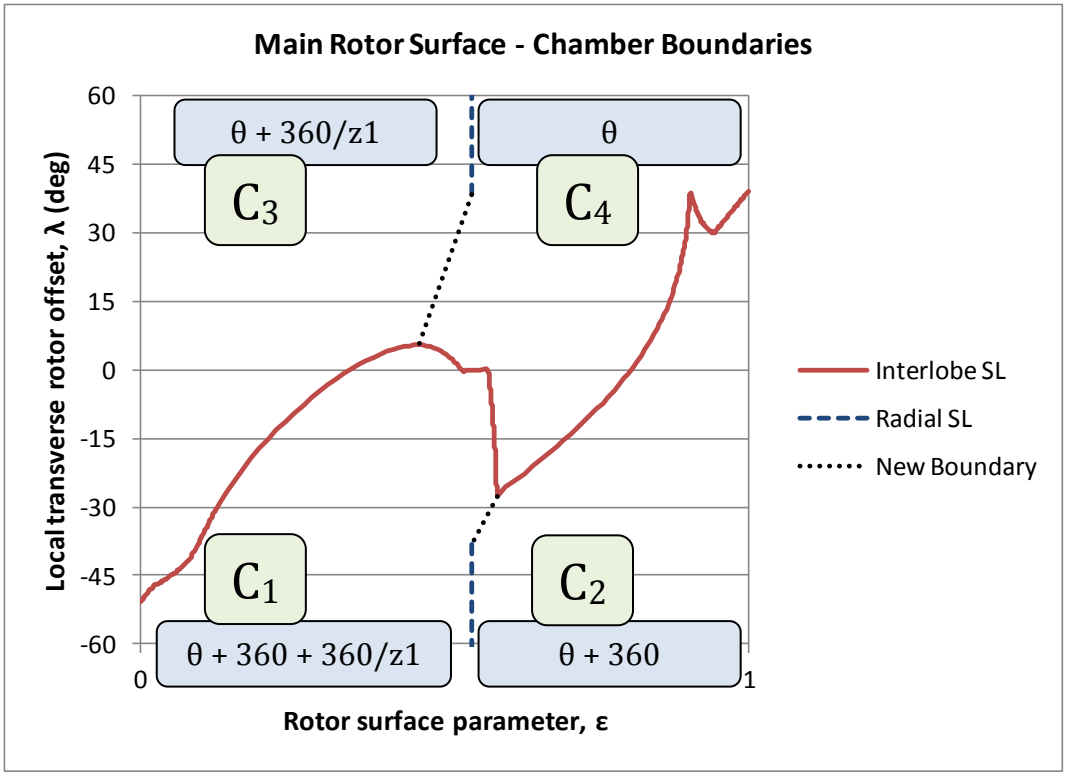

Figure 4-40: Main rotor chamber offsets

If any adjustment is made to λ using equation *(38)* it is important to include that term were calculating the local cycle angle. The general equations for calculation of the local cycle angles for each chamber on the main rotor are given in Table 4-3.

Table 4-3: Local cycle angle corrections on main rotor

Chamber Reference	Calculation of local theta angle , θ_{local}
C_1	$\theta_{local} = \theta + 360 + \frac{360}{z1} + 360n$
C_2	$\theta_{local} = \theta + 360 + 360n$
C_3	$\theta_{local} = \theta + \frac{360}{z1} + 360n$
C_4	$\theta_{local} = \theta + 360n$

Figure 4-41 shows the chamber offsets for the gate rotor boundary map. The boundaries and chambers on this map are the same as those on the main rotor boundary map, albeit with different topography, so it may come as a surprise to see that the equations describing the chamber offsets are slightly different across the interlobe sealing line. The new term highlighted in blue is required to account for any rotor lobe offset that occurs if the difference between z2 and z1 is greater than 1.

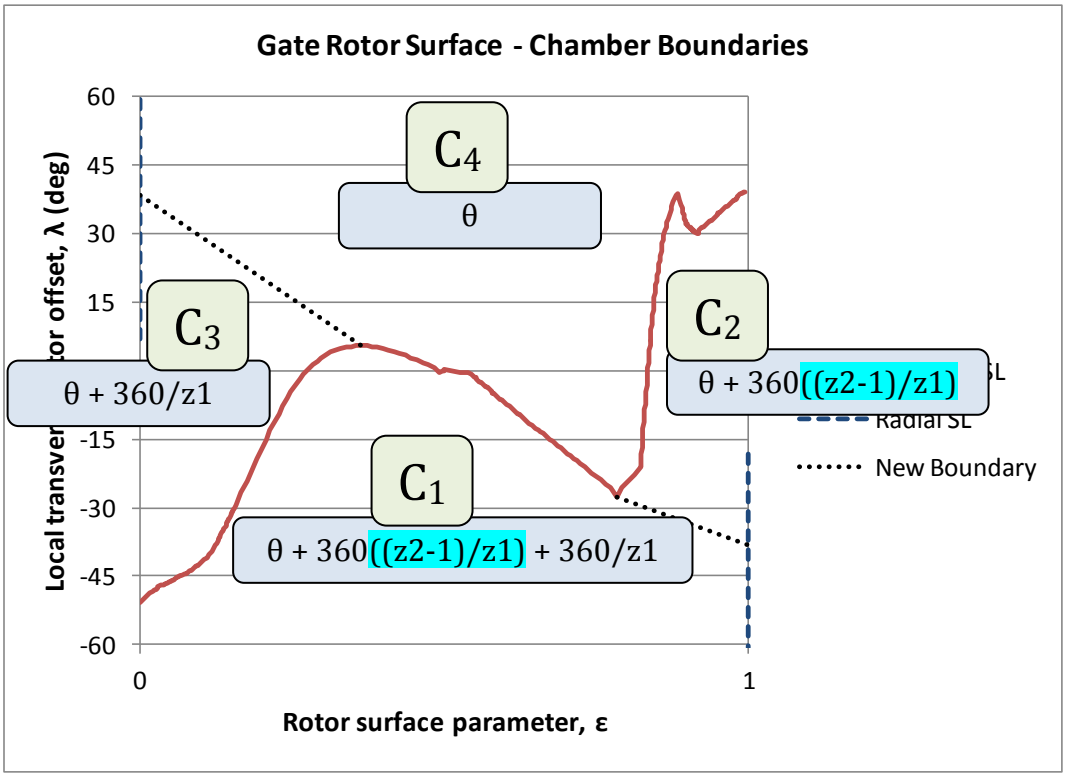

Figure 4-41: Gate rotor chamber offsets

Equations *(31)*, *(33)* and *(36)* all include the rotor lobe offset angle, φ_{off}, which was defined in equation *(16)*. When used in conjunction with the offsets defined above, these equations ensure that the cycle angle calculated for surfaces on each rotor, when exposed to the same chamber near the end of the cycle, is the same. Inevitably this means that the cycle angle will be different for surfaces on each rotor, when exposed to a chamber near the start of the cycle; when the difference between z2 and z1 is greater than 1. The general equations for calculation of the local cycle angles for each chamber on the gate rotor are given

in Table 4-4. The other additional terms highlighted in yellow are due to the difference between equations *(38)* and *(39)*.

Table 4-4: Local cycle angle corrections on gate rotor

Chamber Reference	Calculation of local theta angle , θ_{local}
C_1	$\boldsymbol{\theta_{local} = \theta + 360\left(\frac{z2-1}{z1}\right) + \frac{360}{z1} + 360n\left(\frac{z2}{z1}\right)}$
C_2	$\boldsymbol{\theta_{local} = \theta + 360\left(\frac{z2-1}{z1}\right) + 360n\left(\frac{z2}{z1}\right)}$
C_3	$\boldsymbol{\theta_{local} = \theta + \frac{360}{z1} + 360n\left(\frac{z2}{z1}\right)}$
C_4	$\boldsymbol{\theta_{local} = \theta + 360n\left(\frac{z2}{z1}\right)}$

In one sense it is a fairly trivial task to correct chamber offset across the main interlobe and radial boundaries. However only by analysing the rotor boundary maps can the subtle complexity of the problem be appreciated. All of the rotor profile examples show that along at least some portion of the interlobe SL, the chamber C_1 is adjacent to C_4 due to the discontinuity of the radial SL so the offset across this portion of the interlobe SL is $2\pi + 2\pi/z1$. Referring back to Figure 4-12 in which the sealing boundaries are shown as boundary points, the adjacent chambers in green and red around meshing lobes of the main rotor are equivalent to C_1 and C_4.

The rotor surfaces have been re-plotted in Figure 4-42 with the local cycle angle, θ_{local}, represented by the colour contours. Areas that are the same colour can be easily identified as individual compression chambers. In order to build up the full rotor the procedure was repeated after advancing the reference cycle angle θ for each lobe:

$$\theta' = \theta + \frac{360n}{z1} \qquad (40)$$

On the gate rotor on the right hand side of Figure 4-42 two white dashed lines have been added. These are the newly defined boundaries that were introduced in Figure 4-38 to form a boundary across the blow-hole leakage paths – the more important HP blowhole is the smaller dashed line on the left. The fact that these seem to separate the chambers in a sensible manner provides some degree of validation regarding the boundary definition.

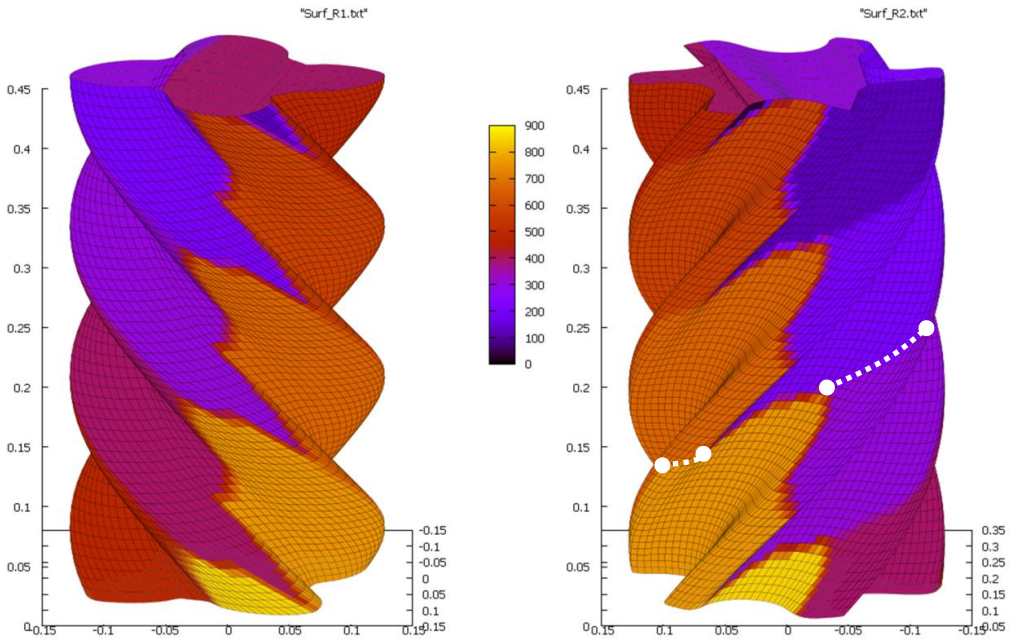

Figure 4-42: Full rotor surfaces with surface contour plot of local cycle angle

In the region of the boundaries some of the tiles used to produce this plot suggest a transition region across the boundary however this is an artefact introduced by the averaging across nodes that fall in different chambers. All computations are done at the nodal positions therefore the calculated values will only fall within the specified local cycle angles.

4.8 Mapping Pressure and Temperature on Surfaces

4.8.1 Temperature Distribution

The homogenous fluid properties within a single compression chamber are calculated for a given operating fluid and duty point using the established chamber model detailed in Chapter 2. The fluid properties are output with respect to the compression cycle angle (in this case normalised to be zero at maximum chamber volume) as presented in Figure 4-43.

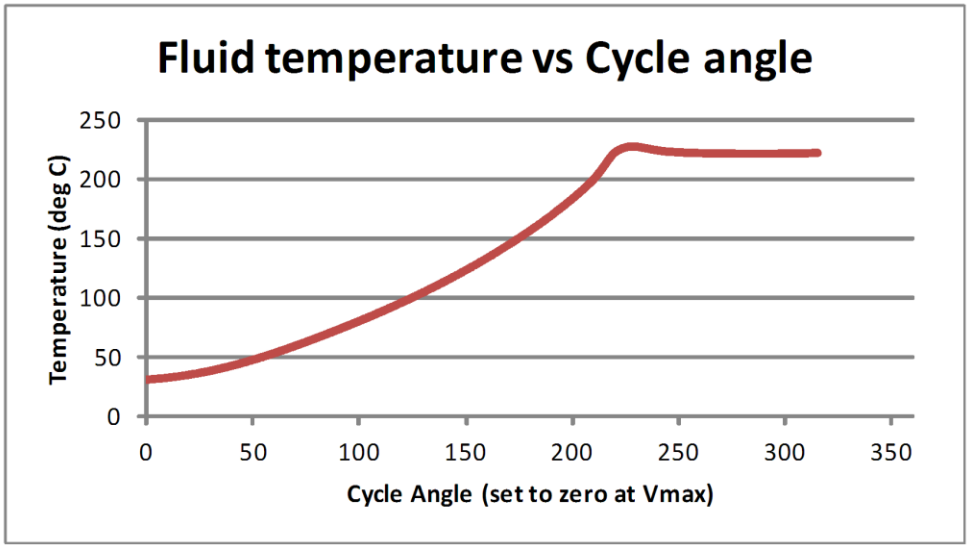

Figure 4-43: Thermodynamic results from chamber model

With these results, and knowing the local cycle angle at any particular point on the rotor and casing surfaces it is a matter of referencing the appropriate fluid properties from the thermodynamic results.

Figure 4-44 shows the instantaneous, homogeneous gas temperature from the chamber model results mapped onto the main and gate rotor surfaces. This output will vary depending on the reference cycle angle θ, which controls the rotor positions, however once the cycle has gone through 360°/z1 the result presented would repeat.

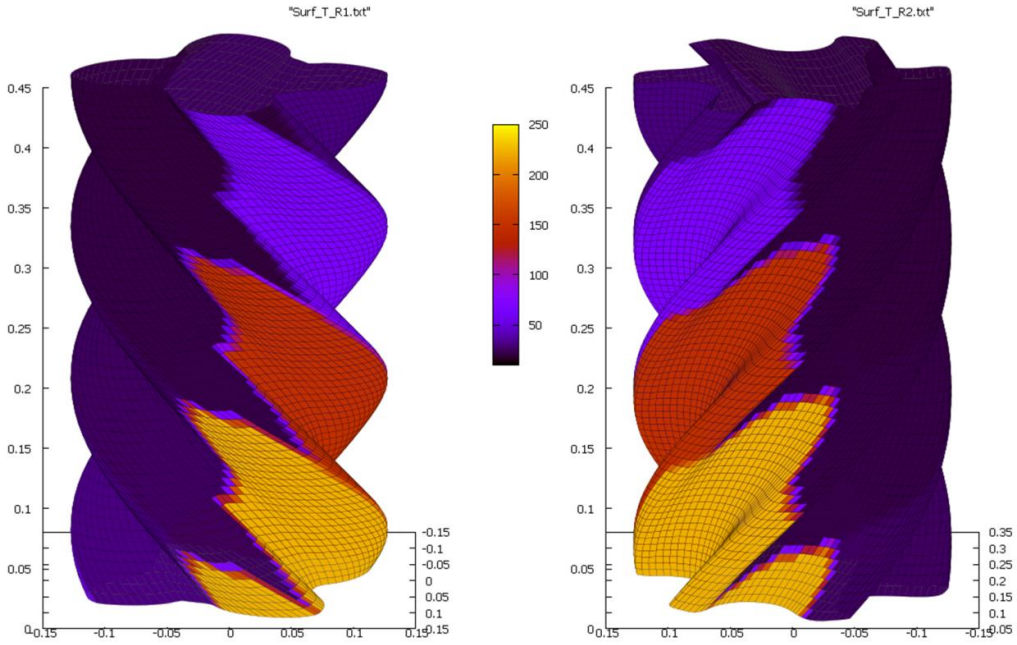

Figure 4-44: Instantaneous gas temperature at rotor surface.

In Figure 4-45 the time-varying fluid properties have been averaged over the full rotor cycle (360°) for each location on the rotor surface in order to approximate steady state boundary conditions. Averaged boundary conditions would greatly simplify any thermal analysis.

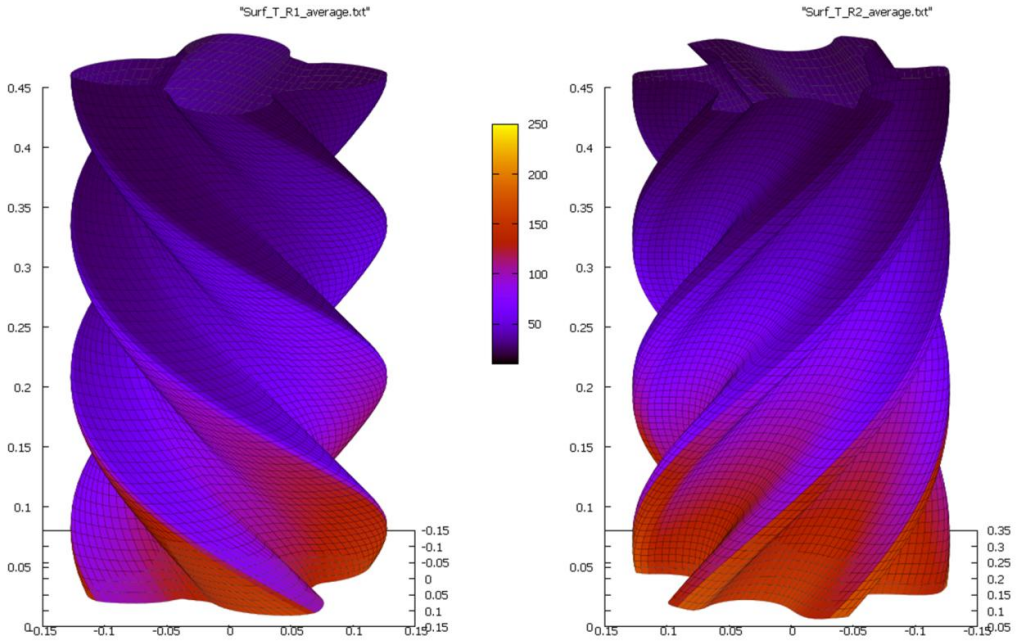

Figure 4-45: Time averaged gas temperature at rotor surface

The temperature results mapped onto the rotors are mapped onto the casing surfaces in the same way using the calculated local casing cycle exposure. The averaging of casing and rotor temperatures is discussed in more detail in the next chapter.

4.8.2 Pressure Distributions

Pressure distributions are found in exactly the same way as the temperature distributions as shown in Figure 4-43 and Figure 4-44. With pressure, the time varying forces on the rotor are of interest therefore it is not appropriate to average the instantaneous pressure distributions. The pressure results would need to be repeated over the range 360°/z1, with appropriate time resolution to capture the full time history for the pressure boundary conditions.

In order for pressure results to be utilised in a useful way it is necessary to resolve the net pressure forces on the rotors due to the pressure distribution on all rotor surfaces i.e. radial loads, axial loads and torque. Calculation of these forces was not included in the scope of this thesis and will be addressed in further work.

4.9 CONCLUDING REMARKS

Accurate surface boundary mapping and calculation of chamber exposure is critical for any kind of analysis that relates fluid properties within the chamber to the actual rotor geometry. This includes determination of thermal boundary conditions which will be utilised in the next chapter, and in future work, the calculation of net forces of the rotor body due to pressure loading.

These procedures will allow existing results from a non-dimensional chamber model to be utilised in new ways such as estimating local operational clearance distortions. In addition it provides a better understanding of the complexities of the chamber interaction for various rotor profiles including: interlobe and radial sealing line interaction with the blow-hole leakage path; and the degree of cycle offset between various adjacent chambers.

This will be used as the basis for an initial estimate of the actual temperature of the rotor metal in the next chapter, without using FEA. This will allow fast, efficient estimation of thermal distortions during rotor design for a specific operating duty.

Other future work that has been identified is the use of the pressure and temperature results for 3D FEA analyses. Another potential use of this kind of result would be to use the instantaneous, homogeneous fluid properties at a fixed rotor position as the initial boundary conditions for CFD simulation.

Chapter 5
Operational Clearance Distortions

5.1 INTRODUCTION

The boundary conditions calculated in the previous chapter can be used for estimation of the surface temperature distribution on the rotors and casing. It is then possible to estimate thermal displacements of individual components and ultimately how this affects the operational clearances.

A procedure is presented here to estimate local clearance distortions in a twin screw compressor using boundary conditions derived from a chamber model. Time varying boundary conditions from the non-dimensional model are mapped onto rotor and casing surface arrays. The fluid boundary temperatures are time-averaged and then used to estimate the local rotor and casing temperatures. Heat transfer assumptions that represent the extreme case for component temperature distributions are presented. This approach aims to meet the objective to provide a fast, efficient, estimation of thermal distortions for any rotor design or operating duty early in the design process. Estimated rotor and casing temperatures will be used to analyse how thermal distortions will change the compressor clearances, and consequently how this affects the compressor performance and reliability. With this procedure, relative local change in clearances between rotors and casing can be estimated without the need for FEA.

5.2 APPROXIMATING TEMPERATURE DISTRIBUTIONS

5.2.1 CASING TEMPERATURE

In the previous chapter a procedure was described to find the local fluid boundary temperature on the internal surfaces of the casing bores, B1 and B2. The local temperatures T_{B1} and T_{B2} are time averaged values which are unique for every position of the rotor bore surfaces; the position is defined by the parameters β and γ so that the local temperature on the main and gate rotor bores are defined respectively: $T_{B1}(\beta_1,\gamma)$ and $T_{B2}(\beta_2,\gamma)$

In Figure 5-1 the average local temperature has been plotted onto the surfaces B1 and B2 as a colour contour which shows the temperature distribution with respect to the surface parameters β and γ.

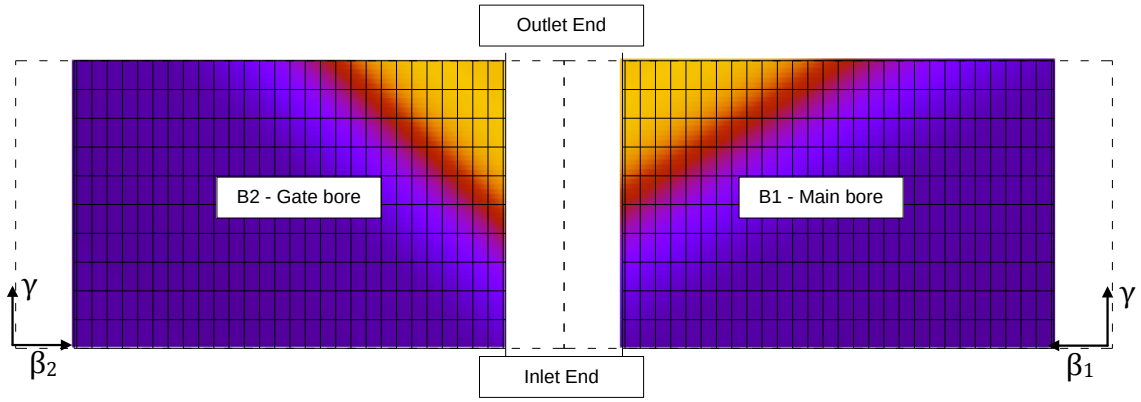

Figure 5-1: Average fluid temperature at casing surfaces

Converting the surface location to be defined on the global co-ordinate system for the compressor, this temperature distribution can be plotted in 3D as shown in Figure 5-2; which shows more intuitively how these temperatures vary around the compressor. This shows the two intersecting cylinders that form the compressor casing bores and is a very limited representation of only the internal casing geometry. Externally, the casing will have some thickness and various other features such as port, ribs, flanges and feet which will all effect the actual temperature distribution in the casing body.

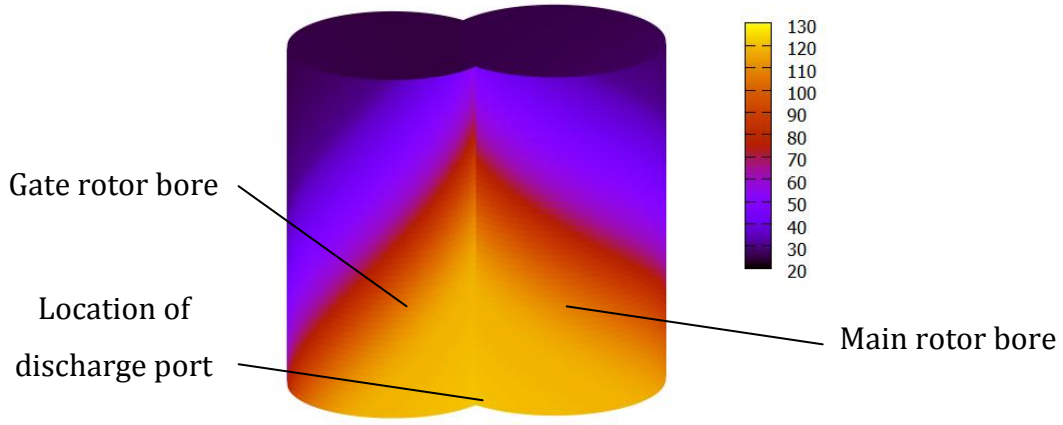

Figure 5-2: Average fluid temperature at casing surfaces in 3D

With such a simplified representation of the actual casing geometry there is limited scope for thermal analysis. By considering a hypothetical scenario; with no conduction across the surface of the casing; and no external heat transfer from the casing, the steady state result is that the casing surface temperature of the metal will be the same as the fluid boundary temperature. This hypothetical case is of interest as it results in the peak local temperatures and temperature gradients that are possible.

As will be discussed later - it is useful to average the temperature over certain regions of the casing – namely, over a transverse cross-section of the casing. For a given transverse plane on the compressor, when the parameter γ, which describes axial position, is fixed, the average temperature over that plane can be found by averaging the temperature around both rotor bores:

$$T_{CP}(\gamma) = \frac{\int_{\varphi_{C1}}^{(360-\varphi_{C1})} T_{B1}(\beta_1,\gamma)\, d\beta_1}{4(180 - \varphi_{C1})} + \frac{\int_{\varphi_{C2}}^{(360-\varphi_{C2})} T_{B2}(\beta_2,\gamma)\, d\beta_2}{4(180 - \varphi_{C2})} \qquad (41)$$

5.2.2 Rotor Temperature

The instantaneous local fluid boundary temperature on the rotor surfaces, R1 and R2 and defined: $T^*_{R1}(\varepsilon_1,\gamma,\theta)$ and $T^*_{R2}(\varepsilon_2,\gamma,\theta)$

The parameters ε and γ describe the location on the surface, while θ describes the cycle angle. An example of the instantaneous boundary temperature distribution is plotted on the surfaces R1 and R2 as shown in Figure 5-3

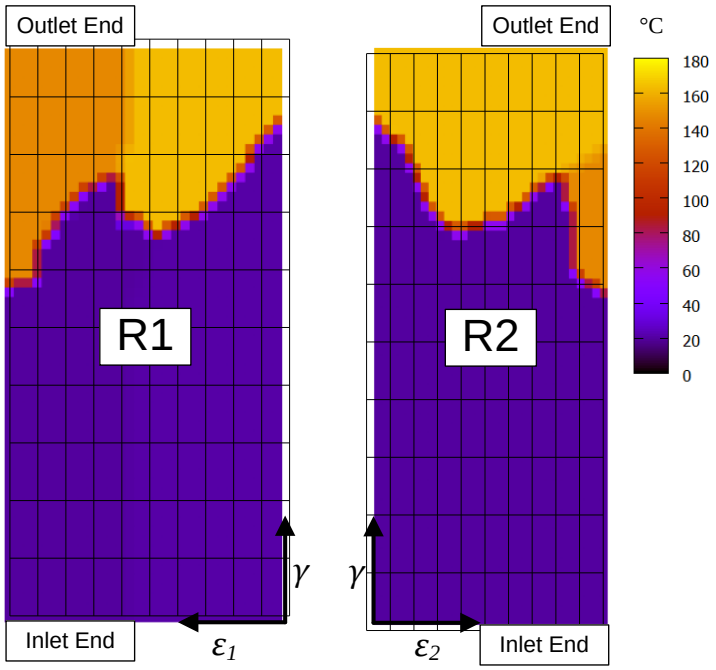

Figure 5-3: Instantaneous boundary temperature at rotor surfaces

Figure 5-3 shows similar chamber boundaries to those that can be observed in the rotor chamber boundary maps of Figure 4-40 and Figure 4-41 in the previous chapter (albeit with different orientation). The subtle difference is that rotor boundary maps were defined using a parameter λ that meant they were independent of the cycle angle. In this case the vertical axis is now represented by the axial parameter γ; as the cycle advances, the chambers appear to translate as shown in Figure 5-4.

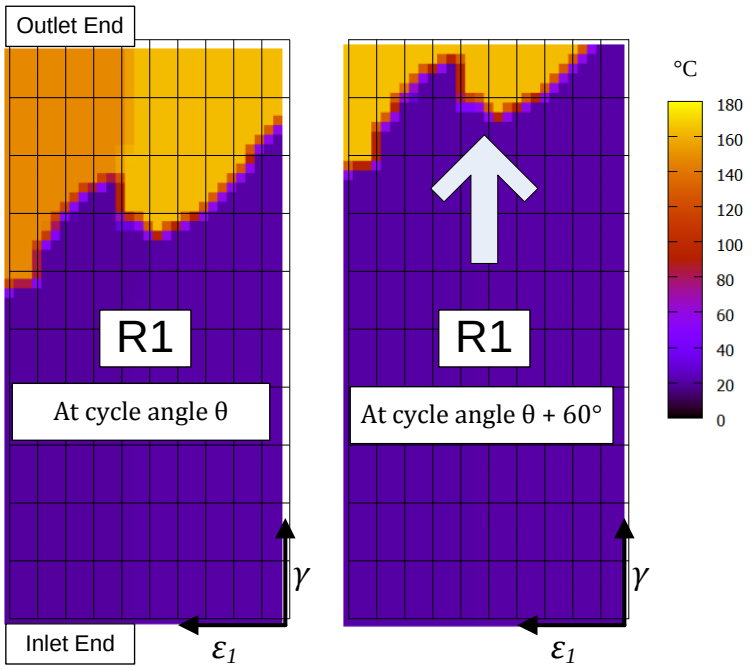

Figure 5-4: Instantaneous temperature at main rotor surface at different cycle angles

The local temperature will cycle every time θ is incremented by 360°. This means that for even a large slow compressor running at 1500rpm, the temperature will cycle every 0.04 seconds. 'Steady state' conditions can be approximated by taking time averaged values that will now only vary as a function of the surface parameters:

$$T_{R1}(\varepsilon_1, \gamma) = \frac{1}{360}\int_0^{360} T^*_{R1}(\varepsilon_1, \gamma, \theta)\, d\theta \tag{42}$$

$$T_{R2}(\varepsilon_2, \gamma) = \frac{1}{360}\int_0^{360} T^*_{R2}(\varepsilon_2, \gamma, \theta)\, d\theta \tag{43}$$

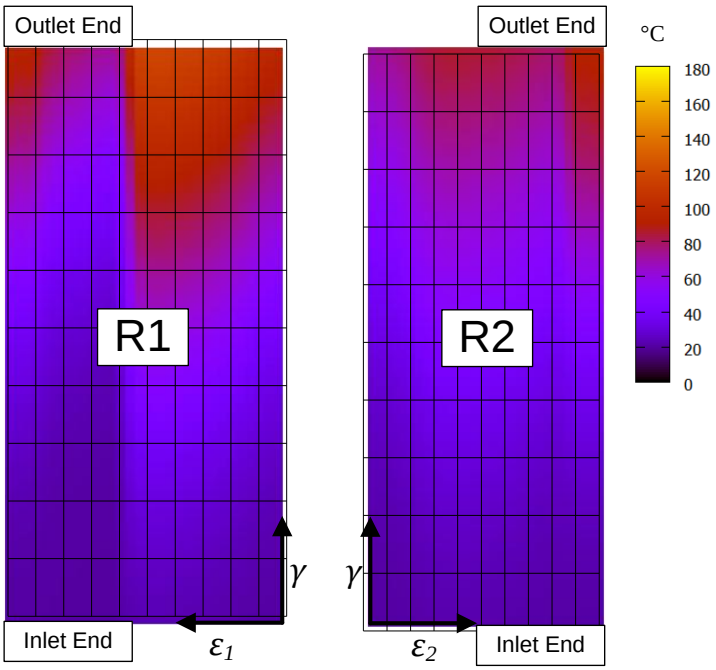

Figure 5-5: Time-averaged boundary temperature at rotor surfaces

Surfaces R1 and R2 have been re-plotted in Figure 5-5 with the colour contour representing the time averaged surface boundary temperature. The colour contours representing temperature have been plotted on the same scale as used in Figure 5-3 which highlights how much lower the peak temperature is after averaging.

In Figure 5-6, the time averaged boundary temperatures have been plotted on the 3D main rotor surface. This is an accurate representation of the main body of the rotor however it is still a simplification of the actual geometry as the details of the rotor shafts that extend from this rotor body are not known. These shafts would of course have an effect of the thermal behaviour of the rotors.

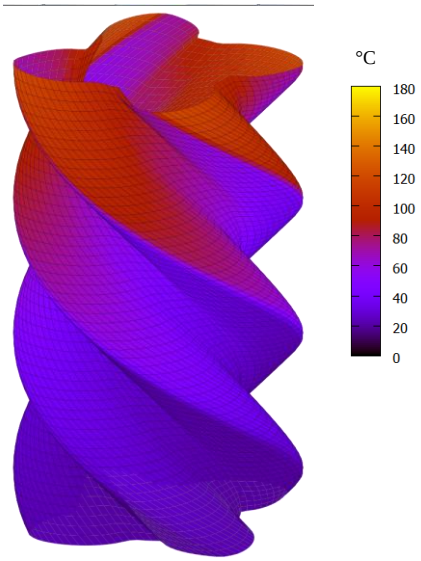

Figure 5-6: Time averaged boundary temperature on main rotor

As was the case for the casing representation, there is a limit to the scope for thermal analysis that can be done without defining the full 3D rotor bodies including all shaft dimensions. To facilitate analysis the following assumption is made: there is no heat conduction in the axial direction along the length of the rotors. This assumes no heat flux from the hot to the cold end of the rotors and no heat flux from the rotor body to the rotor shafts and bearings. Neglecting axial conduction results in the peak transverse temperatures and temperature gradients along the axis of the rotors. This allows the problem to be reduced to a 2D problem for each transverse cross section of the rotors. However, this would still require a numerical solution to determine the 2D temperature distribution due to surface heat transfer and conduction within the rotor.

Averaging the boundary temperature over the transverse cross section of each respective rotor using equations *(44)* and *(45)* yields the rotor 'planar averaged' temperatures; these are plotted in Figure 5-7:

$$T_{RP1}(\gamma) = \int_0^1 T_{R1}(\varepsilon_1, \gamma)\, d\varepsilon \tag{44}$$

$$T_{RP2}(\gamma) = \int_0^1 T_{R2}(\varepsilon_2, \gamma)\, d\varepsilon \tag{45}$$

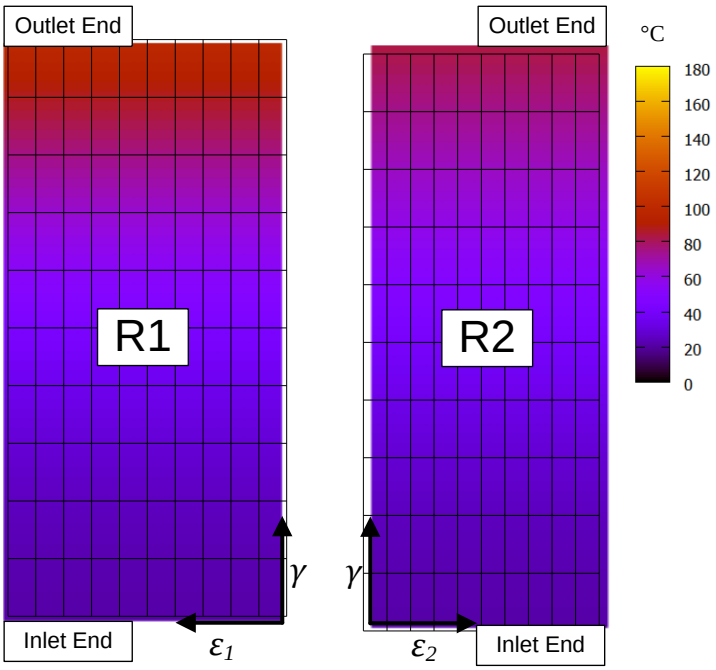

Figure 5-7: Planar averaged boundary temperature on rotor surfaces

As this temperature only varies with axial location the axial temperature distribution for both rotors can be directly compared on a single plot as in Figure 5-8. The reason the discharge end temperature is hotter on the main rotor is because it is exposed to the 4 hottest chambers over a full rotation (since z1 = 4) while the gate rotor is exposed to these same 4 chambers for only 4/6 (z1/z2) of a rotation and the remaining time it is exposed to 2 cooler chambers.

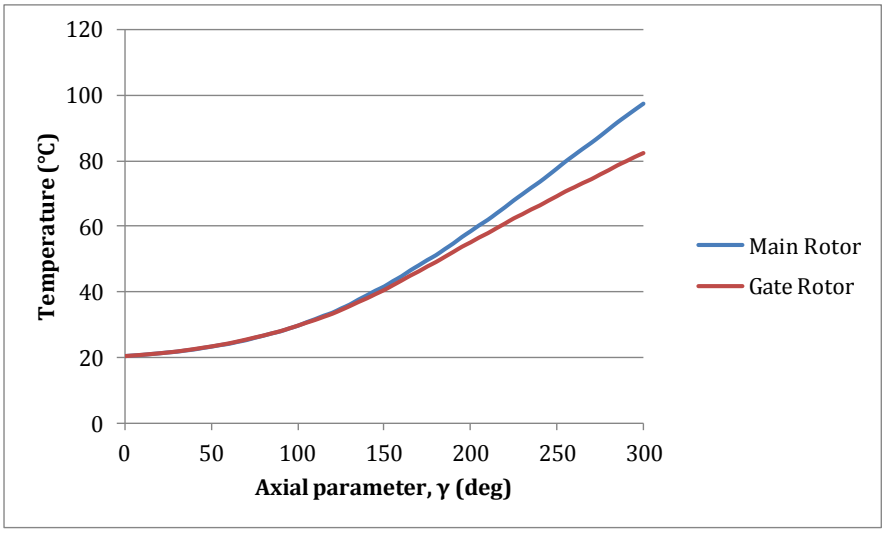

Figure 5-8: Planar averaged temperature distribution on rotors

5.3 THERMAL DISTORTION OF INTERLOBE GAP

5.3.1 INTERLOBE SEALING LINE

The objective here is to approximate the relative change in the local interlobe sealing line gap, ΔG_I, due to thermal distortion of the rotors and casing. This local distortion will be unique for each position along the full length of the sealing line. In addition to this the position of the sealing line changes so that a given point on the sealing line will be formed between rotor surfaces that are exposed to different temperatures resulting in different thermal distortions as the cycle progresses.

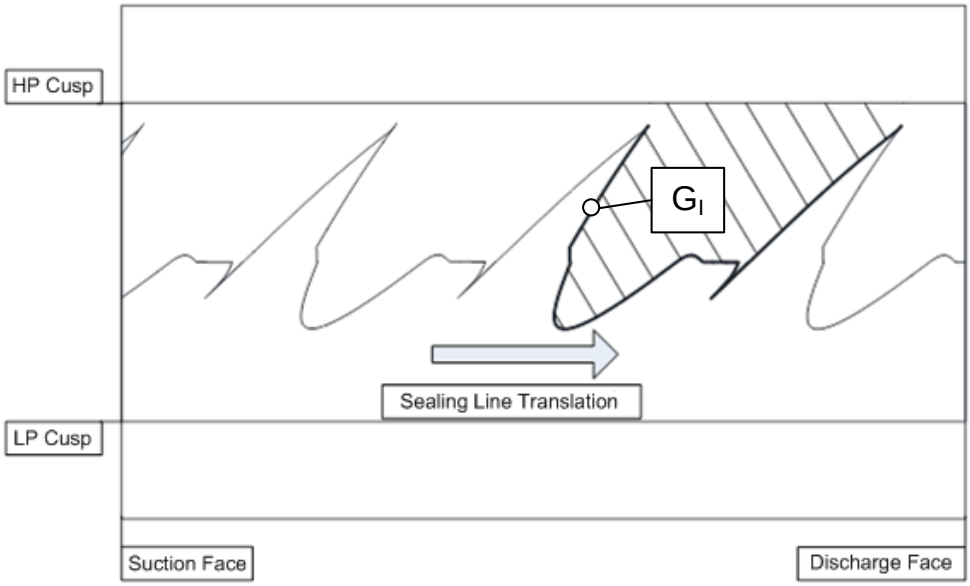

Figure 5-9: Side projection of interlobe sealing line

Figure 5-9 shows the entire length of the interlobe sealing line from a side projection (viewed along the negative X direction of Figure 4-1). The sealing line between the rotors exists between the limits of the low pressure (LP) and high pressure (HP) cusps. As the rotors turn, this sealing line translates from the suction face (LP plane), at the left hand side, to the discharge face (HP plane), at the right hand side.

Over the course of the compression cycle, every location on surfaces R1 and R2 will be in mesh at some point. During steady state operation, the local interlobe

gap, G_I, and, just as importantly, the change in the gap, ΔG_I, will remain constant when defined with respect to a fixed point on each of the rotor surfaces. For this reason it is appropriate to define the local interlobe gap with respect to its corresponding location on the main rotor surface, R_1: $G_I(\varepsilon_1,\gamma)$. Note that this is an equivalent alternative to equation (4) in Chapter 2.4.1, which described the local interlobe gap as a function of the position along the interlobe sealing line and the cycle angle $G_I(l_1,\theta)$.

5.3.2 LOCAL ROTOR DISTORTION

In order to approximate thermal distortion of each rotor a 2D transverse cross section of the rotors was considered. By using the planar averaged temperatures defined previously, a uniform temperature can be assumed across the entire transverse cross section of each rotor. With this assumption uniform thermal expansion occurs without any thermal stresses. This neglects shear stresses between adjacent transverse sections. Taking the axis centre point as a datum, thermal expansion can be calculated for each rotor:

$$\Delta r_1 = r_1 \mu_R (T_{RP1} - T_a) \quad (46)$$

$$\Delta r_2 = r_2 \mu_R (T_{RP2} - T_a) \quad (47)$$

The local radius, r, is known at any location for a given rotor profile and can be identified with respect to the surface parameter, ε: $r_1(\varepsilon_1)$

μ_R, is the coefficient of thermal expansion for the rotor material which is assumed to be common for the main and gate rotors.

The ambient temperature, T_a, is the temperature at which the design clearances are defined. The planar averaged temperature of the rotor varies as a function of the axial surface parameter, γ (see Figure 5-8): $T_{RP1}(\gamma)$

Therefore, for a given rotor pair running at a steady state duty, the local thermal distortion on each rotor can be approximated in such a way that it can be described in terms of its position of the rotor surface: $\Delta r_1(\varepsilon_1,\gamma)$; $\Delta r_2(\varepsilon_2,\gamma)$.

5.3.3 Local Casing Distortion

The bearings that locate the rotors are situated in the casing so the interlobe gap can also be affected by casing thermal distortions. In reality the bearings will be located on the rotor shafts some distance from the meshing region of the rotor bodies. Even if the actual geometry were defined it is not a trivial matter to approximate the casing temperature remote from the compression process. This would require detailed analysis of a specific case which is not the aim of this exercise. For this more general investigation of thermal behaviour, two transverse planes were defined as shown in Figure 5-10, one at the suction end and the other at the discharge end.

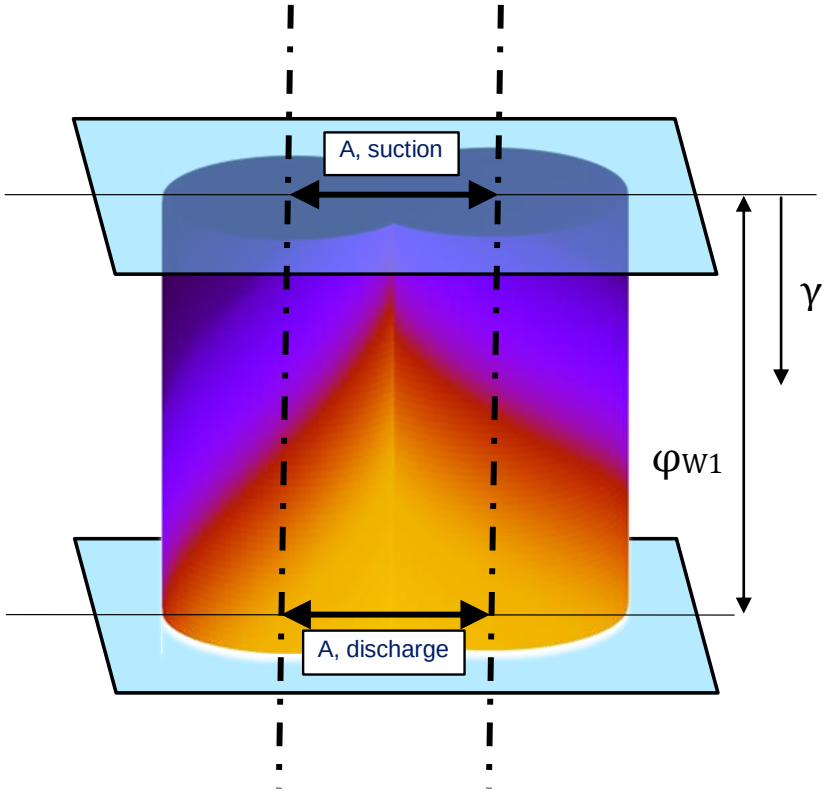

Figure 5-10: Transverse planes at suction and discharge of casing

Where the centre line of each rotor bore intersects with one of these planes the distance, A, has been identified. The averaged temperature on each respective plane will be used to estimate ΔA at each end, resulting in non-parallel axes. The 2D thermal analysis is similar to what was done for the rotors. A uniform casing temperature is estimated on each plane using the casing planar averaged

temperature equation defined previously *(41)*; where these temperatures are defined as follows:

Suction plane temperature: $T_{CP1} = T_{CP}(\gamma = 0)$

Discharge plane temperature: $T_{CP2} = T_{CP}(\gamma = \varphi_{w1})$

Assuming that each rotor axis intersects with the appropriate casing bore axis at these planes; and that rotor deflection due to rotor bending is negligible; the rotor centre distance can be defined at any axial position, γ, by interpolating between the end planes:

$$\Delta A(\gamma) = A\mu_C \left(\left(\frac{\varphi_{w1} - \gamma}{\varphi_{w1}} \right) (T_{CP1} - T_a) + \left(\frac{\gamma}{\varphi_{w1}} \right) (T_{CP2} - T_a) \right) \qquad (48)$$

5.3.4 Relative Gap Distortion

Procedures have now been detailed to find the local distortions: Δr_1, Δr_2 and ΔA for a given cross section of the rotors. This section details how these component distortions are used to calculate the resulting relative distortion at the interlobe gap. The first step of this analysis will be to determine the transverse component of the interlobe gap, G_{IT}.

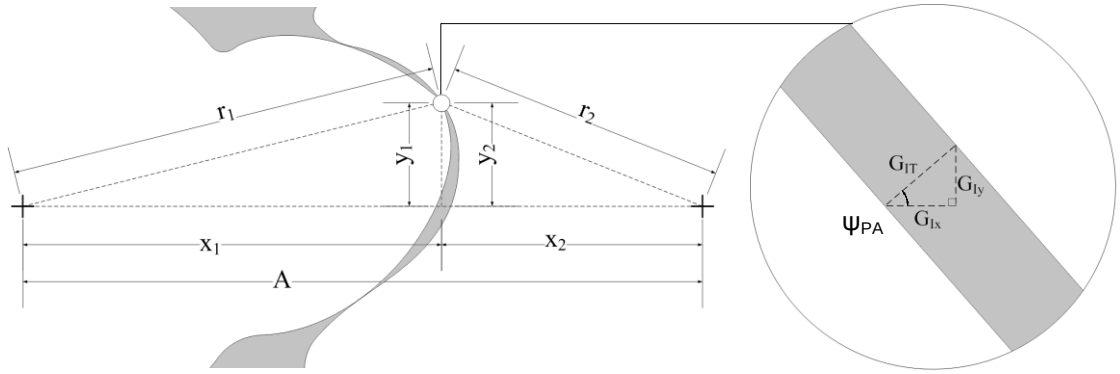

Figure 5-11: Transverse analysis of interlobe gap

The dimensions r_1, r_2, and A have been plotted on Figure 5-11. In order to relate these dimensions to the transverse interlobe gap, G_{IT}, the horizontal and vertical components have been defined. The relationship between the horizontal components is:

$$G_{Ix} = A - x_1 - x_2 \tag{49}$$

Similarly:

$$\Delta G_{Ix} = \Delta A - \Delta x_1 - \Delta x_2 \tag{50}$$

For the interlobe gap highlighted in Figure 5-11 the relationship between the vertical components is:

$$G_{Iy} = y_2 - y_1 \tag{51}$$

However, the above is only true when $|y_2| > |y_1|$ AND when y_1 and y_2 are positive. In the magnified gap in Figure 5-11, the body of the gate rotor is 'above' the body of the main rotor; this is related to the surface normal. For conjugate rotors, the line of the surface normal at any location, currently in mesh, must intersect with the rotor pitch point. This behaviour can be used to set out general rules as illustrated in Figure 5-12. An axial projection of an arbitrary sealing line is shown in red; this is representative of the sealing line path for any profile with an addendum and dedendum. The line of the surface normal will always radiate from the pitch point as shown. Where this line intersects the meshing point between rotors, the rotor closer to the pitch point will be 'smaller' in the y direction. This behaviour was used to construct equation (52) and (53).

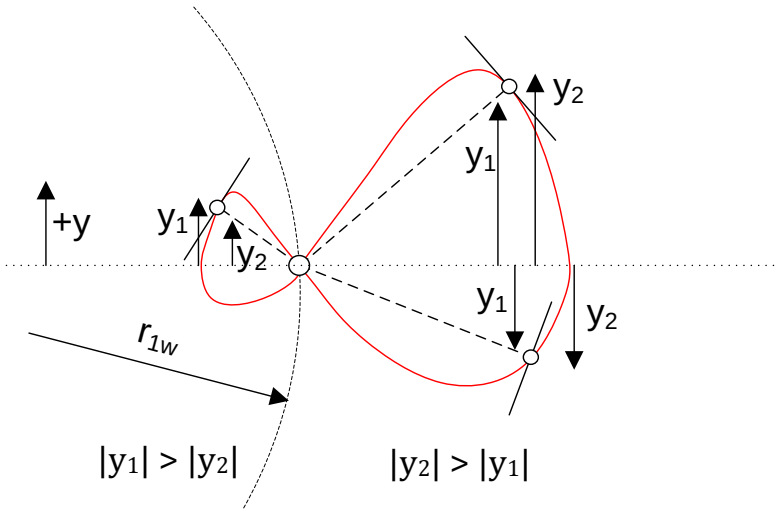

Figure 5-12: Pressure angle intersecting with pitch point

$$G_{Iy} = \frac{(x_1 - r_{w1})}{|(x_1 - r_{w1})|}(|y_2| - |y_1|) \quad (52)$$

$$\Delta G_{Iy} = \frac{(x_1 - r_{w1})}{|(x_1 - r_{w1})|}(|\Delta y_2| - |\Delta y_1|) \quad (53)$$

The change in the transverse interlobe gap can now be calculated as:

$$\Delta G_{IT} = \Delta G_{Ix} sin\,(\psi_{PA}) + \Delta G_{Iy} cos\,(\psi_{PA}) \quad (54)$$

The pressure angle, ψ_{PA}, is defined in Figure 5-13 and is the angle between the x axis and the surface normal line at a meshing point. This angle is measured on the global compressor co-ordinate system and is common for both rotors.

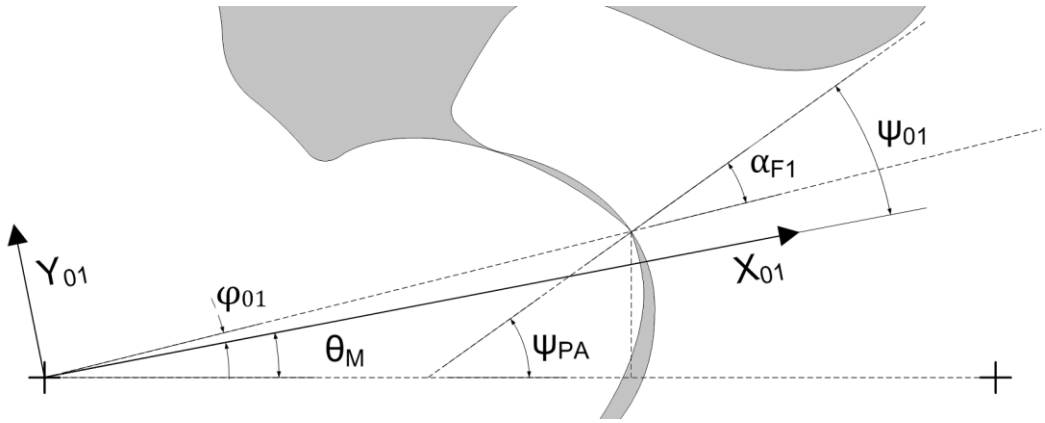

Figure 5-13: Angles on transverse section

$$\psi_{PA} = \theta_M + \psi_{01} \quad (55)$$

θ_M is the meshing angle that describes the rotation of the main rotor. ψ_{01} can be described as the 'home pressure angle' (Holmes 1990); this is the normal to the profile curve measured relative to the profile co-ordinate system S_{01}. Details for calculation of θ_M and ψ_{01} and provided in appendix 'A.2 Meshing Conditions for Conjugate Profile'.

The minimum gap between the surfaces of the main and gate rotors is the distance along a line normal to the rotor surfaces – the *normal* gap. In the case of rotors with no helix angle this gap would be the same as the *transverse* gap, G_{IT}. When a helix angle is introduced the normal gap will be smaller than the transverse gap. The degree to which the normal gap is reduced due to the local

rotor helix also depends on the local steepness of the rotor flank. Holmes (Holmes 1990) provides a derivation of the following equation used to convert from a transverse to a normal gap:

$$G_I = G_{IT} \frac{1}{\sqrt{(1 + tan^2(\psi_{H1}) cos^2(\alpha_{F1}))}} \quad (56)$$

ψ_{H1} is the local helix angle on the main rotor, this increases with an increase in the local radius according to the equation below, where h_1 is the lead length that describes the main rotor helix:

$$\psi_{H1} = tan^{-1}\left(\frac{2\pi r_1}{h_1}\right) \quad (57)$$

α_{F1} is described by Holmes as the polar flank angle, which is measured from a radial line that intersects the meshing point, to the line of pressure. This is included in Figure 5-13 and can be defined as below; where φ_{01} is the local profile angle measured from the profile co-ordinate system:

$$\alpha_{F1} = \psi_{01} - \varphi_{01} \quad (58)$$

Since G_I will typically be many orders of magnitude smaller than the profile dimensions, the following approximations would result in negligible errors. In practical terms this allows the calculations to be performed using only the main rotor profile co-ordinates.

$$x_2 \sim (A + x_1); \quad y_2 \sim y_1 \quad (59)$$

5.4 Thermal Distortion of Radial Gap

5.4.1 Radial Sealing Lines

The radial sealing points between the rotor and casing have been highlighted for the main and gate rotors in Figure 5-14. These occur at the maximum rotor radii, r_{o1} and r_{o2}. In the event that the gate rotor features a region where the OD has the same max value, the radial sealing point has been set to be on the trailing side on the rotor lobe such that this point defines the port opening, when timing is most critical. This is as opposed to choosing a point on the leading side of the lobe that would control the port closing.

Figure 5-14: Radial sealing points on main and gate rotors

A single compression chamber will be enclosed by one radial sealing line on the leading tip of each rotor and one on the trailing tip of each rotor. For the purposes of thermal analysis of the radial gap only one of these sealing lines needs to be considered since one is just an offset of the other. Each of these sealing lines is made up of one helical curve on the main rotor and another on the gate rotor. These sealing lines have been projected onto the casing bore surfaces in Figure 5-15.

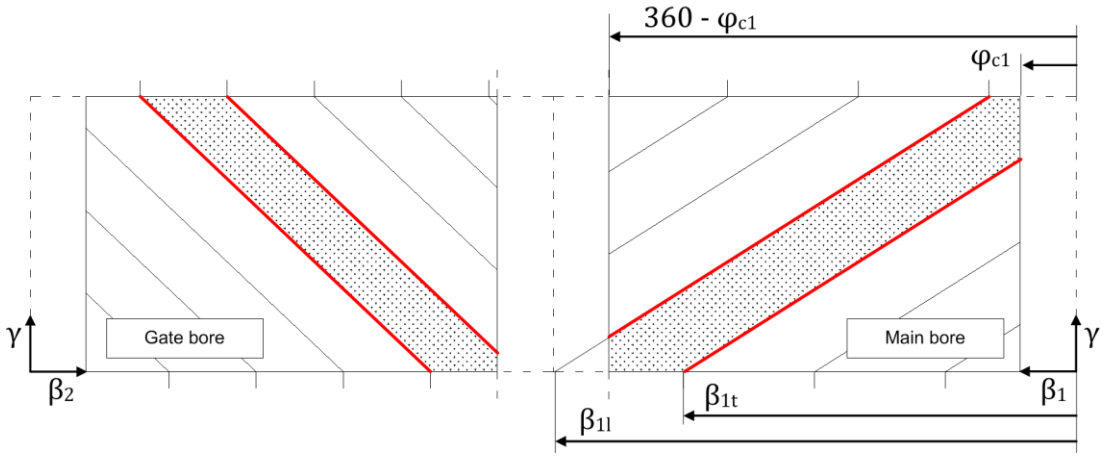

Figure 5-15: Radial sealing lines

On the main rotor on the right hand side of Figure 5-15, the angular position of the radial sealing lines have been identified with β_{1l} and β_{1t} for the leading and trailing tip respectively. These angles have been measured at $\gamma = 0$, on the inlet (LP) plane. Due to the overlap of the rotor bores the surfaces B1 and B2 only extend from one cusp to the other therefore the radial sealing line can only exist in this region where: $\varphi_{c1} < \beta_1 < (360 - \varphi_{c1})$

During steady state operation, the local radial gap, G_R, and the change in the gap, ΔG_R, will remain constant when defined with respect to a fixed point on the casing surface. For this reason it is appropriate to identify the local radial gap with respect to its corresponding location on the casing surfaces surface, B1 or B2 respectively: $G_{R1}(\beta_1,\gamma)$ and $G_{R2}(\beta_2,\gamma)$

5.4.2 Local Distortions

The local rotor distortions calculated previously in equations (46) and (47) are used to calculate the thermal distortion at the tip of the main and gate rotors using the outer radii r_{o1} and r_{o2} respectively:

$$\Delta r_{o1} = r_{o1}\mu_R(T_{RP1} - T_a) \tag{60}$$

$$\Delta r_{o1} = r_{o1}\mu_R(T_{RP2} - T_a) \tag{61}$$

The outer radius is a constant along the full length of the radial sealing line for each rotor. The planar averaged temperature, T_{RP}, will vary with respect to the

axial parameter, γ. As previously stated, these equations assume a datum along the axis of the rotors for the rotor thermal expansion.

The intuitive datum for analysing displacements in the *full* casing due to thermal distortion would generally be where the casing is secured to its base. In this instance the only distortion of interest is along the lines that radiate from the common axis of the rotor and casing bore. For this reason, two datum locations have been defined on the casing - one on the main rotor axis and one on the gate rotor axis; this assumption is discussed in more detail in 'Appendix B.2.2 Datum for Relative Clearance Distortion'. Axial distortions will have a negligible effect on the radial gap therefore these will be neglected. This essentially allows the analysis of the radial gap to be treated as a 1D problem. The rotor distortion has already been discussed so the remaining unknown is the radial distortion on the casing bore, relative to the centre axis of that bore: $\Delta r_{c1}(\beta_1,\gamma)$ and $\Delta r_{c2}(\beta_1,\gamma)$

As for the rotors, the realistic thermal distortion of the casing simply cannot be calculated without taking into account geometrical features and how these interact with temperature gradients to cause thermal stresses. If the casing temperature was approximately uniform over a transverse cross section of the rotors it would be possible to perform a similar analysis as for the rotors since there are zero thermal stresses over a section with uniform temperature (neglecting stresses transferred from adjacent planar cross sections).

Unfortunately, referring back to Figure 5-1, it is clear that the high temperatures on the casing are highly localised to the region of the discharge port. While using a planar average temperature is reasonable for distortions in centre distance, A, this kind of averaging is not appropriate for analysis of the radial gap. The only option, short of creating a finite element model, is to treat each point on the casing in isolation, and deem the rest of the casing to be at the same temperature, circumventing the issue of thermal stresses, for the purpose of estimating the local distortion at that point.

$$\Delta r_{c1} = r_{c1}\mu_C(T_{B1} - T_a) \qquad (62)$$

$$\Delta r_{c2} = r_{c2}\mu_C(T_{B1} - T_a) \quad (63)$$

Providing casing thermal gradients are not very severe; and that the compressor casing has been sensibly designed in such a way that the thermal expansion of the bore will not be restricted; the expectation is that an overall approximation of casing thermal distortion can be achieved; this will be an improvement over completely neglecting casing thermal expansion and in no way attempts to provide a fully realistic thermal analysis of the casing.

The analysis of the local radial gap, normal to the surface of the casing bore, is considerably easier to calculate than for the interlobe gap:

$$G_R = r_{c1} - r_{o1} \quad (64)$$

$$\Delta G_R = \Delta r_{c1} - \Delta r_{o1} \quad (65)$$

5.5 Modelling with Operational Clearance Corrections

5.5.1 Integration with Geometry Calculation Program

The described calculations were implemented in the program GEOM used for the calculation of all geometric parameters. This program outputs only the main geometric characteristics required; namely, the chamber volume and all flow areas through the ports and leakage paths, and how these vary throughout the compression cycle.

The minimum requirement for calculation of the leakage area through a sealing line gap is the instantaneous length of that sealing line and the average gap through the sealing line. With non-uniform clearance distributions around the surface of the rotor profile it is necessary to integrate the local gap along the path of the sealing line:

$$A_I = \int_{s_1}^{s_2} G_I \, ds \qquad (66)$$

For a designed clearance distribution the local gap, G_I, varies along the length of the sealing line. Assuming there is no rotor taper or axis offset towards one end of the rotors, a point fixed on this sealing line, as shown previously in Figure 5-9, would have a constant local gap by design such that the gap could be described as a function of the position on the rotor surface: $G_I(\varepsilon_1)$. In this situation only the limits of integration for the active sealing line are required.

When considering distortions due to local rotor and casing temperature, the position of the sealing line within the compressor must also be calculated since the local distortion depends on the surface location: $\Delta G_I(\varepsilon_1,\gamma)$. The local gap corrected for operational distortions is therefore a function that varies with respect to: $G_I^*(\varepsilon_1,\gamma)$.

In practise, equation (66) is solved numerically by calculating G_I^* at discrete points along the sealing line. For a given point in the cycle, θ, running at a steady state operating condition, the corrected leakage area through the interlobe gap, A_I^*, has a constant value. This calculation is repeated over a finite number of steps during the compression cycle in order to describe the leakage area curve, $A_I^*(\theta)$.

The procedure is similar when calculating the corrected radial gap so that: $G_{R1}^*(\beta_1,\gamma)$ and $G_{R2}^*(\beta_2,\gamma)$.

The leakage area for the radial gap is the sum of the area on the main and gate rotors; where 's' is the length along the relevant curve:

$$A_R^* = \int_{s_1}^{s_2} G_{R1}^* \, ds + \int_{s_1}^{s_2} G_{R2}^* \, ds \qquad (67)$$

Examples of operational clearance distortions and the resulting impact of clearance distributions and area curves will be provided for the case studies in Chapter 6.

5.5.2 Integration with Chamber Model

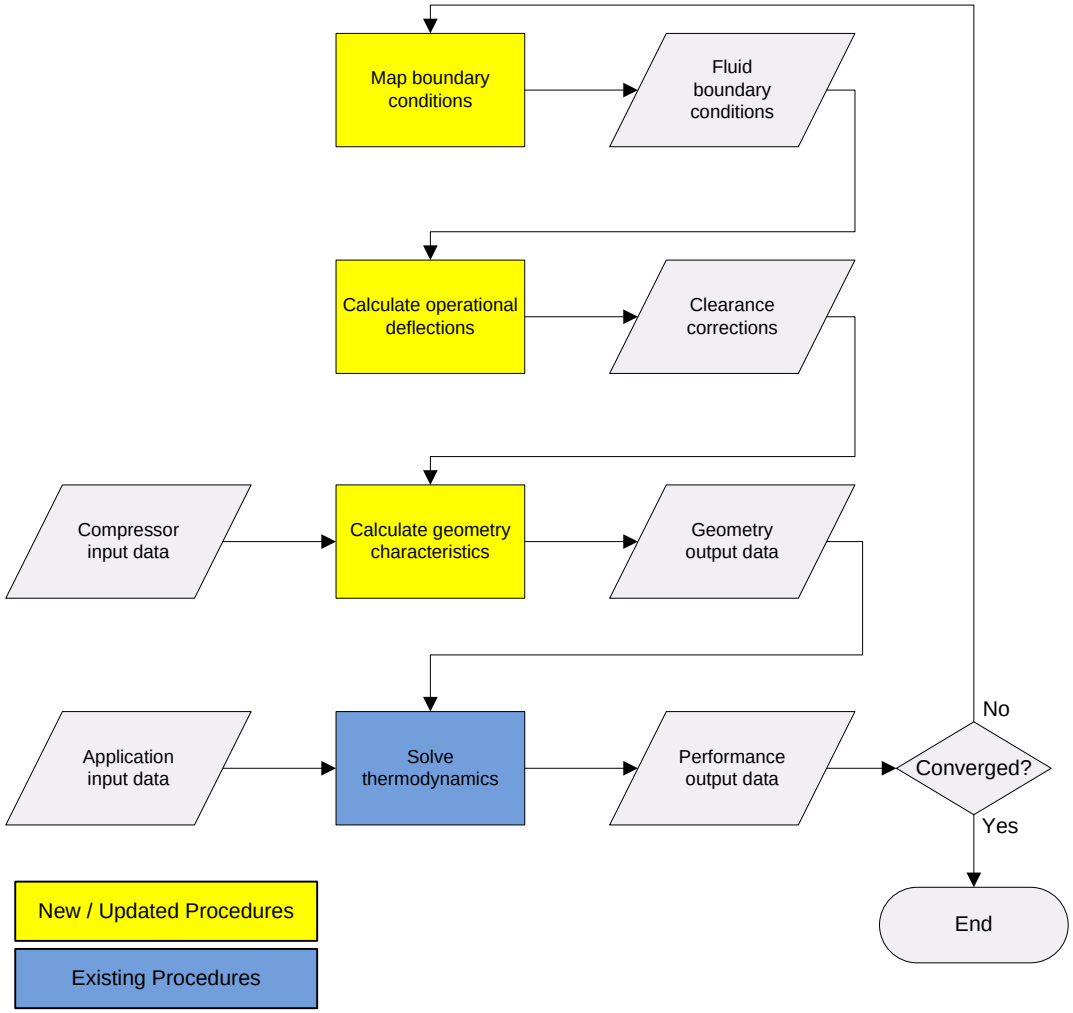

Figure 5-16: Flow chart for performance calculation with operational clearances

The boxes in Figure 5-16 represent the operations that are performed while the parallelograms represent the data that is input and output from each program. More specifically, this data includes:

Fluid boundary conditions:

- Main rotor temperature distribution, $T_{R1}(\varepsilon_1,\gamma)$
- Gate rotor temperature distribution, $T_{R2}(\varepsilon_2,\gamma)$
- Casing surfaces temperature distribution, $T_{B1}(\beta_1,\gamma)$ and $T_{B1}(\beta_1,\gamma)$

Clearance corrections:

- Local change in interlobe gap, $\Delta G_I(\varepsilon_1,\gamma)$

- Local change in radial gap, $\Delta G_{R1}(\beta_1,\gamma)$ and $\Delta G_{R2}(\beta_2,\gamma)$

Compressor input data:

- Rotor profile co-ordinates
- Rotor parameters (such as wrap angle and Vi)
- Clearance parameters including designed clearance distribution

Geometry output data:

- Chamber volume curve, $V(\theta)$
- Flow area curves, $A_1(\theta)$, $A_2(\theta)$…

Application input data:

- Fluid properties (ideal gas properties were used)
- Compression duty, p_1, T_1, pressure ratio
- Compressor parameters (such as bearing type / oil injection)

Performance output data:

- Fluid properties during compression cycle, $p(\theta)$, $T(\theta)$…
- Net flow / volumetric efficiency
- Net power / adiabatic efficiency

The procedures: 'Calculate geometry characteristics' and 'Solve thermodynamics' were introduced in Chapter 2. The procedure to 'Map boundary conditions' was described in the Chapter 4. The procedure to 'Calculate operational deflections' is as detailed in this chapter. All procedures were programmed using FORTRAN. The program to 'Calculate geometry characteristics' was based on existing routines in a program GEOM developed at City University which were modified to support the more complex clearance distributions during calculation of the leakage areas.

'Geometry characteristics' are calculated using the appropriate 'Compressor input data' and 'Clearance corrections' (initially set to zero). These geometry characteristics are used along with the 'Application input data' to solve the thermodynamics, giving the 'Performance output data'. The performance output

data includes the fluid temperature as it varies throughout the compression process, $T(\theta)$. Once available, the temperature curve is used to estimate 'Fluid boundary conditions' and 'Clearance corrections'. If clearance distortions are significant these will alter the flow area through the leakage paths within the compressor therefore the geometry characteristics and thermodynamics should be re-calculated. If the results are significantly different compared to the previous solution, then the process should be iterated until the solution converges.

5.6 CONCLUDING REMARKS

For the purposes of assessing how thermal distortions affect local clearances and performance at a conceptual design stage, significant simplifying assumptions must be made. This approach does not attempt to provide maximum realism for a particular case but rather provides a general approximation of rotor thermal behaviour. An objective in this work to quantify local clearance variations is to assess reliability therefore the assumptions that have been made aim to represent extreme cases for thermal distortions.

Ultimately, temperature distribution and thermal distortion need to be validated as far as possible which will be the subject of the Chapter 6. The effect of the revised clearances on the performance will be quantified and compared with experimental results.

Chapter 6
Case Studies

6.1 INTRODUCTION

Procedures for the analysis of the thermal deformation of clearances have been described in the Chapters 4 and 5. These have been integrated with a well established twin screw compressor modelling procedure, detailed in Chapter 2. The resulting model enables investigation of localised clearance distortions and quantification of how these changes affect the compressor performance. In this chapter, case studies are presented in order to show the capabilities of this model and to assess how accurate and applicable the model is when used in the practical context of designing screw compressors for industrial applications.

This research was performed in a commercial engineering environment. This means that there was a good resource of test data available. However the downside is that there is less flexibility in modifying designs, measuring specific parameters or in running at extended operating duties. The solution to this issue was to utilise test data from various different test cases which each allowed a specific detail or application of the model to be assessed.

The first case covers *Model Sensitivity to Rotor Parameters*. The objectives of this case study were to validate that surface boundary conditions were produced as expected, with sensibly bounded chambers that are consistent with known compressor behaviour. The results were used to assess how these boundary conditions are affected by changes to the rotor geometry to ensure the calculation procedures are robust. This initial validation was only concerned with the distribution of temperature.

In section *'6.3 Model Sensitivity to Clearance Modifications',* the procedures detailed in Chapter 5 to predict clearance distortions were employed. The effect of modified operational clearances on the simulated thermodynamic

performance is presented and compared against available performance tests to give a general assessment of the model behaviour and sensitivity.

Section '*6.4 Investigating Interlobe Clearance Distortion'* particularly focuses on the impact of thermal distortions on the interlobe clearance distribution for an oil injected machine with direct rotor to rotor drive.

'*6.5 Investigating Radial Clearance*' draws on extensive test results obtained from an oil free HS204 compressor, over a wide range of temperatures and speeds. This case study features the added complexity of the compressor casing having a cooling jacket. The results obtained with the HS204 compressor include measurement of the radial clearance gap which was used to provide some verification of the predicted radial clearance deformation.

Table 6-1: Air ideal gas properties

Specific heat ratio, C_P/C_V	1.4
Gas Constant, R_G ($Jkg^{-1}K$)	287
Compressibility factor, Z	1

All tests were performed with atmospheric air. This fluid has been represented in all models as an ideal gas with the properties provided in Table 6-1. All test results presented in this chapter have flows calculated in accordance with the standard ISO 5167-2:2003 (International Organization for Standardization b) and have been corrected to a standard suction pressure of 1 Bar absolute using the corrections described in ISO 1217:2009 (International Organization for Standardization a). The measured flow was also corrected to account for deviations in the actual speed achieved on test; within the acceptable deviations set out in this standard.

6.2 Model Sensitivity to Rotor Parameters

6.2.1 Overview

Assessment of the model sensitivity to rotor parameters was based on an oil free machine compressing air. The modelled temperature throughout the compression process was mapped onto the rotor and casing surfaces. The resulting instantaneous and averaged surface temperature distributions are presented. These are compared with the temperature of the compression fluid at various locations within the compressor. The compressor model was based on the '*DRUM127*' test compressor but different rotor geometry was generated and modelled to evaluate how this changed the temperature distribution when running at a similar duty.

6.2.2 DRUM127 Compressor

Figure 6-1: DRUM127 air compressor

Table 6-2: Basic compressor details

Main rotor diameter, D (mm)	127
Length over diameter ratio, L/D	1.6
Main rotor wrap angle, φ_{w1} (deg)	285°
Lobe combination, z1/z2	3/5
Profile type	N
Volume index, Vi	1.5
Oil injection	No

The DRUM127, shown in Figure 6-1, is a twin screw compressor which features timing gears but has no oil or water cooling within the chamber. The analysis was based on the following operating conditions and assumed machine parameters.

Table 6-3: Air duty

Inlet pressure, p1 (Bara)	1
Outlet pressure, p2 (Bara)	2 - 2.5
Inlet temperature, T1 (°C)	25
Speed, N (rpm)	7000

Table 6-4: Model parameters for thermal analysis

Ambient temperature, T_a (°C)	20
Rotor thermal expansion coef., μ_r ($°C^{-1}$)	$1e^{-5}$
Casing thermal expansion coef., μ_r ($°C^{-1}$)	$1e^{-5}$
Nominal interlobe gap, G_I, (μm)	100
Nominal radial gap, G_R, (μm)	100
Nominal axial gap, G_A, (μm)	100

The model was set up with a uniform interlobe clearance distribution – this is a reasonable assumption for this kind of oil free, N-profile rotor, which mainly features a uniform clearance distribution that only reduces slightly in the pitch areas. Thermal expansion coefficients aren't used at this stage but have been included here as this DRUM127 test case is used later to investigate thermal distortions.

6.2.3 Mapped Boundary Conditions

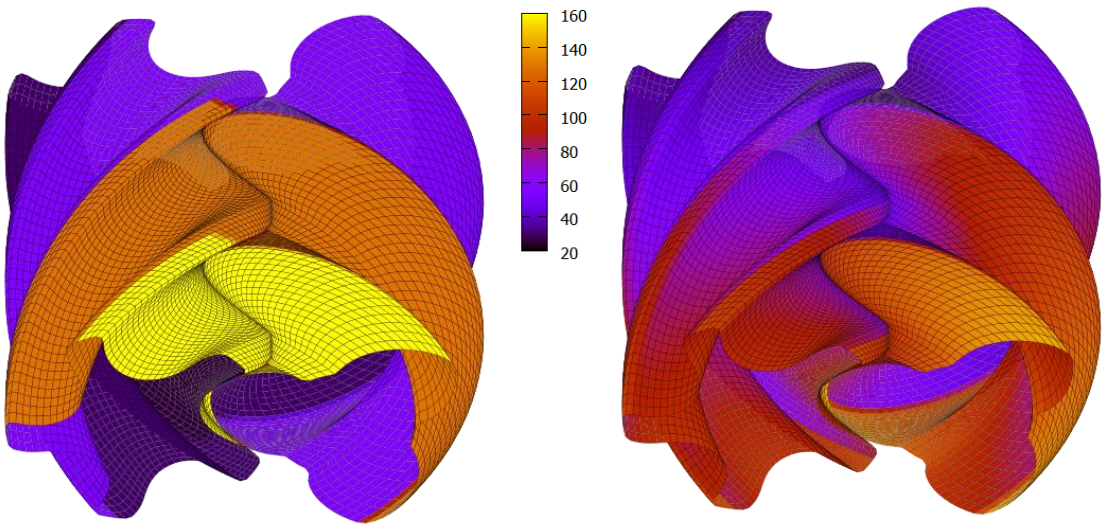

a) instantaneous temperature b) time averaged temperature

Figure 6-2: Rotor boundary temperatures

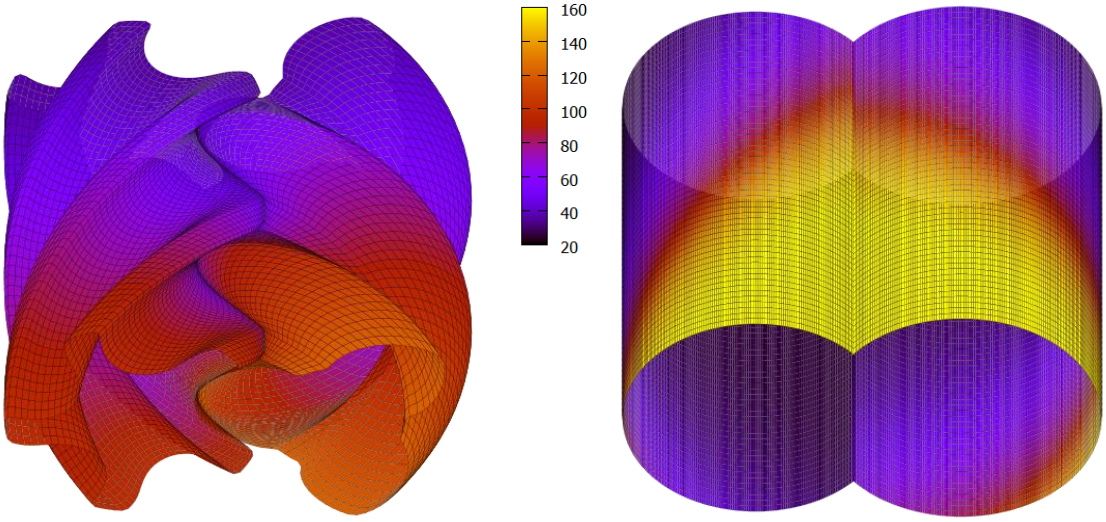

a) planar averaged temperature b) time averaged temperature

Figure 6-3: Averaged boundary temperatures used for thermal analysis

Figure 6-2 and Figure 6-3 show various fluid temperature distributions over the rotor and casing surfaces. The planar averaged temperature on the rotors from Figure 6-3 a) is used to generate a 2D plot in Figure 6-4, which shows how the main rotor is exposed to a higher average temperature than the gate rotor towards the outlet end of the rotors. These rotor results are also tabulated in

Table 6-5. The averaged rotor temperature exposure is not as extreme as the minimum and maximum fluid temperatures. However, on the static casing, the time averaged temperature exposure limits are very similar to the minimum and maximum fluid temperatures.

Table 6-5: Temperatures at specific locations

Temperature (°C)							
Fluid		Main Rotor		Gate Rotor		Casing	
Inlet	Outlet	Inlet	Outlet	Inlet	Outlet	Min	Max
25	161	37	122	35	98	24	160

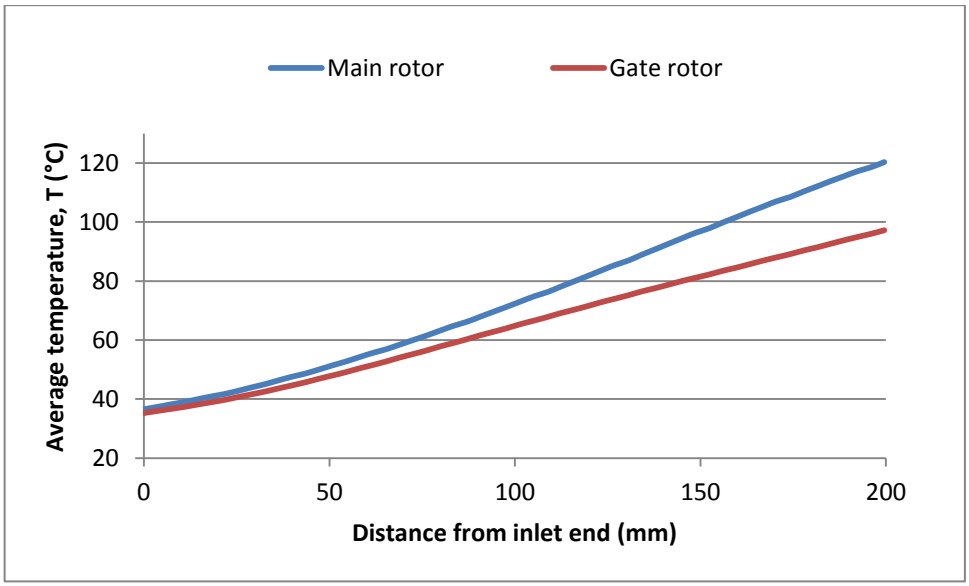

Figure 6-4: Rotor temperature distribution

6.2.4 Sensitivity to Lobe Combination

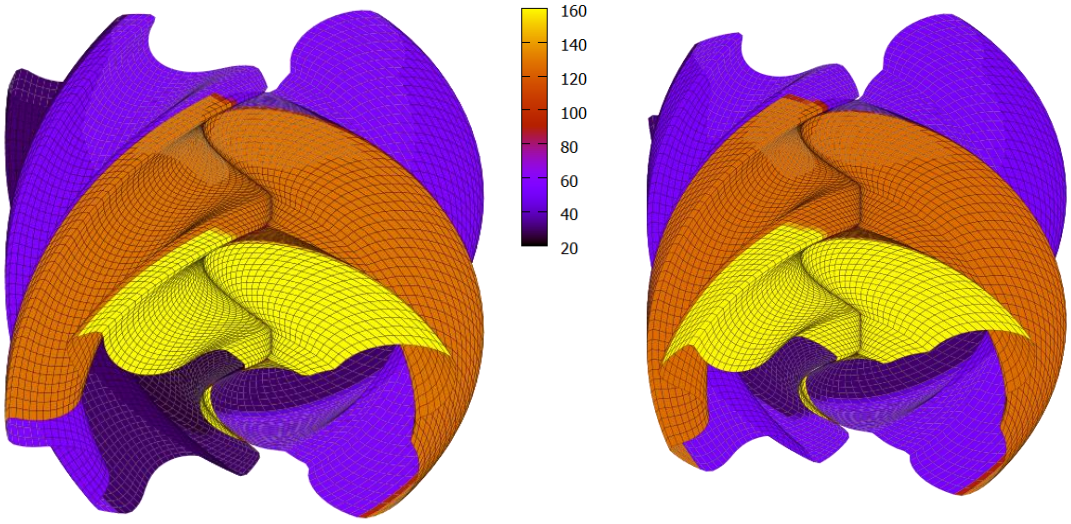

a) tested 3/5 lobe rotors b) 3/4 lobe model comparison

Figure 6-5: Comparison of rotor models with different lobe combinations

New rotors were generated with a 3/4 lobe combination. The new rotors are shown next to the original 3/5 rotor geometry in Figure 6-5. The length to diameter ratio and wrap angle on the main rotor is the same for each rotor pair.

The results, given in Table 6-6 and Figure 6-6 show that reducing the number of lobes on the gate rotor from 5 to 4 has increased the average temperature at the outlet so that the main and gate rotor outlet temperatures are similar. An additional case with 4/5 rotor geometry was run and added to Table 6-6; this supports the theory that the larger lobe difference between the 3/5 rotors is what causes the temperature difference.

Table 6-6: Temperatures with different lobe combinations

	Temperature (°C)					
	Fluid		Main Rotor		Gate Rotor	
Lobe Comb.	Inlet	Outlet	Inlet	Outlet	Inlet	Outlet
3/5	25	161	37	122	35	98
3/4	25	156	35	118	36	114
4/5	25	172	37	130	38	124

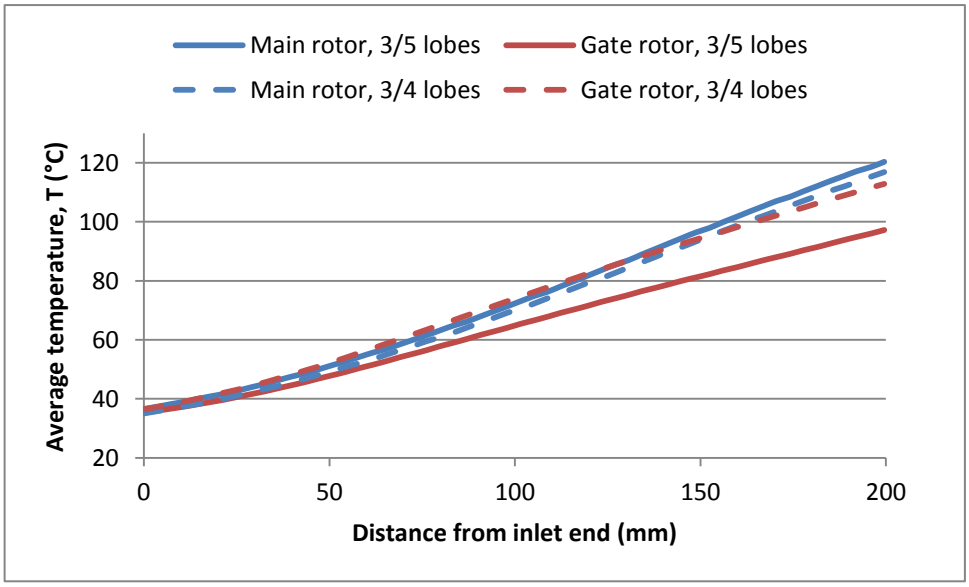

Figure 6-6: Rotor temperature distributions with different lobe combinations

6.2.5 Sensitivity to Wrap Angle

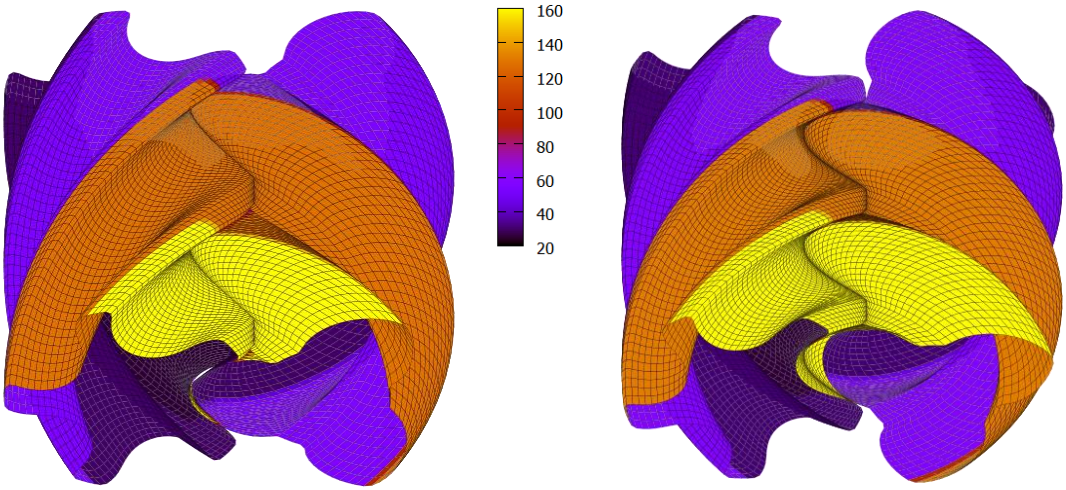

a) model with 255° wrap angle b) model with 315° wrap angle

Figure 6-7: Comparison of rotor models with different wrap angles

Figure 6-7 shows an example of rotors with different wrap angles. In this case the length to diameter ratio and lobe combinations are preserved. It is shown in Figure 6-8 and Table 6-7 that, with increased wrap angle, there is a modest decrease in the rotor temperature at the inlet and an increase in the rotor temperature at the outlet. This is as expected, since if the rotors had a wrap angle of zero, as is the case for roots blowers, then the temperature exposure would be the same along the full length of the rotors.

Table 6-7: Temperatures with different wrap angles

	Temperature (°C)					
	Fluid		Main Rotor		Gate Rotor	
Wrap Angle	Inlet	Outlet	Inlet	Outlet	Inlet	Outlet
255	25	159	38	117	37	94
285	25	161	37	122	35	98
315	25	163	35	129	34	104

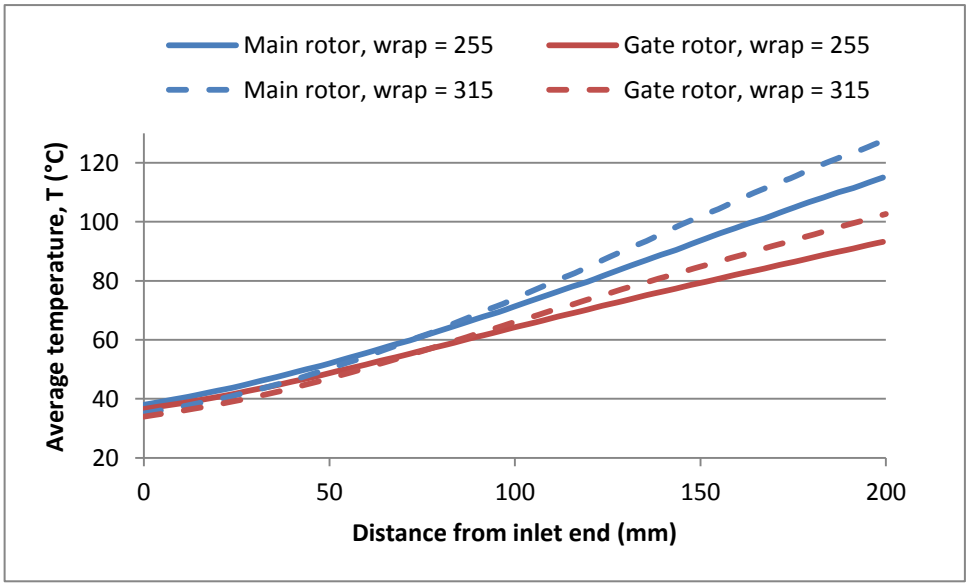

Figure 6-8: Rotor temperature distributions with different wrap angles

6.2.6 Sensitivity to Volume Index

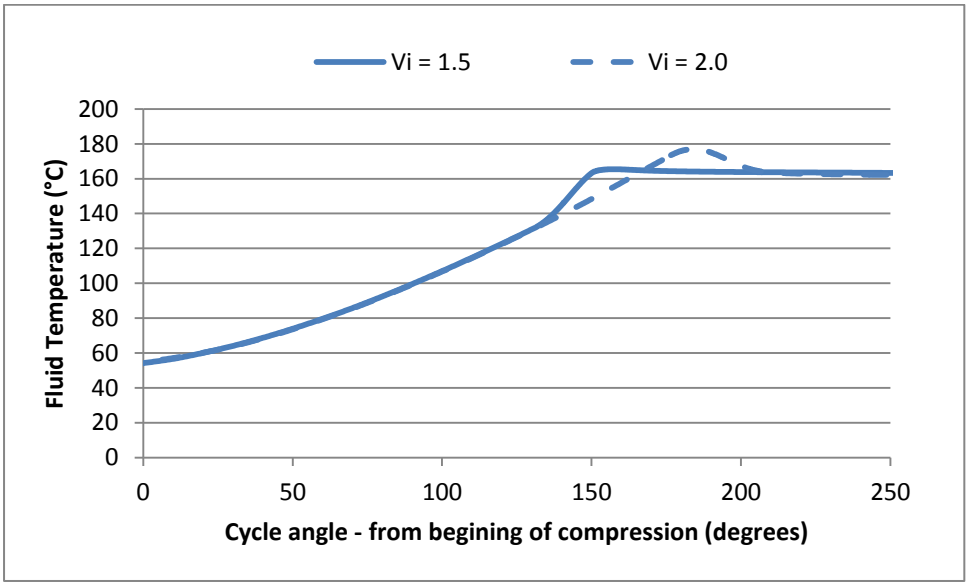

Figure 6-9: Modelled temperature during cycle with different volume index

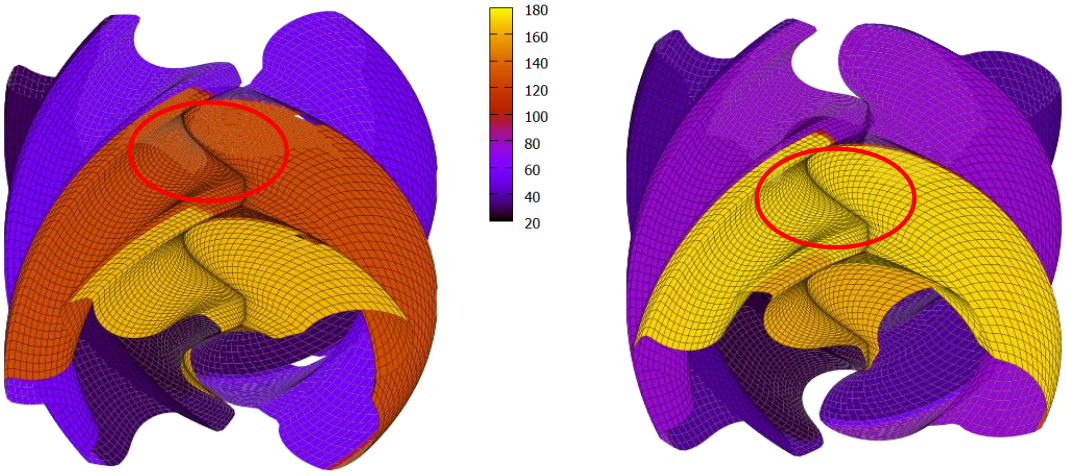

a) model with Vi = 1.5 b) model with Vi = 2.0

Figure 6-10: Comparison of rotor models with different volume index

In this case the rotor geometry in unchanged but the casing has been modified. In fact this 'casing geometry' modification was simply achieved by changing the timing of the port opening in the thermodynamic model, resulting in a different temperature curve as shown in Figure 6-9. In Figure 6-10 the chambers highlighted with the red ellipse show the instantaneous fluid temperature immediately prior to opening of the discharge port. With Vi = 1.5 the temperature is less than discharge in this chamber but once open to discharge will be exposed to a higher temperature earlier in the cycle. With Vi = 2.0 the

temperature is greater than the final discharge temperature because it will decrease once expanded to the lower discharge pressure. Both scenarios result in higher than ideal temperatures at different points in the cycle however it is shown in Table 6-8 and Figure 6-11 that the overall effect on the rotor temperature exposure is similar.

The most notable difference in the surface temperature distribution was on the casing bores, as shown in Figure 6-12. The minimum and maximum time averaged temperatures are similar. However, with Vi = 1.5, a larger area of the casing bores is exposed to the higher temperatures.

Table 6-8: Temperatures with different volume index

	Temperature (°C)					
	Fluid		Main Rotor		Gate Rotor	
Volume Index	Inlet	Outlet	Inlet	Outlet	Inlet	Outlet
1.5	25	161	37	122	35	98
2	25	159	36	122	35	98

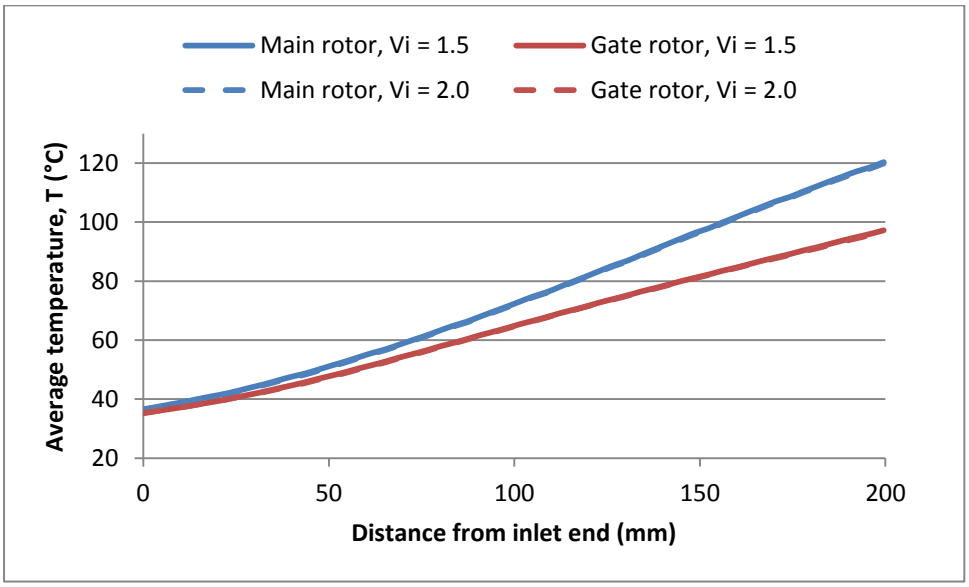

Figure 6-11: Rotor temperature distributions with different volume index

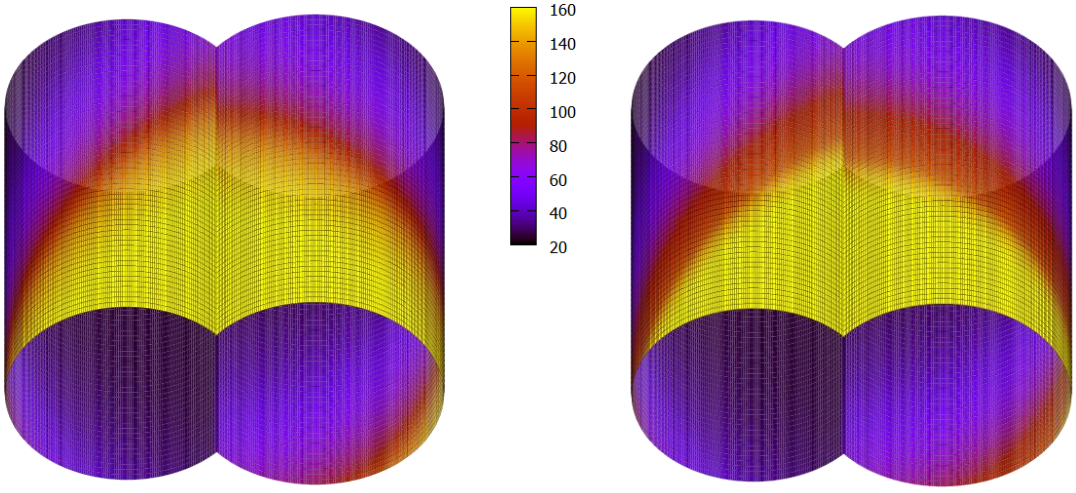

a) model with Vi = 1.5 b) model with Vi = 2.0

Figure 6-12: Comparison of casing temperatures with different volume index

6.2.7 DISCUSSION

These results confirm that surface boundary conditions have been mapped as expected. Testing with different rotor geometry has confirmed that the procedures outlined in Chapter 4 are sufficiently robust and furthermore have been correctly implemented.

This exercise demonstrates how the procedures developed in this work can be readily applied to the evaluation of rotor designs at a very early stage in the design process. Further case studies, in this thesis, utilise these temperature distributions in order to investigate operational clearances due to thermal distortions.

6.3 Model Sensitivity to Clearance Modifications

6.3.1 Overview

The estimated thermodynamic performance is compared with experimental results. The aim of this exercise was to evaluate the sensitivity of the model performance to predicted operational clearance variations.

6.3.2 DRUM127 Compressor

This case is based on the same setup as detailed in 6.2.2 'DRUM127 Compressor'.

6.3.3 DRUM127 Test Measurement

Air test data was provided by City, University of London, for the range of operating duties detailed previously. Due to the lack of compressor cooling and the high adiabatic exponent of air, the achievable pressure ratio was restricted by the operating temperature; however this is well suited to investigate thermal distortions.

A torque meter was installed on the motor shaft while the digital encoder for the speed measurement was mounted on the male rotor shaft. The pressure and temperature of the gas were measured at the inlet, the discharge, and upstream of the orifice plate. The air flow through the compressor was measured by use of an orifice plate installed in the discharge line of the system. The discharge line contained a control valve for regulation of the discharge pressure. A simplified schematic of the test setup is shown in Figure 6-13 and a list of instrumentation used in provided in Table 6-9.

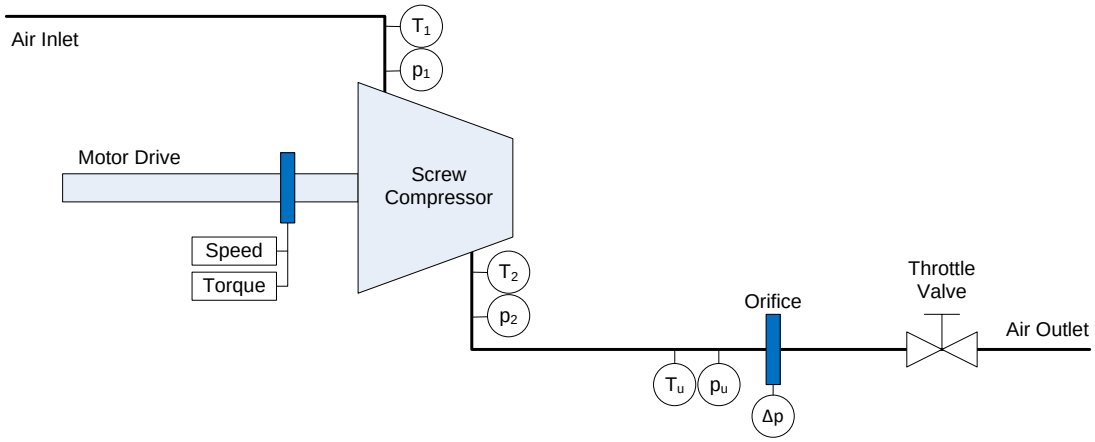

Figure 6-13: DRUM127 schematic

Table 6-9: DRUM127 instrumentation

Measured Parameter	**Instrument**	**Description**
shaft speed	Shaft Encoder. (BHG 16.25W.3600-B2-5)	360 TTL pulses per revolution.
shaft torque	TRP-500 torque meter. (strain gauge transducer)	max capacity: 500Nm, Calibration level: 335Nm Range = 0 - 6000 rpm, Supply volt=10v dc
inlet pressure, p_1	PDCR 110/w –pressure transducer	Operating range = 3.5bar(abs). Excite voltage=10V dc
inlet temp. , T_1	Platinum Resistance Thermometer	Range= -75^0C to 350^0C
outlet pressure, p_2	PDCR 922-pressure transducer	Operating range =15 bar (abs). Excite voltage=10V dc, Output voltage= 100 mV
outlet temp., T_2	Platinum Resistance Thermometer	Range= -75^0C to 350^0C
orifice inlet pres., p_u	PDCR 922-pressure transducer	Operating range =15 bar (abs). Excite voltage=10V dc, Output voltage= 100 mV
orifice inlet temp., T_u	Platinum Resistance Thermometer	Range= -75^0C to 350^0C
orifice diff. pres., Δp	PDCR 2120- pressure transducer	Pressure diff= 0.35 bar, Excitation Voltage=10V dc

Data acquisition and logging was done using a National Instrument Compact-RIO (CRIO-9022) Real-Time with an 8 slots chassis CRIO-9114. Programming

was done using LabVIEW FPGA (Field Programmable Gate Array) which is suitable for high frequency data acquisition.

6.3.4 DRUM127 CLEARANCE SENSITIVITY

Three different model cases have been described in Table 6-10. Case A uses the unmodified design clearances, set up in the model for the radial and interlobe leakage paths, in order to provide a benchmark. In Case B the interlobe and radial gaps have both been modified for rotor thermal distortion only, while in Case C the estimated thermal distortion of the casing has been included.

Table 6-10: Modelled clearance adjustments

Clearance Adjustments	Case A	Case B	Case C
ROTOR thermal distortion	No	Yes	Yes
CASING thermal distortion	No	No	Yes

In Figure 6-14, the local interlobe clearance gap is plotted against the relative position along the interlobe sealing line for a single compression chamber. In Figure 6-14 the location of the rotor root and tip is annotated and the local rotor radius is plotted on the secondary axis, to provide an indication of the local clearance positions.

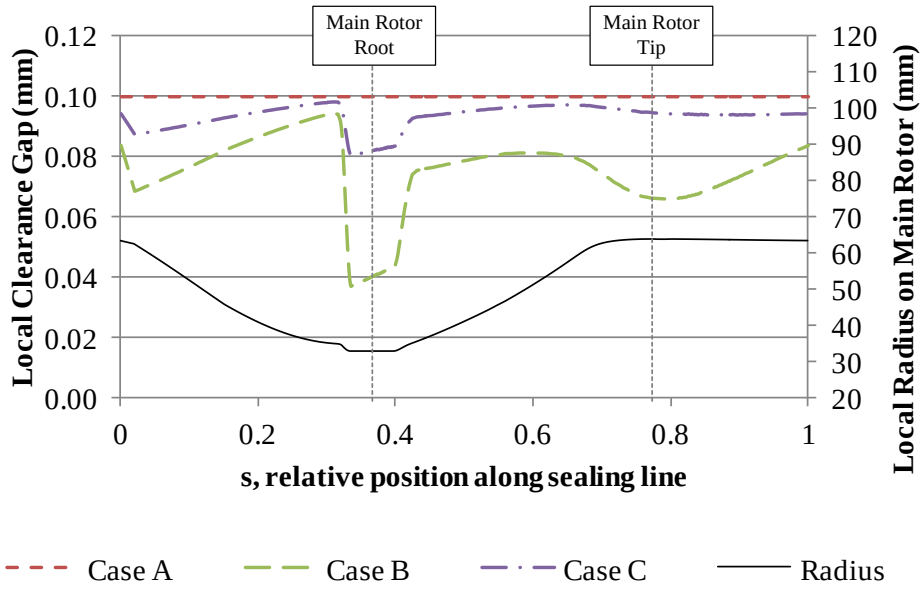

Figure 6-14: Interlobe clearance distribution corrected for thermal deformations

In Case A the local clearance gap has been taken to be constant with a value of 0.1mm. With the introduction of the rotor thermal expansion in Case B, significant clearance reduction will occur with some local areas more affected than others. The location of the biggest clearance reduction is at the root of the main rotor. This indicates the location where rotor contact is most likely to occur. The thermal expansion of the casing in Case C mitigates the rotor expansion, as would be expected. However, there is still a slight net decrease in the interlobe clearances for this case.

The results shown in Figure 6-14 are for a specific instant in the compression cycle when the interlobe sealing line is fully developed i.e. the full length of the sealing line is an active leakage path. The instantaneous interlobe leakage area is taken as the area under the relevant curve (corrected for the actual sealing line length). As the cycle progresses, the length and position of the sealing lines change and the local clearance deformations need to be re-evaluated based on the new location. The changing history of two leakage areas is shown in Figure 6-15, beginning at the start of compression (in this case when $\theta = 0°$). The interlobe leakage area curve is shown on the left graph of Figure 6-15. This is related to the clearance distribution of Figure 6-14. The combined leakage area curve for all out-flow radial clearances is shown in the right hand graph. It is interesting to note that for Case C, with both rotor and casing expansion included, a net increase in the radial gap is predicted in the latter stages of the compression cycle due to the local hot spot on the compressor casing. The radial leakage area is greater than the interlobe leakage area. Note the different scales used on each y-axis. However, the cycle offset and consequently the pressure difference across the radial leakage area is significantly smaller than across the interlobe gap which determines the relative significance of how these flow areas affect the thermodynamic performance. Note that a similar radial in-flow leakage area would feed some mass flow back into the rotor chamber from the previous chamber, though this is not shown.

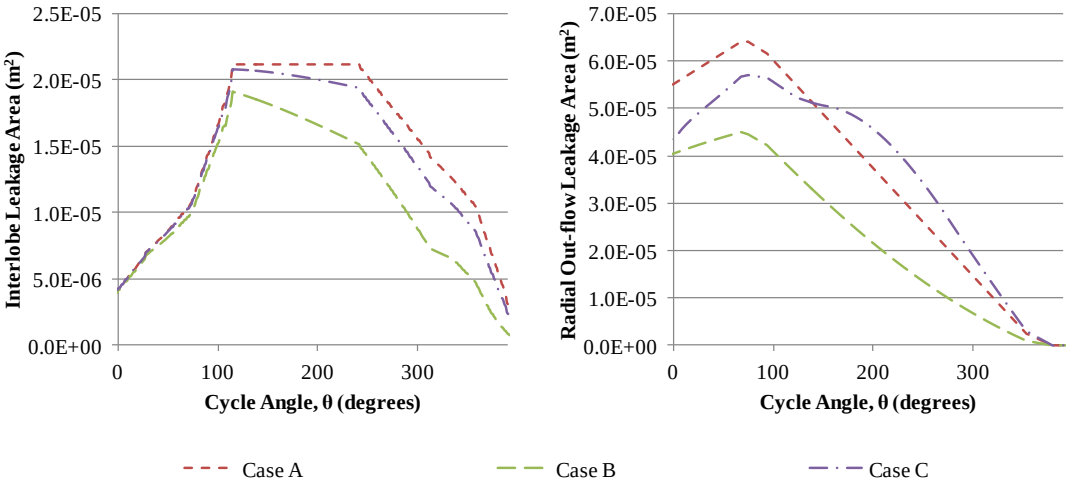

Figure 6-15: Variation of leakage areas throughout compression cycle

6.3.5 DRUM127 PERFORMANCE SENSITIVITY

As shown in Figure 6-16, measured tests results of compressor flow and discharge temperature have been used as a benchmark to compare model predictions. Initial temperature boundary conditions were always calculated, based on results from a chamber model with no clearance modifications (as in Case A). For case B and C these initial temperatures were used to calculate new *operational* clearances so the thermodynamic model had to be recalculated (following the flowchart of Figure 5-16), to include the temperature boundary conditions. Further iteration was required until the clearance corrections had no significant effect on the recalculated thermodynamic performance. After 3 iterations, the discharge temperature varied by less than 0.3% compared to the previous iteration. This was taken to be satisfactory therefore 3 iterations were used in all models where clearance modification was included.

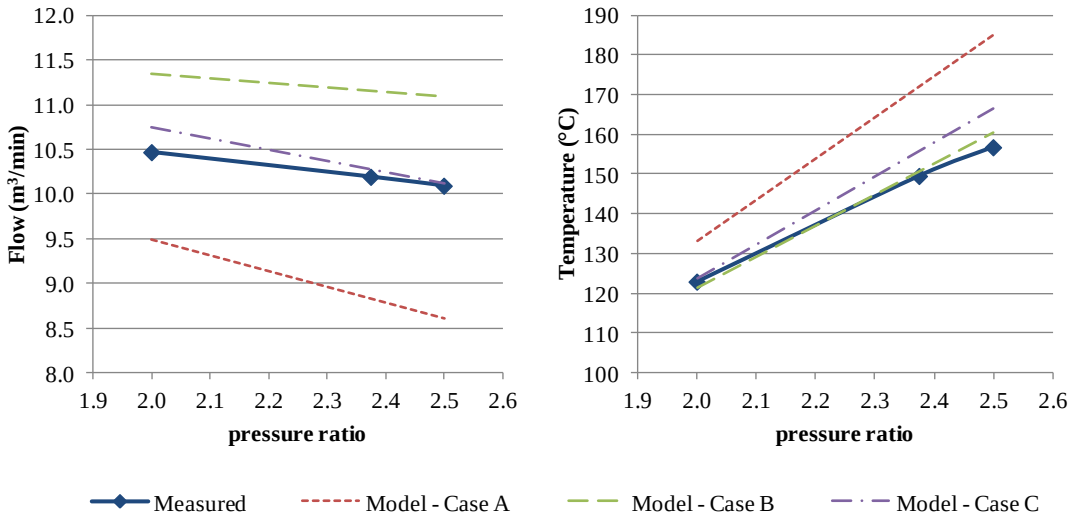

Figure 6-16: Compressor performance from test and model

The results of the model running Case B - with interlobe and radial clearances corrected for rotor thermal growth only - show a significant increase in flow compared to the results of Case A. Case B also has a smaller drop off in flow with increased pressure ratios (flatter gradient) that is closer to the measured gradient than Case A. The results of the model running Case C, with interlobe and radial clearances corrected for rotor and casing thermal growth, show an improvement in the absolute flow values. However there is a deviation from the measured gradient. The modelled temperature, shown in the right hand diagram in Figure 6-16 is closer to the measured results in terms of absolute values and gradient (with respect to pressure ratio) for both cases with clearance corrections. For temperature comparison the measured discharge temperature (T_2 in Figure 6-13) directly downstream from the compressor is used; the equivalent model temperature is used as discussed in Appendix B.1.1.

6.3.6 Discussion

Results show that the modelled flow is highly sensitive to changes in the operational clearances. The largest deviation in predicted performance is between Case A – with no clearance modification and Case B – with clearances adjusted due to rotor distortion only. These are the two extreme cases for clearance values and it's a reasonable assumption that actual operational clearances will be somewhere in between.

In the case presented, the model accuracy improved with the introduction of local clearance corrections used to calculate leakage areas iteratively. However care must be taken when drawing conclusions, based on absolute test values, because it is difficult to know, with absolute certainty, that the unmodified model clearances are representative of the actual assembled clearances; which are subject to a complex array of manufacturing and assembly tolerances.

The predictions shown in Case C are closest to the test results, in terms of flow prediction. However the predicted temperature shown in the results of Case B was closer. Put another way, the modelled discharge temperature is slightly high for a given flow compared to test results. It is difficult to say if this is the result of something inherent to the chamber model used; or if the relative size of the various clearances during set-up is not representative of the actual assembled clearances; or if the relative adjustment for operational distortions is inaccurate.

6.4 Investigating Interlobe Clearance Distortion

6.4.1 Overview

This case focuses on the impact of thermal distortions on the interlobe clearance distribution. As before, the predicted operational interlobe clearances are presented for different combinations of rotor and casing distortion in order to assess how sensitive the calculated clearances are to each.

This case study is on an oil injected WCVTA510 compressor. In contrast to the previous DRUM127 case, this adds further complexity to the clearance analysis due to the lack of timing gears and direct rotor to rotor drive. More emphasis is put on representing the actual interlobe clearance distribution around the rotor profile accurately. The test results are from two different compressors, before and after a design revision of the interlobe clearances was made in order to address reliability concerns when running at higher than normal temperatures.

6.4.2 WCVTA510 Compressor

The WCVTA510 is an oil injected compressor which at the time of testing was the largest manufactured by Howden Compressors, Figure 6-17 gives a sense of the scale and Figure 6-18 shows how the rotors are situated.

Figure 6-17: WCVTA510 compressor

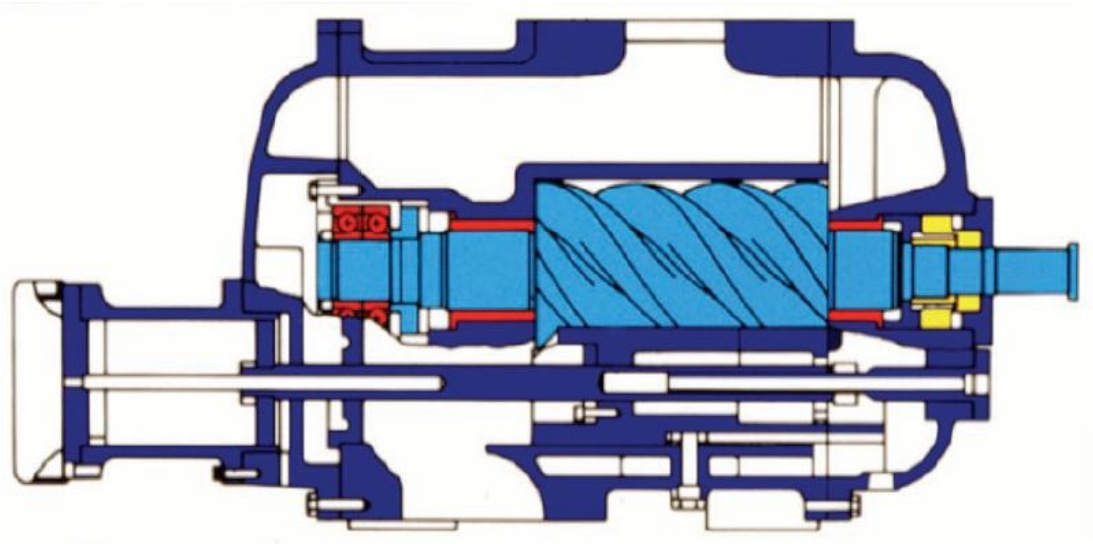

Figure 6-18: WRV range compressor vertical section

Table 6-11: Basic compressor details

Main rotor diameter, D (mm)	517
Length over diameter ratio, L/D	1.904
Main rotor wrap angle, φ_{w1} (deg)	330°
Lobe combination, z1/z2	4/6
Profile type	N
Volume index, Vi	2.6 (fixed)
Oil injection	Yes

Table 6-12: Air test for contract duty

Inlet pressure, p1 (Bara)	1
Outlet pressure, p2 (Bara)	5
Inlet temperature, T1 (°C)	20
Outlet temperature, T2 (°C)	90 (targeted)
Speed, N (rpm)	1400

Table 6-13: Air test for high temperature

Inlet pressure, p1 (Bara)	1
Outlet pressure, p2 (Bara)	11
Inlet temperature, T1 (°C)	20
Outlet temperature, T2 (°C)	120 (targeted)
Speed, N (rpm)	750*

*Due to power restrictions on the testing of this large compressor, the speed was reduced from the contract speed of 1400rpm to 750rpm during the overload testing. It is this overload testing at higher discharge temperature which was of interest for clearance analysis.

6.4.3 WCVTA510 Test Measurement

Test data was provided from contract testing in Howden Compressors. A typical test setup is shown in Figure 6-19. Though not visible in the photo, an orifice plate for flow measurement is situated in the inlet ducting. Some details of test instrumentation are provided in Table 6-14.

Figure 6-19: WRVTA compressor on test stand

Table 6-14: WRVTA510 instrumentation

Manufacturer	Description	Range
Budenberg	Discharge Pressure	0-400psig
Budenberg	Discharge Pressure	0-100psig
Kosmos	Discharge Temperature	
G & W	Tachometer	1500rpm
Elliott	Electrical power to motor	0-1200W

6.4.4 WCVTA510 Thermal Analysis

The overload test condition, with a discharge temperature of 120°C, was modelled to determine how the temperature varied throughout the compression cycle for this duty.

As before, the fluid temperature from the compression cycle was mapped onto the surfaces of the rotors and the casing bores. The temperature of the fluid boundary on the main and gate rotor surfaces is shown in Figure 6-20 . The left image shows the instantaneous fluid temperature for a particular rotor position. In the right hand image these instantaneous temperatures has been averaged over one full rotation and over each transverse plane of the rotors.

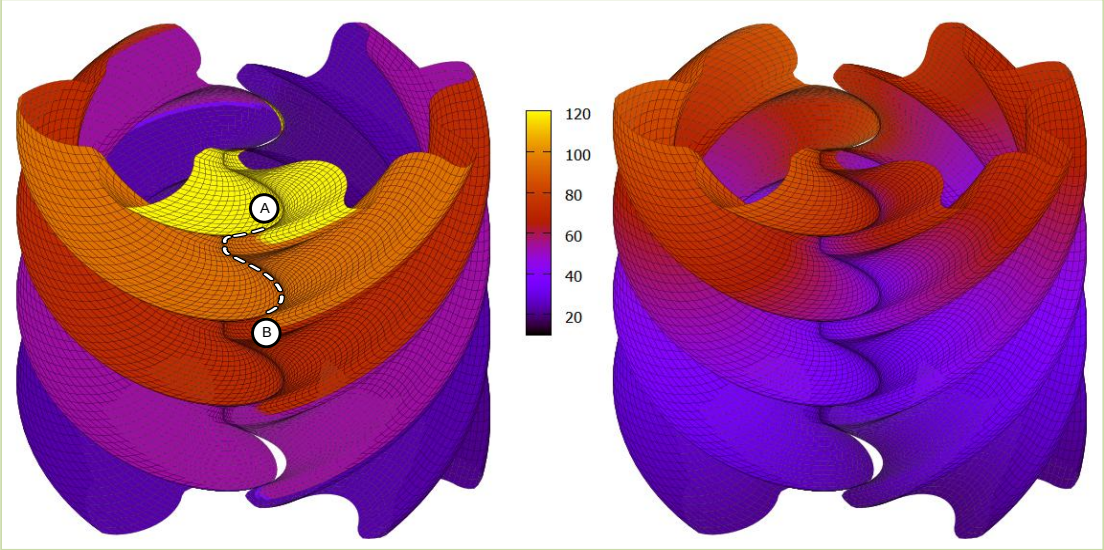

Figure 6-20: Instantaneous and averaged fluid boundary temperature. Line AB highlights the interlobe sealing line for a single compression chamber.

Table 6-15: Average fluid boundary temperature across outlet plane

Component Description	Temperature (°C)
Main rotor	86.8
Gate rotor	73.2
Casing	69.4

The peak temperatures occur at the outlet plane of the rotors. Therefore the analysis presented in this work was based on the average fluid boundary

temperatures presented in Table 6-15. It is clear that the averaged fluid boundary temperatures at critical locations on the compressor are actually much lower than the peak fluid discharge temperature of 120°C. Note that while the peak temperature that the casing is exposed to is close to the discharge temperature the planar average used in this case is the average of the temperature all the way around the rotor bores in the discharge plane.

6.4.5 WCVTA510 CLEARANCE PRESENTATION

Due to the 3D nature of the interlobe sealing line it is difficult to present clearance information clearly. Figure 6-21 shows an example of clearances mapped onto each of the rotors as vectors normal to the transverse rotor curve. The magnitude of the vectors actually shows the magnitude of clearances normal to the 3D rotor surface. This approach is very intuitive and clearly shows how clearances relate to difference areas on the rotor profiles. The difficulty with this clearance presentation is comparing small differences in similar clearance distributions. Magnifying the vectors quickly distorts the apparent clearance gap due to the curvature of the profiles. In the previous case, of the DRUM127, local clearances were plotted against the 'relative position on the sealing line' but this makes it difficult to determine where the clearances actually occur on the rotors. For this example, where the design clearance is non-uniform, a different approach has been taken in order to show local clearances more clearly.

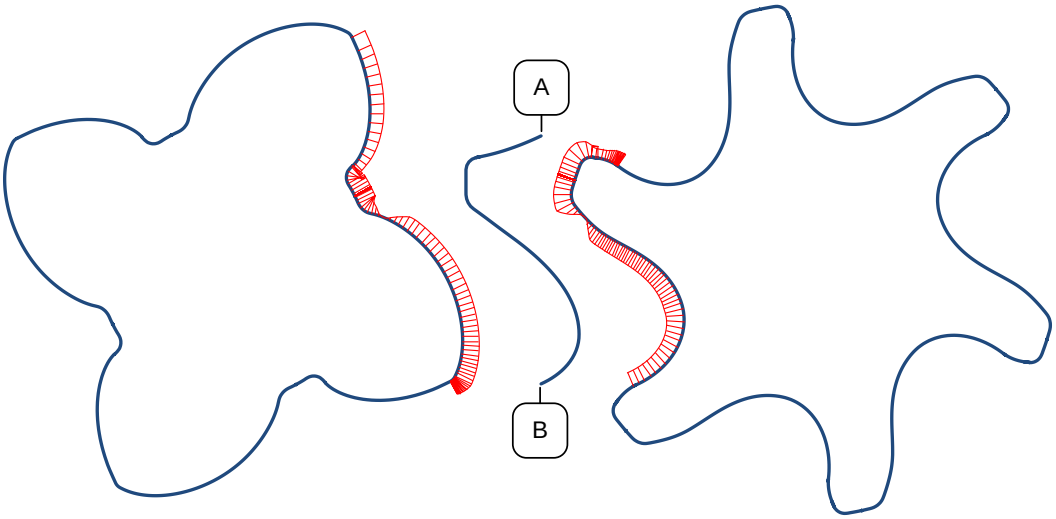

Figure 6-21: Transverse cross section of rotors showing interlobe clearance distribution of rotor surfaces

The compromise that has been taken is to plot the local clearances on the axis of a rack projection along which the rack would translate. Thus, the magnitude of the local clearances can be simply graphed and superimposed against the somewhat familiar shape of the rack as presented in Figure 6-22. Rather than putting numerical values on the horizontal axis, vertical lines have been added to identify key points along the length of this sealing line projection, details of which are provided in Table 6-16.

Line AB represents the conjugate rack, common to both rotors. The limits of this rack segment, points A and B, are shown in Figure 6-20 where it can be observed that these points occur on the boundary between different compression chambers. This point is important as the distortions over this specific section of the interlobe sealing line are used when calculating the interlobe leakage area for that chamber at that moment.

The original and revised clearance distributions are both presented in Figure 6-22. In all cases the relative rotation between the rotors has been adjusted in order to provide zero clearance at location 3: the pitch radius on the round side of the rotors. This is where the driving force is transferred from the main to the gate rotor. In the revised clearance design the main difference is that the clearance in the main rotor root has been increased and to a lesser extent also

at the main rotor tip. Notice that the clearance on the round, or *drive,* flank of the rotors (between locations 3 and 4) has actually been decreased in the revised clearance design – this clearance will not significantly reduce during operation because the gap is maintained due to the nearby contact at the pitch point (location 3, where the main rotor drives the gate rotor), therefore this clearance was deemed to be unnecessarily large. Conversely, on the opposite flank (from 4 to B, and from A to 1) the gap is adversely affected by thermal distortions at location 3 which are transferred over to the non-drive flank. Therefore it was necessary to increase the clearances on the non-drive flank.

To quantify how these clearance changes impact the leakage area through the interlobe gap, the local clearances were integrated over the length of the 3D sealing line. The total leakage area is 108.5mm^2 for the original design and 142.7mm^2 for the revised design, an increase of 31.5%.

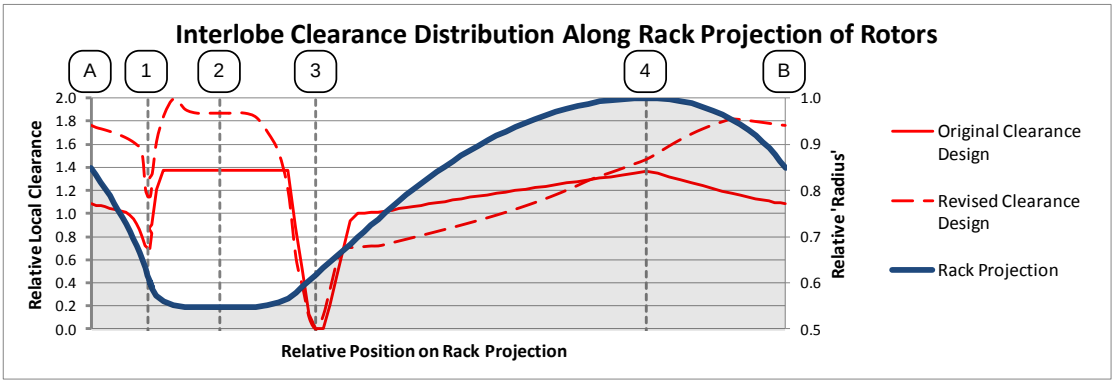

Figure 6-22: Comparison of example interlobe clearance distributions along rack projection of rotors

Table 6-16: Key Clearance Locations

Location on rack	**Description**
A	Limit of sealing line for single chamber
1	Pitch radius on straight (undercutting) side of rotors
2	Root of main rotor / tip of gate rotor
3	Pitch radius on round (non-undercutting) side of rotors
4	Tip of main rotor / root of gate rotor
B	Limit of sealing line for single chamber

6.4.6 WCVTA510 Clearance Distortion Results

The following results show the predicted operational clearance distributions for the original and revised designs respectively. As previously discussed, a similar temperature increase, in both the rotors and casing, results in little net change in the operational clearances. This case has been presented with the longer dashed lines on each figure and the trend is not far off the original clearance.

A second case has also been presented where the rotors do not move apart due to casing thermal expansion. This case is quite possible in the event that sudden temperature changes cause the rotors to heat up faster than the casing, or, alternatively the outlet end bearings might be situated remotely from the rotor outlet plane in a location where the casing temperature is much lower than estimated in Table 6-15. Unfortunately the distance between the two dashed curves for the different operational scenarios results in a large band of uncertainty but it does serve to highlight 1) where rotor contact is most likely to occur for a given clearance design, and 2) where clearances can be further reduced without compromising reliability.

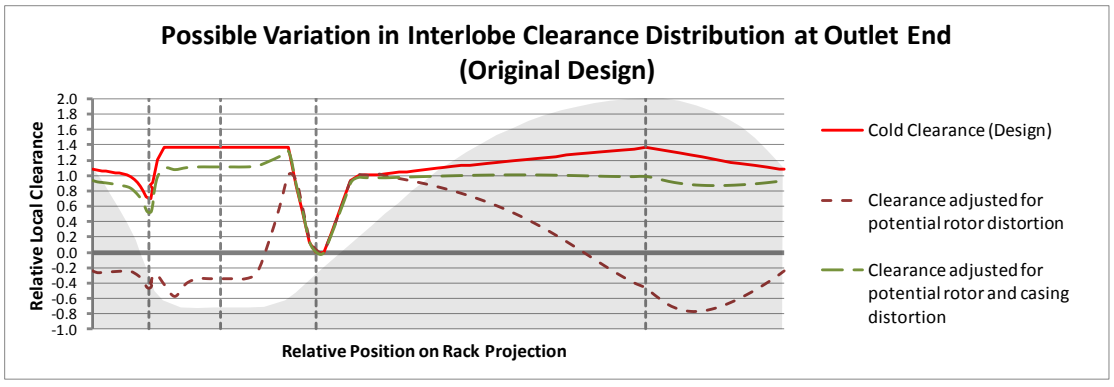

Figure 6-23: Original design clearance variations

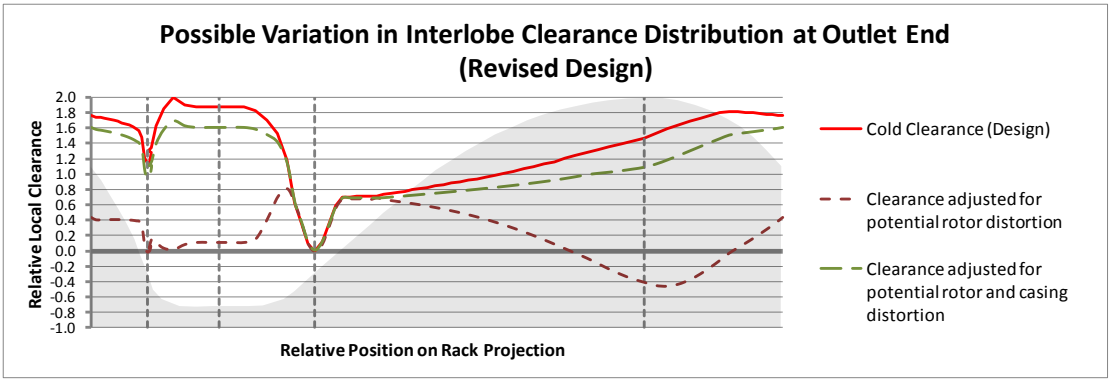

Figure 6-24: Revised design clearance variations

This analysis supports the suitability of the revised clearance design. The results show that at the root of the main rotor, contact cannot now occur due to thermal distortion alone. The chance of contact at the tip of the main rotor has been significantly reduced but the analysis suggests contact is still possible there under extreme circumstances.

The most problematic clearance area is on the non-drive (undercutting) flank of the rotors. Since distortions are transferred over from the contacting drive flank, these non-drive clearances vary more than in other areas. What the figures do not show is that this represents a long part of the sealing line path due to the effect of undercutting. So this has a large effect on the overall leakage area. This area also experiences faster relative sliding motion between the rotor surfaces. So contact in that region should certainly be avoided.

6.4.7 WCVTA510 Performance Results

The models were also run at the nominal air test duty which is closest to the designed operating conditions: with a speed of 1400rpm, a pressure ratio of 5 and a discharge temperature maintained at approximately 90°C. The modelled deviation in the volume flow due to the revised design is compared with the deviation measured on test in Table 6-17.

Table 6-17: Performance penalty with revised interlobe clearance

	change in volumetric flow
Modelled	-0.5%
Measured on Test	-1.7%

The difference between the model result and the test result suggests that the model is slightly underestimating the effect of leakages through the interlobe gap. Unfortunately as the test results were obtained using two completely different compressors the effect of other manufacturing and assembly tolerances cannot be ruled out for the test results.

Importantly, the resulting change in flow on test was small enough for the performance of both compressors to still be within normal operating tolerances. With the reduced flow there was a similar reduction in shaft power so there was very little change in overall efficiency.

6.4.8 WCVTA510 TEARDOWN RESULTS

In the absence of direct measurement of the operational interlobe clearances tear down of the compressors often provides useful insight. On the compressor with the original clearance design, tear down inspection revealed that rotor to rotor contact had occurred at the root of the main rotor, resulting in a polished surface finish as highlighted in Figure 6-25. In other words the clearance had reduced to zero locally.

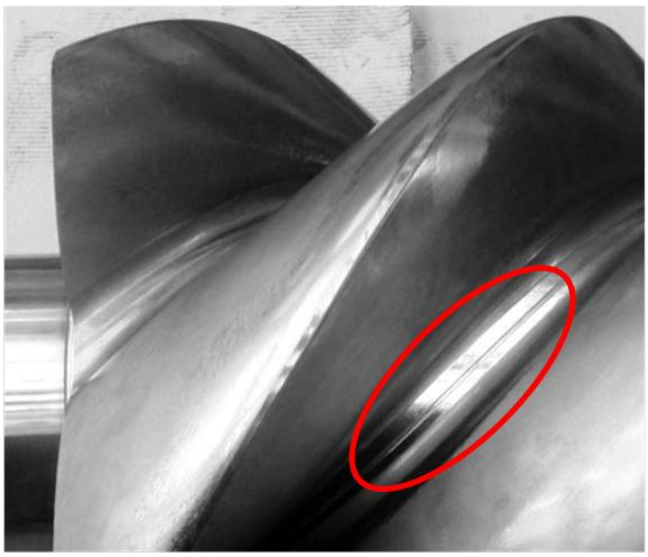

Figure 6-25: Evidence of rotor rooting on main rotor of WCVTA510

The type of contact observed and the fact that this standard compressor had not presented any problems, while operating within normal temperature limits, points to thermal distortion of the rotors being the most likely cause of this

rotor contact. This tear down also indicated that some rotor to casing contact had occurred as well as some localised interlobe contact around the tip of the main rotor.

The revised clearance design was implemented on a different compressor at a later date and though teardown inspection revealed some minor localised rotor contact, related to the tip sealing strip, there was no contact over the main part of the root.

6.4.9 DISCUSSION

Local variations in the interlobe clearance distribution, due to thermal distortions, have been approximated. This provides valuable data at an early design stage about where and when, in the compression process, clearances are not adequate for a given compression application. Integrating this information into the rotor design process will allow a more optimised balance between reliability and compressor performance.

For validation purposes, the analysis was repeated for two interlobe clearance designs, when operating at an elevated rotor discharge temperature of 120°C in an oil injected compressor, with direct rotor drive. While there is a fairly large uncertainty on the predicted clearance deviations, the modelled results are in agreement with the available experimental findings because they predicted a high likelihood of rotor contact at the main rotor root on the original clearance design.

6.5 INVESTIGATING RADIAL CLEARANCE DISTORTION

6.5.1 OVERVIEW

This case study draws on extensive test results obtained from an oil free HS204 compressor, operating over a wide range of temperatures and speeds. This allows a more comprehensive comparison of modelled and measured compressor behaviour than provided in the previous case studies.

In addition to performance results from the tests, these results include real time measurement of the radial clearance gap which was used for more direct verification of the predicted clearance deformations.

6.5.2 HS204 COMPRESSOR

The HS204 is an oil free twin screw compressor which features timing gears at the suction end and mechanical seal arrangements on the shafts between the bearings and main rotor bodies. Hence there are two seals per rotor. A sectional arrangement of this compressor is shown in Figure 6-26. The rotors used in these tests were newly designed with an N rotor profile as shown in detail in Figure 6-27.

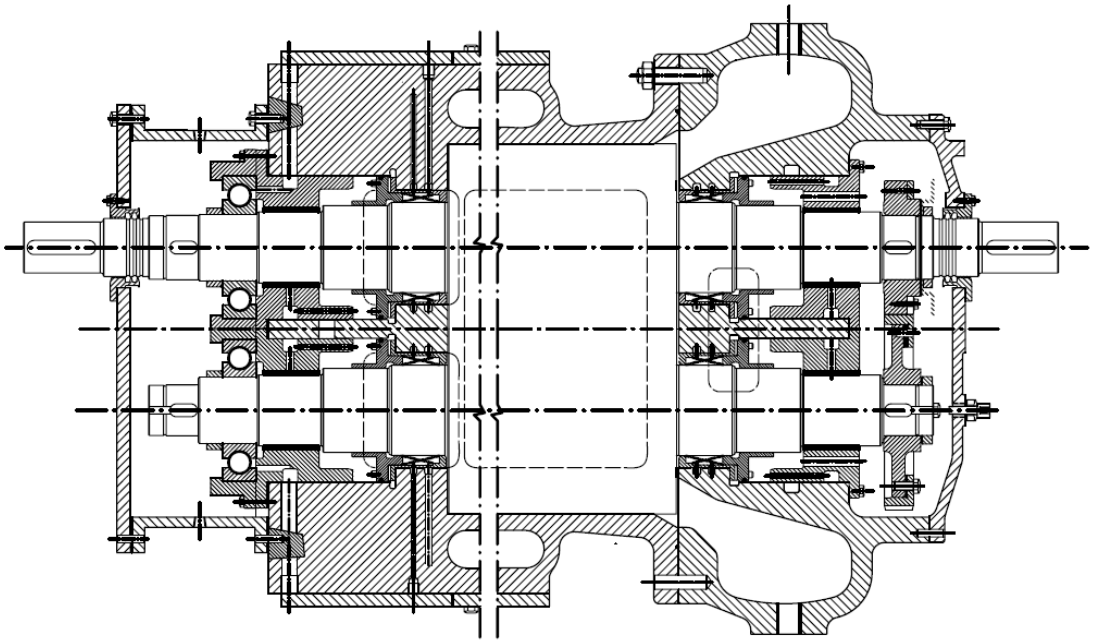

Figure 6-26: Horizontal section of HS204 compressor

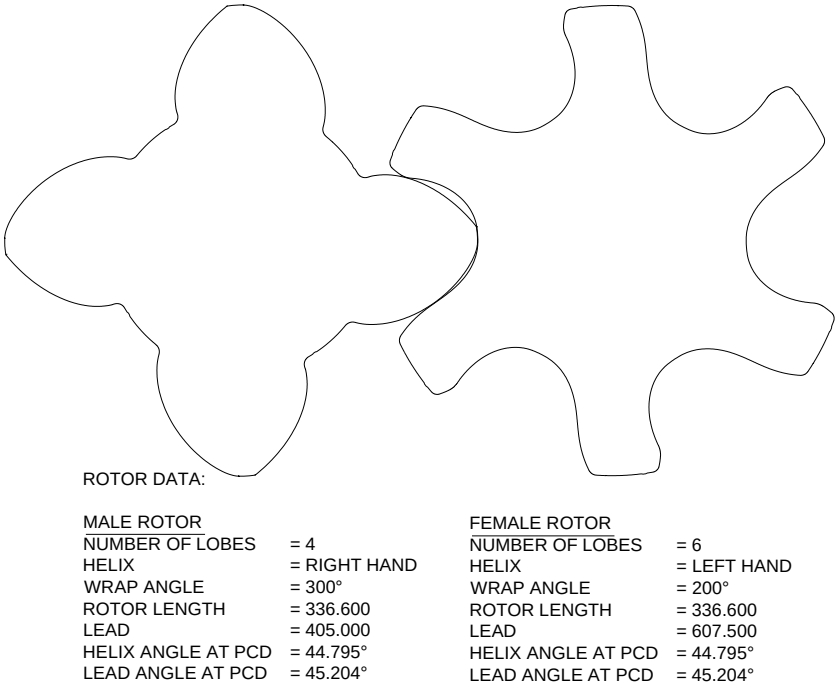

Figure 6-27: Rotor profiles and design data

All of the basic compressor parameters are given in Table 6-18 and more details of the interlobe clearance distribution are shown in Figure 6-28. The radial clearance gap for this compressor is nominally 0.150mm – this was the initial value used in the models.

Table 6-18: Basic compressor details

Main rotor diameter, D (mm)	204
Length over diameter ratio, L/D	1.65
Main rotor wrap angle, φ_{w1} (deg)	300°
Lobe combination, z1/z2	4/6
Profile type	N
Volume index, Vi	1.98
Oil injection	No
Jacket Cooling	Yes

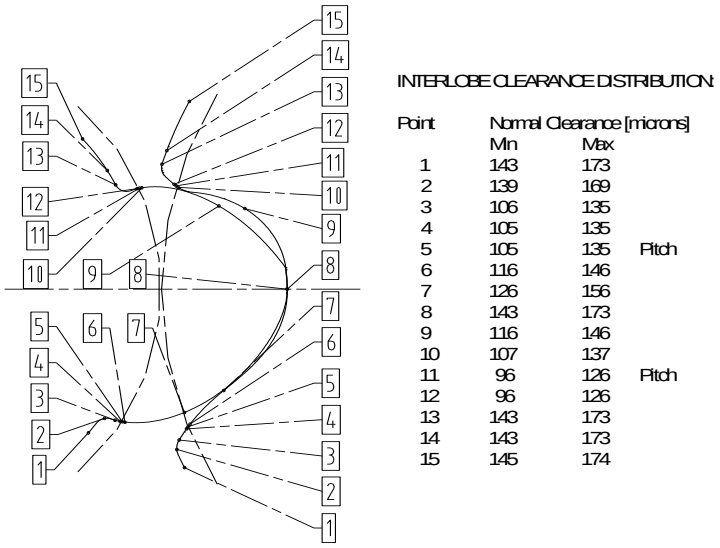

Figure 6-28: Interlobe clearance design data

The compressor was tested over a range of speeds and pressures as detailed below:

Table 6-19: Air test duty

Inlet pressure, p1 (Bara)	1
Outlet pressure, p2 (Bara)	1.5 – 2.5
Inlet temperature, T1 (°C)	20
Speed, N (rpm)	4000 – 7000

6.5.3 HS204 TEST MEASUREMENT

Extensive test data for this oil free compressor was available from previous R&D work at Howden Compressors. The compressor is shown on the test stand in Figure 6-19. Real time data monitoring and logging equipment was used to continuously record the parameters shown in Figure 6-30; details of the instrumentation used are provided in Table 6-20 and Table 6-21. By using the continuously monitored results, sufficient dwell time was allowed between different operating points to ensure that the measurements had stabilised. Furthermore, each stabilised results were averaged over a 10 second period.

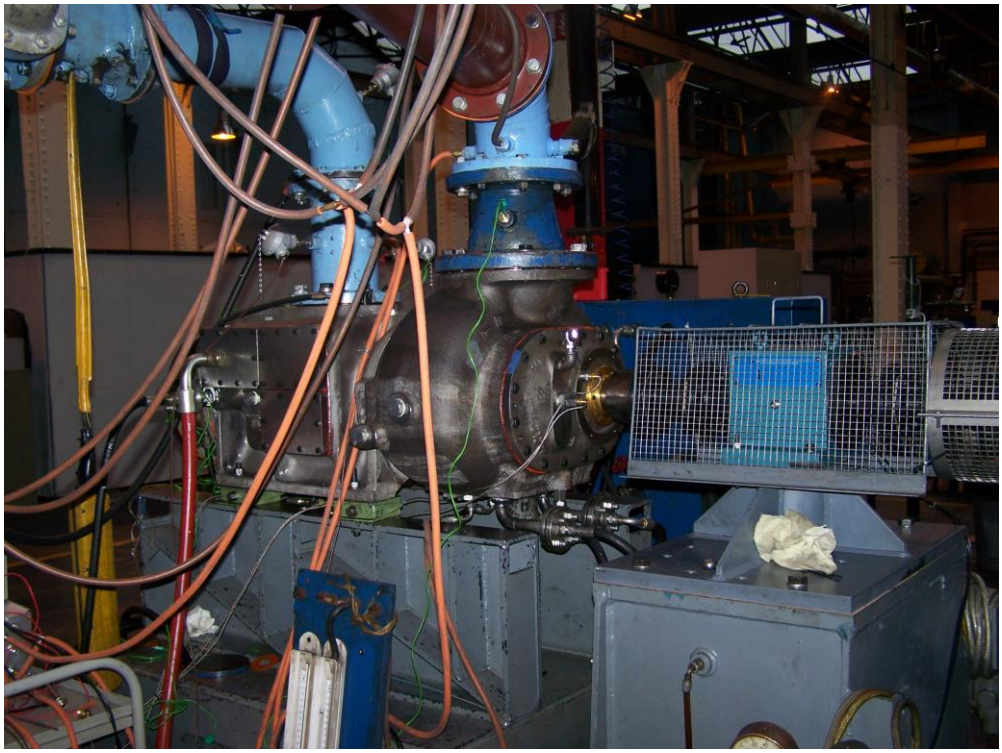

Figure 6-29: HS204 on test stand

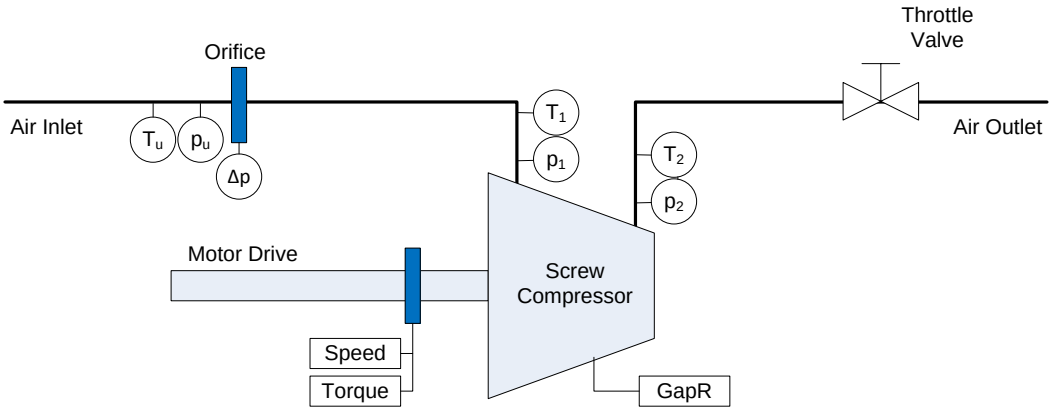

Figure 6-30: HS204 instrumentation schematic

Table 6-20: HS204 instrumentation

Parameters	Supplier	Part No	Description
pu, p1	Omni Instruments	Pi610C3-2BarA	0 to 2 BarA, 2mV/V, pressure transducer
p2	Omni Instruments	Pi610C3-6BarA	0 to 6 BarA, 2mV/V, pressure transducer
orifice Δp	RS Components	455-5071	Honeywell Comp SCX press sensor, 0-5psi, differential
Tu, T1, T2	TC Direct	405-987	Mineral insulated type thermocouple with IP67 standard weatherproof head (Type T, 6 mm x 150 mm)
ΔGapR	Omni Instruments	PRS02/2.0A01	Proximity Probe: Straight mount, 5mm tip, 2.0 m cable, armoured, female SMC connector, 30 mm M6 x 0.75 thread, 0 to 2.5 mm range.
speed, torque	Torquemeters	02-2350-00, 613/M	ET2350 Torque meter and readout unit

Table 6-21: HS204 additional hardware

Use	Supplier	Part No	Description
data aq.	National Instruments	779508-06	NI cDAQ-9172 8-slot USB 2.0 Chassis for CompactDAQ
data aq.	National Instruments	779014-01	NI 9221 8-channel, +/- 60V, 12-bit analogue input module
data aq.	National Instruments	779519-01	NI 9205 32-channel, +/- 10V, 16-bit analogue input module
data aq.	National Instruments	780493-01	NI 9213 16-channel, 24-bit, thermocouple module
driver unit	Omni Instruments	ECD02/20	Probe Driver: 2.0m cable, 0 to 2.5 mm range (8mV/um, API 670)

Proximity probes were used to measure the radial gap, GapR, on both the main and gate rotors. The probes situated in the bores of the casing at the bottom, 30mm from the discharge end face, as shown in Figure 6-31. Note that the probes are situated opposite the discharge port which is located on the top of the casing.

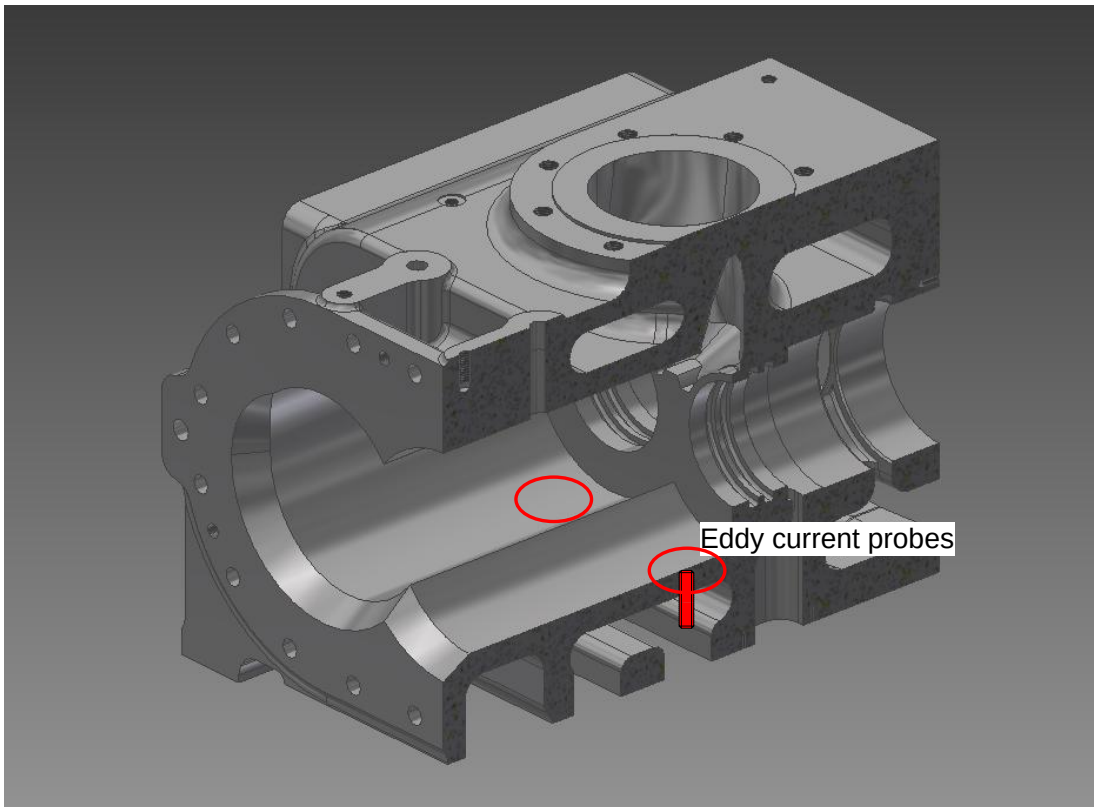

Figure 6-31: Position of radial proximity probes in the test compressor

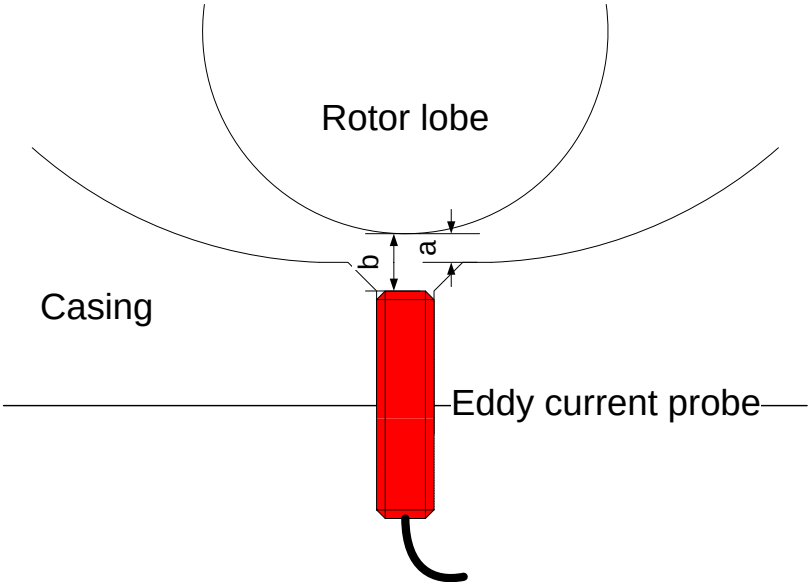

Figure 6-32: Proximity probe location

The proximity probe is slightly recessed into the casing bore as shown in Figure 6-32. The measured gap 'b' is therefore slightly bigger than the radial gap 'a'. While the compressor was running the gap obviously varies due to passing of the rotor lobe and the objective here was to record the minimum value.

Due to the nature of this set-up, the static gap could not be measured and instead the value of 'b' was recorded immediately after start-up to provide a reference *un-deformed* measurement. Once thermally stable at each operating point the *change* in the value of 'b' was used to assess gap distortion.

6.5.4 HS204 PERFORMANCE RESULTS WITH JACKET COOLING

At each test speed, the discharge pressure was adjusted for each measurement point and the compressor was given time to stabilise before measurements were taken. Model results were produced for the same range of operating points. Table 6-22 shows the measured volumetric efficiency and discharge temperature at each test point; with the values corrected for suction pressure and speed. The results at new pressure points have been linearly interpolated from the actual pressure points in Table 6-23. This has been done in order to provide test reference points so that the model error can be calculated at specific pressure ratios. In all the graphs presented, the originally tested pressure ratios will be used.

Graphs that compare the model results against the test results are shown in Figure 6-33 and Figure 6-34. In this case the model is based on nominal design clearances that are unmodified. These model results are denoted 'MODEL'. The relative error of the model across the range of operating points is tabulated in Table 6-24.

Similar results for a model that predicts clearance distortion due to rotor thermal expansion only, denoted by 'MODEL R', are given in Figure 6-35 and Figure 6-36 and Table 6-25.

The same set of results, produced by a model that predicts clearance distortion due to both rotor AND casing thermal expansion, denoted 'MODEL RC, are shown in Figure 6-37 Figure 6-38 and Table 6-26 .

Table 6-22: HS204 performance test results

Speed (rpm)	Pressure Ratio	Volumetric efficiency	T2 (K)
4000	1.63	78.3%	349.2
	1.79	77.3%	361.3
	1.97	76.3%	373.2
	2.07	75.8%	379.7
5000	1.63	81.8%	354.3
	1.81	80.9%	364.3
	2.00	80.1%	375.5
	2.10	79.5%	381.5
6000	1.65	84.2%	355.6
	1.84	83.4%	367.5
	2.01	82.9%	376.9
	2.11	82.5%	381.9
7000	1.69	85.7%	363.1
	1.88	85.1%	371.3
	2.06	84.5%	380.6
	2.16	84.3%	386.7

Table 6-23: HS204 interpolated performance test results

Speed (rpm)	Pressure Ratio	Volumetric efficiency	T2 (K)
4000	1.50	79.0%	340.7
	1.75	77.5%	357.9
	2.00	76.1%	375.1
	2.25	74.7%	392.3
	2.50	73.3%	409.5
5000	1.50	82.4%	346.7
	1.75	81.2%	361.2
	2.00	80.0%	375.6
	2.25	78.8%	390.1
	2.50	77.6%	404.6
6000	1.50	84.7%	347.7
	1.75	83.8%	361.8
	2.00	82.9%	376.0
	2.25	82.0%	390.2
	2.50	81.1%	404.4
7000	1.50	86.3%	352.9
	1.75	85.5%	365.4
	2.00	84.7%	377.9
	2.25	84.0%	390.3
	2.50	83.2%	402.8

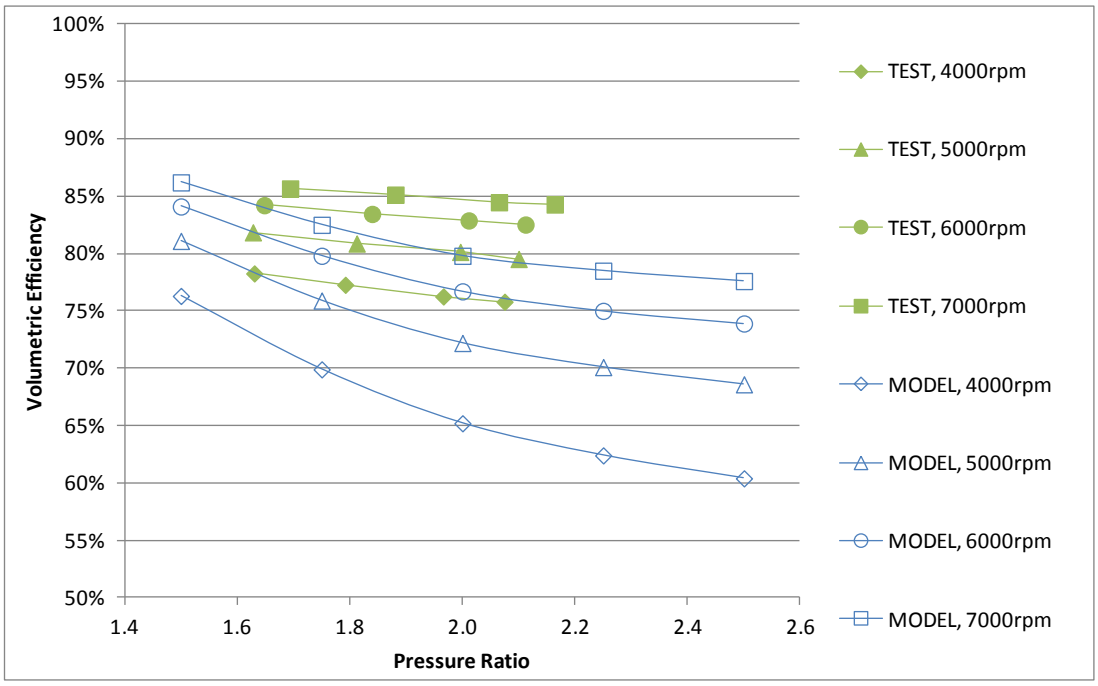

Figure 6-33: HS204 volumetric efficiency with unmodified model clearances

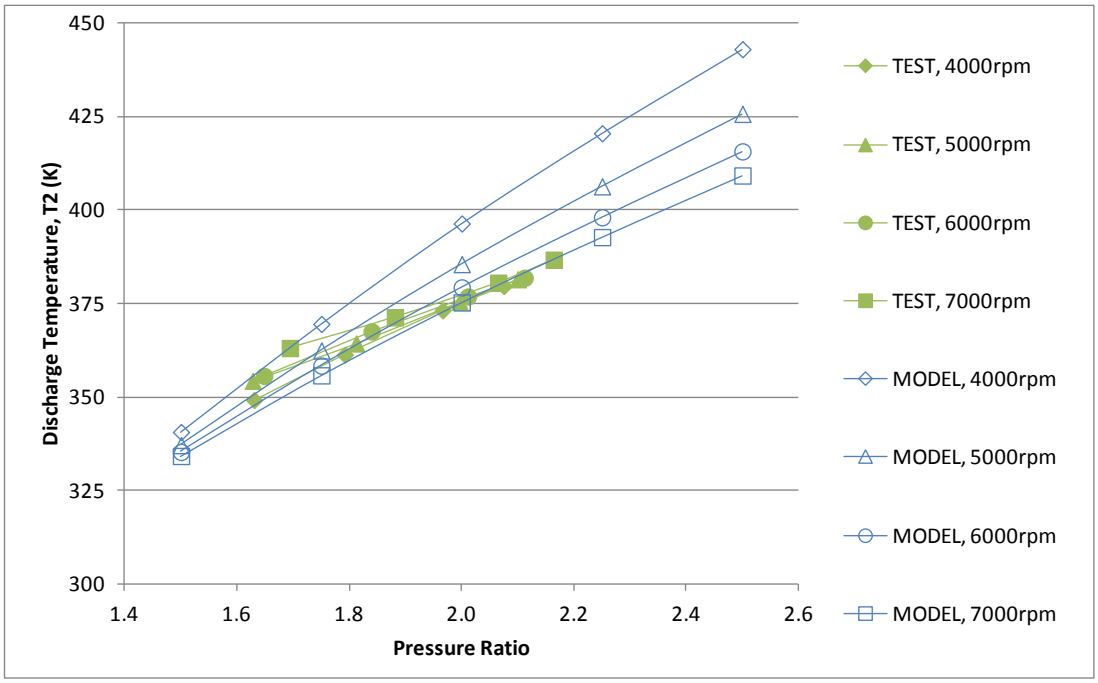

Figure 6-34: HS204 discharge temperature with unmodified model clearances

Table 6-24: HS204 model performance results with unmodified clearances

Speed (rpm)	Pressure Ratio	Volumetric efficiency	*Relative Error*	T2 (K)	*Relative Error*
4000	1.50	76.3%	*-3.4%*	340.6	*0.0%*
	1.75	69.9%	*-9.9%*	369.5	*3.3%*
	2.00	65.2%	*-14.4%*	396.4	*5.7%*
	2.25	62.4%	*-16.5%*	420.6	*7.2%*
	2.50	60.4%	*-17.6%*	443.1	*8.2%*
5000	1.50	81.1%	*-1.6%*	337.1	*-2.8%*
	1.75	75.9%	*-6.6%*	362.4	*0.4%*
	2.00	72.2%	*-9.8%*	385.6	*2.6%*
	2.25	70.1%	*-11.1%*	406.4	*4.2%*
	2.50	68.6%	*-11.6%*	425.8	*5.2%*
6000	1.50	84.1%	*-0.7%*	335.3	*-3.6%*
	1.75	79.8%	*-4.8%*	358.4	*-1.0%*
	2.00	76.7%	*-7.5%*	379.3	*0.9%*
	2.25	75.0%	*-8.5%*	398.1	*2.0%*
	2.50	73.9%	*-8.9%*	415.7	*2.8%*
7000	1.50	86.2%	*-0.1%*	334.2	*-5.3%*
	1.75	82.5%	*-3.5%*	355.8	*-2.6%*
	2.00	79.8%	*-5.8%*	375.3	*-0.7%*
	2.25	78.5%	*-6.5%*	392.8	*0.6%*
	2.50	77.6%	*-6.7%*	409.3	*1.6%*
		average relative error:	*-7.8%*		*1.4%*
		maximum relative error:	*-17.6%*		*8.2%*

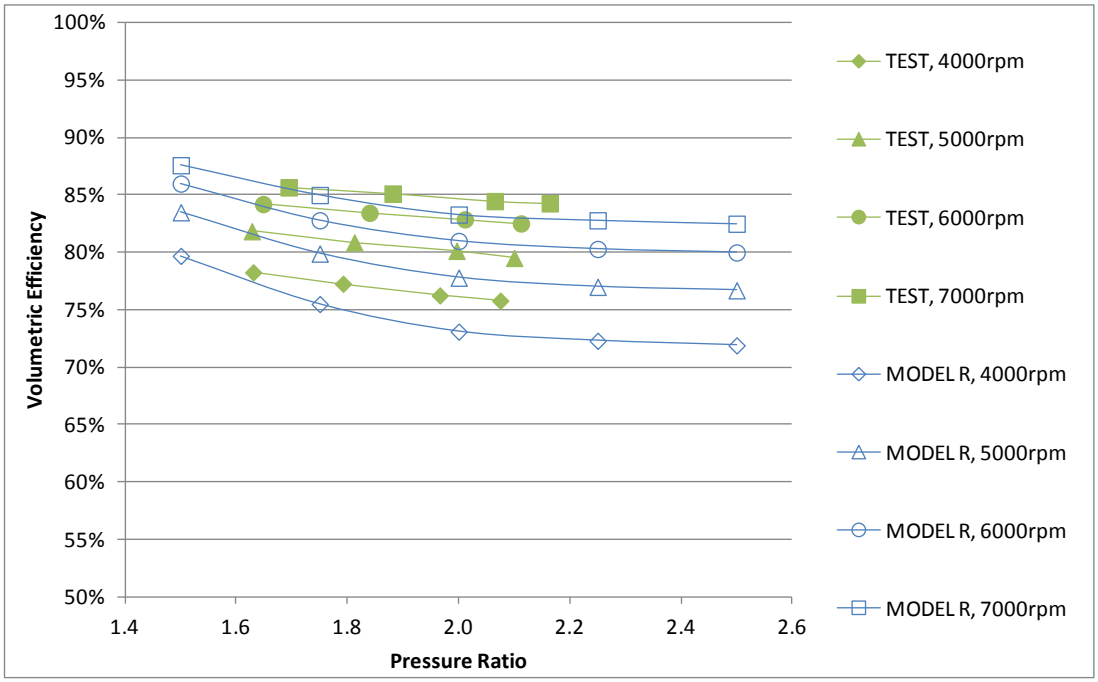

Figure 6-35: HS204 volumetric efficiency with modelled rotor thermal distortion

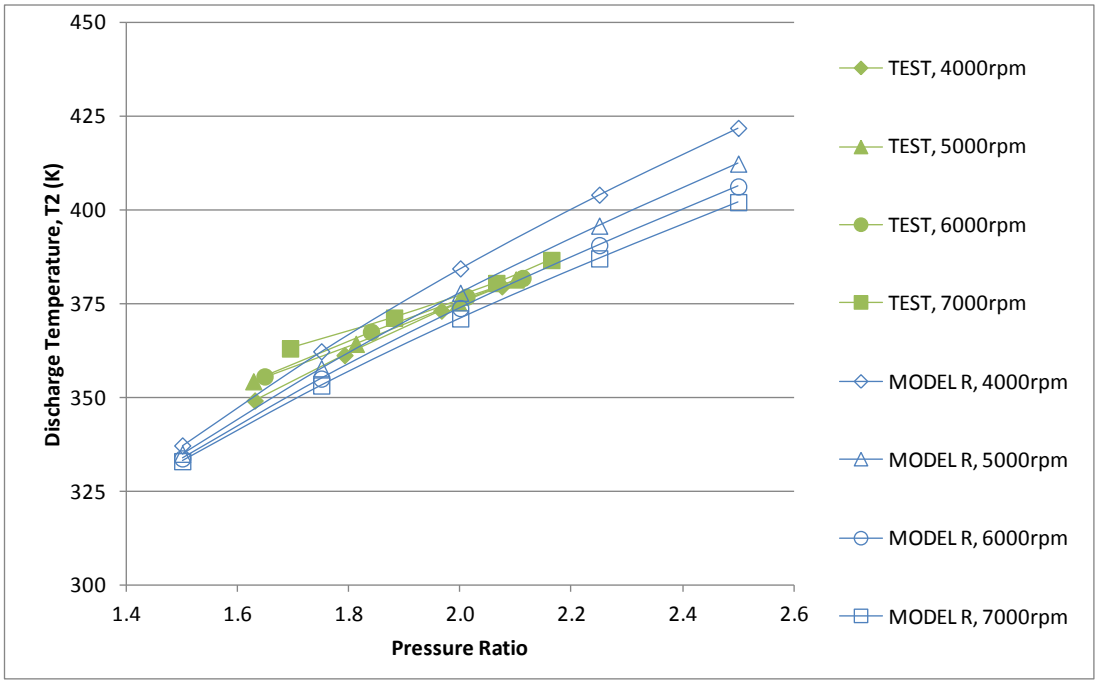

Figure 6-36: HS204 discharge temperature with modelled rotor thermal distortion

Table 6-25: HS204 model performance results with rotor thermal distortion

Speed (rpm)	Pressure Ratio	Volumetric efficiency	*Relative Error*	T2 (K)	*Relative Error*
4000	1.50	79.7%	*0.9%*	337.2	*-1.0%*
	1.75	75.5%	*-2.6%*	362.3	*1.2%*
	2.00	73.1%	*-4.0%*	384.5	*2.5%*
	2.25	72.3%	*-3.3%*	404.1	*3.0%*
	2.50	71.9%	*-2.0%*	422.0	*3.1%*
5000	1.50	83.5%	*1.3%*	335.0	*-3.4%*
	1.75	79.9%	*-1.6%*	357.8	*-0.9%*
	2.00	77.8%	*-2.8%*	377.9	*0.6%*
	2.25	77.0%	*-2.3%*	395.9	*1.5%*
	2.50	76.7%	*-1.2%*	412.5	*1.9%*
6000	1.50	86.0%	*1.5%*	333.7	*-4.0%*
	1.75	82.8%	*-1.2%*	355.0	*-1.9%*
	2.00	81.0%	*-2.3%*	373.9	*-0.6%*
	2.25	80.3%	*-2.1%*	390.7	*0.1%*
	2.50	80.0%	*-1.4%*	406.3	*0.5%*
7000	1.50	87.6%	*1.5%*	333.0	*-5.6%*
	1.75	85.0%	*-0.6%*	353.2	*-3.3%*
	2.00	83.3%	*-1.7%*	371.1	*-1.8%*
	2.25	82.8%	*-1.4%*	387.1	*-0.8%*
	2.50	82.5%	*-0.9%*	402.2	*-0.2%*
		average relative error:	*-1.3%*		*-0.5%*
		maximum relative error:	*-4.0%*		*-5.6%*

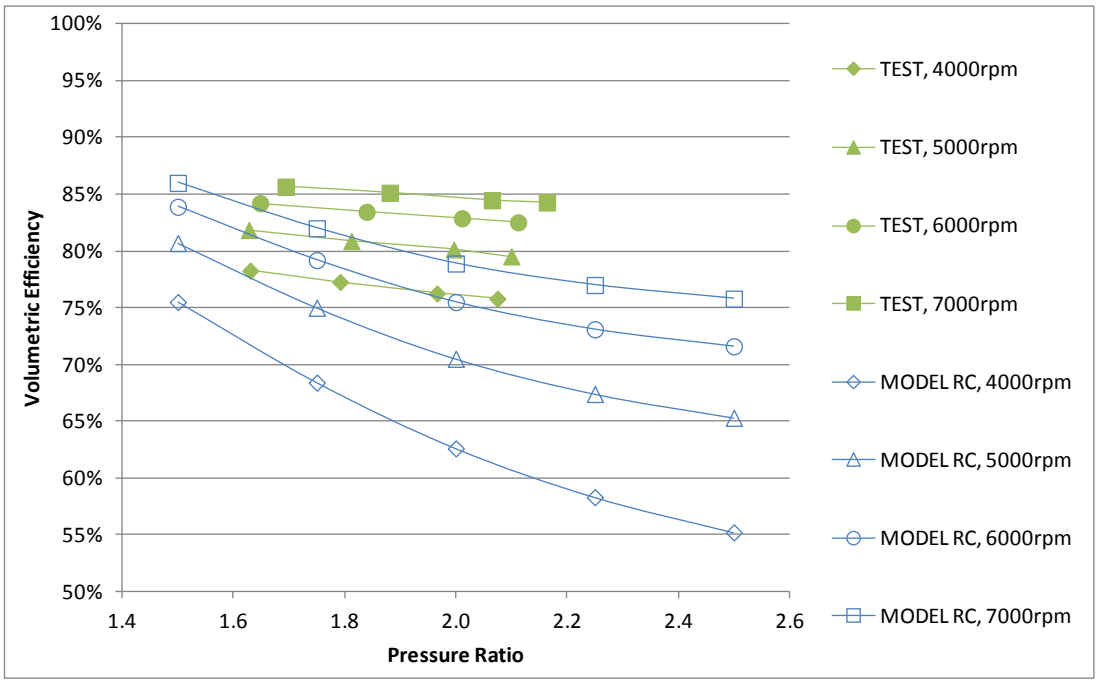

Figure 6-37: HS204 volumetric efficiency with modelled rotor and casing thermal distortion

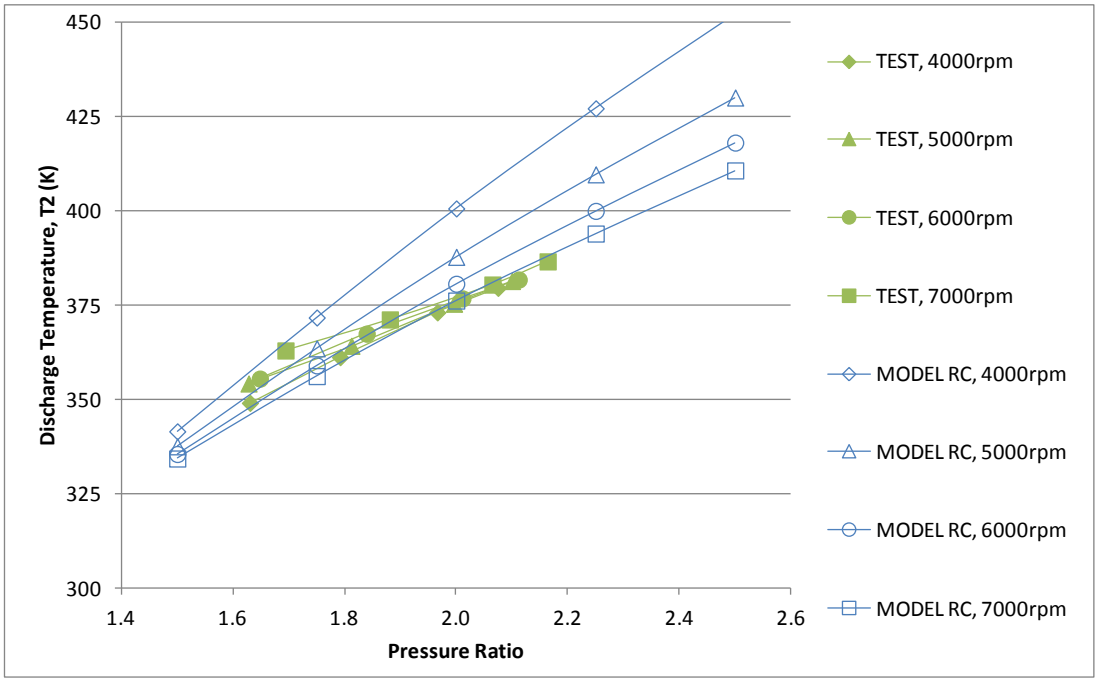

Figure 6-38: HS204 discharge temperature with rotor and casing thermal distortion

Table 6-26: HS204 model performance results with rotor and casing thermal distortion

Speed (rpm)	Pressure Ratio	Volumetric efficiency	*Relative Error*	T2 (K)	*Relative Error*
4000	1.50	75.5%	*-4.4%*	341.6	*0.3%*
	1.75	68.4%	*-11.8%*	371.8	*3.9%*
	2.00	62.6%	*-17.8%*	400.8	*6.8%*
	2.25	58.3%	*-22.0%*	427.3	*8.9%*
	2.50	55.2%	*-24.7%*	452.2	*10.4%*
5000	1.50	80.7%	*-2.1%*	337.7	*-2.6%*
	1.75	75.0%	*-7.7%*	363.7	*0.7%*
	2.00	70.5%	*-11.9%*	387.9	*3.3%*
	2.25	67.4%	*-14.5%*	409.8	*5.0%*
	2.50	65.3%	*-15.9%*	430.2	*6.3%*
6000	1.50	83.9%	*-1.0%*	335.6	*-3.5%*
	1.75	79.2%	*-5.5%*	359.1	*-0.7%*
	2.00	75.5%	*-8.9%*	380.8	*1.3%*
	2.25	73.1%	*-10.9%*	400.1	*2.5%*
	2.50	71.6%	*-11.7%*	418.2	*3.4%*
7000	1.50	86.0%	*-0.3%*	334.4	*-5.2%*
	1.75	82.0%	*-4.1%*	356.3	*-2.5%*
	2.00	78.9%	*-6.9%*	376.3	*-0.4%*
	2.25	77.0%	*-8.3%*	394.1	*1.0%*
	2.50	75.8%	*-8.9%*	410.8	*2.0%*
		average relative error:	*-10.0%*		*2.0%*
		maximum relative error:	*-24.7%*		*10.4%*

6.5.5 HS204 Performance Results Without Jacket Cooling

Additional tests were performed to investigate the effect of the casing water cooling jacket on the compressor performance. This repeat testing did not cover all of the original test points and therefore only results at 6000rpm are presented.

In Table 6-27 the test results with and without jacket cooling are summarised and as before these have been adjusted, through linear interpolation, to produce the results in Table 6-28 at specific pressure ratios.

Table 6-27: HS204 performance test results at 6000rpm with and without jacket cooling

Test	Pressure Ratio	Volumetric efficiency	T2 (K)
jacket cooling	1.65	84.2%	355.6
	1.84	83.4%	367.5
	2.01	82.9%	376.9
	2.11	82.5%	381.9
no jacket cooling	1.57	78.4%	355.6
	1.80	77.5%	365.3
	2.09	76.2%	385.1
	2.60	73.8%	412.1

Table 6-28: HS204 interpolated performance test results at 6000rpm with and without jacket cooling

Test	Pressure Ratio	Volumetric efficiency	T2 (K)
jacket cooling	1.50	84.7%	347.7
	1.75	83.8%	361.8
	2.00	82.9%	376.0
	2.25	82.0%	390.2
	2.50	81.1%	404.4
no jacket cooling	1.50	78.8%	350.5
	1.75	77.7%	364.5
	2.00	76.6%	378.5
	2.25	75.4%	392.5
	2.50	74.3%	406.5

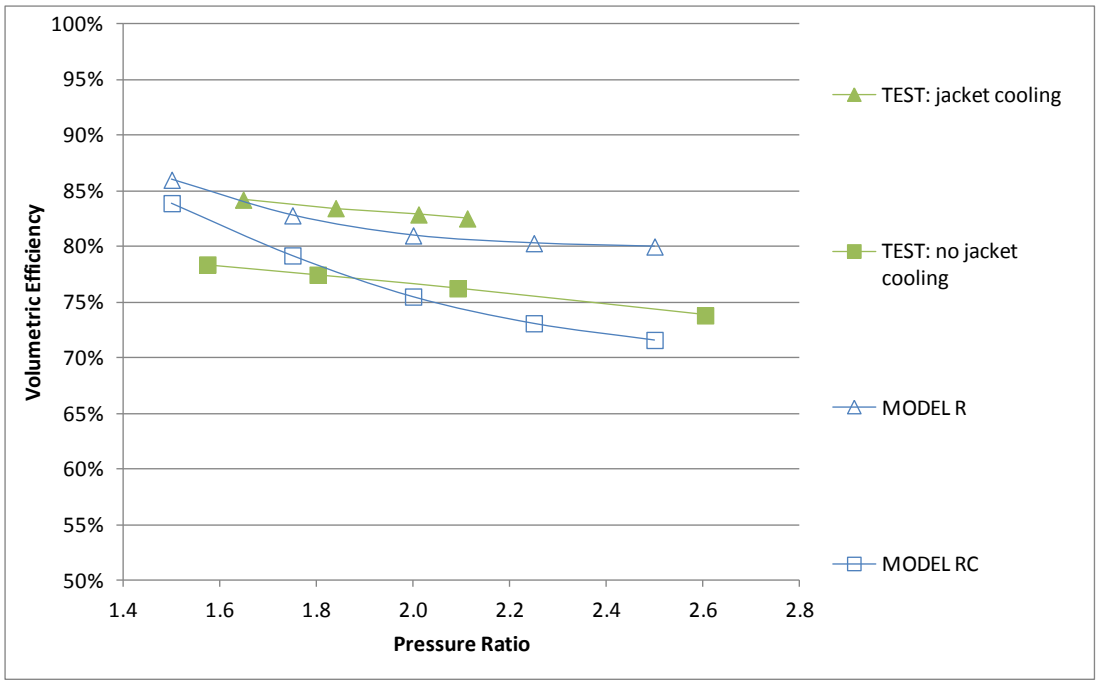

Figure 6-39: HS204 volumetric efficiency at 6000rpm with and without jacket cooling

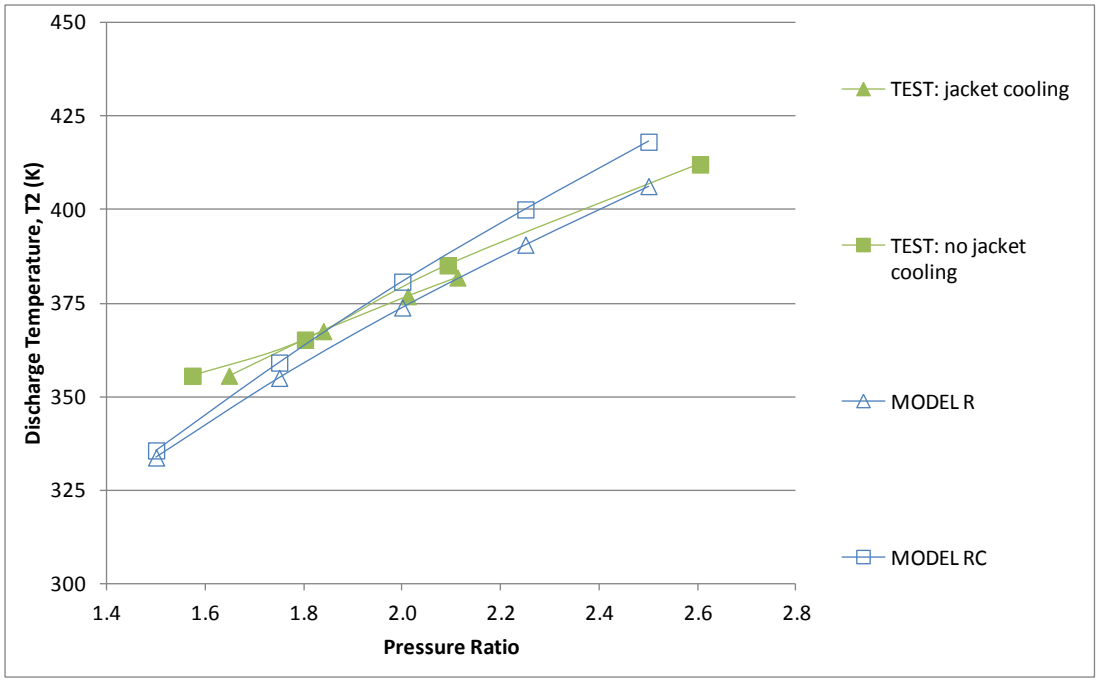

Figure 6-40: HS204 discharge temperature at 6000rpm with and without jacket cooling

The results from MODEL R and MODEL RC are given in Figure 6-39 and Figure 6-40 for testing with and without jacket cooling. MODEL R is more closely aligned to the test results with jacket cooling and MODEL RC is more closely aligned to the test results without jacket cooling. These results are presented in Table 6-29 which compares MODEL R against each test case. Then in Table 6-30, MODEL RC is compared with the same test cases.

Table 6-29: HS204 'MODEL R' performance results at 6000rpm with rotor thermal expansion

Test reference	Pressure Ratio	Volumetric efficiency	*Relative Error*	T2 (K)	*Relative Error*
jacket cooling	1.50	86.0%	*1.5%*	333.7	*-4.0%*
	1.75	82.8%	*-1.2%*	355.0	*-1.9%*
	2.00	81.0%	*-2.3%*	373.9	*-0.6%*
	2.25	80.3%	*-2.1%*	390.7	*0.1%*
	2.50	80.0%	*-1.4%*	406.3	*0.5%*
		average relative error:	*-1.1%*		*-1.2%*
		maximum relative error:	*-2.3%*		*-4.0%*

Test reference	Pressure Ratio	Volumetric efficiency	*Relative Error*	T2 (K)	*Relative Error*
no jacket cooling	1.50	86.0%	*9.2%*	333.7	*-4.8%*
	1.75	82.8%	*6.6%*	355.0	*-2.6%*
	2.00	81.0%	*5.8%*	373.9	*-1.2%*
	2.25	80.3%	*6.4%*	390.7	*-0.5%*
	2.50	80.0%	*7.6%*	406.3	*0.0%*
		average relative error:	*7.1%*		*-1.8%*
		maximum relative error:	*9.2%*		*-4.8%*

Table 6-30: HS204 'MODEL RC' performance results at 6000rpm with rotor and casing thermal expansion

Test reference	Pressure Ratio	Volumetric efficiency	*Relative Error*	T2 (K)	*Relative Error*
jacket cooling	1.50	83.9%	*-1.0%*	335.6	*-3.5%*
	1.75	79.2%	*-5.5%*	359.1	*-0.7%*
	2.00	75.5%	*-8.9%*	380.8	*1.3%*
	2.25	73.1%	*-10.9%*	400.1	*2.5%*
	2.50	71.6%	*-11.7%*	418.2	*3.4%*
		average relative error:	*-7.6%*		*0.6%*
		maximum relative error:	*-11.7%*		*-3.5%*

Test reference	Pressure Ratio	Volumetric efficiency	*Relative Error*	T2 (K)	*Relative Error*
no jacket cooling	1.50	83.9%	*6.5%*	335.6	*-4.2%*
	1.75	79.2%	*2.0%*	359.1	*-1.5%*
	2.00	75.5%	*-1.4%*	380.8	*0.6%*
	2.25	73.1%	*-3.1%*	400.1	*1.9%*
	2.50	71.6%	*-3.7%*	418.2	*2.9%*
		average relative error:	*0.1%*		*-0.1%*
		maximum relative error:	*6.5%*		*-4.2%*

6.5.6 HS204 RADIAL GAP DISTORTION RESULTS

The changes in the radial gap at the location of the proximity probe; as measured on test, and as predicted by the model, are shown in Figure 6-41 and Figure 6-42. For clarity, these have been plotted as the absolute value of the local radial gap. Where there is some uncertainty about the absolute clearance values, as is the case for the test results, this has been set to a nominal gap size of 0.150 mm and then adjusted by the actual measured clearance distortion. It is the degree of operational distortion from this nominal gap at a given operating temperature that is the focus of interest.

The corresponding temperatures, used to calculate the modelled distortions, are given in Figure 6-43 and Figure 6-44. These give some additional insight into the model behaviour. The differences in temperature between the rotor and casing, ΔR and ΔRC for each respective model, are related to the gap distortion as set out in equations (60) to (65) in Chapter 5.

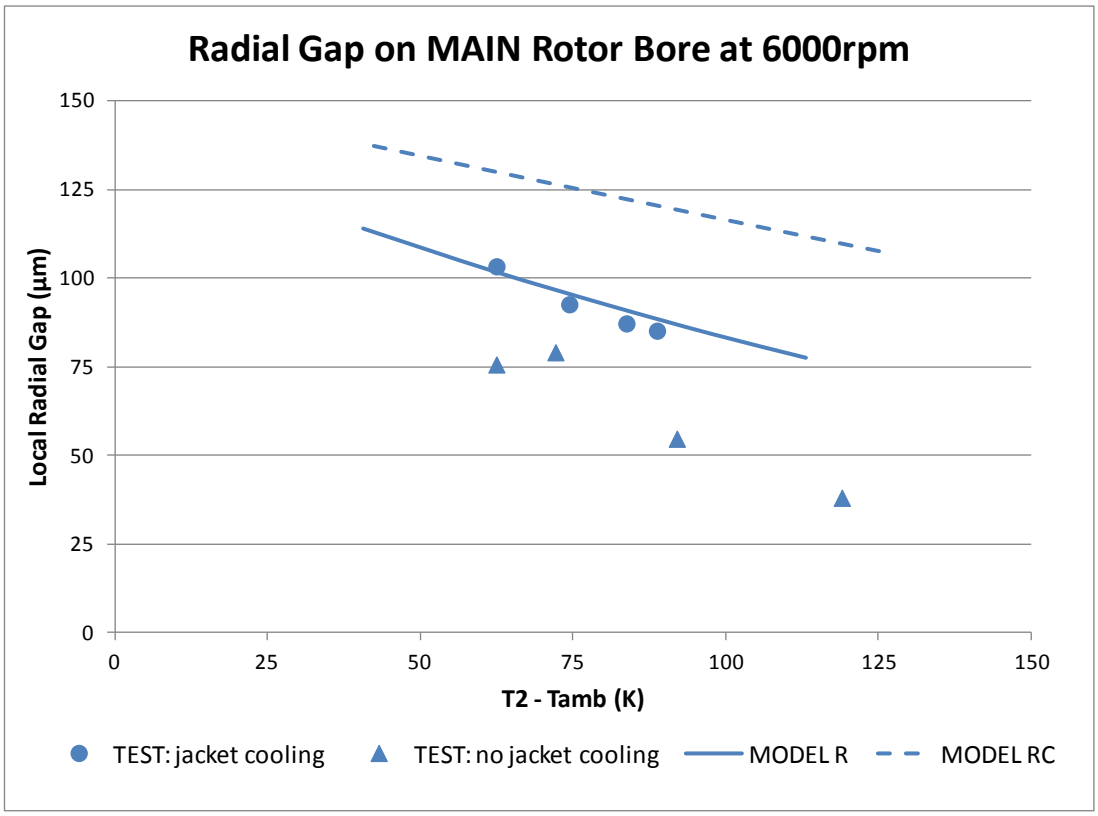

Figure 6-41: Measured and modelled radial gap on MAIN rotor bore

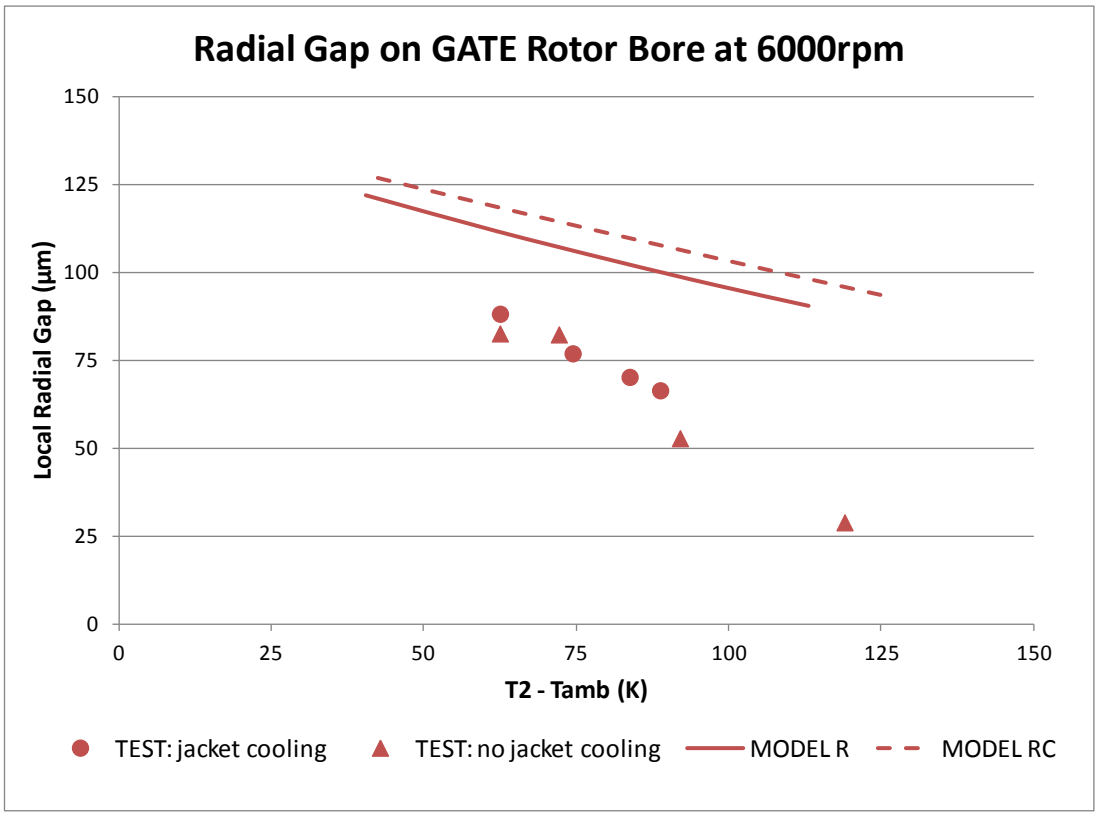

Figure 6-42: Measured and modelled radial gap on GATE rotor bore

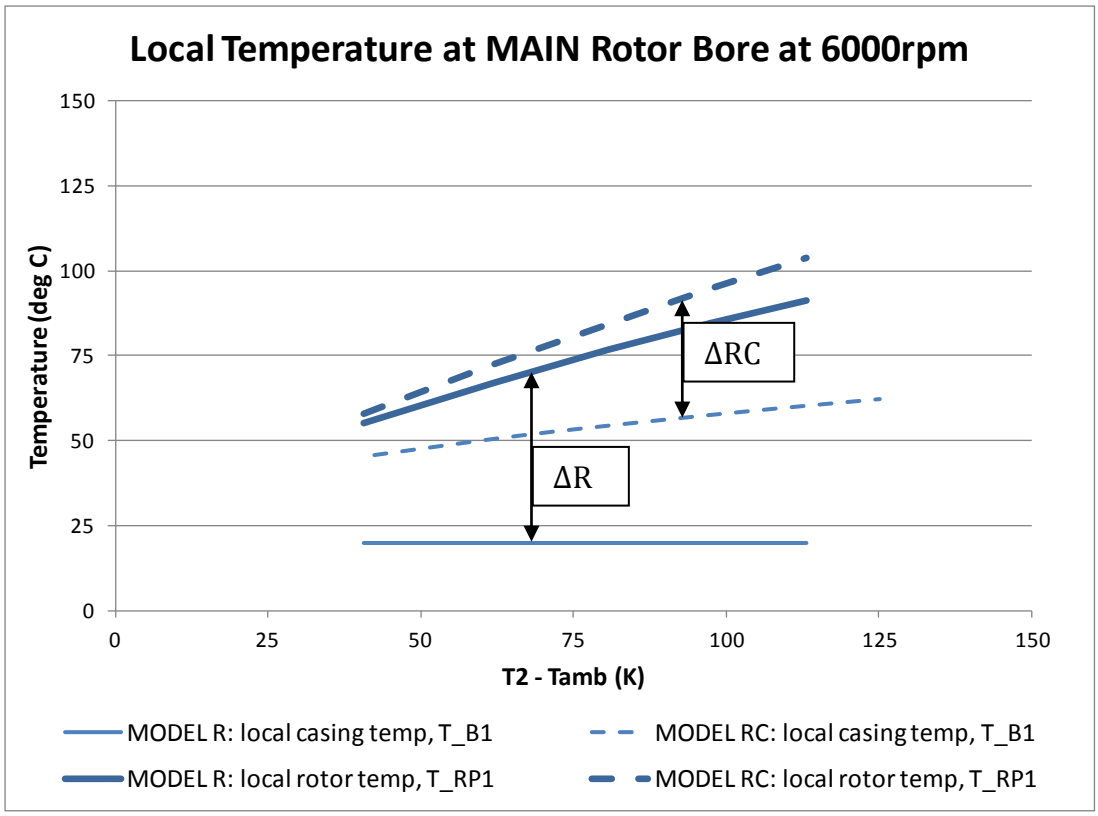

Figure 6-43: Local temperatures at MAIN rotor bore radial gap

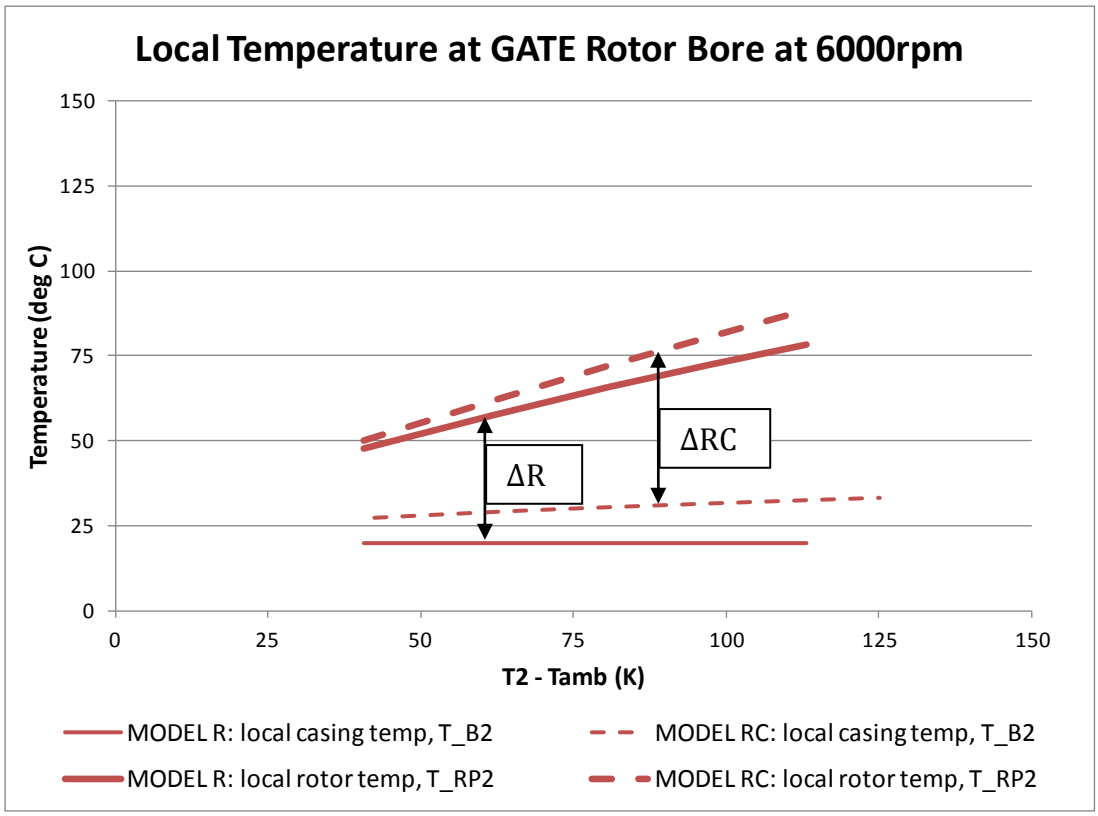

Figure 6-44: Local temperatures at GATE rotor bore radial gap

6.5.7 DISCUSSION

All test results indicate that the volumetric efficiency and temperature vary more or less linearly with the pressure ratio and suggest that there is a limiting volumetric efficiency that will not be exceeded regardless of how low the external pressure ratio is; this is due to the internal compression that occurs within the compressor. In contrast, the model results do show some nonlinearity, particularly at lower pressure ratios where the rate of change in volumetric efficiency is higher. When operating at higher, more realistic pressure ratios for the designed volume index, the model shows a more linear relationship between volumetric efficiency and pressure ratio. The discrepancy at lower pressures merits further investigation and possible refinement to the setup of the chamber model used. However it should not impede the current investigations significantly.

Assuming no heat transfer from the gas to the compressor and surroundings prior to measurement of the outlet temperature, T_2, on test, the adiabatic efficiencies were calculated to range from 70.6% (at the lowest speed and highest pressure ratio) to 83.2% (at the highest speed and lowest pressure ratio). These efficiencies are in the expected range which supports the assumption that heat transfer from the gas can be neglected up to the point of measurement. The same assumption is made in the compressor model to ensure that the temperature comparisons presented are appropriate. More discussion on the calculation of T_2 is included in appendix 'B.1.1 Model Discharge Temperature'. More detail on the measurement of T_2 and how this is used to calculate efficiency is provided in appendix 'C.1 Compressor Boundaries' and 'C.4 Adiabatic Efficiency'.

Initial results with the first model that uses unmodified nominal design clearances (labelled MODEL), underestimate flow and overestimate the discharge temperature. In addition, the range of modelled volumetric efficiency and temperature over both speed and pressure ratio is greater than that measured on test.

The second set of modelled results, with clearances corrected for rotor thermal distortion (MODEL R) show a considerably smaller error against the test results over the full range of operating points.

The third set of modelled results, with clearances corrected for rotor and casing thermal distortion (MODEL RC) show the largest deviations from the test results.

For the results shown in Figure 6-33 to Figure 6-38, where the test compressor casing jacket is water cooled, the most accurate performance predictions were achieved using Model R, based on nominal design clearances that are modified to estimate rotor thermal distortion only. The fact that this model, which resulted in the closest match to the measured flow, shown in Table 6-25, also resulted in the closest match to the measured temperature, provides some validation of the model assumptions.

A comparison of the model predicted results at 6000rpm, with additional test results, with no jacket cooling and the covers for the cooling jacket removed, is given in Figure 6-39 and Figure 6-40. The model predictions that agreed with the test results, with no jacket cooling, most closely, was MODEL RC, which estimated rotor AND casing thermal distortion. This is an important result that further confirms that operational temperature distributions and clearances are indeed changing compressor performance and need to be accounted for during modelling.

Figure 6-41 shows good agreement between the measured radial gap on the MAIN rotor bore when tested with jacket cooling and the MODEL R results. On the GATE rotor bore (Figure 6-42) these results are not as good and the measured radial gap is smaller than predicted by MODEL R. Figure 6-43 and Figure 6-44 help illustrate how the modelled gaps are calculated - the modelled change in radial gap (from the nominal 0.150mm) is proportional to the difference between the rotor and casing temperatures for each respective model. In MODEL R the casing is constant at 20 deg C and the bigger reduction in the main rotor is simply due to that rotor being hotter in the model (based on the transverse plane average temperature). The measured clearances have

actually reduced more on the GATE rotor bore with jacket cooling; it is not possible to say whether this is due to the gate rotor actually being hotter because the actual temperature distribution and distortion of the casing are unknown. Considering the simple nature of the thermal assumptions used in each model, the overall agreement between the jacket cooled radial gap measurements and the MODEL R predictions are fairly reasonable.

For MODEL RC the modelled clearance reduction is less than for MODEL R because the local casing expansion mitigates the local rotor expansion to some extent. This ties in with the modelled performance results as the bigger radial clearances reduce volumetric efficiency. Based on this theory, the hypothesis was that the measured radial gap without jacket cooling would be bigger than with jacket cooling however the results from the proximity probes on the MAIN and GATE rotor bores show the opposite case to be true. This seems to contradict the performance results without jacket cooling which suggest a net clearance increase had occurred. The logical conclusion is that the measured radial clearance reduction is a localised phenomenon.

The simplified thermal analysis, implemented in the model, is useful for capturing net changes in the compressor clearance in order to adjust the predicted performance but it is limited in its ability to predict localised thermal distortions accurately, particularly as a result of casing thermal distributions and distortions. The complexity of this problem is illustrated in Figure 6-45 which was produced using FEA, in an investigation performed by Howden Compressors Ltd (Howden Compressors Ltd. 2013). This was not created within the scope of the current research and is only included to illustrate possible distortion. The casing temperature distribution was predicted, based on boundary temperatures and assumed heat transfer coefficients. The distortions due to thermal expansion and resulting stress distributions were then calculated. The colour contours show the total magnitude of the displacement in any direction, where zero displacement occurs at the compressor feet. The suction side of the casing on the right hand side of the image has actually moved downward slightly. The approximate locations of the rotor body and the proximity probe have been superimposed on to the figure.

With the opposing movement of the bearings at each end and the position of the constraints at the feet of the compressor, it is easier to understand how it could be possible for the local radial gap to be reduced with a hotter casing temperature.

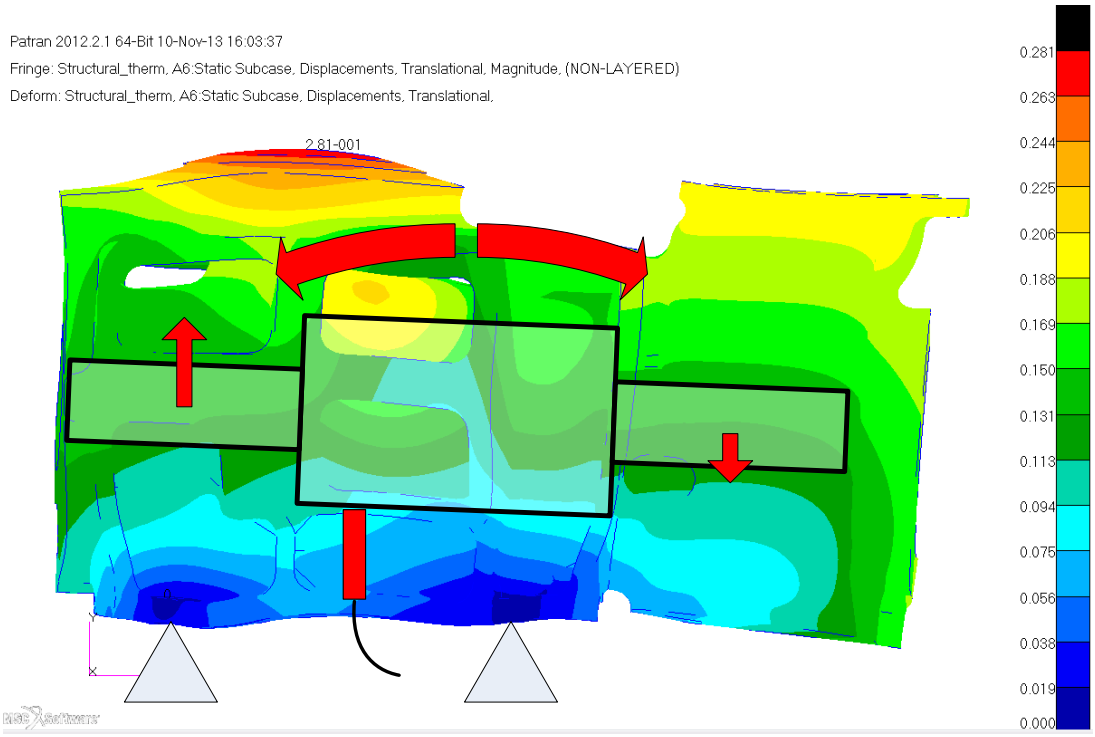

Figure 6-45: Example of overall casing displacement due to thermal loading (courtesy of Howden Compressors Limited.) with approximate rotor body and proximity probe location superimposed

Effectively, the compressor is hotter on top than it is on the bottom due to the location of the high pressure discharge port on top. The temperature difference causes the entire compressor to bow downwards at each end so that the relative position of the proximity probe is higher, resulting in reduced clearance to the rotor. This would be accompanied by a larger than anticipated increase of the radial clearance at the top of the compressor and it is likely that the net radial leakage area does increase, as predicted.

6.6 CONCLUDING REMARKS

The applied routines for mapping boundary conditions from a chamber model onto the compressor rotor and casing surfaces work as expected, with sensibly bounded chambers. When used to update operational clearances and thermodynamic performance, iteratively, a significant change in the net performance was predicted for the DRUM127 compressor. This varied, depending on whether just the rotors, or both the rotors and the casing were distorted. At a minimum, this provides useful details of any modelled uncertainty due to thermal effects. With some additional analyses and understanding of the thermal behaviour of a given compressor this can be used to improve the accuracy of performance predictions without the need to correct operating clearance values manually.

Measuring the change in performance due to predicted change in operational clearances, as was done for the DRUM127 case, is not the ideal way to validate the modelled thermal distortions themselves. Ideally, direct measurements of the operating interlobe gap should be obtained. The fact is that it is very difficult to measure the rotor temperatures directly, let alone the distorted clearance gap, and it was not possible to obtain these results during this study. In the absence of direct operational measurements, the tear down results for the WCVTA510 oil injected case are particularly useful as they show evidence of rotor contact that was predicted by the model. Results suggest that the developed model is a useful tool in the evaluation and design of interlobe clearance distributions for a given operating duty.

In the case of the HS204 oil free case study, in addition to performance results, a direct measurement of the radial gap between the rotors and casing was utilised to assess the model. This showed that while an appropriate thermal distortion model could improve performance results for a specific operating duty and cooling regime, it was not an appropriate tool for detailed thermal analysis of *localised* rotor to casing clearances which are too dependent on the full casing geometry and this is not represented by this model.

Chapter 7
Conclusions and Future Work

7.1 CONCLUSIONS

This research was carried out while working full time in the R&D department at Howden Compressors Ltd; working on various projects but primarily in the design of new retrofit rotors for an existing range of compressors. From this it soon became clear that, from an industrial viewpoint a major problem in optimising performance was to be able to evaluate how internal clearances could be minimised, without the risk of failure as a result of distortion due to thermal effects during operation. A detailed literature survey showed very little published in this area and clearance design was found to be mostly dependent on empirical data and historical experience. It was clear that this was the single most critical area of rotor design and manufacture in terms of performance and reliability. This is particularly true for Howden whose products serve a wide range of applications and operating duties.

A validated procedure has therefore been developed whereby a chamber model has been adapted to predict and correct for duty dependant thermal effects. This can readily be applied to the design and optimisation of twin screw compressors for specific applications.

In the case studies reviewed, the inclusion of thermal clearance corrections generally improved the accuracy of the model when compared with test results. However, it has been shown from the oil free case studies that the most applicable type of clearance corrections, i.e. whether only rotor thermal distortions or rotor and casing distortions are used, is dependent on the compressor configuration such as whether the casing is cooled. This shows that while this approach can improve model performance there is not a universal setup that works for all compressor types.

Case studies show that this work is useful and applicable in the design and review of *interlobe* clearance distributions for specific applications; in terms of

predicting the likelihood of rotor to rotor contact; and predicting where contact is most likely to occur. Mapping thermodynamic results from the chamber model on to the rotor geometry has provided useful insight into rotor temperature exposure, how this varies between the main and gate rotors, and how it's affected by other rotor parameters. Wrap angle and lobe combination are two examples of parameters that have been shown to change rotor temperature exposure. Calculated *local* rotor temperature exposure was used in an analytical clearance correction procedure which was shown to predict the same interlobe clearance behaviour evident from tear down inspection of an oil injected compressor.

Investigation of *localised* radial clearances did however highlight the limited applicability of these procedures to detailed analysis of rotor to casing clearances. Without a cooling jacket, the predicted change in the radial gap due to thermal distortion was different to the measured change in the gap. While the thermal model used can predict general trends in the overall clearance change, as supported by the modelled performance results, it can't adequately capture local distortions on the compressor casing which are dependent on the full casing geometry and temperature distribution.

A useful outcome of developing this mapping procedure was the novel Rotor Boundary Map which provides a unique way of visualising and comparing the key geometrical properties of different profiles such as the length of the sealing lines and how the sealing lines are related to the formation of the blow hole leakage area.

7.2 FUTURE WORK

One of the biggest challenges in this work was obtaining results that would provide direct, simple, verification of the basic constituent parts of the model. For example, as well as measuring the radial gap on test and comparing it with the modelled gap, it would ideally be possible to make direct comparisons of the modelled and tested rotor and casing temperatures at this location. As mentioned, there were limitations to this research in the test data that could be obtained. Furthermore, it is a considerable challenge measuring the temperature of the rotor while running and direct measurement is sometimes not possible as in the case of the interlobe gap. Improving test instrumentation for clearance and thermal analysis would be very useful.

In the absence of more extensive test results it would be useful to compare the thermal distortions predicted by this model against FEA results for the same case. Similarly it would be useful to compare the performance sensitivity to clearances against CFD results for the same case.

The developed model would be a useful tool in a more general and comprehensive rotor optimisation and design framework. This would also include rotor profile optimisation. During profile optimisation there is a trade off between features such as interlobe sealing line length and blow-hole area. Better understanding of how the clearance gap along the interlobe sealing line is affected by thermal distortion at a particular operating temperature would be a valuable input to this. Some performance indicators of a given profile such as specific displacement for a given rotor size can contribute to rotor optimisation prior to thermodynamic simulation: similarly there may be potential to evaluate different rotor designs by using the Rotor Boundary Map to review the interaction between the various sealing lines and the blow-hole.

In very high pressure applications rotor movement and deflection will become more significant and may be worth including in duty dependent operational clearance distortions, in the same way that temperature distribution on the rotor and casing surfaces has been utilised in this work. It follows that there is

clear potential to use pressure distribution for a wide range of purposes including rotor optimisation, bearing design, and rotor deflection analysis.

References

AMOSOV, P.E., 1977. *Vintovie kompresornie mashinii – Spravochnik (Screw Compression Machines-Handbook).* Mashinstroienie, Leningrad.

ASTBERG, A., 1984. *US Patent 4435139 'Screw Rotor Machine and Rotor Profile Therefor'.*

BELL, I.H., GROLL, E.A., BRAUN, J.E. and HORTON, W.T., 2012. A computationally efficient hybrid leakage model for modelling leakage in positive displacement compressors, *International Compressor Engineering Confernce at Purdue* 2012, Paper 2038.

BUCKNEY, D., KOVACEVIC, A. and STOSIC, N., 2011. Consideration of Clearances in the Design of Screw Compressor Rotors, *7th International Conference on Compressors and their Systems, London*, 5th - 6th September 2011.

FLEMING, J.S. and TANG, Y., 1995. Analysis of leakage in a twin screw compressor and its application to performance improvement. *Proceedings of the Institution of Mechanical Engineers, Part E: Journal of Process Mechanical Engineering,* **209**, pp. 125-136.

FLEMING, J.S., TANG, Y. and COOK, G., 1998a. The twin helical screw compressor. Part 1: development, applications and competitive position. *Proceedings of the Institution of Mechanical Engineers, Part C: Journal of Mechanical Engineering,* **212**(5), pp. 355-367.

FLEMING, J.S., TANG, Y. and COOK, G., 1998b. The twin helical screw compressor. Part 2: a mathematical model of the working process. *Proceedings of the Institution of Mechanical Engineers, Part C: Journal of Mechanical Engineering,* **212**(5), pp. 369-380.

FLEMING, J.S., YOU, C.X. and TANG, Y., 1994. Rotor tip design in oil injected helical twin screw compressors with respect to viscous friction loss, *INSTITUTION OF MECHANICAL ENGINEERS CONFERENCE PUBLICATIONS* 1994, pp. 115-115.

FUJIWARA, M., MORI, H. and SUWAMA, T., 1974. Prediction of the Oil Free Screw Compressor Performance Using Digital Computer, *International Compressor Engineering Conference at Purdue* 1974, Paper 119.

FUJIWARA, M. and OSADA, Y., 1995. Performance analysis of an oil-injected screw compressor and its application. *International Journal of Refrigeration,* **18**(4), pp. 220-227.

FUJIWARA, M., KASUYA, K., MATSUNAGA, T. and WATANABE, M., 1984. Computer Modeling for Performance Analysis of Rotary Screw Compressor.

Proceedings of the 1984 International Compressor Engineering Conference - At Purdue. 1984, Paper 503, pp. 536-543.

GAO, T.Y., YANG, D.F., CAO, F. and JIAO, J.C., 2011. Temperature and thermodynamic deformation analysis of the rotors on a twin screw multiphase pump with high gas volume fractions. *Applied Physics and Engineering,* **12**(9), pp. 720.

HANJALIC, K. and STOSIC, N., 1997. Development and optimization of screw machines with a simulation model - Part II: thermodynamic performance simulation and design optimization. *Journal of Fluids Engineering, Transactions of the ASME,* **119**(3), pp. 664-670.

HAUSER, J. and BRUMMER, A., 2010. Geometrical abstraction of screw compressors for thermodynamic optimization. *Proceedings of the Institution of Mechanical Engineers, Part C: Journal of Mechanical Engineering Science,* (225), pp. 1399.

HAUSER, J., BRUMMER, A. and KAUDER, K., 2008. Rotor Profile Generation and Optimization of Screw Machines Using NURBS, *International Compressor Engineering Conference at Purdue* 2008, Paper 1861.

HOLMES, C., 1990. *A study of screw compressor rotor geometry leading to a method for inter-lobe clearance measurement*, Huddersfield Polytechnic.

HOLMES, C.S., 2008. Form grinding of precision helical rotors and gears using closed-loop profile control, *10th International Power Transmission and Gearing Conference, presented at - 2007 ASME International Design Engineering Technical Conferences and Computers and Information in Engineering Conference, IDETC/CIE2007, September 4, 2007 - September 7*, American Society of Mechanical Engineers, pp. 775-781.

HOWDEN COMPRESSORS LTD., 2013. *HCLRD0111.* Glasgow, UK: Howden Compressors.

HOWDEN COMPRESSORS LTD., 2008. *Howden Academy: Screw Compressor Selection Aspects.*

HSIAO, H.H., WU, Y.R. and HSIEH, H.C., 2012. Non-Uniform Clearance between Rotor Surfaces and Its Effect on Machine Performance in Twin-Screw Compressors, *International Compressor Engineering Conference at Purdue* 2012, Paper 2193.

HSIEH, S.H., SHIH, Y.C., HSIEH, W., LIN, F.Y. and TSAI, M.J., 2011. Calculation of temperature distributions in the rotors of oil-injected screw compressors. *International Journal of Thermal Sciences,* **50**(7), pp. 1271-1284.

INTERNATIONAL ORGANIZATION FOR STANDARDIZATION, a. ISO 1217:2009 Displacement compressors -- Acceptance tests.

INTERNATIONAL ORGANIZATION FOR STANDARDIZATION, b. *ISO 5167-2:2003 Measurement of fluid flow by means of pressure differential devices inserted in circular cross-section conduits running full -- Part 2: Orifice plates.* International Organization for Standardization;.

KOVACEVIC, A., STOSIC, N. and SMITH, I.K., 2002a. The Influence of Rotor Deflection upon Screw Compressor Performance. *VDI BERICHTE,* **1715**, pp. 17-28.

KOVACEVIC, A., STOSIC, N. and SMITH, I.K., 2002b. Numerical simulation of fluid flow and solid structure in screw compressors, *ASME 2002 International Mechanical Engineering Congress and Exposition, IMECE2002, November 17, 2002 - November 22*, 2002 2002b, American Society of Mechanical Engineers, pp. 409-416.

KOVACEVIC, A., STOSIC, N. and SMITH, I.K., 2003. Three Dimensional Numerical Analysis of Screw Compressor Performance. *Journal of Computer Methods in Applied Mechanics and Engineering,* **3**(2), pp. 259.

KOVACEVIC, A., STOSIC, N., MUJIC, E. and SMITH, I.K., 2006a. Influence of thermal dilation upon design of screw machines. *International Design Conference - Design 2006, Dubrovnik - Croatia,* .

KOVACEVIC, A., STOSIC, N. and SMITH, I.K., 2006b. Numerical simulation of combined screw compressor-expander machines for use in high pressure refrigeration systems. *Simulation Modelling Practice and Theory,* **14**(8), pp. 1143-1154.

LITVIN, F.L. and FUENTES, A., 2004. *Gear Geometry and Applied Theory.* 2nd edn. Cambridge.

MUJIC, E., KOVACEVIC, A., STOSIC, N. and SMITH, I.K., 2010. Advanced Design Environment for Screw Machines, *International Compressor Engineering Conference at Purdue* 2010, Paper 1971.

MUJIC, E., 2009. *A numerical and experimental investigation of pulsation induced noise in screw compressors*, City University London.

NIKOLOV, A. and BRUMMER, A., 2012. Influence of thermal deformation on the characteristic diagram of a screw expander in the automotive application of exhaust heat recovery, *International compressor engineering conference at Purdue* 2012, Paper 2128.

OHAMA, T., KURIOKA, Y. and TANAKA, H., 2006. Process gas applications where API 619 screw compressors replaced reciprocating and centrifugal compressors, *Proceedings of the Thirty-Fifth Turbomachinery Symposium*, 2006 2006.

O'NEILL, P., 1977. The Screw Compressor: A Short History of its Development and its Application to the Fields of Air Conditioning and Mine Cooling, *A paper presented to the symposium 'Latest Concepts in Cooling of Deep Mines'. South Africa*.

O'NEILL, P.A., 1966. *Mechanical Design and Efficiency of Screw Compressors.* Paper presented to the Institute of Mechanical Engineers: .

POWELL, G., WEATHERS, B. and SAULS, J., 2006. Transient Thermal Analysis of Screw Compressors, Part III: Transient Thermal Analysis of a Screw Compressor to Determine Rotor-to-Rotor Clearances, *Proceedings of International compressor Engineering Conference at Purdue* 2006, Paper 1813.

RINDER, L., 1987. *Screw rotor profile and method for generating.* US4643654 A edn. US: .

RINDER, L., 1979. *Schraubenverdichter (Screw Compressors).* New York: Springer Verlag.

SACHS, R., 2002. *Experimental Investigations of Gas Flows in Screw Machines*, University of Dortmund.

SAKUN, I.A., 1960. *Vintovie kompresorii (Screw Compressors).* Mashinostroenie Leningrad: .

SANGFORS, B., 1984. Computer Simulation of the Oil Injected Twin Screw Compressor, *International Compressor Engineering Conference at Purdue* 1984, Paper 502.

SAULS, J., POWELL, G. and WEATHERS, B., 2006a. Transient Thermal Analysis of Screw Compressors, Part I: Use of Thermodynamic Simulation to Determine Boundary Conditions for Finite Element Analyses, *Proceedings of International Compressor Engineering Conference at Purdue* 2006a, Paper 1811.

SAULS, J., 2011. Use of finite element and computational fluid dynamics analysis in the development of positive displacement compressor simulations, *7th International Conference on Compressors and Their Systems 2011, September 5, 2011 - September 6*, 2011 2011, Woodhead Publishing Limited, pp. 5-13.

SAULS, J., 1996. Development of a Comprehensive Thermodynamic Modelling System for Refrigerant Screw Compressors, *Proceedings of International Compressor Engineering Conference at Purdue* 1996, 1098.

SAULS, J. and POWELL, G., Influence of Manufacturing and Operational Effects on Screw Compressor Rotor Pair Clearances, *Tagung Schraubenmaschinen*, October 2010.

SAULS, J., POWELL, G. and WEATHERS, B., 2007. Thermal deformation effects on screw compressor rotor design, *International Conference on Compressors and*

their Systems, September 10, 2007 - September 12, 2007 2007, Chandos Publishing, pp. 159-168.

SAULS, J., POWELL, G. and WEATHERS, B., 2006b. Transient thermal analysis of screw compressors part I - Development of thermal model. *VDI Berichte,* (1932), pp. 19-29.

SAULS, J., POWELL, G. and WEATHERS, B., 2006c. Transient thermal analysis of screw compressors part II - Application. *VDI Berichte,* (1932), pp. 195-204.

SCHIBBYE, L.B., 1979. *US Patent 4140445 'Screw-Rotor Machine with Straight Flank Sections'.*

SESHAIAH, N., GHOSH, S.K., SAHOO, R.K. and SARANGI, S.K., 2007. Mathematical modeling of the working cycle of oil injected rotary twin screw compressor. *Applied Thermal Engineering,* **27**(1), pp. 145-155.

SINGH, P.J., 1990. Exact analytical representation of screw compressor rotor geometry, *International Compressor Engineering Conference at Purdue* 1990, Paper 785.

SINGH, P.J. and BOWMAN, J.L., 1990. 'Calculation of blow-hole area for screw compressors'. *Proceedings of the 1990 International Compressor Engineering Conference,* , pp. 938-938.

SINGH, P.J. and ONUSCHAK, A.D., 1984. Comprehensive, Computerized Method for Twin-Screw Rotor Profile Generation and Analysis. *Proceedings of the 1984 International Compressor Engineering Conference - At Purdue.* 1984, Purdue Univ, Ray W. Herrick Lab, pp. 519-527.

SRM, 1966. *Oil Injected Slide Valve Controlled Refrigeration Compressor K-211 (Howden WRVD 204).* K371129. SRM.

SRM, 1954. *Calculation of the Characteristics of the Screw Compressor .* 839/K-74. SRM.

SRM, 1953. *Calculation of the volume curves of screw compressors.* 892/K-109. SRM.

SRM, 1952. *Standardisation of Rotor Dimensions of 1-Stage Screw Compressor with 4+6 Lobe Combination and Profile According to K.364942.* 887/K-99. SRM.

SRM, 1950. *The temperature of noncooled screw compressor rotors.* 838/K73. SRM.

STOSIC, N., 2001. *US Patent 6296461 B1 'Plural Screw Positive Displacement Machines'.*

STOSIC, N., HANJALIC, K. and KOPRIVICA, J., 1986. A Contribution to the Mathematical Modelling of Screw Compressor Working Processes, *Strojarstvo Journal, Zagreb,* **28**(2), pp. 95-100.

STOSIC, N., MUJIC, E., SMITH, I.K. and KOVACEVIC, A., 2008. Profiling of Screw Compressor Rotors by Use of Direct Digital Simulation, *International Compressor Engineering Conference at Purdue* 2008, Paper 1860.

STOSIC, N., SMITH, I.K. and KOVACEVIC, A., 2005. *Screw Compressors: Mathematical Modelling and Performance Calculation.* UK: Springer.

STOSIC, N., SMITH, I.K. and KOVACEVIC, A., 2003. Optimisation of screw compressors. *Applied Thermal Engineering,* **23**(10), pp. 1177-1195.

STOSIC, N., SMITH, I.K., KOVACEVIC, A. and MUJIC, E., 2010. Three decades of modern practise in screw compressors, *International Engineering Compresssor Conference* 2010, Paper 1942.

STOSIC, N., 1998. On gearing of helical screw compressor rotors. *Proceedings of the Institution of Mechanical Engineers, Part C: Journal of Mechanical Engineering,* **212**(7), pp. 587-594.

STOSIC, N. and HANJALIC, K., 1997. Development and optimization of screw machines with a simulation model - Part 1: profile generation. *Journal of Fluids Engineering, Transactions of the ASME,* **119**(3), pp. 659-663.

STOSIC, N., SMITH, I. and KOVACEVIC, A., 2003. Rotor interference as a criterion for screw compressor design. *Journal of Engineering Design,* **14**(2), pp. 209.

STOSIC, N., 2005. Identification of constraints in the optimal generation of screw compressor rotors by the pressure angle method, *, September 4, 2005 - September 7*, 2005 2005, John Wiley and Sons Inc, pp. 33-42.

STOSIC, N., 2015. On heat transfer in screw compressors*, International Journal of Heat and Fluid Flow*, **51**, pp. 285-297.

SUNDT, C.V., 1997. *Method and apparatus for generating profiles of cooperating screw rotors.* US5608648 A edn. US: .

TANG, Y., 1995. *Computer aided design of twin screw compressors*, University of Strathclyde.

TANG, Y. and FLEMING, J.S., 1992. Obtaining the optimum geometrical parameters of a refrigeration helical screw compressor, *Proceedings of the International Compressor Engineering Conference, Purdue, USA* 1992, pp. 221-227.

TANG, Y. and FLEMING, J.S., 1994. Clearances between the rotors of helical screw compressors: their determination, optimization and thermodynamic

consequences. *Proceedings of the Institution of Mechanical Engineers, Part E: Journal of Process Mechanical Engineering,* **208**, pp. 155-170.

WEATHERS, B., SAULS, J. and POWELL, G., 2006. Transient Thermal Analysis of Screw Compressors, Part II: Transient Thermal Analysis of a Screw Compressor to Determine Rotor-to-Housing Clearances, *Proceedings of International Compressor Engineering Conference at Purdue* 2006, Paper 1812.

WEISSTEIN, E.W., , "Epitrochoid." From *MathWorld*--A Wolfram Web Resource. Available: http://mathworld.wolfram.com/Epitrochoid.html2015].

WILLIAMS, T., KELLEY, C. and 'MANY OTHERS', 2013-last update, Gnuplot 4.6: an interactive plotting program. Available: www.gnuplot.info/.

WU, Y., 1995. *Novel Design Methods of Rotor and Cutter Profiles for the Twin-Screw Compressor*, National Chung-Cheng University, Chia-Yi, Taiwan.

WU, Y. and FONG, Z., 2009. Optimization design of an explicitly defined rack for the generation of rotors for twin-screw compressors. *Mechanism and Machine Theory,* **44**(1), pp. 66-82.

ZAYTSEV, D. and INFANTE FERREIRA, C.A., 2005. Profile generation method for twin screw compressor rotors based on the meshing line. *International Journal of Refrigeration,* **28**(5), pp. 744-755.

Appendix A
Geometry Calculations

A.1 Basic Geometry and Terminology

There are a number of general rotor profile features that are common for all twin screw compressor rotors. The rotor pair always comprises of a main and a gate rotor. The main rotor has a smaller number of lobes than the gate resulting in a gear ratio that reduces the speed of rotation of the gate. Despite having fewer teeth the main rotor is often close or equal to the gate rotor in diameter, this is because the main rotor has protruding rounded lobes which mesh with scalloped recesses in the gate rotor known as flutes. This arrangement results in rotors with an interlobe sealing line that extends most of the way between the two cusps on the casing thus reducing the leakage area between the rotors and the casing.

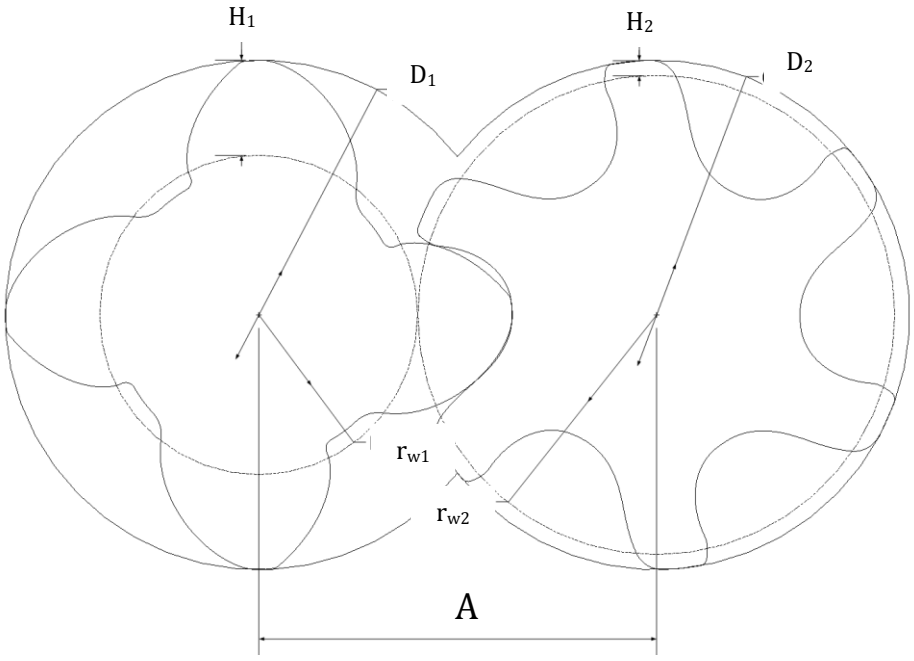

Figure A-1: Basic rotor dimensions

Figure A-1: Basic rotor dimensions, shows the cross section of a 4-6 rotor combination in the transverse plane (perpendicular to the rotor axis).

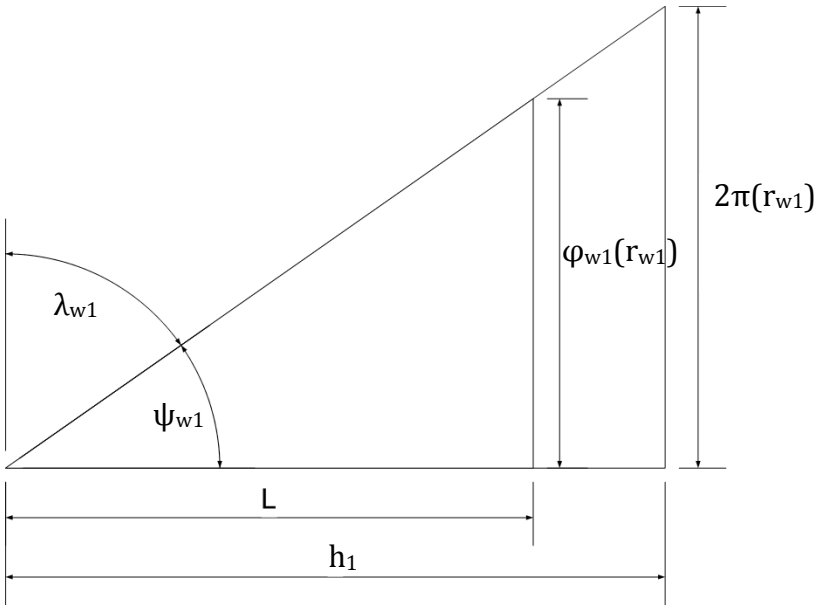

Figure A-2: Helix angle calculation

The relationship between the main pitch radius, r_{w1}, and the helix angle at this particular radius is described geometrically in Figure A-2 which is a triangle of the unwrapped helix where the horizontal line is parallel with the rotor axis. In this figure the larger of the similar triangles represents the helix for a full 360°, the parameter h is known as the 'lead length'. The smaller triangle is truncated to the actual rotor length, L. The parameter φ_{w1} is the wrap angle and is proportional to the rotor length for a given helix angle, ψ. The lead angle, λ, is defined as the complement of the helix angle. The wrap angle is typically about 300° for the main rotor but can vary. The helix angle defined at the pitch point is common for the main and gate rotors so that $\psi_{w1} = \psi_{w2}$. The actual rotor length is usually defined by the ratio L/D and similarly the main addendum and dedendum are sometimes defined as a proportion of the rotor diameter, D, this makes for easier scaling of rotors and provides a more intuitive feel for how the parameters affect the profile geometry. The following equations are commonly used in rotor geometry calculations:

Pitch circles:

$$r_{w1} = A\left(\frac{z_1}{z_1 + z_2}\right) \qquad (1)$$

$$r_{w2} = A\left(\frac{z_2}{z_1 + z_2}\right) \quad (2)$$

The gate rotor wrap angle is:

$$\varphi_2 = \varphi_1\left(\frac{z_1}{z_2}\right) \quad (3)$$

The L/D is defined for the main rotor therefore the main rotor outer diameter is used to find the length:

$$L = D_1('L/D') \quad (4)$$

Rotor lead lengths:

$$h_1 = L\left(\frac{2\pi}{\varphi_1}\right) \quad (5)$$

$$h_2 = L\left(\frac{2\pi}{\varphi_2}\right) \quad (6)$$

The lead per unit angle (usually degrees) for the main and gate rotors are:

$$p_1 = \frac{h_1}{360} \quad (7)$$

$$p_2 = \frac{h_2}{360} \quad (8)$$

Rotor helix angle at pitch radius (common for both rotors):

$$\psi_w = \tan^{-1}\left(\frac{2\pi r_{w1}}{h_1}\right) \quad (9)$$

Lead angle at pitch radius (common for both rotors):

$$\lambda_w = \frac{\pi}{2} - \psi_w \quad (10)$$

The lobe offset angles are useful for adjusting the rotor profiles therefore these are defined:

$$\theta_{z1} = \frac{2\pi}{z_1} \quad (11)$$

$$\theta_{z2} = \frac{2\pi}{z_2} \qquad (12)$$

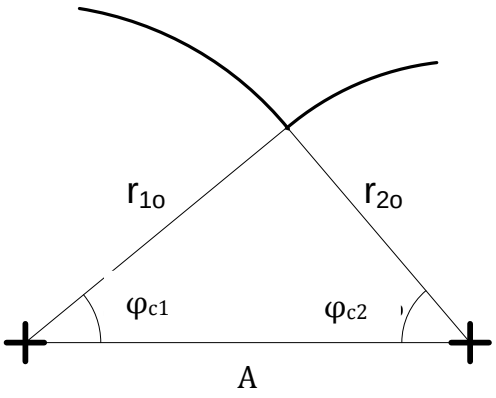

Figure A-3: Angles to casing cusp

The position of the casing cusp (neglecting clearances) is calculated using the outer radii of each rotor and the rotor centre distance by applying the Cosine Rule (see Figure A-3: Angles to casing cusp):

$$\varphi_{c1} = cos^{-1}\left(\frac{r_{o1}^2 + A^2 - r_{o2}^2}{2r_{o1}A}\right) \qquad (13)$$

$$\varphi_{c2} = cos^{-1}\left(\frac{r_{o2}^2 + A^2 - r_{o1}^2}{2r_{o2}A}\right) \qquad (14)$$

The Cartesian cusp co-ordinates can thus be calculated:

$$x_{c1} = r_{o1}\cos(\varphi_{c1}) \qquad (15)$$

$$y_{c1} = r_{o1}\sin(\varphi_{c1}) \qquad (16)$$

These cusp angles define the limiting values for the parameter β that describes the angular position on the casing bore surfaces:

$$\varphi_{c1} \leq \beta_1 \leq (2\pi - \varphi_{c1}) \qquad (17)$$

$$\varphi_{c2} \leq \beta_2 \leq (2\pi - \varphi_{c2}) \qquad (18)$$

A.2 MESHING CONDITIONS FOR CONJUGATE PROFILE

For an effective positive displacement machine the main and gate rotors must mesh to form a continuous seal along the full length of the rotors at all times. This requires that the gate rotor is conjugate to the main rotor so that the rotors mesh with continuous line contact (if zero clearance) between the rotors. This conjugate condition can be used to calculate the sealing line co-ordinates.

Note that when there is interlobe clearance between the rotors and other geometrical features such as sealing strips are present the actual rotors are not necessarily an exact conjugate pair and calculating the sealing line in this way can potentially introduce errors.

The meshing angle, θ_m, for a given point, n, is defined as the angle through which the main rotor must be rotated so that meshing line contact occurs at that point. The follow steps describe how this meshing angle is calculated.

Pressure angle, ψ_{01}

The pressure angle defined on the local rotor co-ordinate system is calculated as the inverse tan of the main rotor surface normal:

$$\psi_{01} = \tan^{-1}\left(-\frac{dx_{01}}{dy_{01}}\right) \qquad (19)$$

As the gradient of the surface normal does not give the direction of the transverse surface vector the angle, ψ_{01}, must be corrected based on the quadrant in which the point lies and the known orientation of the main rotor co-ordinates.

Profile angle, φ_{01}

The local profile angle is the polar angle, φ_{01}, calculated from the Cartesian rotor co-ordinates, x_{01} and y_{01}.

Meshing angle, θ_m

The meshing angle, θ_m, is defined in Figure A-4 as the angle of rotation of the local profile co-ordinate system, $x_{01}y_{01}$, measured relative to a static co-ordinate system, X_1Y_1. The angles φ_{01} and ψ_{01} are defined relative to the local profile system, $x_{01}y_{01}$. For conjugate meshing, the line of pressure (normal to the rotor surface) at the meshing point, M, will always intersect the pitch point, P. Thus, the meshing angle, θ_m, can be defined geometrically. This meshing angle is the same whether the main rotor profile shown is meshing with a rack or any gate rotor defined on this transverse plane.

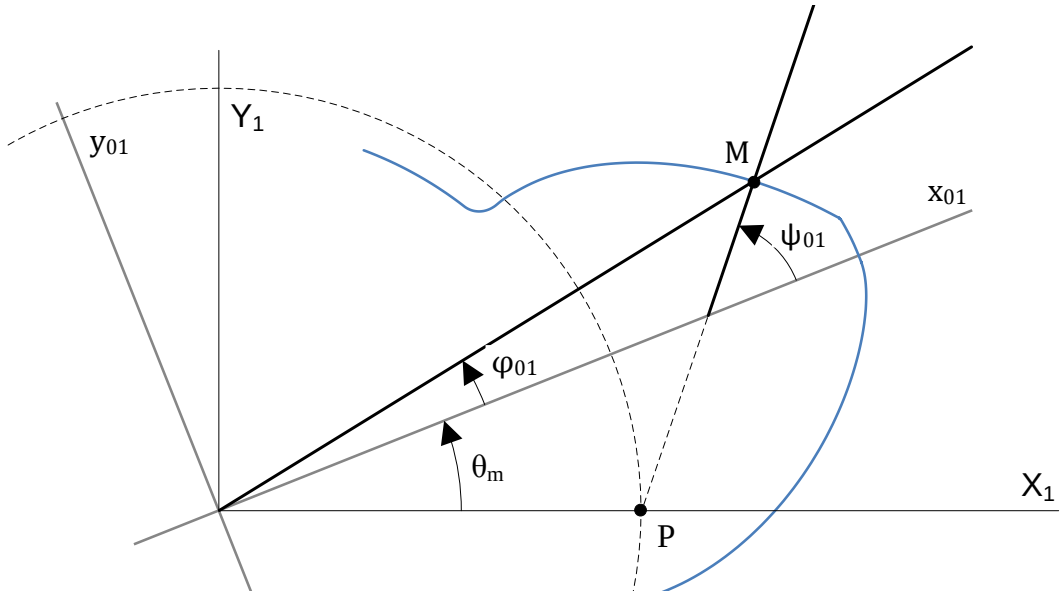

Figure A-4: Meshing condition

In Figure A-5, two right angle triangles are defined, the angles identified can be related to the common opposite length, a, as given in equation (20).

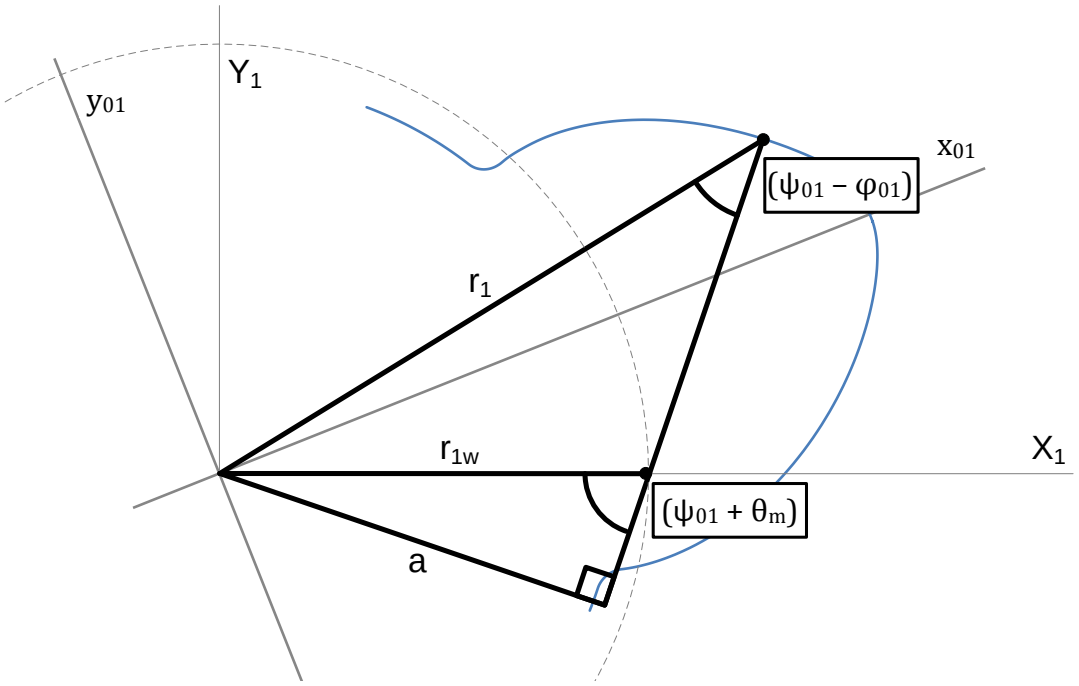

Figure A-5: Solving for meshing angle

$$a = r_1 sin(\psi_{01} - \varphi_{01}) = r_{1w} sin(\psi_{01} + \theta_m) \quad (20)$$

After rearranging this is an explicit equation that is used to calculate the meshing angle at each point.

$$\theta_m = sin^{-1}\left(\left(\frac{r_1}{r_{1w}}\right) sin(\psi_{01} - \varphi_{01})\right) - \psi_{01} \quad (21)$$

Interlobe sealing line co-ordinates

The x and y sealing line co-ordinates are found by rotating each co-ordinate on the main rotor by its respective meshing angle:

$$x_{SL} = x_{01} cos(\theta_m) - y_{01} sin(\theta_m) \quad (22)$$

$$y_{SL} = x_{01} sin(\theta_m) + y_{01} cos(\theta_m) \quad (23)$$

The axial co-ordinate, z, is directly related to the meshing angle using the unit lead, p:

$$z_{SL} = p_1 \theta_m \quad (24)$$

The sealing line co-ordinates x_{SL}, y_{SL}, z_{SL} can be calculated for a number of discrete points around the rotors in order to generate the full interlobe sealing line as presented in Figure A-6; the interlobe sealing has been superimposed onto the main rotor body.

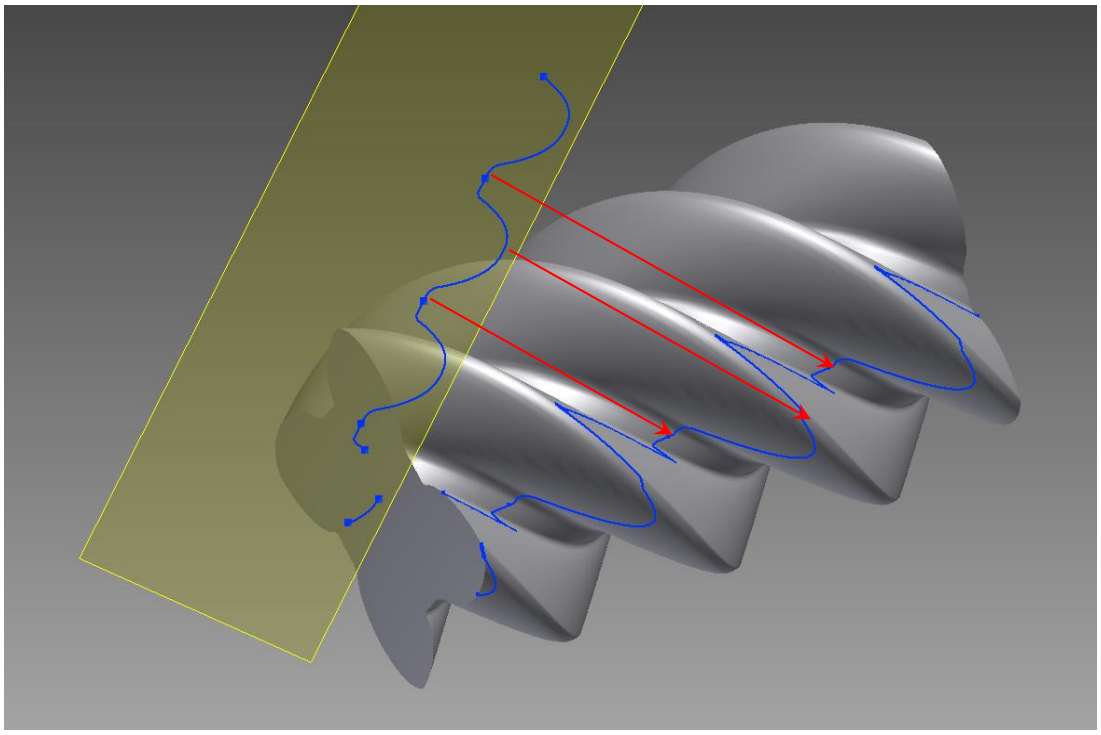

Figure A-6: Interlobe sealing line and normal projection

The interlobe sealing line follows a complex 3D path and it is commonly presented using axial or 'side-on' 2D projections. Figure A-6 shows that when projected onto a 'normal' plane (offset from the transverse plane by ψ_w) the 'normal' rack is generated. When viewing a meshed rotor pair from this orientation the entire sealing line, and consequently the clearance gap between the rotors, can be viewed by shining a light between the rotors.

A.3 CALCULATING GEOMETRY CHARACTERISTICS

A.3.1 CHAMBER AREA AND VOLUME

Chamber cross-sectional areas are initially formed between the two rotors and then between each rotor and the casing before finally reducing between the rotors again. The biggest challenge to develop an area calculation procedure is therefore in identifying the correct area boundaries for each rotor position. This problem is exacerbated by the fact that the rotors and casing never actually come into contact. A numerical approach using a trapezoidal rule has been adopted for robust area calculation with all profile types (Mujic 2009). The cross section is divided into a number of divisions along the radius for each respective rotor as shown in Figure A-7.

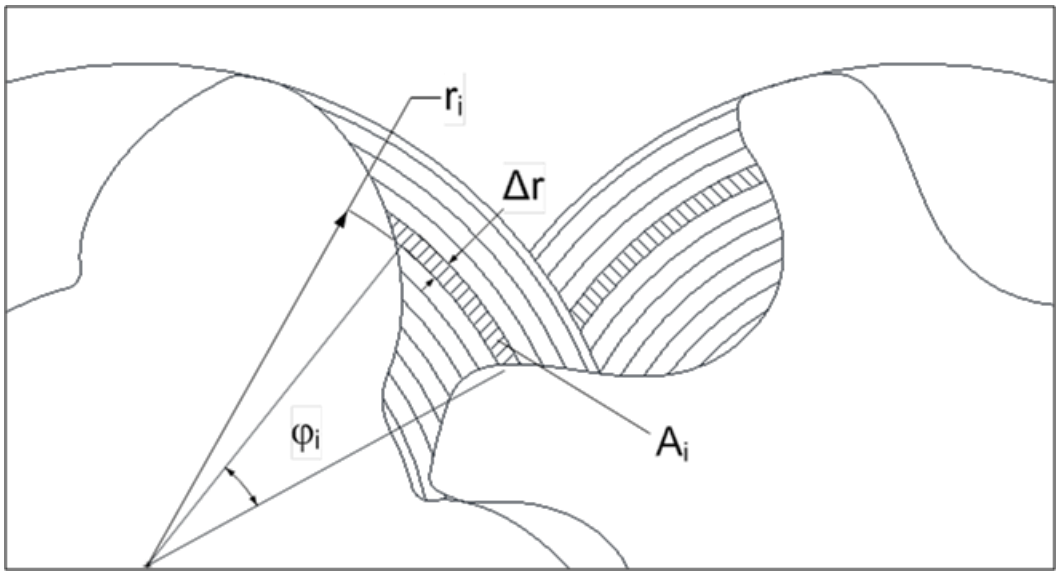

Figure A-7: Cross sectional area calculation using trapezoidal rule

The maximum theoretical chamber volume is achieved when the both the main and gate cross sectional areas are fully formed. In this case the volume is the sum of the cross sectional area multiplied by the rotor length. In practise, the chamber cross section is not always fully formed along the full length of the rotor and the maximum volume is therefore reduced. For this reason it is far more reliable to determine the volume curve by integrating the area curve between limits that are defined by the cycle angle. This is described by equation (25) with the limits of integration shown in Figure A-8. This figure includes a

representation of the rotors in an attempt to show, in what is hopefully a more intuitive way, how the 'volume' in the rotor chambers corresponds to the 'volume' under the area curve.

$$V(\theta) = \frac{dz}{d\theta}\int_{a(\theta)}^{b(\theta)} A(\theta)\, d\theta \qquad \textbf{(25)}$$

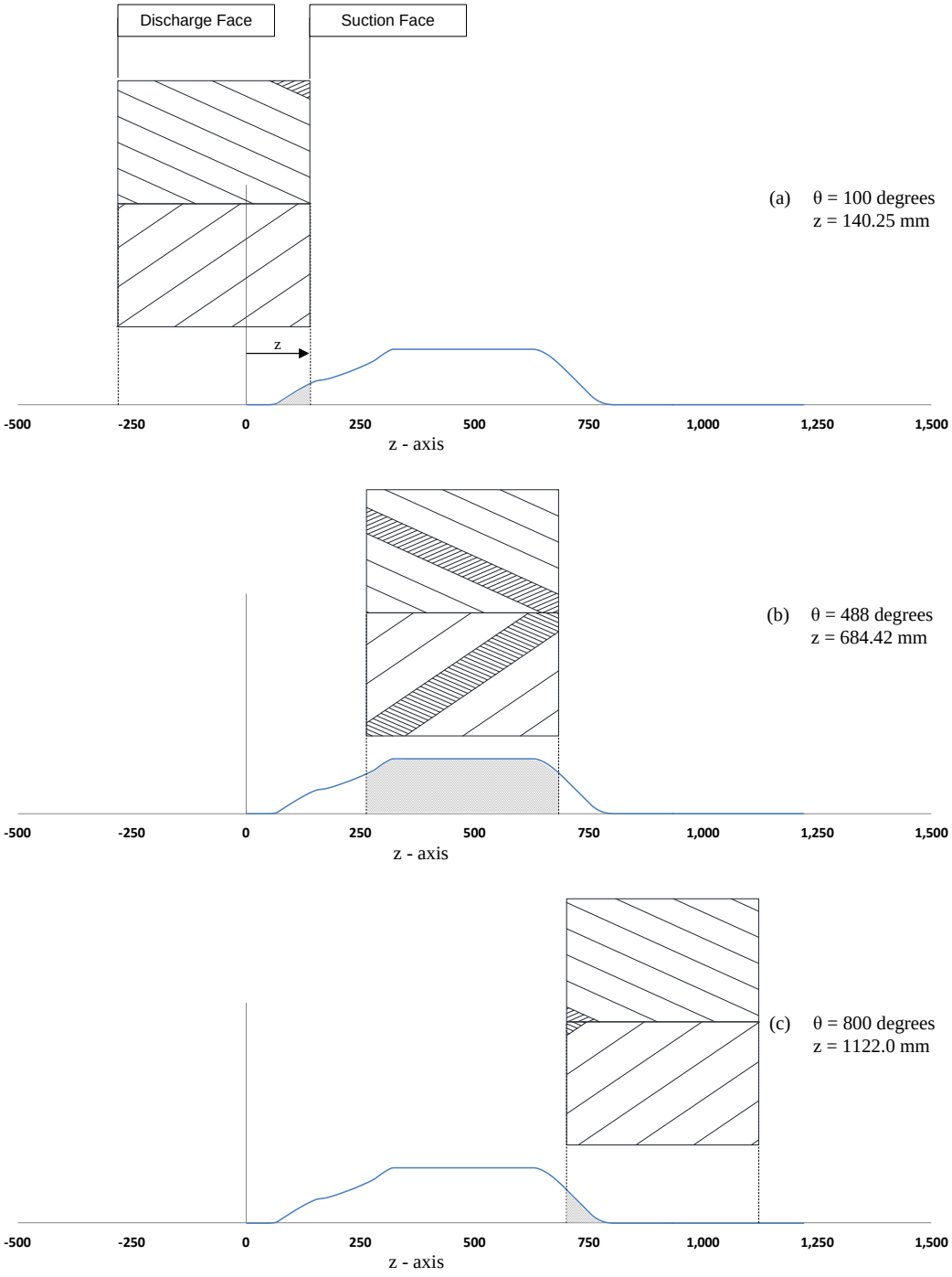

Figure A-8: Area integration limits for volume

A.3.2 SUCTION PORT AREAS

In Figure A-9 the suction port is abbreviated to SP and the discharge to DP. Each port comprises of the area on the main rotor and the area on the gate rotor; identified by subscripts 1 and 2 respectively. In addition the ports can be situated axially or radially or be made of both parts; these identified by subscripts 'a' and 'r'.

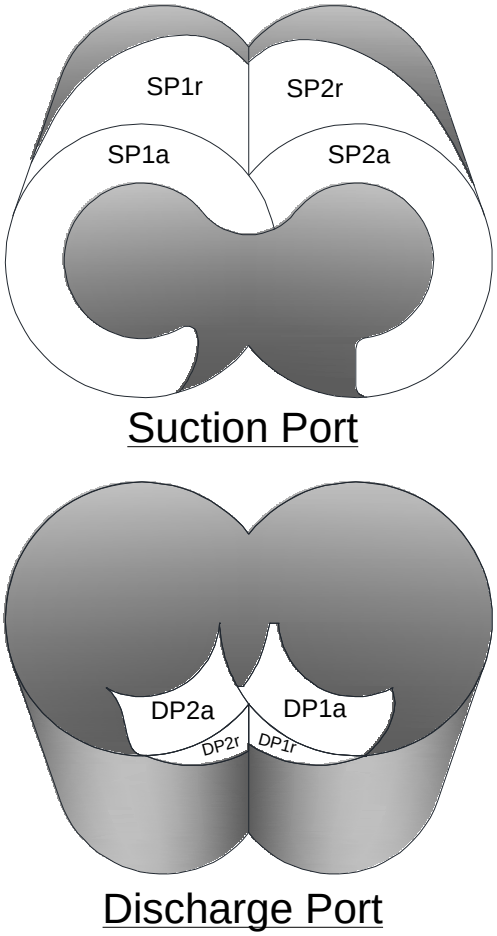

Figure A-9: Designated port names

The shape of the suction and discharge ports is defined by the rotor profile shape and helix at the rotor tips. The size of the discharge port is defined by the rotor position at which the required volume index, V1/V2, has been achieved.

The ports highlighted in Figure A-9 are the full port windows; the effective port areas, for a given compression chamber, depends how the rotors interact with these port windows. The areas through the main suction and discharge ports as

the rotors interact with the casing are calculated using a similar procedure to that used with the chamber cross sectional areas.

A.3.3 BLOW HOLE AREA

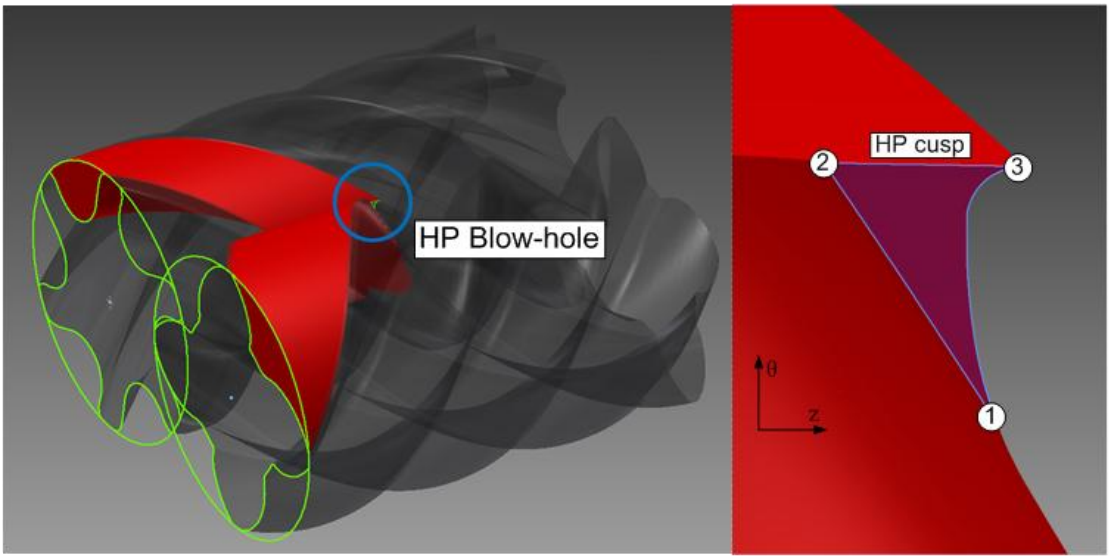

Figure A-10: Blow-hole leakage area

The blowhole area is formed between the tip of the main, the tip of the gate and the cusp of the casing where the rotors meet. For most practical rotor designs the main rotor, gate rotor and casing cusp will not coincide at the same point resulting in the leakage area highlighted in Figure A-10. The area is solely defined by the transverse rotor profiles (highlighted in green) and the rotor helix. This leakage area is handled with its own subroutine that calculates the area between lines 1-2 and 1-3 in Figure A-10b.

A.3.4 SEALING LINES

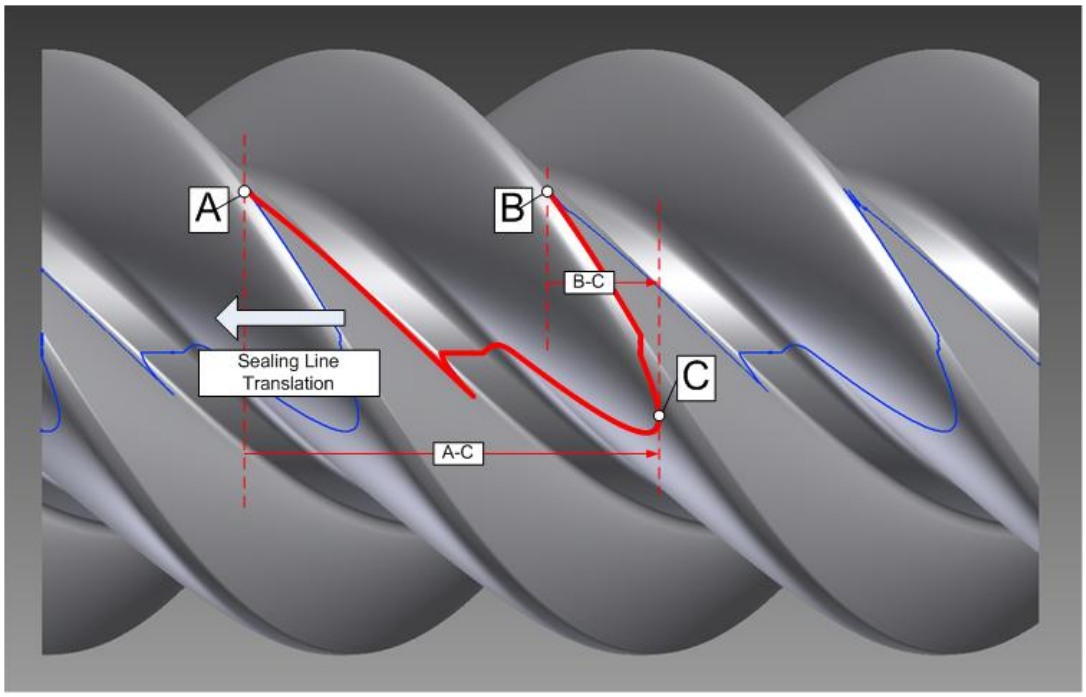

Figure A-11: Interlobe sealing line

Figure A-11 shows the interlobe sealing line - the blue line shows where the main rotor is in closest proximity to the gate rotor when the rotors are in mesh. The part of the line highlighted in red represents the interlobe sealing line for a single compression volume therefore it is the leakage area through this segment that is of interest. Calculation of the sealing lines co-ordinates was explained previously. The length of the sealing line through a discrete number of sealing lines points can be numerically approximated:

$$s_{SLn} = \sum_{i=2}^{n} \sqrt{\left(x_{SLi} - x_{SL(i-1)}\right)^2 + \left(y_{SLi} - y_{SL(i-1)}\right)^2 + \left(z_{SLi} - z_{SL(i-1)}\right)^2} \quad (26)$$

In order to calculate the sealing line length for a given compression chamber, it is necessary to check that the sealing line is within the limits of the rotor length. At the rotor position shown in Figure A-11 the interlobe sealing line highlighted in red is fully formed within the limits of the rotor so the leakage area is maximum. As point A moves beyond the discharge face on the LHS of the figure

the sealing line length and consequently the leakage area will reduce until point C reaches the same discharge face and the leakage area has reduced to zero.

The interlobe area curve shown in blue in Figure A-12 assumes a constant, uniform interlobe clearance distribution. By introducing a relative rotation between the rotors the clearance distribution was altered and the resulting area curve was plotted in green. This serves to demonstrate how changing the clearance distribution, whether by design, due to rotation, reduced centres or some other manufacturing or assembly variation can change both the magnitude and the shape of the interlobe leakage area.

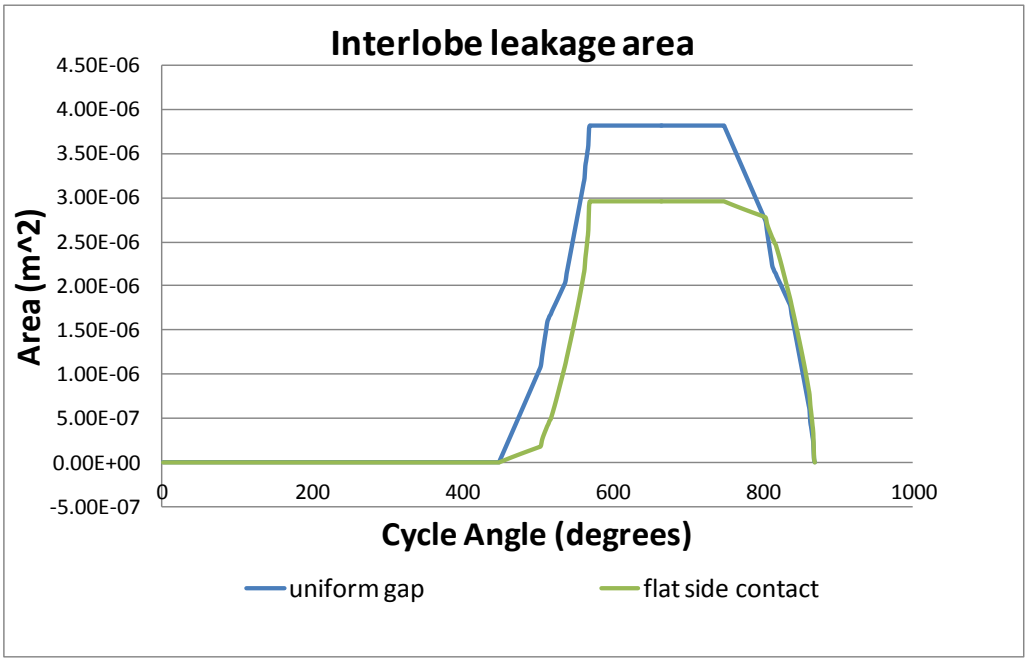

Figure A-12: Interlobe leakage area curves

It is evident in Figure A-12 that there is a region, when the sealing line is fully formed, where the leakage area is constant. This would not be the case if clearances vary along the length of the rotors due to non-parallel rotors or operational distortions caused by high pressures or temperatures. In order to investigate these scenarios the GEOM program was modified to allow the clearance distribution to vary along 2 dimensions: around the transverse rotor profile; and along the length of the rotors. In other words – the surface of the rotor lobe under investigation is divided up using a 2 dimensional grid where the local clearance at each node is unique. The same approach was applied for

the radial sealing line – the local radial clearance at any position on the casing bore can be uniquely defined.

Appendix B
Compressor Modelling

B.1 Chamber Model Details

B.1.1 Model Discharge Temperature

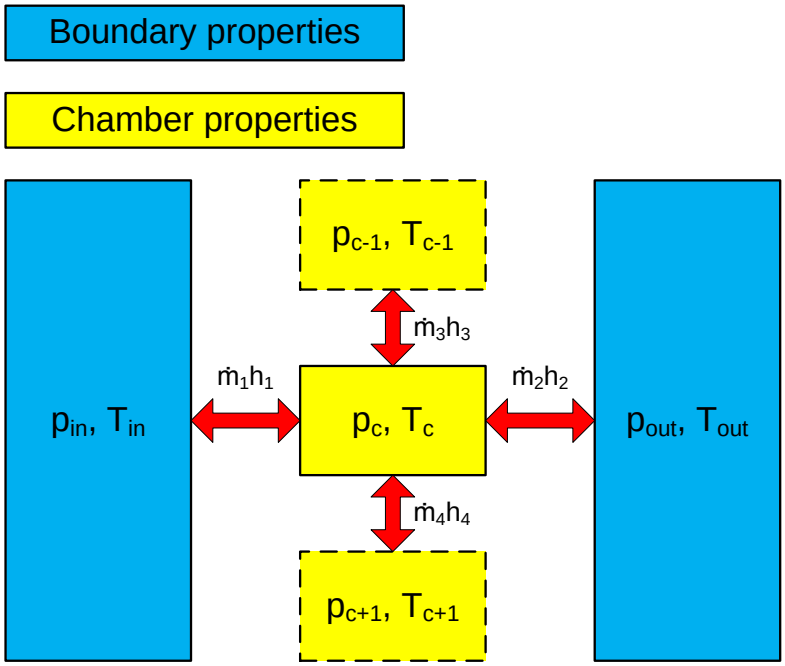

Figure B-1: Chamber model setup

A high level explanation of how the single chamber thermodynamic model works is shown in Figure B-1. In practise, each of the paths along which mass, and therefore enthalpy, can be transported comprise of various ports and leakage paths but these have been grouped to show the overall chamber interaction. The enthalpy can transfer to or from other 'chambers' which are offsets of the single chamber or to or from inlet and outlet boundaries which can be thought of as very large chambers with constant pressure and temperature. The parameters p_{in}, T_{in}, and p_{out} are constant input boundary properties; T_{out} is constant but unknown.

Prior to running the cycle convergence loop, T_{out} is initially calculated as the adiabatic discharge temperature based on the pressure ratio. This initial T_{out} is

used to calculate the initial specific enthalpy at discharge which is in turn used to calculate the isentropic flow through the discharge port. Knowing the flow rate to the outlet and the specific enthalpies in the chamber or outlet (depending on flow direction) at any given time, the total enthalpy change to outlet can be integrated over the cycle duration. The average specific enthalpy of the gas to outlet is calculated as the total enthalpy to outlet divided by the total mass to outlet – this specific enthalpy is then used as the outlet boundary enthalpy in the next iteration for flow calculation. For an ideal gas, the average temperature, T_{out}, at the outlet boundary can be calculated as the average specific enthalpy divided by the specific heat, C_p.

In the version of the chamber model used in this research, the outlet temperature, T_2, was taken to be the value of the temperature in the compression chamber, T_C, at the end of the compression process. In this single chamber model, the instantaneous T_C value at the end of compression is similar to the averaged boundary temperature, T_{out}, providing there isn't significant over or under compression.

B.1.2 ADIABATIC FANNO FLOW

An available description of the leakage flow calculation is repeated here for reference, further detail can be found in (Stosic et al, 2005) and (Stosic, 2015). The leakage velocity through the clearances is considered to be adiabatic Fanno-flow through an idealised clearance gap of rectangular shape and the mass flow of leaking fluid is derived from the continuity equation. The effect of fluid-wall friction is accounted for by the momentum equation with friction and drag coefficients expressed in terms of the Reynolds and Mach numbers for each type of clearance.

$$\dot{m} = \rho v A = \sqrt{\frac{\gamma(p_2^2 - p_1^2)}{c^2\left(\zeta + 2ln\left({}^{p_2}/_{p_1}\right)\right)}} \qquad (27)$$

where c is the speed of sound, $\zeta = FL/D + \Sigma\zeta$ characterises the leakage flow resistance, L the clearance length in the leaking flow direction, f the friction factor and ζ the local resistance coefficient.

B.2 THERMAL ANALYSIS SIMPLIFYING ASSUMPTIONS

B.2.1 ROTOR THERMAL DISTORTION

In isolation, equation (46) in '5.3.2 Local Rotor Distortion' describes 1D thermal distortion but when applied to the radius, for which the angular position is known, and with the stated assumption of a uniform planar temperature, this equation can be used for calculation of 2D thermal distortions.

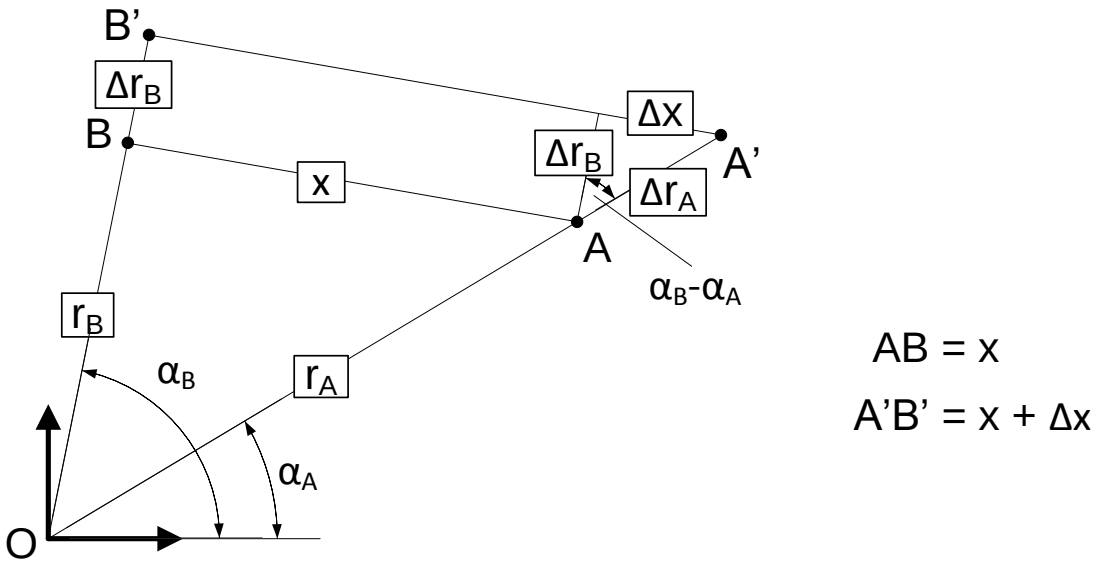

Figure B-2: Uniform 2D thermal distortion

With uniform 2D thermal distortion all relative proportions are preserved. Providing the direction of the radial distortions, Δr_A and Δr_B, of points, A and B, are applied in the correct direction using the appropriate angles, α_A and α_B respectively, then the relative distortion, Δx, between points A and B will be accounted for. This has been demonstrated with the use of similar triangles in Figure B-2.

B.2.2 DATUM FOR RELATIVE CLEARANCE DISTORTION

While the interlobe clearance gap was analysed by investigating the thermal distortion of each rotor and centre distance using a 2D approach, as explained in '5.3 Thermal Distortion of Interlobe Gap', the analysis of the radial gap was, in contrast, reduced to a 1D analysis, as explained in '5.4 Thermal Distortion of Radial Gap'. The main assumption that allows this simplification is the use of

each respective rotor axes, on the main and gate rotor bores respectively, as a common datum so that only radial distortions in the rotors and casing are considered.

The validity of this assumption will be assessed in more detail by considering transverse cross sections of the rotors and casing with uniform temperatures obtained by averaging the surface temperature exposure across that plane. Simplified FEA analysis was considered however as shown in the previous section, if the 2D expansion of each component is uniform it can simply be analysed by considering a representative dimension; in this case the centre distance, A.

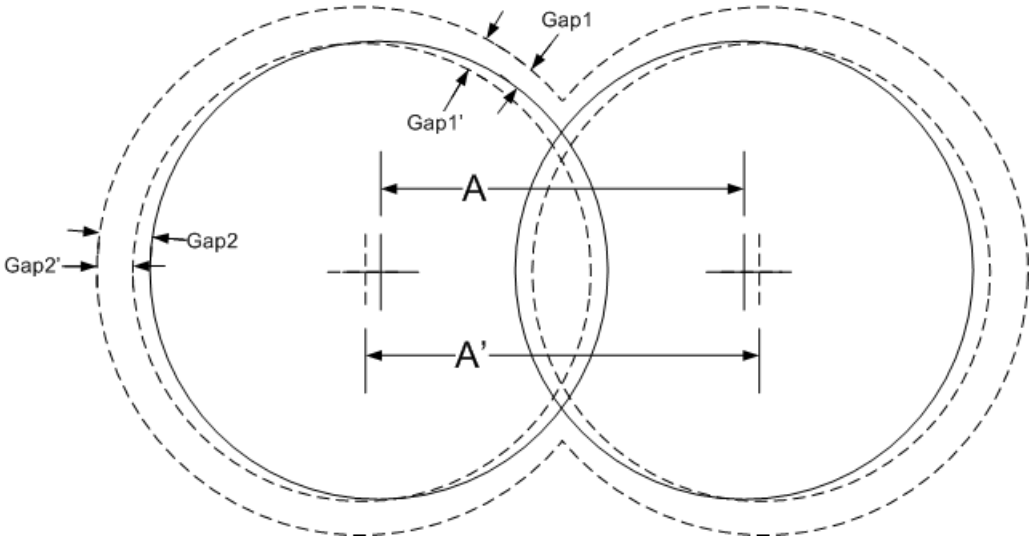

Figure B-3: 2D rotor and casing distortion

In Figure 1-1 two casing distortion scenarios have been presented. The outer dashed line shows the distorted casing bores where the centres of the bores are also marked as dashed lines. In the first scenario the solid circles that represent the rotors are positioned in the undistorted centre distance, A. This kind of scenario could occur in a compressor where the casing is relatively cooler in the vicinity of the bearings than the cross section being analysed, thus resulting in rotors that are not concentric to the casing bore. As a consequence of this the radial clearance will be non uniform so that near the cusp Gap1 would be reduced while Gap2 would be increased.

In the second scenario the rotor positions are represented by the circles with dashed lines that have been adjusted to the same distorted centre distance as the casing at that particular plane. This results in rotors that are concentric to the casing bore and in this case with uniform rotor and casing temperatures across the plane the radial gap is constant so that Gap1' = Gap2'.

Obviously, if the distorted centre distance of the casing is different from the centre distance of the rotors this should ideally be accounted for by using a single common datum for both rotors and casing and calculating the resulting non-uniformity of the radial gap due to the non-concentric rotors. In the current procedure which simplifies the calculations by defining a datum on each axis, the rotors are assumed to be concentric to the casing.

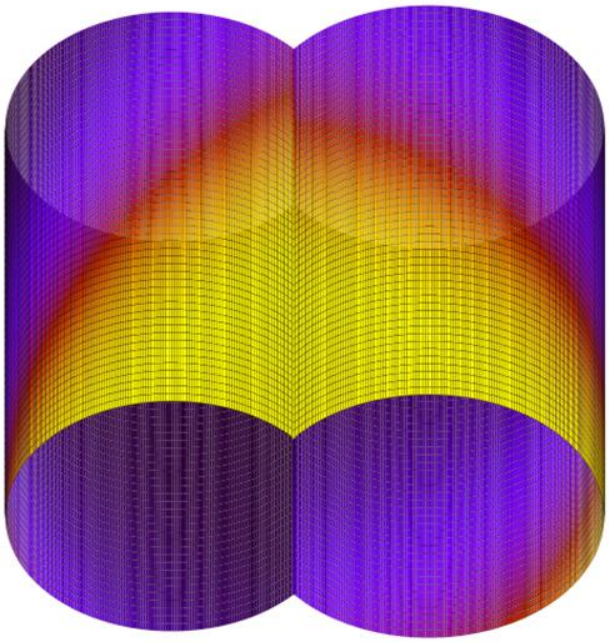

Figure B-4: DRUM127 casing temperature exposure

In the current model the distortion of the rotor axis is based on the distortion of the casing centre distance, A, at the inlet and outlet end planes, as described in '5.3.3 Local Casing Distortion'. So by definition each rotor will be concentric to the casing bore at the inlet and outlet plane. Between these end planes the rotor centre distance will vary linearly since the rotor axes are taken to be straight. However, the axial variation in the average temperature of each casing cross section is not necessarily linear and there is likely to be some deviation between

the rotor and casing centre distances. In order to quantify this effect, results from the DRUM127 compressor model are used; the casing exposure is shown in Figure B-4 where the temperature ranges from 25°C to 160°C. The temperature exposure was averaged at each transverse plane in order to estimate the average 2D casing temperature at that plane. The variation in the casing temperature, which describes distortion of the casing centre distortion, is compared against the interpolated temperature, which describes the rotor centre distortion, in Figure B-5. Note that the temperature shown in this figure is actually the ΔT, which is the different between the absolute temperature and the reference ambient temperature which has been taken as 20°C.

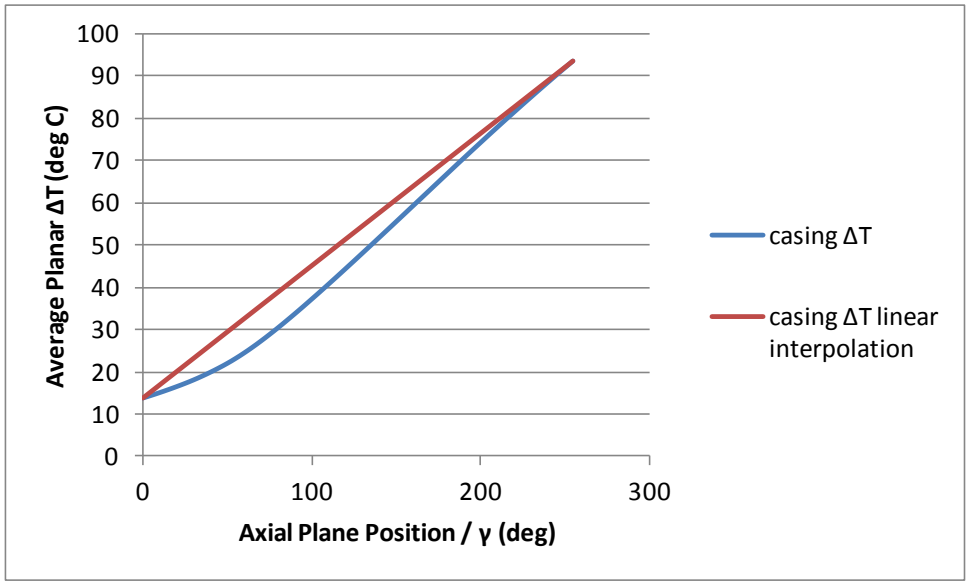

Figure B-5: DRUM127 axial casing temperature variation

The maximum variance between the casing ΔT and the interpolated ΔT is 8.4°C. When applied to the centre distance for this compressor, where A = 0.093m, for cast iron, this equates to an error of less than 10μm. This results in a concentricity error of less than 5μm on each rotor. The nominal radial clearance for this compressor is 100 μm therefore the maximum relative error due to non-concentricity (along a limited region of the axial length) is +/- 5%. Recall from the example presented in Figure B-3 that the non-concentric rotor results in opposing changes between Gap1 and Gap2 which further mitigates this error in terms of the net radial leakage area used for performance calculation. In

conclusion the assumption of using each rotor axis as a datum in justified for the current model.

Appendix C
Definition of Performance Characteristics

C.1 Compressor Boundaries

In order to evaluate the compressor performance the metrics used must be clearly defined. The compressor can be considered to be a 'black box' that can be dropped into any system and described by only its inputs and outputs. The inputs will be defined at the inlet flange, the outputs at the outlet flange and the work in for a compressor is defined at the drive shaft – this has been shown in Figure C-1.

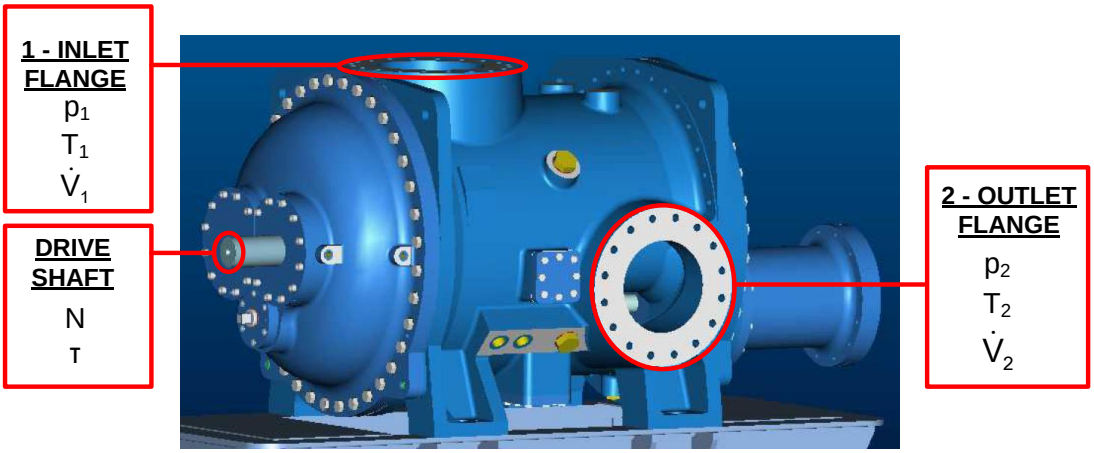

Figure C-1: Compressor boundaries for performance evaluation

For a full energy balance of the compressor there would be additional inputs and outputs to describe heat rejection to surroundings or oil. However, for an evaluation of the compressor performance it is usually sufficient to measure the useful work done on the gas by considering these described inputs and outputs.

For a known fluid, all thermodynamic properties can be derived if both pressure, p, and the temperature, T, are known. For example, knowing p_1 and T_1 at the inlet, the density, ρ_1, can be derived. Similarly the density at the outlet, ρ_2, can be calculated using the pressure at temperature at that flange.

C.2 MASS FLOW

The other crucial measurement for performance evaluation is the mass flow, ṁ. This is usually measured remotely from the compressor, usually with an orifice situated upstream of the compressor on the low pressure ducting. There is an assumption here that no leakage occurs to the surroundings between the position of flow measurement and the discharge of the compressor. This is a reasonable assumption since the only external seal is on the drive shaft which under normal operating conditions will leak only a small volume of oil that is negligible relative to the gas flow. From mass continuity, the actual volume flow at a specific location with a known density can be found. In this work, the volume flow is always defined at the inlet using, $\dot{V}_1$, which is calculated:

$$\dot{V}_1 = \dot{m}/\rho_1 \qquad (28)$$

The shaft power, P_{SHAFT}, is simply calculated as the product of the measured speed and torque. This shaft power is often referred to as the 'total power' as it is the sum of the power supplied to the compression fluid and the power lost to all other inefficiencies including mechanical losses incurred in the bearings, shaft seals and timing gears, if applicable. The focus of this research was on the thermodynamic model of the compression process therefore the shaft power was not used for model evaluation because of the uncertainty in the proportion of work acting on the gas.

C.3 VOLUMETRIC EFFICIENCY

Generally, absolute flow results can be used to compare the modelled performance against test measurements, as was done in the DRUM127 case study. In the HS204 case study the volumetric efficiency was compared instead of absolute flow – this provides essentially the same comparison while giving a little more insight into how well the compressor is performing. In this work the volumetric efficiency is defined as the ratio of the actual inlet volume flow rate to the theoretical volume flow rate for that compressor at the same operating speed:

$$\eta_{VOL} = {\dot{V}_1}/{\dot{V}_{TH}} \quad (29)$$

The theoretical volume flow rate is calculated using the volume displacement constant; this is expressed as the displaced volume per revolution of the drive shaft and is a geometric feature of the compressor.

C.4 ADIABATIC EFFICIENCY

Typically, the adiabatic efficiency is described as the 'total efficiency' using the shaft power:

$$\eta_{ADI} = {P_{ADI}}/{P_{SHAFT}} \quad (30)$$

However, as discussed previously the shaft power was not investigated in this research - instead the adiabatic efficiency can be described using the indicated power from the thermodynamic compression process – this includes the effect of any heat transfer during compression but neglects any mechanical losses:

$$\eta_{ADI} = {P_{ADI}}/{P_{IND}} \quad (31)$$

This is the most suitable efficiency for evaluation of the thermodynamic performance at it captures the influence of all heat transfer, leakages, and under or over compression. Indicated power is not normally available from compressor test results so a useful way to approximate the adiabatic efficiency of the thermodynamic process is to use the actual measurements p_1, p_2, T_1 and T_2, as defined in Figure C-1. The gas properties at the inlet and outlet of the compressor are used to define a polytropic process path. This is an approximation of the indicated process path that doesn't account for effects such as over or under compression and as such the efficiency calculated in this way can be slightly higher than the value from the indicated power:

$$\eta_{ADI} = {\Delta h_{ADI}}/{\Delta h_{POLY}}\,\eta_{VOL} \quad (32)$$

Where the specific enthalpy for the adiabatic process is defined:

$$\Delta h_{ADI} = \frac{k}{(k-1)} R(T_{2\_ADI} - T_1) \quad (33)$$

The specific enthalpy for the polytropic process is defined:

$$\Delta h_{POLY} = \frac{n}{(n-1)} R(T_2 - T_1) \quad (34)$$

And the polytropic exponent is calculated using:

$$n = \frac{1}{\left(1 - \frac{\ln\left(\frac{T_2}{T_1}\right)}{\ln\left(\frac{p_2}{p_1}\right)}\right)} \quad (35)$$

In practise for an oil free compressor, the measured outlet temperature, T_2, is higher than the adiabatic outlet temperature, T_{2_ADI}, resulting in a polytropic exponent: n > k. This implies that there is heat transfer to the compression gas which reduces efficiency. In reality, this heat is primarily supplied due to a net enthalpy increase introduced through leakage flows into the control volume.

Both specific enthalpies changes in equations (33) and (34) are calculated assuming a system with constant mass. This is ok for the adiabatic process curve as that represents the ideal compression process however the polytropic process curve is intended to approximate an open system with net leakage losses therefore the specific enthalpy change calculated in equation (34) is not representative of the actual process. To compensate for the difference in specific enthalpy change caused by the theoretical and the actual delivered mass flow the volumetric efficiency was included in equation (32).

An example case was modelled in order to evaluate the approximate polytropic curve, as shown in Figure C-2. The adiabatic efficiency based on the indicated PV curve was 71.0% while the efficiency based on the temperatures and polytropic path was 72.7%. The indicated curve captures a slight over-compression hence that efficiency is a little lower.

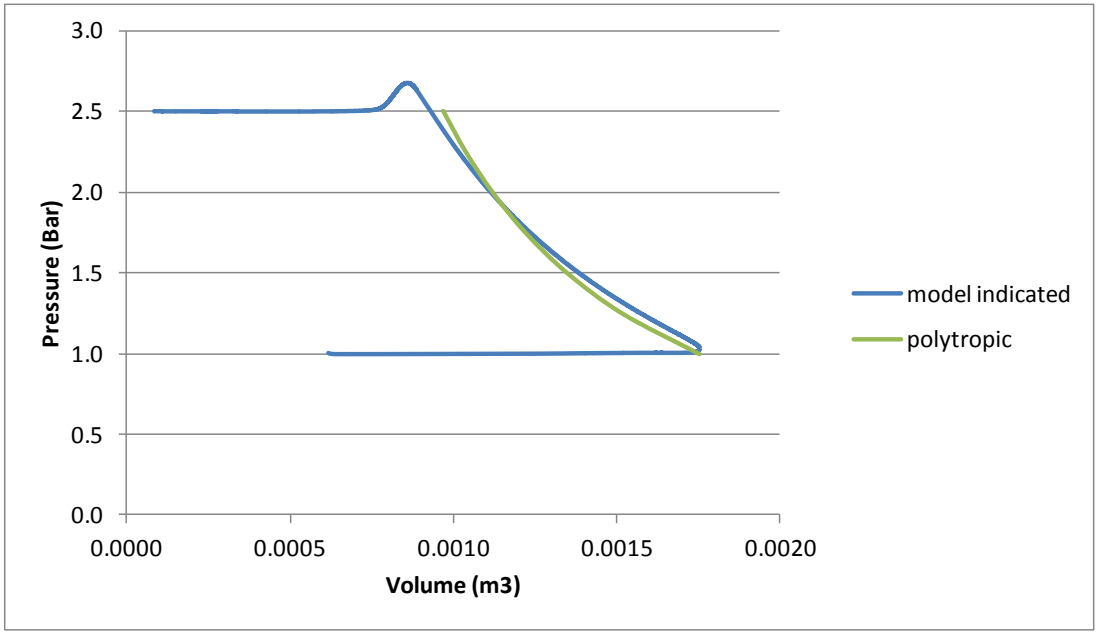

Figure C-2: Comparison of model indicated PV curve and polytropic curve